



OPTICAL AND THERMAL  
OPTIMISATION OF PARABOLIC  
TROUGH SOLAR COLLECTORS FOR  
HEATING APPLICATIONS VIA A  
NOVEL RECEIVER TUBE

A Thesis submitted by

**Khaleel Saleem Jebur Al-Ogaili**

For the award of

**Doctor of Philosophy**

2019

# Abstract

Non-renewable energy sources (fossil fuels) remain economically advantageous because of their abundance and capacity to generate a large amount of energy in single location. Pollution is a major issue of utilising this energy, while it is becoming more challenging to extract them. In the world in each second approximately 1.2 million kilograms of CO<sub>2</sub> are released into the atmosphere; non-renewable resources contribute the majority of these emissions, because they are mostly responsible for energy generation. The resultant climate change increases the earth's surface temperature, leading to loss of ice mass, elevation of sea level and flooding. Therefore, due to the increase in the world's fossil fuel energy consumption, limit to its resources and growing worldwide pollution issues, there is an urgent need for environmentally-friendly and sustainable energy resources. Renewable energy resources are sustainable resources that produce zero greenhouse gas emissions while producing the energy. It should be noted that pollution is generated during the manufacture and decommissioning of renewable technology components. Solar energy is the most abundant and geographically widespread resource and it has tremendous advantages over other renewable energy resources. Concentrating solar power (CSP) is the main solar thermal technology for commercially converting solar energy into electricity, in addition to its ability to provide energy for heating applications.

Among all of the CSP technologies, Parabolic Trough Solar Collectors (PTSC) are the most mature, efficient and cost-effective technology. The main principle of PTSC operation is to reflect direct solar radiation from a parabolic mirror (the reflector) that focusses the radiation on the receiver tube to heat a Heat Transfer Fluid (HTF). The receiver tube is constructed by encasing the metal absorber tube (through which the HTF flows) with a glass envelope; the space between the absorber tube and glass envelope is evacuated in many existing designs.

There are some challenges with the operation of PTSC systems. PTSC optical efficiency is principally reduced by the reflected radiation deviating from the focal line due to geometric inaccuracies, such as collector and receiver tube misalignments, in addition to wind changes. Moreover, the HTF temperature can reach 400 °C, increasing the temperature of the glass cover surrounding the absorber tube. The

resultant heat losses reduce the useful heat gain and decrease the PTSC thermal efficiency. In addition, the bottom portion of the receiver tube is normally exposed to concentrating sunlight, whereas the upper part of the receiver is subjected to direct normal solar radiation. As a result the heat flux distribution on the absorber tube receiver surface is highly non-uniform, which results in high temperature gradients. Consequently thermal deformation in the absorber tube occurs, could break the glass cover. The evacuated receiver tube is costly, amounting to 30% of the total initial material cost of the PTSC solar field; it is difficult to repair any faults, which results in a high replacement cost.

Therefore, the goal of this thesis is to design, model and investigate an alternative receiver tube for PTSC systems. This new design can reduce the optical and heat transfer losses in addition to improving (making more uniform) the solar heat flux and temperature distributions on the absorber tube. By achieving this goal there is an economic benefit due to improving PTSC performance (producing more heat), while simultaneously reducing the maintenance and replacement costs. This will result in greater acceptance of PTSC technology, improving its commercial market. To achieve this goal, optical and thermal enhancements have been implemented.

For the optical aspect, a PTSC heating system consisting of two identical collectors has been designed and manufactured; one collector was used as a control during each test. To confirm the suitability of the control, the collectors were setup identically; the tests confirmed that there was no bias in the system. The standard configuration (a parabolic collector and absorber tube) was designated “Cp”. The other collector was modified by attaching a smaller, secondary parabola (SP) with a mirror sheet (SPM) on the opposite side of the absorber tube so that the primary collector and SP shared the same focal line. This configuration was called Cs. The purpose of the SPM is to reflect any deviated solar radiation towards the absorber tube, and also to potentially distribute some of the reflected heat flux onto the upper part of the absorber tube. The Cs was directly compared to Cp in some experiments to assess the potential improvements in efficiency of the SPM.

Because the SPM blocks some of the solar radiation from reaching the absorber tube or the primary mirror in Cs configuration, another SP was painted black (SPB). The SPB was setup in the same manner as the SPM in configuration “Cb”. Therefore, the

effect of the lost direct radiation was isolated by comparing Cs and Cb directly. Two types of experimental tests were performed for the two configuration comparisons: tracking tests, where the PTSC tracked the sun throughout the day from sunrise until sunset; and fixed tests, where the PTSC was aimed at the noon position of the sun (simulating the noon position of the sun throughout the year). The experimental results for the Cs and Cp overall average efficiencies during the tracking stage were  $44.94\% \pm 0.04\%$  and  $44.55\% \pm 0.04\%$  respectively (Cp efficiency equals 99% of the Cs efficiency), while their overall average annual noontime efficiencies during the fixed stage were  $23.74\% \pm 0.02\%$  and  $20.55\% \pm 0.02\%$  respectively (Cp efficiency equals 86% of the Cs efficiency). This means that the SPM improved the optical efficiency of the Cs collector, because 8.5% of its aperture area was blocked by the SPM aperture area. The mirror on the SP improved the thermal efficiency of the Cs when compared to the Cb efficiency. The experimental results for the Cs and Cb overall average efficiencies during the tracking stage were  $42.92\% \pm 0.03\%$  and  $38.52\% \pm 0.03\%$  respectively (Cb efficiency equals 86% of the Cs efficiency), while their overall average annual noontime efficiencies during the fixed stage were  $18.43\% \pm 0.02\%$  and  $13.95 \pm 0.02\%$  respectively (Cb efficiency equals 75% of the Cs efficiency).

Improving the PTSC optical performance by using an SPM increased the HTF temperature. However, this increased fluid temperature could augment the receiver tube heat loss. Therefore, the blocked area that resulted due to utilising the SPM geometry (optical enhancement) was employed for receiver tube thermal enhancement by including thermal insulation in the receiver tube. The insulation layer that was placed on the inner surface of the upper part of the receiver glass envelope has the same shape and covered the same area as the SPM. This configuration was investigated using 3D Computational Fluid Dynamics (CFD). Due to the low thermal conductivity of the insulation layer, conduction heat transfer across the glass cover is reduced and therefore the glass cover outer surface temperature was reduced. This reduced the heat transfer loss between the glass outer surface and the atmosphere. In addition, the insulation layer also increased the air temperature between the absorber tube and the glass envelope for a non-evacuated receiver tube, especially in the upper portion of this region. This produced a better temperature distribution on the absorber tube outer surface, which would reduce its propensity for thermal deformation. Several designs of receiver tube cross-section were tested for various wind speeds. It was found that

the insulation enhanced the collecting efficiency for each cross-section, and the efficiency of the circular receiver tube was the highest.

These results demonstrate that modification of the receiver tube is a viable possibility for a future design that improves the operating efficiency and working life of the receiver tube.

# Certification of Thesis

This Thesis is entirely the work of **Khaleel Saleem Jebur Ogaili** except where otherwise acknowledged. The work is original and has not previously been submitted for any other award, except where acknowledged.

Principal Supervisor: Assoc. Prof. Andrew Wandel

Associate Supervisor: Prof. Talal Yusaf

Student and supervisors signatures of endorsement are held at the University.

# Acknowledgements

With the number of days and nights that have passed, and the huge number of ideas that have circulated in my mind, I thank my God who was on my side to get this work up out from the darkness and into the light. I would like to bow down and offer thanks and praises to the Almighty God for providing me with the good health, wisdom and courage required to pursue this research.

The most beautiful words in the language and the first words of thanks and my foremost gratitude goes to my supervisor, Assoc. Prof. Andrew Wandel. I am perpetually grateful to him and offer him my deepest thanks and warmest appreciation for his consistent support and direction throughout my academic journey. He was by my side as a brother and friend as a good help to complete this work, he has been a great example of an individual who has achieved excellence in both scientific research and as a human being. His kindness and patience are greatly appreciated.

I would like to thank my co-supervisor Prof. Talal Yusaf for his support during my PhD study journey.

I wish also to present my warm thanks to Mrs Weide Wandel for her kind assistance in the proof-reading. Also, I would also like to express my gratitude to the workshop staff and technicians who helped me by their efforts in manufacturing the heating system.

I would like to give a heartfelt thanks to my wonderful family, my mother, my wife, my sisters and my lovely daughter Larren who made all this possible to complete my studies.

My warmest regards go to my Iraqi government, Ministry of Higher Education and Scientific Research, for providing me the PhD scholarship and supporting me financially to complete my PhD study. Their support is gratefully acknowledged.

Finally, I dedicate this work:

...to the soul of my father (Saleem Jebur Al-Ogaili); I wish he was alive to see what I have achieved and to share my happiness for completing this research. I hope that this work makes you proud and happy.

...to everyone who looks at the golden sun's radiation as a treasure of science,

...to science students all over the world,

...to the next generation of students that they take my advice to patiently undertake their research, and thereby successfully achieve their goals,

...to all the teachers who paved our way.

***Khaleel Saleem Jebur Al-Ogaili***

University of Southern Queensland

March 2019

# Table of Contents

## Contents

Abstract .....	i
Certification of Thesis .....	v
Acknowledgements .....	vi
Table of Contents .....	viii
List of Figures .....	xi
List of Tables.....	xix
Abbreviations .....	xx
Chapter 1 Introduction.....	1
1.1 Non-renewable energy and its effect.....	1
1.2 Solar energy and concentrating solar power technologies .....	2
1.3 Aim and objectives of the thesis.....	3
1.4 Thesis outlines .....	4
Chapter 2 Optical and thermal losses of the PTSC system and available solutions.....	5
2.1 Introduction .....	5
2.2 Sources of PTSC optical losses and optical enhancement technologies. ....	11
2.2.1 Sources of PTSC optical losses .....	11
2.2.2 PTSC optical enhancement techniques.....	34
2.3 Receiver tube thermal loss and enhancement technologies.....	38
2.3.1 Convection heating loss of PTSC receiver tube .....	38
2.3.2 Receiver tube enhancement techniques .....	46
2.4 Summary of the project .....	66
2.4.1 PTSC Optical loss.....	66
2.4.2 PTSC thermal loss .....	68
Chapter 3 Experimental structure and instruments of solar heating system.....	70
3.1 Introduction .....	70
3.2 Collector reflector (mirror).....	71
3.3 Structure of the reflector support frame .....	72
3.4 Main parts of collector base .....	74
3.4.1 Secondary parabola (SP).....	77
3.4.2 Heat collection element .....	82
3.5 Tracking system .....	83

3.6 Storage tank .....	87
3.7 Pumps and water cycles .....	88
3.8 Electronic Control System .....	90
3.9 Instruments and testing methods.....	91
3.9.1 Solar data meter.....	91
3.9.2 Temperatures measurement.....	92
3.9.3 Flow meter measurement .....	93
3.9.4 Data recording.....	93
3.10 Installing the solar heating system on the selected site.....	93
Chapter 4 Experimental tests of the PTSC optical and thermal performance.....	95
4.1 Introduction.....	95
4.2 System Verification .....	95
4.3 Configuration of experimental cases.....	96
4.4 Solar collector thermal efficiency.....	98
4.5 Results of tracking stage .....	99
4.5.1 Effect of adding secondary mirror (case 1).....	100
4.5.2 Effect of adding secondary mirror (Case 2).....	108
4.6 Results of fixed stage .....	117
4.6.1 Effect of adding secondary mirror (case 3).....	122
4.6.2 Effect of adding secondary mirror (case 4).....	128
4.7 Effect of modified collector for different seasons.....	135
4.8 Summary .....	136
4.8.1 Outcomes of the optical enhancement experimental investigations.....	136
4.8.2 Optical enhancement evaluation .....	138
Chapter 5 Alternative Receiver Tube CFD Model .....	139
5.1 Introduction.....	139
5.2 Solar heat flux calculation .....	141
5.3 Physical model of the alternative receiver tube. ....	145
5.4 Heat transfer analysis.....	148
5.5 Mesh independence.....	150
5.6 Boundary conditions .....	151
5.7 Setup of the numerical model .....	152
5.8 Model validation .....	152
5.9 Summary .....	153
Chapter 6 Analysing effects of thermal insulation on alternative receiver tube performance .....	155
6.1 Introduction.....	155

6.2 Circular receiver tube .....	155
6.2.1 Glass envelope and annular domains temperatures distribution.....	155
6.2.2 Temperature distribution of the absorber tube and HTF domains.....	159
6.2.3 Outer surface of glass envelope average temperature.....	161
6.2.4 Average temperature difference between absorber tube and HTF .....	162
6.2.5 System heat transfer.....	163
6.3 Hybrid and parabolic receiver tubes.....	165
6.3.1 Annular air and glass envelope domain temperature distribution .....	166
6.3.2 Absorber tube and HTF domains temperature contour of the hybrid and parabolic .....	169
6.4 Comparing between the three types of the receiver tubes .....	172
6.4.1 Glass cover temperature .....	172
6.4.2 System heat transfer.....	173
6.5 Summary .....	175
6.5.1 Outcomes of the thermal enhancement numerical investigations.....	175
6.5.2 Thermal enhancement evaluation .....	176
Chapter 7 Conclusions.....	178
7.1 Parabolic trough solar collector heating system challenges .....	178
7.2 Optical solution and limitations .....	178
7.3 Thermal solution and limitations.....	181
7.4 Commercial opportunity.....	183
7.5 Recommendations and future work.....	183
References .....	185
Appendix A Circular receiver tube .....	193
Appendix B Hybrid receiver tube .....	197
Appendix C Parabolic receiver tube.....	201
Appendix D Economic calculations for the modified receiver tubes.....	206

# List of Figures

Figure 1.1 History and projection of world energy consumption from renewable and non-renewable energies from 1990 to 2040 (U.S. Energy Information Administration 2018). .....	1
Figure 1.2 Yearly average global temperature on Earth from 1880 to 2014 (National Aeronautics and Space Administration 2019, June 1). .....	2
Figure 2.1: View of PTSC solar thermal plants in California’s Mojave Desert in the USA (Quaschnig & Muriel 2002). .....	6
Figure 2.2: Schematic of a parabolic-trough collector showing the collector aperture width, receiver, reflector and tracking system. Structure of collector’s receiver tube is also shown (Cabrera et al. 2013). .....	7
Figure 2.3: Main components of the PTSC system (Quaschnig & Muriel 2002). .....	8
Figure 2.4: 3D scheme of the outer and inner mirrors of the reflector, $f$ is the collector focal length (Lüpfert & Ulmer 2009). .....	13
Figure 2.5: The intercept factor and the focus deviation on the inner and outer mirrors of the PTSC (Lüpfert & Ulmer 2009). .....	13
Figure 2.6: Cross section of the PTSC showing key geometric parameters in addition to path of the solar reflection (Chafie et al. 2016). .....	14
Figure 2.7: Slope error values under variety of incident angles (from $0^\circ$ to $75^\circ$ ) and rim angles (from $0^\circ$ to $180^\circ$ ) (Huang & Han 2012). .....	15
Figure 2.8: The effect of slope errors on the solar heat flux distribution on the collector absorber tube under (a) zero specular errors and (b) under 3 mrad specular errors (Mwesigye et al. 2016). .....	17
Figure 2.9: The effect of slope errors on (a) collector intercept factor and (b) collector thermal efficiency (Mwesigye et al. 2016). .....	18
Figure 2.10: Installation errors of PTSC receiver tube in the $y$ (left) and $x$ directions (right) (Zhao et al. 2016). .....	19
Figure 2.11: The solar heat flux distribution on receiver tube for (a) $x$ axis for different installation errors and under zero degree incident angle & CR=20. (b) for different CR (20, 30 and 40) with 0.2% $y$ axis installation errors (Zhao et al. 2016). .....	19
Figure 2.12: Deviation of incident sunrays at cross section of PTSC aperture area (Simonović et al. 2016). .....	20
Figure 2.13 Receiver support location and $x$ deviation of two typical alignment data of Euro trough solar collector out of specs (red line) showing the receiver tube misalignment in $x$ -direction before the improvement, while the in space (green line) showing the receiver tube misalignment in $x$ -direction after the improvement (Pottler et al. 2014). .....	21
Figure 2.14: Solar heat flux distribution on receiver tube at various rim angles and CR (Mwesigye et al. 2014a). .....	22

Figure 2.15 Solar heat flux distribution on receiver tube under several CR and various rim angles of PTSC (He et al. 2011). .....	23
Figure 2.16: RMS slope and focus deviation for outer (right) and inner (left) mirrors that fixed onto ideal, elastic and cantilever PTSC reflector model structure(Meiser et al. 2015).....	25
Figure 2.17: The shape of the solar heat flux for tracking errors under (a) CR 20, zero incident angle and various tracking errors, (b) under 3 mrad tracking error CR 20 and various solar incident angles The non-symmetrical heat flux on absorber tube surface is due to the reflected heat flux being predominantly distributed on one side of the absorber tube because of collector tracking error (Zhao et al. 2016).....	27
Figure 2.18: Optical efficiency (Y-axis) of a PTSC at different tracking errors (varying from 0 mrad to 18 mrad) and various incident angles (X-axis) (Huang et al. 2012).....	28
Figure 2.19: Influences of tracking errors varying from 0° to 1.25° on the PTSC optical efficiency (Islam et al. 2017).....	29
Figure 2.20: Fluctuation of total wind load on the collector aperture area for various collector orientations and wind speeds (Naeeni & Yaghoubi 2007b).....	30
Figure 2.21: Instantaneous wind speed field (Mier-Torrecilla et al. 2014).....	31
Figure 2.22: Wind velocity distribution around PTSC structure under different collector pitch angles: (a) $\theta=0^\circ$ , (b) $\theta=45^\circ$ and (c) $\theta=90^\circ$ , and under Reynolds number $3.9 \times 10^5$ (top) and $1 \times 10^6$ (bottom) (Hachicha et al. 2014). .....	32
Figure 2.23: Wind load on shallow and deep trough of PTSC, under 30° pitch angle and 0° yaw angle (top row) and 30° pitch angle and 45° yaw angle (bottom row) (Paetzold et al. 2015).....	33
Figure 2.24: Views of cross sections of the glass mirror and film mirror of PTSC reflector with receiver tube (Xu et al. 2014). .....	35
Figure 2.25: Schematic of the PTSC models. The concrete (left) and prototype (right) both have same aperture area dimensions (Forman et al. 2015). .....	37
Figure 2.26: Schematic of the trough collector model consisting of five reflecting panels with 12 m length and 6 m overall aperture width (Prahl et al. 2011). .....	38
Figure 2.27: Thermal loss of the HCE and end joint points of the receiver tube (Wu et al. 2015).....	40
Figure 2.28: Parabolic collector with absorber tube at Shiraz solar power plant (Naeeni & Yaghoubi 2007). .....	41
Figure 2.29: HCE heat loss and the absorber tube temperature (Hachicha et al. 2013). .....	42
Figure 2.30: Heat loss per unit length for various HCE temperatures (Patil, Panse, et al. 2014).....	44
Figure 2.31: Influences of the external wind velocity on the heat loss from the receiver glass envelope for different absorber tube temperatures (Patil, Panse, et al. 2014).....	44
Figure 2.32: Thermal loss of three different diameters of HCE under different operating temperatures (Navarro-Hermoso et al. 2016).....	46

Figure 2.33: Cross section of the cavity absorber. The glass cover (lower part of the receiver) is exposed to the reflector, thereby receiving the concentrated solar radiation on the absorbing surfaces for transfer to the working fluid; the upper part (facing the incident solar radiation) is insulated (Chen et al. 2015). .....	47
Figure 2.34: Effect of fins on the relationship between the absorber temperature ( $t_i$ ) and HTF temperature ( $t_f$ ) (Chen et al. 2015).....	48
Figure 2.35 Schematic of the alternative receiver tube (HTA) structure, consisting of three absorber tubes placed inside a glass cover. The lower part of the modified receiver tube is subjected to the concentrated solar radiation in addition to diffuse radiation. The upper part (which consists of an absorber plate that covers the three tubes) is subjected to the normal solar radiation (Kajavali et al. 2015).....	49
Figure 2.36: Solar intensity data and the efficiency comparison between the single tube absorber (STA) and the header tube absorber (HTA) (Kajavali et al. 2015). ....	49
Figure 2.37: Schematic of the receivers (a) non-evacuated, (b) evacuated and (c) evacuated shell receiver (Daniel et al. 2011). .....	50
Figure 2.38: Difference of heat loss for three receivers at different temperatures and wind speeds (Daniel et al. 2011). .....	51
Figure 2.39: Longitudinal and cross section of the structure of the PTSC optimised receiver tube structure with distribution shape of pin fin array inserts (PFAI) (Gong et al. 2017).....	52
Figure 2.40: Cross section of (a) reflector and conventional receiver and (b) reflector and novel receiver. Yellow lines are the solar rays (Fan et al. 2018). .....	53
Figure 2.41: Plain twisted tape (a) and Nails with twisted tape (b) geometries. $y$ is the twist ratio of the tape ( $y=H/W$ ), $H$ is the pitch for 180° rotation of twisted tape (m), while $W$ represents the width of the twisted tape (m). Nail dimensions equal 11 mm length, 1.5 mm diameter and 3 mm head diameter(Jafar & Sivaraman 2017). .....	55
Figure 2.42: Absorber tube wall temperatures for plain and modified absorber tube under various twist ratios ( $Y=2, 3, 5$ ) (Jafar & Sivaraman 2017).....	56
Figure 2.43: Geometry of the Louvered twisted tape with perforations (Ghadirijafarbeigloo et al. 2014).....	57
Figure 2.44: Schematic of modified absorber tube by porous medium along the length of the HCE (Kumar & Reddy 2012). .....	60
Figure 2.45: Heat loss of various absorber tube configurations under different mass flow rate values (Reddy & Satyanarayana 2008).....	61
Figure 2.46: Cross section of the absorber tube with the metal foam insertion (Wang et al. 2013).....	62
Figure 2.47: Absorber tube section with the metal foam layout (Wang et al. 2013). .....	62
Figure 2.48: Mesh section and 3D view of the corrugated absorber tube (Fuqiang et al. 2016).....	63
Figure 3.1: The experimental solar heating system installed on site. ....	71
Figure 3.2: Super mirror stainless steel grade 316 (left) and the installed mirrors of the solar heating system (right), consisting of two symmetrical parabola collectors. ....	72

Figure 3.3: Plans of the symmetrical primary reflectors, $\theta_r$ is the rim angle of the aperture area. ....	73
Figure 3.4: Primary collector structure showing the mounting of the mirrors (reflector), pivot for hourly tracking (frame shaft) and mounting supports for the absorber tube and secondary reflector (blue components), alignment indicator and tracking sensor.....	74
Figure 3.5: The assembled support structure for the mirrors. ....	75
Figure 3.6: Bearer parts of the collector structure.....	76
Figure 3.7: Seasonal tracking support (U tool) has a number of holes for tilt angles. Pins are used to mount this component onto the front bearing of the ground base. Holes are used to mount the seasonal tracking base onto the seasonal tracking support to adjust the collector seasonal angle. ....	76
Figure 3.8: Heating system ground base. Front bearings used for mounting the seasonal tracking support, and rear bearings used for mounting the seasonal tracking base.....	77
Figure 3.9: Cross section of the secondary parabola (SP).....	78
Figure 3.10: Schematic of the primary and secondary reflectors in operation. ....	78
Figure 3.11: Cross section of aluminium tube used to create the two secondary parabolas with focal length 15 mm. The segments of aluminium tube used for the secondary parabolas were cut a focal length from the top/bottom as indicated.....	79
Figure 3.12 Comparison of actual secondary reflector shape (from Figure 12) and theoretical shape (red colour).....	80
Figure 3.13: Geometries of secondary parabola with mirror film (SPM) (upper) and secondary parabola painted black (SPB) (lower).....	81
Figure 3.14: Heating system and the SPM and SPB before installation. ....	81
Figure 3.15: Wooden block is acting as absorber tube housing and secondary parabola support. ....	83
Figure 3.16: Hourly and seasonal tracking system of the collectors.....	84
Figure 3.17: Dimensions of the motor actuator and range of tracking angles. ....	85
Figure 3.18: PV solar panel installation, showing its mounting points onto reflector support (welded point) and bearing. Also shown is the solar meter box (contains the solar power meter).....	86
Figure 3.19: Structure body of the collector indicator. ....	87
Figure 3.20: Storage water tank before installing the thermal insulation, showing sites of water temperature sensors and zoomed on the tank cover showing the safety valve, pressure gauge, water tap and sight glass with hexagonal head. ....	88
Figure 3.21: Diagram of the solar heating system. ....	90
Figure 3.22: Diagram of the electronic control system. Solar charger controller link and control between two PV solar panels, two batteries and electric system load. Total load. Three 12 VDC solar pumps, solar tracer (actuator motor) and temperature data logger. ....	91
Figure 3.23: The site of the experimental prototype at USQ Toowoomba. ....	94

Figure 4.1: Flowchart of the stages and cases of the experimental tests of the PTSC heating system. The tracking stage is the hourly tracking. The fixed stage is when the collector is aimed at the sun noon position. Cp is the primary collector (normal design), Cs is the primary collector with secondary parabola mirror (SPM), Cb is the primary collector with secondary parabola painted black (SPB).....	95
Figure 4.2: Schematic of Cp and Cs configurations for cases 1 and 3. Cp is the primary collector, Cs is the modified design and SPM is the secondary parabola mirror. A is the 3D structure; B is the 2D structure; yellow lines are the solar rays, with some deviation from the absorber tube due to geometry misalignment. ....	97
Figure 4.3: Schematic of Cb and Cs configurations for cases 2 and 4. Cb is the primary collector with the black secondary parabola (SPB), Cs is the modified design and SPM is the secondary parabola mirror. A is the 3D structure; B is the 2D structure; yellow lines are the solar rays, with some deviation from the absorber tube due to geometry misalignment. ....	98
Figure 4.4: Experimental setup of case 1 for the tracking stage and case 3 for the fixed stage. A is the concentrating solar radiation on the absorber tube of the primary collector. B is the structure of Cp (on the left) and Cs (on the right).....	100
Figure 4.5: Variation of wind velocities during first and second tracking tests of Cs and Cp during case 1. The third-order polynomial lines are the general trends of the variations during the day .....	101
Figure 4.6: Measured data of solar radiation during first and second tracking tests of Cs and Cp of case 1. The third-order polynomial lines are the general trends of the variations during the day .....	102
Figure 4.7: Water temperature increase from the inlet to the outlet of Cs (A) and Cp (B) during tracking tests of case 1.....	103
Figure 4.8: Experimental performance of Cs (A) and Cp (B) during first and second tracking tests of case 1. ....	105
Figure 4.9: Overall average efficiency data of the two days of the Cs and Cp during tracking tests of case 1. ....	107
Figure 4.10: Experimental setup of case 2 for the tracking stage and case 4 for the fixed stage. SPM is the secondary parabola with mirror sheet; SPB is the secondary parabola painted black. A is the structure of the Cb and CS; B is the concentrating solar radiation on the absorber tube of the collectors. ....	109
Figure 4.11 Variation of wind velocities during first and second tracking tests of Cs and Cb during case 2. The third-order polynomial lines are the general trends of the variations during the day .....	110
Figure 4.12: Measured data of solar radiation during first and second tracking tests of Cs and CP of case 2. The third-order polynomial lines are the general trends of the variations during the day .....	111
Figure 4.13 Water temperature increase from the inlet to the outlet of Cs (A) and Cb (B) during tracking tests of case 2.....	112
Figure 4.14: Experimental performance of Cs (A) and Cb (B) during first and second tracking tests of case 2. ....	114

Figure 4.15: Overall average efficiency data of the two days of the Cs and Cb during tracking tests of case 2. ....	116
Figure 4.16: PTSC orientation during the year for the fixed operation. ....	118
Figure 4.17: Seasonal noon sun angles for a site and the orientation of the PTSC during the fixed stage. A is ground view of seasonal noon angle when installed in practice. B is the fixed orientation of the PTSC during the experimental tests of cases 3 and 4 for the fixed stage. ....	121
Figure 4.18: Variation of wind velocities during first and second fixed tests of Cs and CP of case 3. The third-order polynomial lines are the general trends of the variations during the day. ....	122
Figure 4.19: Measured data of solar radiation during first and second fixed tests of Cs and CP of case 3. The third-order polynomial lines are the general trends of the variations during the day ....	123
Figure 4.20: Water temperature increase from the inlet to the outlet of Cs (A) and Cp (B) during fixed tests of case 3. ....	124
Figure 4.21 Experimental annual midday average performance of Cs (A) and Cp (B) during first and second fixed tests of case 3. ....	126
Figure 4.22: Overall annual midday average efficiency data of the Cs and Cp during fixed tests of case 3. ....	128
Figure 4.23: Variation of wind velocities during first and second fixed tests of the Cs and Cb during case 4. The third-order polynomial lines are the general trends of the variations during the day ....	129
Figure 4.24: Measured data of solar radiation during first and second fixed tests of Cs and Cb of case 4. The third-order polynomial lines are the general trends of the variations during the day ....	130
Figure 4.25: Water temperature increase from the inlet to the outlet of Cs (A) and Cb (B) during fixed tests of case 4. ....	131
Figure 4.26: Experimental annual midday average performance of Cs (A) and Cb (B) during first and second fixed tests of case 4. ....	134
Figure 4.27: Overall average annual midday efficiency data of the Cs and Cp during fixed tests of case 4. ....	135
Figure 5.1: 2D structure of the experimental setup: absorber tube, secondary parabolic mirror (SPM), primary reflector and dead zone (produced due to employing the SPM). ....	140
Figure 5.2: Non-insulated (first column) vs insulated (second column) cross-section area of the proposed receiver tubes. The first row represents the parabolic receiver tubes. The second row represents the hybrid receiver tubes. The third row represents the circular receiver tubes. "SPM dead zone" is the same width as the SP. ....	141
Figure 5.3: SolTrace 3D diagram of the incident solar radiation (yellow collar) reflecting off the PTSC system and onto the receiver tube. ....	143
Figure 5.4: Average flux distribution of the incident solar rays (insolation of 1000 W.m <sup>-2</sup> ) around the absorber tube circumference, calculated by averaging the Figure	

4 flux distribution along the absorber length. The X-axis shows the absorber tube's circumference; 0° is the top of the absorber.....	144
Figure 5.5: Fluent presentation of the solar heat flux distribution on the collector absorber tube from the profile in Figure 5.4. ....	145
Figure 5.6: Cross-section area of parabolic receiver tube showing the absorber tube, parabolic glass envelope, thermal insulation and the heat transfer behaviours. Air fills the space between absorber and glass cover; water used as HTF.....	147
Figure 5.7: Longitudinal and cross-section mesh of the non-insulated and insulated parabolic receiver tubes of the PTSC.....	148
Figure 5.8: Numerical results of the CFD model vs experimental results of the PTSC heating system. X axis cases refers to the cases in Table 5.5 .....	153
Figure 6.1: Temperature distribution of annular air and glass envelope domain of non-insulated and insulated circular receiver tubes (shapes E and F in third row in figure 5.2) for smallest and largest variation wind speed (WS): 1.5 m/s and 6.5 m/s. Results are shown for different stations along the tube (0.0L, 0.5L and L).....	158
Figure 6.2 Temperature distribution of absorber tube wall and HTF domain of non-insulated and insulated circular receiver tube for smallest and largest variation wind speed (WS): 1.5 m/s and 6.5 m/s. Results are shown for different stations along the tube (0.0L, 0.5L and L). ....	160
Figure 6.3: Glass cover outer surface temperature for the insulated (black) and non-insulated (blue) circular receiver tube with wind speed variation and constant solar heat flux ( $1000 \text{ W.m}^{-2}$ ), water volume flow rate ( $0.06 \text{ L.s}^{-1}$ ), ambient and HTF inlet temperatures (300 K).....	162
Figure 6.4: Average temperature difference between inner surface of the absorber tube and the HTF for the insulated (black) and non-insulated (blue) circular receiver tubes' collecting efficiency with wind speed variation and constant solar heat flux ( $1000 \text{ W.m}^{-2}$ ), water volume flow rate ( $0.06 \text{ L.s}^{-1}$ ), ambient and HTF inlet temperatures (300 K).....	163
Figure 6.5: Heat loss of the insulated (black) and non-insulated (blue) circular receiver tubes under effect of wind speed variation and constant solar heat flux ( $1000 \text{ W.m}^{-2}$ ), water volume flow rate ( $0.06 \text{ L.s}^{-1}$ ), ambient and HTF inlet temperatures (300 K).....	164
Figure 6.6: Insulated (black) and non-insulated (blue) receiver tubes' collecting efficiency with wind speed variation and constant solar heat flux ( $1000 \text{ W.m}^{-2}$ ), water volume flow rate ( $0.06 \text{ L.s}^{-1}$ ), ambient and HTF inlet temperatures (300 K).165	165
Figure 6.7: Temperature distribution of annular air and glass envelope domains of non-insulated and insulated hybrid receiver tubes (shapes C and D in the second row in figure 5.2) for smallest and largest variation wind speeds (WS): 1.5 m/s and 6.5 m/s. Results are shown for different stations along the tube (0.0L, 0.5L and L).....	167
Figure 6.8: Temperature distribution of annular air and glass envelope domains of non-insulated and insulated parabolic receiver tubes (shapes A and B in the first row in figure 5.2) for smallest and largest variation wind speeds (WS): 1.5 m/s and 6.5 m/s. Results are shown for different stations along the tube (0.0L, 0.5L and L).....	168
Figure 6.9: Temperature distribution of absorber tube wall and HTF domain of non-insulated and insulated hybrid receiver tubes for smallest and largest variation wind	

speeds (WS): 1.5 m/s and 6.5 m/s. Results are shown for different stations along the tube (0.0L, 0.5L and L). .....	170
Figure 6.10: Temperature distribution of absorber tube wall and HTF domain of non-insulated and insulated parabolic receiver tubes for smallest and largest variation wind speeds (WS): 1.5 m/s and 6.5 m/s. Results are shown for different stations along the tube (0.0L, 0.5L and L). .....	171
Figure 6.11: Glass envelope temperature of the insulated and non-insulated circular (red), hybrid (blue) and parabolic (green) receiver tubes under effect of wind speed variation, constant solar heat flux ( $1000 \text{ W.m}^{-2}$ ), water volume flow rate ( $0.06 \text{ L.s}^{-1}$ ) and ambient temperature (300 K).....	173
Figure 6.12: Heat loss of the insulated and non-insulated circular (red), hybrid (blue) and parabolic (green) receiver tubes under effect of wind speed variation, constant solar heat flux ( $1000 \text{ W.m}^{-2}$ ), water volume flow rate ( $0.06 \text{ L.s}^{-1}$ ) and ambient temperature (300 K). .....	174
Figure 6.13: Receiver tube collecting efficiency of the insulated and non-insulated circular (red), hybrid (blue) and parabolic (green) receiver tubes under the effect of wind speed variation, constant solar heat flux ( $1000 \text{ W.m}^{-2}$ ), water volume flow rate ( $0.06 \text{ L.s}^{-1}$ ) and ambient temperature (300 K).....	175

# List of Tables

Table 3.1: Dimensions of the proposed collector. ....	73
Table 3.2 Secondary reflector dimensions .....	79
Table 3.3: Optimum tilt angle of solar collector by month.....	86
Table 4.1: Daily gained energy for the Cs and Cp configurations during 20 days of experimental tests (Case 1). The Ratio is the ratio of Cp to Cs. ....	108
Table 4.2 Daily gained energy for the Cs and Cb configurations during 20 days of experimental tests (Case 2). The Ratio is the ratio of Cb to Cs. ....	117
Table 4.3 Overall average performance of Cs and Cp during tracking tests at different times of the year for similar solar radiation and wind speed but with different ambient temperatures. ....	136
Table 5.1: Optical properties of the PTSC components.....	142
Table 5.2: Geometrical values of the PTSC experimental model and the alternative receiver tube materials used in this numerical work.....	146
Table 5.3 Dimension and parameter properties used in numerical simulation. $T_{amb}$ is the ambient temperature, $T_{sky}$ is the sky temperature, $D_{hg-P}$ is the hydraulic diameter of the glass envelope for the parabolic receiver tube, $D_{hg-H}$ is the hydraulic diameter of the glass envelope for the hybrid receiver tube and $D_{OD-C}$ is the outer diameter of the circular receiver tube.....	150
Table 5.4 Number of mesh elements and the calculation of useful heat gain for the insulated and non-insulated of the proposed receiver tubes.....	151
Table 5.5 CFD results vs experimental results in addition to testing environment conditions. Volume flow rate equal to $0.06 \text{ L.s}^{-1}$ . SR is the solar radiation ( $\text{W.m}^{-2}$ ), $T_{amb}$ is the ambient temperature ( $^{\circ}\text{C}$ ), and WS is the wind speed ( $\text{m.s}^{-1}$ ). $T_{in}$ is the inlet temperature ( $^{\circ}\text{C}$ ), $T_{out}$ is the outlet temperature ( $^{\circ}\text{C}$ ). % T is the percentage increase in the raised temperature computed by the simulations compared to the experiments. ....	153

# Abbreviations

<i>Cb</i>	<i>Primary collector with Secondary parabola painted black</i>
<i>CFD</i>	<i>Computational Fluid Dynamic</i>
<i>Cp</i>	<i>Primary collector</i>
<i>CR</i>	<i>Concentrating Ratio</i>
<i>Cs</i>	<i>Primary collector with Secondary parabola mirror</i>
<i>CSP</i>	<i>Concentrating Solar Power</i>
<i>FVM</i>	<i>Finite Volume Method</i>
<i>HCE</i>	<i>Heat Collection Element</i>
<i>HTF</i>	<i>Heat Transfer Fluid</i>
<i>MCRT</i>	<i>Monte Carlo Ray Tracing</i>
<i>PTSC</i>	<i>Parabolic Trough Solar Collector</i>
<i>SPB</i>	<i>Secondary Parabola painted black</i>
<i>SPM</i>	<i>Secondary Parabola with mirror film</i>
<i>USQ</i>	<i>University of Southern Queensland</i>

## Nomenclature

$A_c$	<i>Collector aperture area (<math>m^2</math>)</i>
$C_p$	<i>Water specific heat (<math>J/kg.K</math>)</i>
$D_{ai}$	<i>Absorber tube inner diameter(<math>m</math>)</i>
$D_{gh}$	<i>hydraulic diameter (<math>m</math>)</i>
$f$	<i>Friction factor</i>
$h_F$	<i>Convective heat transfer coefficient (<math>W/m^2K</math>)</i>
$I_b$	<i>Normal solar radiation (<math>W/m^2</math>)</i>
$K_F$	<i>Water thermal conductivity (<math>W/mK</math>)</i>
$L$	<i>Absorber tube length(<math>m</math>)</i>
$L$	<i>Collector aperture area length (<math>m</math>)</i>

$\dot{m}$	<i>Mass flow rate (kg/s)</i>
$Nu$	<i>Nusselt number</i>
$Pr$	<i>Prandtl number</i>
$Q_u$	<i>Useful heat gain (W)</i>
$Re$	<i>Reynolds number</i>
$SP$	<i>Secondary Parabola</i>
$T_{aa}$	<i>Average temperature of absorber tube inner surface (K)</i>
$T_{amb}$	<i>Ambient temperature (K)</i>
$T_{Fa}$	<i>Water mean temperature (K)</i>
$T_{inlet}$	<i>Inlet temperature (K)</i>
$T_{og}$	<i>outer surface temperature of receiver glass envelope (K)</i>
$T_{outlet}$	<i>Outlet temperature (K)</i>
$T_{sky}$	<i>sky temperature</i>
$u_w$	<i>Wind speed (m/s)</i>
$W$	<i>Collector aperture width (m)</i>
$WS$	<i>Wind speed (m/s)</i>
$X$	<i>Half of collector aperture width (m)</i>
$Y$	<i>Collector aperture area high (m)</i>
$y$	<i>Twist Ratio</i>

### **Greek symbols**

$\alpha$	<i>Absorptivity</i>
$\gamma$	<i>Intercept Factor</i>
$\eta_o$	<i>Optical efficiency</i>
$\eta_{th}$	<i>Thermal efficiency</i>
$\theta_r$	<i>Rim Angle(degree)</i>
$\rho$	<i>Reflectivity</i>
$\tau$	<i>Transmissivity</i>

$\varepsilon$       *Emissivity*

$\mu_F$       *Fluid dynamic viscosity (kg/m.s)*

# Chapter 1 Introduction

## 1.1 Non-renewable energy and its effect

Each second approximately 1.2 million kilograms of CO<sub>2</sub> are released into the atmosphere (Chafie et al. 2016) and most of this emission arises from non-renewable resources like fossil fuels and nuclear energy. This is because most energy consumption is generated from non-renewable energy: approximately 86% of energy is generated from fossil fuels while only around 0.8% is provided from renewable energy (U.S. Energy Information Administration 2018). World consumption of energy, especially for coal and oil, has increased steadily since 2000 and is expected to continue to grow rapidly for the next twenty years (International Energy Agency 2018). In addition, Figure 1.1 shows trends of the history and projection of world fuel consumption between 1990 and 2040.

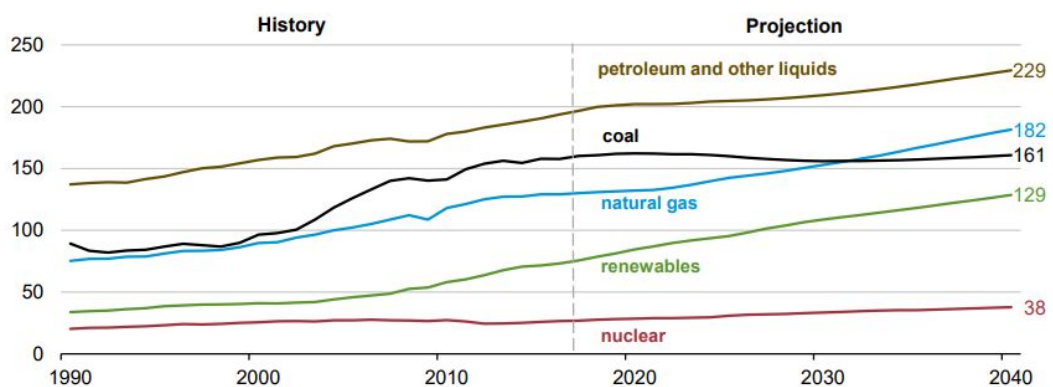


*Figure 1.1 History and projection of world energy consumption from renewable and non-renewable energies from 1990 to 2040 (U.S. Energy Information Administration 2018).*

It can be clearly seen from this figure that there is increasing non-renewable world energy consumption. This can lead to increasing the greenhouse gases emission ratio which results in climate change problems. Over the last century the average global temperature on Earth has increased by around 0.15-0.20°C per decade (National Aeronautics and Space Administration 2019, June 1). One of the consequences of the increasing surface temperature of the Earth is loss of ice mass, elevation of sea levels and flooding. Figure 1.2 illustrates the annual average global temperature on Earth

from 1880 to 2014. It can be seen that there has been a rapid warming in the past few decades and it also displays that the last decade is the warmest.

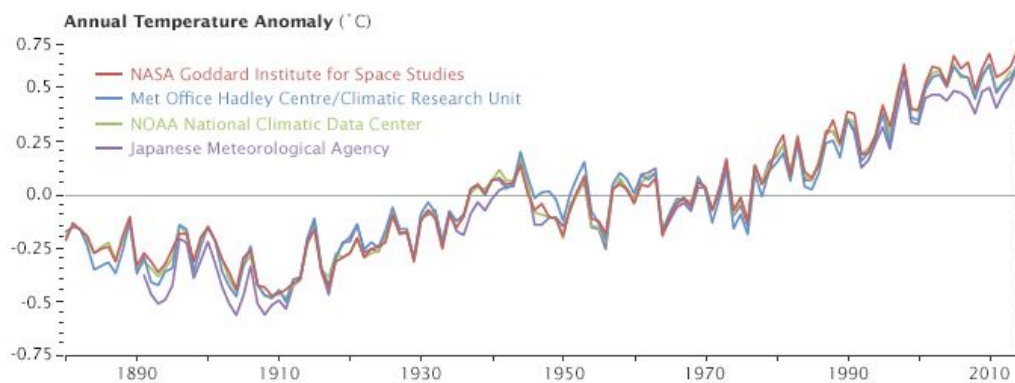


*Figure 1.2 Yearly average global temperature on Earth from 1880 to 2014 (National Aeronautics and Space Administration 2019, June 1).*

## **1.2 Solar energy and concentrating solar power technologies**

Due to the increasing world fossil fuel energy consumption and decrease in its resources, in addition to growing worldwide pollution issues, there is an urgent need for environmental and sustainable energy resources. Renewable energy resources like solar and wind energies are sustainable resources which produce zero greenhouse gas emissions.

However, even though solar energy is variable due to weather or latitude, it is one of the major renewable energy resources. It is the most abundant and geographically widespread resource and it has tremendous advantages over other renewable energy resources (Chafie et al. 2016). It is estimated that around 84 minutes of solar energy radiation is enough to meet global energy needs for about one year (Kalogirou 2013). Solar towers, linear Fresnel reflectors, parabolic dishes, and parabolic trough solar collectors are the most common solar concentrating solar power (CSP) technologies utilized for producing electric and also for industrial heat applications. Among all of the CSP technologies, the Parabolic Trough Solar Collector (PTSC) is the most mature and cost-effective technology and it is found that the annual average optical efficiency of PTSC is the highest among these technologies (Navarro-Hermoso et al. 2016; Yang et al. 2018).

However, there are two main challenges of the parabolic trough solar collector technology are. Firstly, there are optical losses, which occurs due to some of the sunlight reflected from the main dish not reaching the collector receiver tube (Lüpfert & Ulmer 2009; Christian & Ho 2010; Huang & Han 2012; Salamanca et al. 2015; Paetzold et al. 2016; Simonović et al. 2016; Zhao et al. 2016; Fraidenraich et al. 2017; Islam et al. 2017; Meiser et al. 2017). Secondly, heat losses occur due to the high temperature difference between the fluid that absorbs the solar radiation (reaching up to 400 °C) and the surrounding environment (Padilla et al. 2011; Hachicha et al. 2013; Lei et al. 2013; Wu et al. 2014; Navarro-Hermoso et al. 2016; Prahel et al. 2017).

### **1.3 Aim and objectives of the thesis**

The aim of this thesis is to improve the PTSC performance in a manner that is economically beneficial in addition to enhancing the PTSC performance under high wind conditions. This can be achieved via four main objectives:

1. Improve the optical efficiency of conventional PTSC systems with tracking by experimentally testing the effect of a secondary reflector that can capture and use sunlight that has been deviated from the receiver tube due to misalignments in the system (potentially caused by flexing from wind, or manufacturing or installation errors).
2. Design a new configuration for the PTSC system which enables operation of the PTSC under high wind conditions by configuring the conventional PTSC length (axis) to be parallel with the East-West orientation and permanently angling the collector aperture area based on the latitude of a site (this setup of the fixed case is the standard for PV solar panels).
3. Develop a unique experimental methodology to test the annual performance of the fixed case using a single day of testing. The test provides performance data for midday for every day of the year. This test is performed by orienting the PTSC axis in the North-South direction and aiming the collector aperture area at the sun throughout the day. The noon time of the test simulates the sun's position at noon at the equinox, while the test time of 10 am represents noon at the winter solstice and 2 pm simulates noon at the summer solstice noon.
4. Improve the PTSC's thermal efficiency by numerically testing the effect of including annular thermal insulation to reduce the PTSC receiver tube heat

losses to the environment, and thereby increase the efficiency of the PTSC system in addition to enhancing the receiver tube's operational life.

## **1.4 Thesis outlines**

This thesis is organised as follows:

Chapter 2 contains the review of optical and thermal investigation studies in addition to the available solutions for improving the optical and thermal performance of a PTSC heating system. The review focuses on studying the main factors that lead to optical and thermal loss. It also looks at the reasons that lead to failure of the receiver tube and its economic influences.

Chapter 3 explains the methodology of the design and manufacture of the PTSC test heating system at a system and component level.

Chapter 4 presents the experimental results from investigating the secondary reflector's effect on the PTSC performance for both tracking and fixed setups.

Chapter 5 describes the 3D CFD simulation of thermal insulation in the modified PTSC's receiver tube.

Chapter 6 presents and analyses the numerical simulation results of the insulated and non-insulated models by comparing the HTF outlet temperature, glass cover temperature, heating loss, and efficiencies.

Chapter 7: Thesis conclusion and recommended future work.

# Chapter 2 **Optical and thermal losses of the PTSC system and available solutions**

## **2.1 Introduction**

Parabolic trough solar collector technology is the most widely applied in solar thermal plants and it supplies a significant portion of electricity generation (Navarro-Hermoso et al. 2016). Also, it is the first commercial concentrating solar power technology (Pitz-Paal et al. 2007; Grena 2010; Padilla et al. 2011) with the first plants constructed in 1984 (Wu et al. 2014). These successful PTSC plants were made and developed by the Luz Solar Electric Generating System (SEGS). Some of the solar thermal plants installed in California's Mojave Desert in the USA cover around 200 hectares of collector area. Figure 2.1 shows an overview of the PTSC solar thermal plants in the Mojave. They range in size between 14 and 80 MW and the total installed capacity is 354 MW. Over the course of the first three decades of commercial solar power plants, approximately 96% of solar electric generating capacity worldwide used PTSC technology (Wu et al. 2014).



*Figure 2.1: View of PTSC solar thermal plants in California's Mojave Desert in the USA (Quaschnig & Muriel 2002).*

Moreover, the parabolic trough solar collector technology turned out to be one of the most cost-effective, proven and sustainable technologies among concentrating solar power technologies (Navarro-Hermoso et al. 2016; Yang et al. 2018). It is widely and effectively used for heating applications that require heat transfer fluid (HTF) at high temperatures, from electricity generation to industrial hot water applications (Patnode 2006; Hachicha et al. 2014). Also it is considered one of the most popular and best solar technologies, especially for moderate heating temperatures (between 150 °C and 400 °C).

As illustrated in Figure 2.2, the main principle of PTSC operation is reflecting the direct solar radiation from the reflector towards the receiver tube and heating an HTF by focusing the solar heat flux on the outer surface of the absorber tube.

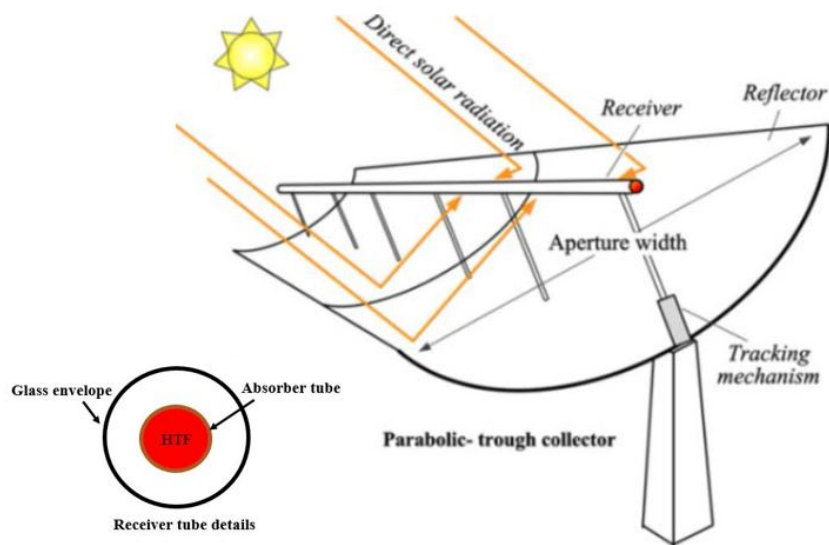


Figure 2.2: Schematic of a parabolic-trough collector showing the collector aperture width, receiver, reflector and tracking system. Structure of collector's receiver tube is also shown (Cabrera et al. 2013)

Only direct solar radiation is collected by this technology. Therefore, a single-axis tracking system is usually used in this technology. The tracking system allows a reflector to track the sun's path about one axis (parallel to the receiver tube) from sunrise to sunset (Dunlap 1994). In addition, this type of collector can be aligned either in a north-south direction, tracking from east to west, or oriented in an east-west direction, tracking the sun from north to south (Reddy & Satyanarayana 2008).

As illustrated in Figure 2.2, PTSC components generally consist of: a parabolic reflector, a receiver tube, supportive structure and a heat transfer fluid. The parabolic reflector is the reflective concentrating mirror for collection of incident solar light and reflecting it to the focal axis of the PTSC (Cabrera et al. 2013). Generally, a highly-reflective material is used for coating the reflector and producing excellent, reliable optical performance for many years (Price et al. 2002) (Price et al. 2002). However, conventional glass mirrors are expensive and prone to breakage, so require a rigid supporting structure. Therefore, thinner glass or metallic panels, coated with a polymer reflector, have been proposed as an alternative reflector (Price et al. 2002; Fernández-García et al. 2010).

The receiver tube, also called a Heat Collection Element (HCE), is located on the focal axis of the collector geometry (Fan et al. 2018). This element is comprised of a

stainless-steel pipe, also called an absorber tube, painted with a special absorbent coating. The special coating usually has high absorptivity and low emissivity for solar radiation, which minimises radiation loss. The absorber tube is often surrounded by a glass cover to minimise convection and radiation thermal losses. Borosilicate glass is usually used to manufacture the HCE glass envelope (Amina et al. 2016; SCHOTT 2019). Both sides of the glass envelope (borosilicate tube) have anti-reflective coating to minimise reflection loss and also to increase its transmissivity above 95%. The air inside the glass cover is normally evacuated to further help with thermal heat loss. However, PTSC non-evacuated receiver tubes are also used for supplying hot water in addition to being employed in some industrial solar technologies (Kearney 2007; Fernández-García et al. 2010). The supporting structures (normally made of steel) connect the reflector with a trough frame and hold the receiver tube, as illustrated in Figure 2.3.



*Figure 2.3: Main components of the PTSC system (Quaschnig & Muriel 2002).*

The final component of a PTSC is an HTF that flows through the absorber tube to absorb the concentrated solar radiation. Synthetic oils are normally used as an HTF in PTSC due to their applicability for operating temperatures up to 400 °C, by virtue of their low viscosity and remaining in liquid phase between room temperature and 400 °C (Price et al. 2002). The HTF can be used to generate a high-pressure super-heated steam by using a heat exchanger. The HTF flows through the absorber tube and absorbs the solar energy that is distributed on the outer diameter of the absorber tube.

As a result, the HTF can be efficiently heated up to 400 °C, especially for collectors that have a high Concentrating Ratio (CR). The CR is the ratio between the aperture area of the reflector and the aperture area of the absorber tube. Therefore, a synthetic oil is used as an HTF in this technology because of its thermal properties (Krüger et al. 2008; Sokhansefat et al. 2014).

PTSC technology is mainly used to produce electricity power in solar thermal plants. These types of solar thermal plants are suitable for large-scale electricity generation of the order of 600 MW. Because they have the option of thermal storage, they can deliver the electricity reliably and avoid grid instability during cloudy days (low solar radiation). A PTSC solar thermal plant with a CR range between 20 and 30 is able to heat the HTF to temperatures between 300 °C and 400 °C. For solar thermal applications, typical PTSC collector aperture area dimensions are 6 m in width and between 100 and 150 m in length (Fernández-García et al. 2010).

PTSC technologies can be also employed for other applications like industrial process heat (IPH) that require steam temperatures below 250 °C (Patil, Panse, et al. 2014). Also, it can be used for other heating applications such as space heating and water desalination that require temperatures between 100 °C and 150 °C. Around 80% of IPH require temperatures ranging between 92 °C and 204 °C (Patil, Panse, et al. 2014). For these applications, the dimensions of the PTSC aperture area are between 1 and 3 m in width and between 2 and 10 m in length. The CR varies between 15 and 20 (Fernández-García et al. 2010).

In order to make the PTSC able to be used as an essential and reliable replacement technology for fossil fuels to generate electricity, overcoming solar energy reductions during overcast or night-time periods, Thermal Energy Storage (TES) technology must be integrated into the PTSC plant design. TES allows solar energy to be stored during periods of excess sunshine (when there is low load demand) and despatched during periods of limited or no solar irradiation (Powell & Edgar 2012; Pelay et al. 2017). By using TES technology PTSC thermal plants increase the active utilisation of solar energy by shifting electricity generation from periods when solar energy is available (during low load demand period) to the periods of weak or no solar irradiation. The first usage of TES technology was in the SEGS plant built in 1984, with thermal storage capacity for approximately 3 hours (Herrmann et al. 2004). Nowadays, the

TES is considered an essential part in PTSC solar thermal plants and its capacity can reach up to 15 hours (DEWA CSP Trough Project 2019).

There are two main types of thermal energy storage systems: latent storage systems and sensible storage systems (Gil et al. 2010). In the latent storage systems, thermal energy is stored or released by material while changing its phase (solid-liquid phase transition); this occurs during a purely material physical process at a constant temperature. Although the latent storage system permits a large amount of thermal energy to be stored in a small volume, the main drawback of this TES type is the low thermal conductivity, which results in very slow phase change processes (Pelay et al. 2017).

Sensible storage systems use a set of materials that change temperature without changing phase (Gil et al. 2010). Therefore, the heat storage capacity relies heavily on the materials' thermal capacity (the specific heat and density), as well as other important properties such as operating temperatures, the thermal conductivity of the materials and the cost. The challenge of this TES type is its limited energy density. Sensible heat storage materials in liquid form are at an advanced stage of development and widely utilised in CSP thermal plants (Pelay et al. 2017). Molten salt is one of the best materials for concentrating solar power applications because of favourable properties such as thermal stability at high temperatures, high thermal conductivity, and low viscosity (Hale 2000; Gil et al. 2010; Zhao et al. 2010).

A PTSC plant that includes TES technology operates by the HTF from the solar field absorbs the concentrated solar energy within the absorber tubes, then passes through a heat exchanger system to charge the thermal storage system. This heats salt from the cold storage up to 385 °C which is pumped into the hot salt storage tank. During night or periods of low or no solar radiation, salt flows from the hot storage tank to heat the HTF via a heat exchanger. The hot HTF is always used (regardless of whether it is heated by the sun or salt) to generate superheated steam that passes through a steam turbine, producing electricity (Herrmann et al. 2004).

As illustrated in Figure 2.2, the optical performance of PTSC technology depends on its reflector geometry accuracy or, in other words, how accurately the reflected solar radiation is concentrated on the absorber tube surface area. Reflected solar radiation

misses the absorber tube due to the reflector deviating from the designed slope (this deviation, called “slope error” is waviness in the mirror from its proposed plane), which deviates the reflected rays from the ideal direction (Huang & Han 2012). Several factors normally contribute to this deviation of the mirror from ideal, including: manufacturing or assembly errors, gravitational load, tracking error, and wind load. These factors influence the optical performance of the PTSC, reducing its thermal performance. Optimising the optical performance enhances both the optical and thermal efficiency of a PTSC and reduces the overall size of the solar heating system, thereby reducing the installation cost.

Moreover, the HTF in this technology reaches up to 400 °C, which increases the glass cover temperature. Therefore, substantial radiative and convective heat losses occur because of the significant difference between the outer surface temperature of the PTSC receiver glass envelope and the ambient temperature (Padilla et al. 2011; Prahll et al. 2017).

Therefore, to achieve a high PTSC performance and reduce the effects of optical and thermal losses, the purpose of this chapter is to review the factors that influence the performance of the PTSC and therefore propose suitable solutions to overcome these optical and thermal losses.

## **2.2 Sources of PTSC optical losses and optical enhancement technologies.**

### **2.2.1 Sources of PTSC optical losses**

Because the operation of a PTSC relies on the redirection of solar radiation from the mirror to the receiver tube, the mirror geometry accuracy and focal line of the receiver tube have several influences on optical and thermal performance of the PTSC. Therefore, precision in reflector (mirror) shape and receiver tube alignment are required to harness the maximum amount of reflected solar rays to enhance the PTSC's efficiency. A small deformation in mirror shape or in receiver tube axial alignment can significantly reduce the PTSC's efficiency.

### 2.2.1.1 Parabolic mirror shape accuracy

Lüpfer and Ulmer (2009) presented a numerical study of the mirror reflecting accuracy and the mirror slope error effects on a PTSC's optical performance. The authors observed that a deviation has a clear effect on both the accuracy of reflecting sunlight onto the PTSC receiver tube and the efficiency of the system. They also found that a slope deviation has a double influence on the direction of the reflected sunlight, which could deviate some of the reflected sunlight rays from the receiver tube focal line. Figure 2.4 shows the inner and outer mirrors of the particular reflector design, while Figure 2.5 presents the relationship between the intercept factor ( $\gamma$ ) (which is defined as the ratio between total incident solar radiations on the collector aperture area to the number of reflected rays that are received by receiver) and the mirror focus deviation. It can be seen that the increasing value of the mirror deviation has a detrimental impact on the value of the intercept factor, thereby reducing the optical and thermal performance.

Based on the presented study (Figure 2.5), it can be seen that when the focus deviation in the x-direction ( $FD_x$ ) reaches approximately 8 mm for the outer mirror, or when it reaches around 10 mm for the inner mirror, a high drop in the collector intercept factor (sharp deviation) occurred. This consequently reduced the collector optical performance and therefore that reduced the solar heating system efficiency. Therefore, it is important to reduce the effect of this deviation by installing an optical correction (such as secondary reflector) for this solar technology to reduce optical losses by reflecting some of the deviated rays towards the receiver tube.

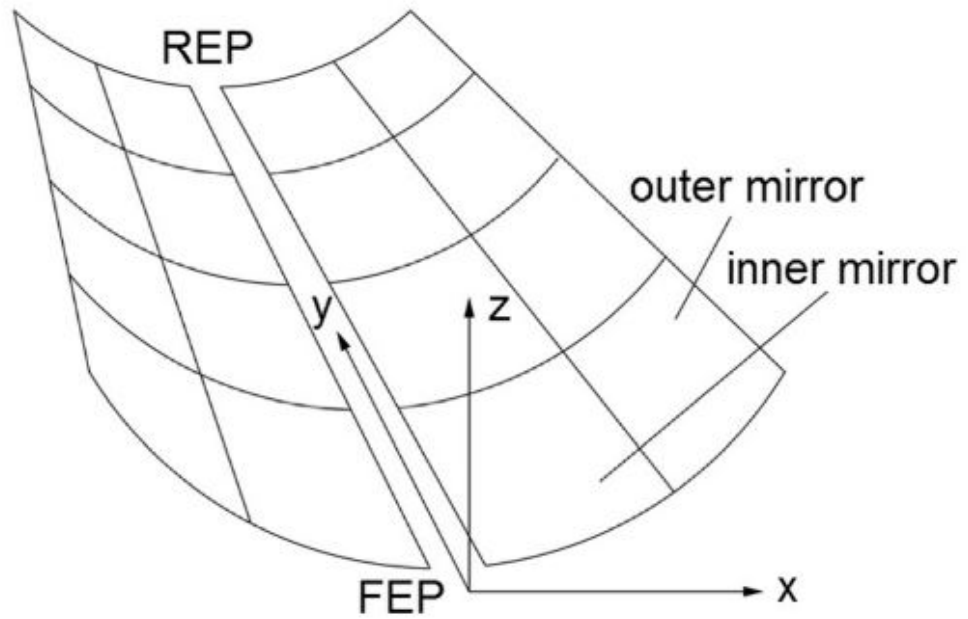


Figure 2.4: 3D scheme of the outer and inner mirrors of the reflector,  $f$  is the collector focal length (Lüpfert & Ulmer 2009).

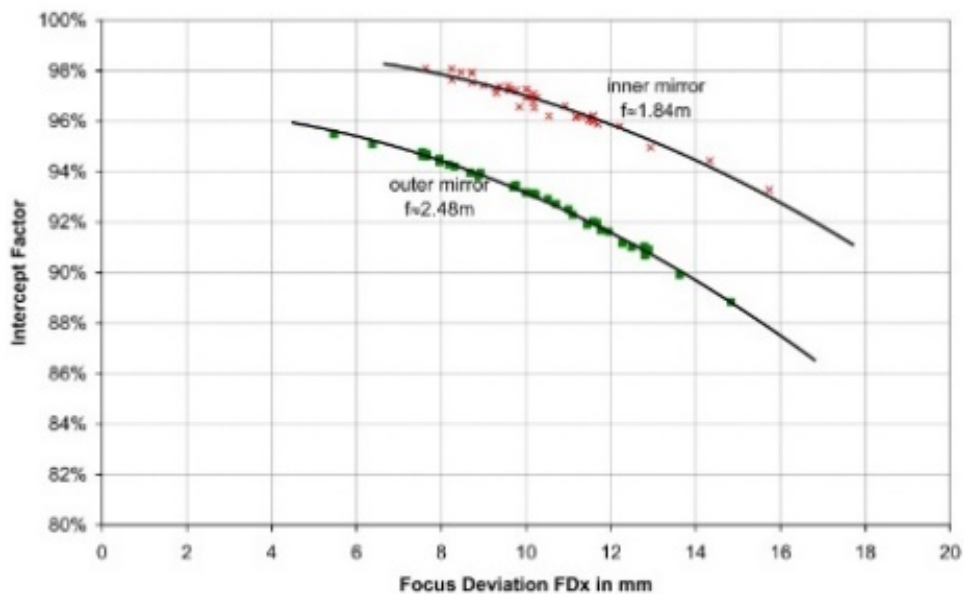
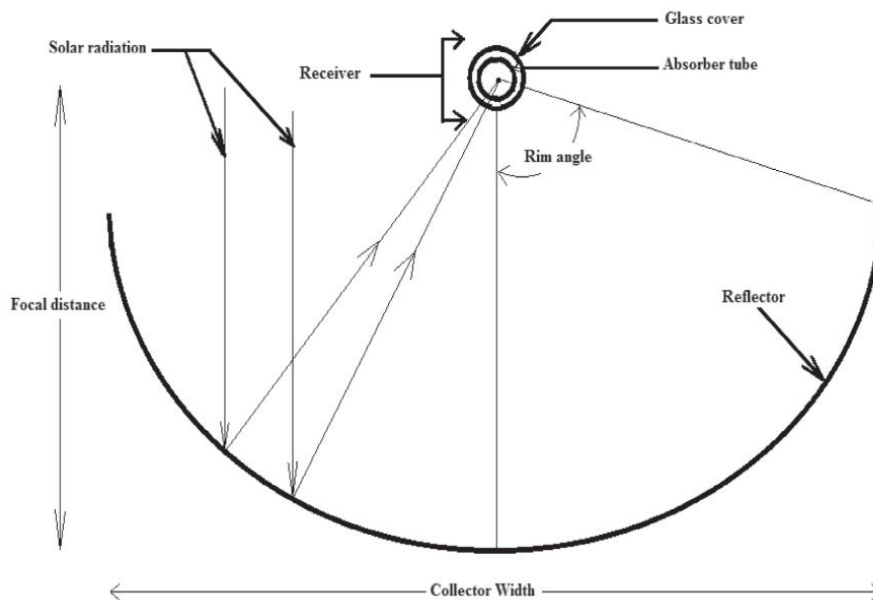


Figure 2.5: The intercept factor and the focus deviation on the inner and outer mirrors of the PTSC (Lüpfert & Ulmer 2009).

Due to the direct effect of the waviness of the reflector (waviness of the reflector means mirror misalignment or mirror slope error that deviates the reflected sunlight from hitting the proposed collector focal line) on the concentration of solar rays, Huang and Han (2012) have studied the influences of the mirror slope error on performance of the PTSC in addition to other kinds of solar concentrating reflectors. The study also presented the effect of the slope error with rim angle ( $\theta_r$ ) for different incident angles

(from  $0^\circ$  to  $75^\circ$ ). Rim angle is defined as half the angle between the reflector rims when rotating about the focal axis (Figure 2.6). The authors found that the slope error for the incident solar angles is increased by increasing value of the rim angles, as shown in Figure 2.7. Thus, based on that, it can be concluded that the effect of increasing slope error—for solar collectors that included high rim angles—should be reduced somehow to decrease the number of deviated reflected solar rays and also to improve optical PTSC performance. In this study, the author also presented a general equation to calculate the standard deviation of the reflected ray error is presented in the study. The authors recommended that the equation for the reflected sunlight errors is generally appropriate for all reflection plants without deflection and can also be useful to control the errors in designing a biaxial optical system.



*Figure 2.6: Cross section of the PTSC showing key geometric parameters in addition to path of the solar reflection (Chafie et al. 2016).*

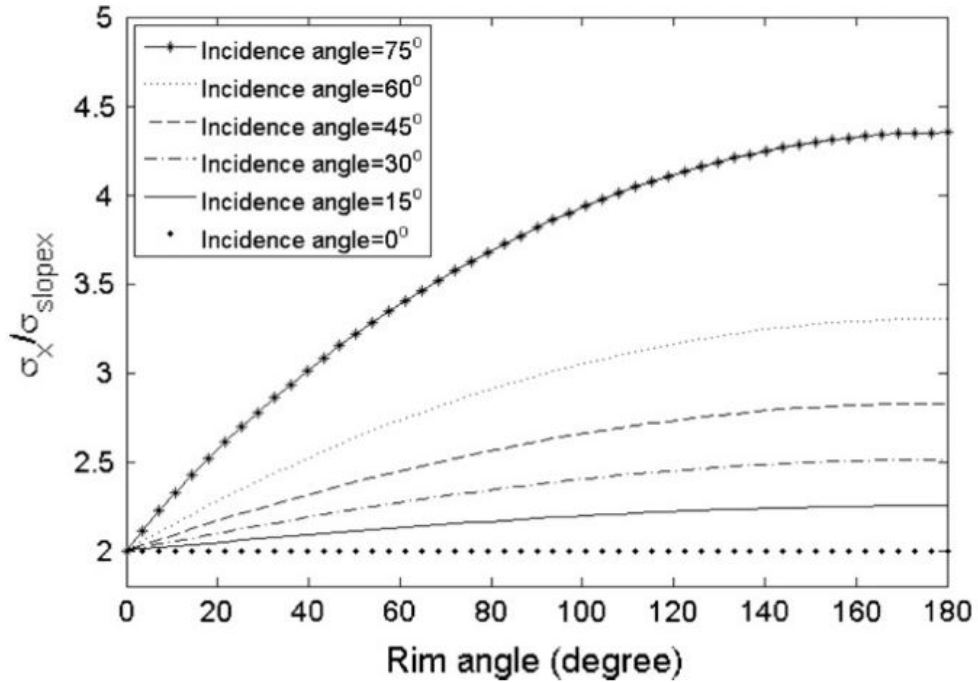
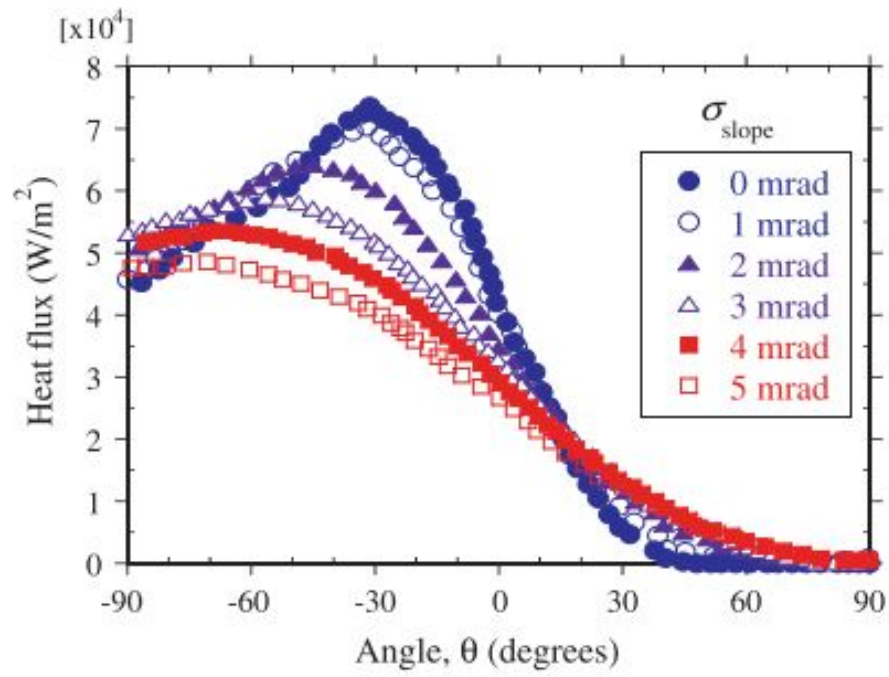


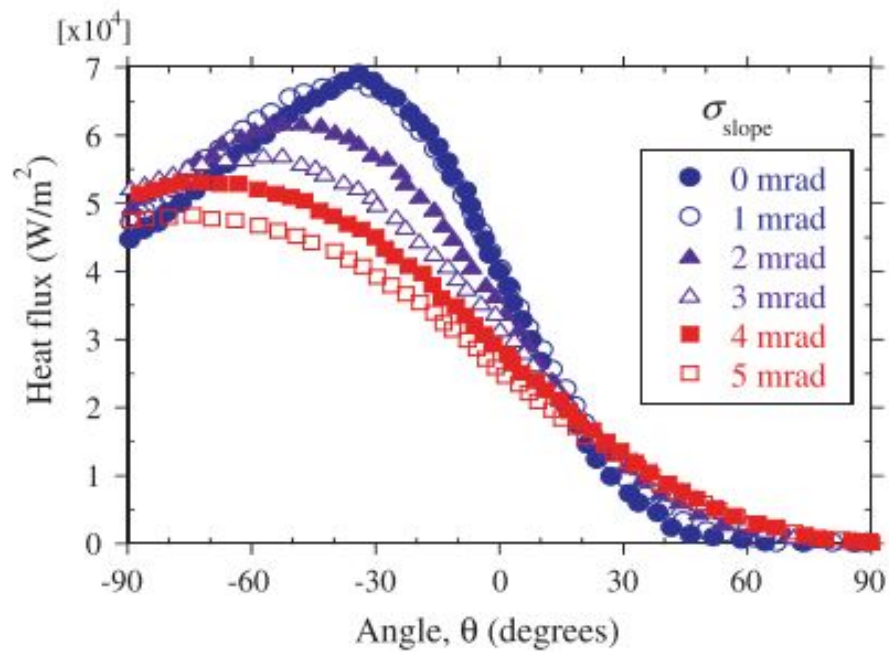
Figure 2.7: Slope error values under variety of incident angles (from  $0^\circ$  to  $75^\circ$ ) and rim angles (from  $0^\circ$  to  $180^\circ$ ) (Huang & Han 2012).

The impacts of the slope errors in addition to specular errors (where mirror reflected angle do not equals the incident angle) on the PTSC optical and thermal performances have been investigated under rim angle  $80^\circ$  and CR 86 values. Figure 2.8 (a & b) shows the effect of slope errors on the solar heat flux distribution on the collector absorber tube under zero mrad and 3 mrad of specular errors respectively. In this study, Monte Carlo Ray Tracing (MCRT) was used to calculate the solar heat flux distribution around the outer surface of the absorber tube. The results show that the slope error has a clear influence on the distribution of the solar heat flux around the outer surface of the PTSC absorber tube. Therefore, this phenomenon could produce significant thermal strain on the absorber tube surface due to the highly asymmetrical concentrating heat flux around the absorber tube's circumference. The study also shows that the specular errors do not have a significant influence on the optical or thermal performance of the collector, especially for ranges less than 3 mrad. In addition, the study also investigated the effect of the optical error on the collector efficiency and intercept factor ( $\gamma$ ) as shown in Figure 2.9. The results found that increasing the slope errors from 0 to 5 mrad reduced the intercept factor value by around 21% while it was reduced by only 5% as the specular errors reached around 4 mrad. For the slope and specular error effects on the collector efficiency, it is

found that increasing the slope error from 0 mrad to around 5 mrad leads to reduced thermal efficiency by around 17%, while the authors did not observe any significant influence for the specular errors on the collector thermal efficiency (Mwesigye et al. 2016). Consequently, the reduction in the collector thermal efficiency (17%) due to collector slope error reduced the PTSC performance. Based on that, this loss should be reduced by creating a thermal or optical enhancement for this solar technology, as mentioned previously.



(a)



(b)

Figure 2.8: The effect of slope errors on the solar heat flux distribution on the collector absorber tube under (a) zero specular errors and (b) under 3 mrad specular errors (Mwesigye et al. 2016).

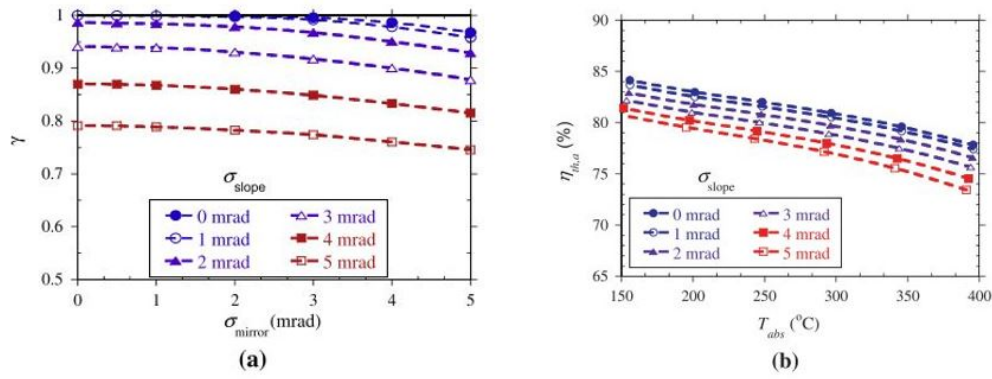


Figure 2.9: The effect of slope errors on (a) collector intercept factor and (b) collector thermal efficiency (Mwesigye et al. 2016).

### 2.2.1.2 Focal error (Receiver tube misalignment)

The focal axis and centre position of collector receiver tube error and sunlight distribution around the receiver tube of a PTSC have been numerically and experimentally investigated in many research studies in order to point out their influences on PTSC performance. Via numerical study combining the MCRT method with a simulation software, Zhao et al. (2016) investigated the influence of receiver tube installation errors in  $x$ - and  $y$ -axes on the PTSC performance (Figure 2.10). The values of CR and  $\theta_r$  in the study were considered to be 20 and  $90^{\circ}$  respectively. This could be due to the fact that these values make a balance between the receiver heat loss and the thermal strain that occurred due to concentrating flux. For perfectly-aligned reflectors, as the installation error in  $x$  direction increases to 1.0%, the solar heat flux changes significantly [Figure 2.11 (a)]. Installation error leads to overheating some parts of the receiver tube, which could damage the receiver. In addition, it is recommended that the  $x$  axis installation errors should be controlled to within  $\pm 0.2\%$ . From this part of the study, it can be concluded that the receiver tube deviation in the  $x$ -direction could effectively deviate the concentrated solar heat flux from the absorber tube in addition to producing absorber tube surface overheating. And therefore a conventional receiver tube structure should be modified somehow to reduce the influences of the receiver tube  $x$ -axis misalignment. The effects of the  $y$  installation error also have a clear effect on the PTSC performance, but this effect decreased while the CR increased. Figure 2.11 (b) illustrates the effect of 0.2%  $y$  direction installation error on the solar heat flux on the receiver tube wall under several concentration ratios and zero incident angle. The simulation results were validated with experimental data. When incident solar radiation increased, the deviation of the reflected solar light

slightly increased due to the installation errors, while the effects of these errors can be decreased by increasing the CR. However, the +y direction installation error for a collector with a high CR can also overheat the surface on the lower part of the absorber tube (as shown in Figure 2.11). Therefore, for collectors that included both low rim angles (low rim angle equivalent or simulating the effect of receiver tube deviation in the +y direction) and high CR, a modification or an optimisation technology should be created somehow to reduce the absorber tube surface overheating.

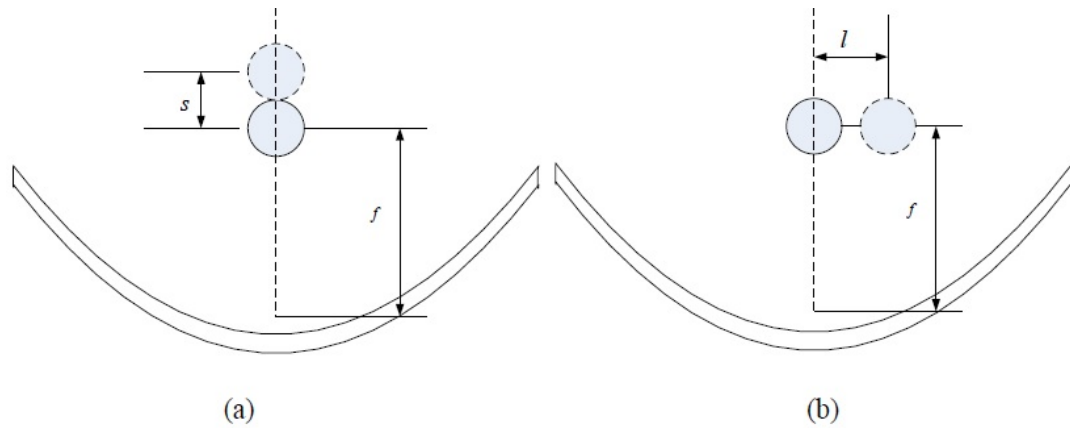


Figure 2.10: Installation errors of PTSC receiver tube in the y (left) and x directions (right) (Zhao et al. 2016).

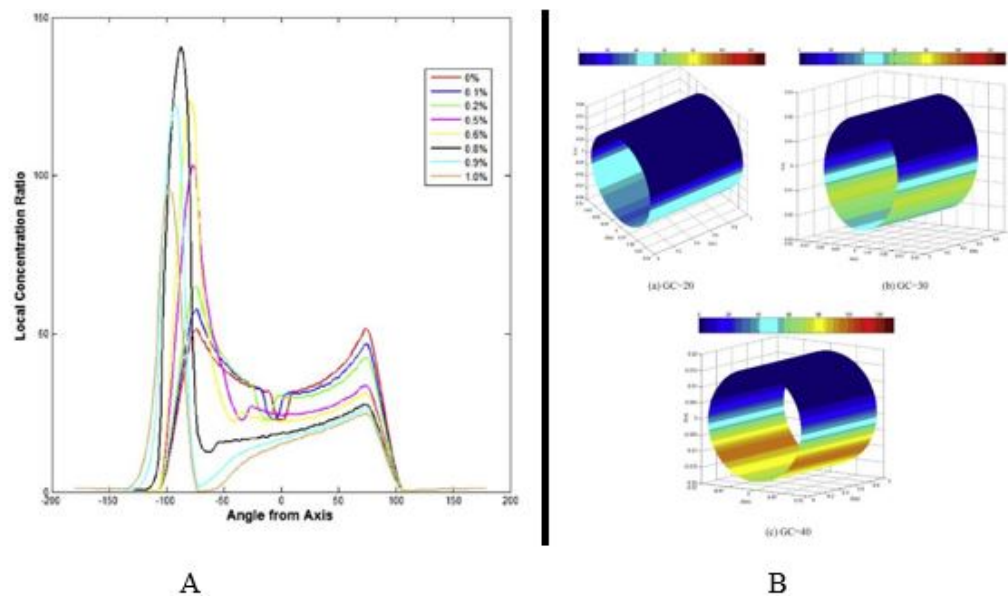


Figure 2.11: The solar heat flux distribution on receiver tube for (a) x axis for different installation errors and under zero degree incident angle & CR=20. (b) for different CR (20, 30 and 40) with 0.2% y axis installation errors (Zhao et al. 2016).

Figure 2.12 shows how deviation of incident solar rays affect which reflected rays reach the receiver tube. The PTSC optical performance and focal direction errors have also been investigated by Simonović et al. (2016). In this study, the influence of range of deviation of reflected rays to receiver focal line and its effect on PTSC thermal efficiency been analysed. The thermal performance of PTSC could be affected by any error in the focal axis of the absorber tube. Also, the study focused on a limited range of deviation angle between the incident beam and the focal plane. Mathematical relations between PTSC dimensions such as focal distance and absorber tube diameter and minimal and maximal deviation angles were illustrated. The study found that both the efficiency of a PTSC can be reached by a minimum value and its useful reflected area can be decreased due to reaching the maximum value of deviation angle. This work, as in previous studies, also produced further evidence about the influences of deviated reflected sunlights on PTSC performance. This shows clearly that the modification for this solar technology has become an essential matter to reduce the influence of the deviated reflected rays.

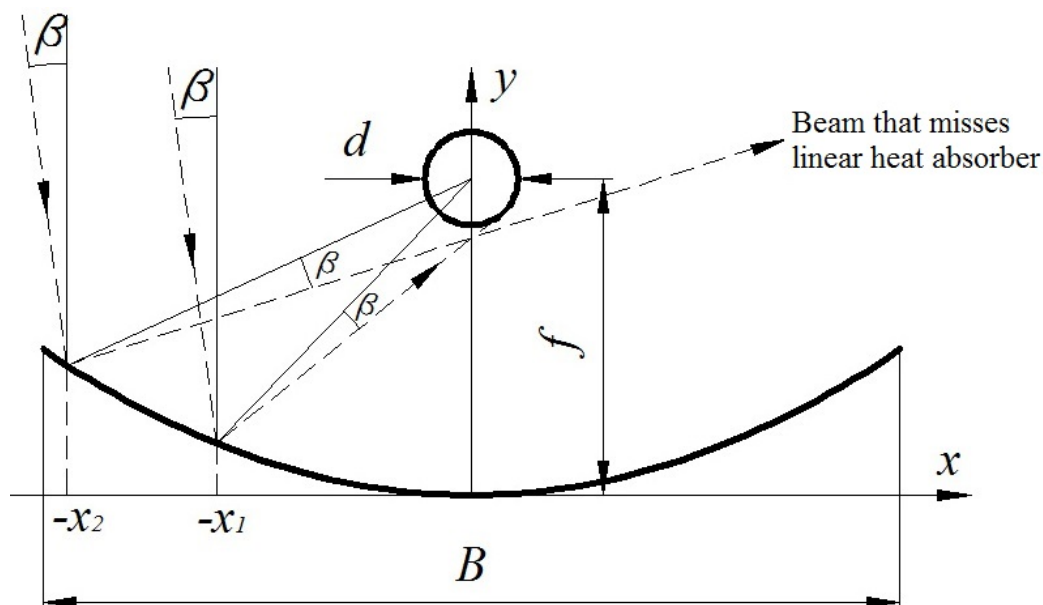


Figure 2.12: Deviation of incident sunrays at cross section of PTSC aperture area (Simonović et al. 2016).

The thermal and optical PTSC efficiencies depend on the thermal, geometrical and optical parameters of the installed collector. The quality of the collector components, the accuracy of the collector design and proper PTSC component assembly have a direct influence on the collector performance (Pottler et al. 2014). The authors analysed several geometry factors and their influence on PTSC performance. The

authors established the influence of receiver tube misalignment errors, mirror reflectivity and torsion on the intercept factor of the collector. A Euro trough collector was considered as a PTSC prototype in this study. Figure 2.13 displays the effect of the Euro trough receiver tube misalignment in  $x$  direction before (out of specs) and after improvement (in specs). Finally, the authors concluded that the collector intercept factor can be spoiled, and the ray beams spread due to a single high deviation in collector parameters. The study failed to evaluate the effect of the receiver tube deviation in the  $y$ -direction, which would be useful to evaluate the potential different effects of deviations in either direction.

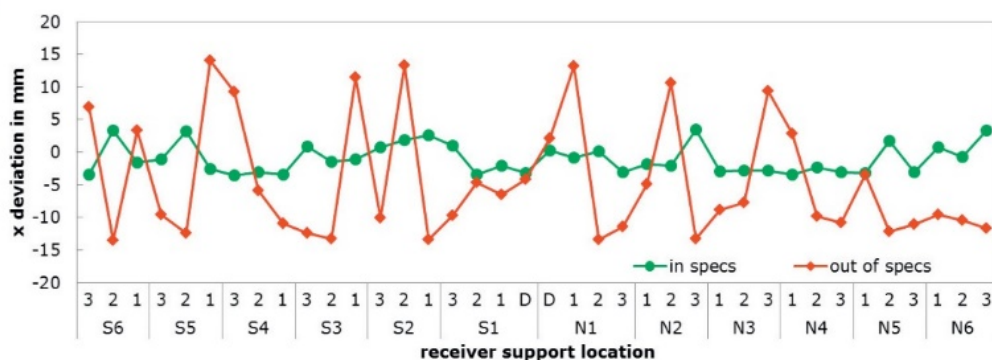


Figure 2.13 Receiver support location and  $x$  deviation of two typical alignment data of Euro trough solar collector out of specs (red line) showing the receiver tube misalignment in  $x$ -direction before the improvement, while the in space (green line) showing the receiver tube misalignment in  $x$ -direction after the improvement (Pottler et al. 2014).

### 2.2.1.3 Concentration ratio (CR) and rim angle ( $\theta_r$ )

The magnitude and degree of some PTSC parameters like CR and rim angle have an obvious influence on PTSC performance due to their effects on sunlight distribution on the absorber tube, HTF temperature and also heat generated. Therefore, some researchers have presented numerical and experimental studies to analyse and investigate the influence of these parameters on PTSC efficiency.

In analysing the effects of the rim angle on PTSC performance, by coupling MCRT and Computational Fluid Dynamics (CFD) software, an investigation of a PTSC has been done for rim angles  $40^\circ$ - $120^\circ$  and CR 57-143 (Figure 2.14). In addition, the flux distribution on absorber tube and minimum entropy generation were investigated. At low rim angles and high CR, the high entropy generation rates were due to high temperatures in the receiver tube outer surface and fluid flow inside the receiver tube

of the PTSC. Any increase in CR can lead to an increase in solar heat flux on the receiver tube wall in addition to the peak flux values as the rim angles reduces. In addition, it was noticed that the low rim angles give high receiver tube wall temperature gradients due to high heat flux peaks. However, this could potentially produce an absorber tube surface thermal strain due to concentrating the reflected heat flux on a small surface area of the absorber tube for a collector with both a low rim angle and a high CR. Therefore, this could consequently reduce the collector receiver tube operational life or cause the absorber tube component to fail. Figure 2.14 illustrates the variation of the heat flux around the receiver tube circumference at different rim angles ( $40^\circ$ - $120^\circ$ ) for 86 and 143 CR in addition to displaying the heat flux at various CR (from 57-143) for rim angles  $40^\circ$  and  $100^\circ$  (Mwesigye et al. 2014a).

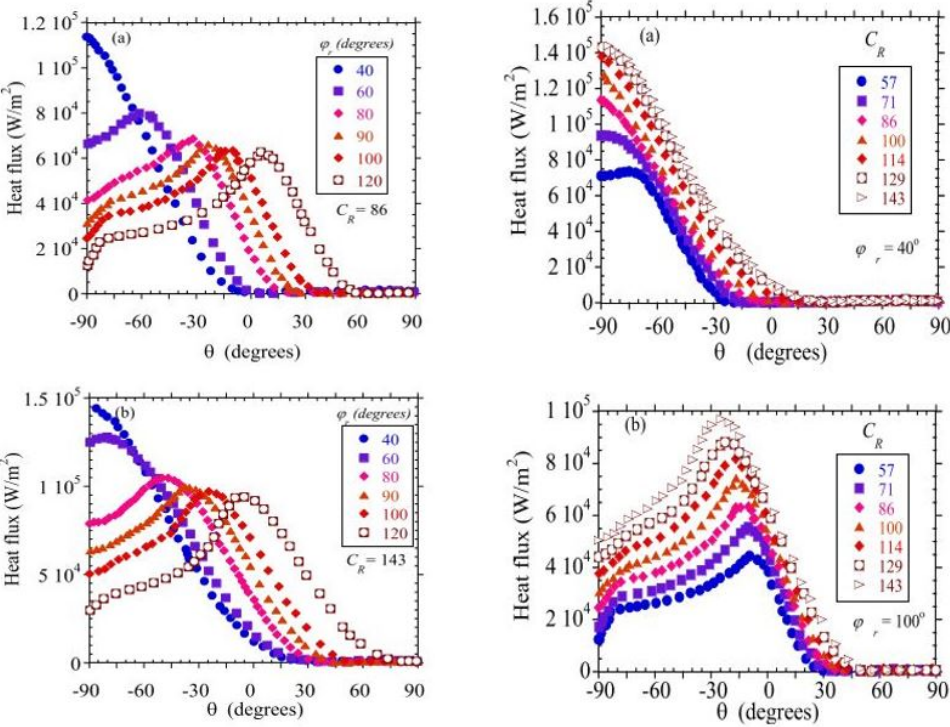


Figure 2.14: Solar heat flux distribution on receiver tube at various rim angles and CR (Mwesigye et al. 2014a).

Generally, an optimisation in PTSC parameters like  $\theta_r$ , slope structure, CR and receiver glass transmissivity can lead to reduced PTSC thermal loss. This improves the PTSC performance. He et al. (2011) carried out the reflected solar radiation distribution on an LS-2 solar collector receiver tube. The study was based on the coupled MCRT method with the Finite Volume Method (FVM). The authors investigated the effects of various CRs and rim angles on PTSC receiver tube heat flux distribution and on PTSC performance. Figure 2.15 shows the distribution of the heat flux on the outer

surface of the receiver tube under various CR and rim angles. It was noticed that the HTF temperature was also influenced by the solar heat flux distribution and became higher when increasing the CR. This (increasing the CR value and reducing the rim angle) possibly can enhance the effect of convective cooling by wind around the receiver tube surface, due to increasing the receiver surface temperatures, and also it can increase the absorber tube thermal strain as well. These two matters should be overcome by creating a receiver tube enhancement, such as insulating the upper part of the receiver tube glass envelope, which can reduce the influence of these factors. On the other hand, the solar flux concentrating ratio value reduced when the rim angle became too large, due to distributing the same heat flux on a larger absorber surface area, thereby increasing heat loss. When the rim angle is too small, a significant portion of sunlight is reflected by the glass envelope, thereby reducing collector efficiency.

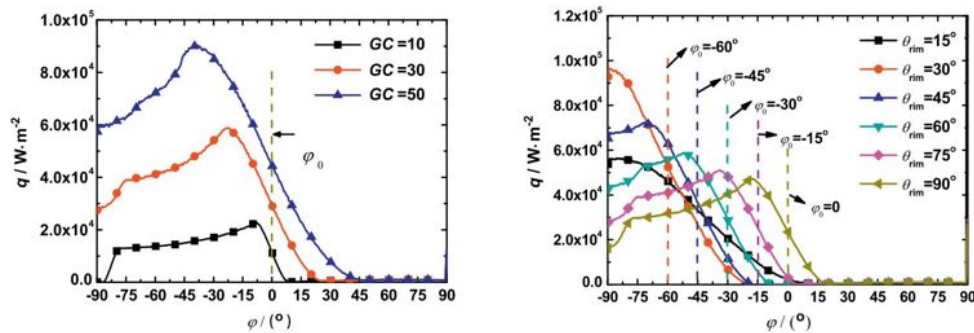


Figure 2.15 Solar heat flux distribution on receiver tube under several CR and various rim angles of PTSC (He et al. 2011).

In order to achieve more cost effective and high PTSC performance, the CR of PTSC was theoretically evaluated by Yang et al. (2010). The study focused on the optical simulation of the PTSC by using the MCRT method using various collector rim angles. In addition, the author also analysed the effect of tracking errors on the PTSC performance.

Islam et al. (2017) analysed and evaluated the influence of physical and optical factors on PTSC optical performance. Parameters such as CR, optical efficiency and the average light concentration were also investigated using the MCRT method. The obtained results showed that the collector optical efficiency reduced by around 4% for 90° rim angle while it was improved by around 2% for 70° rim angle. Even though the

reduction in collector rim angle enhanced the collector optical performance, the collector thermal performance needs to be investigated in addition to observing the shape of the concentrating solar heat flux distribution on the collector absorber tube surface when the collector rim angle is reduced from 90° to 70°.

#### **2.2.1.4 Gravity effect**

The PTSC mirror shape accuracy is one of the main collector structure parameters that can significantly influence the optical and thermal collector performance. Mirror deformation due to self-weight can lead to a double influence on the mirror focusing accuracy. It results in reflecting the sunlight away from the intended area (both axially and transversally from the collector focal line), which consequently reduced the receiver heat gain and decreased the PTSC performance.

Meiser et al. (2015) evaluated the effect of gravity load on the reflector slope of the PTSC. The obtained results show that the less rigid the support structure, the higher is the impact on size and characteristic of gravity-induced deformation. The authors also illustrated various support structures for the collector mirror and compared them with an ideal case (without deformation) as shown in Figure 2.16. The authors also reported that the gravity load of the PTSC structure contributed to the mirror deformation, which increased the value of the reflected sunlight missing the absorber tube. The study presented a credible numerical evaluation about the gravity effect for different PTSC reflector structures, but it would be more useful if the numerical results had been validated experimentally.

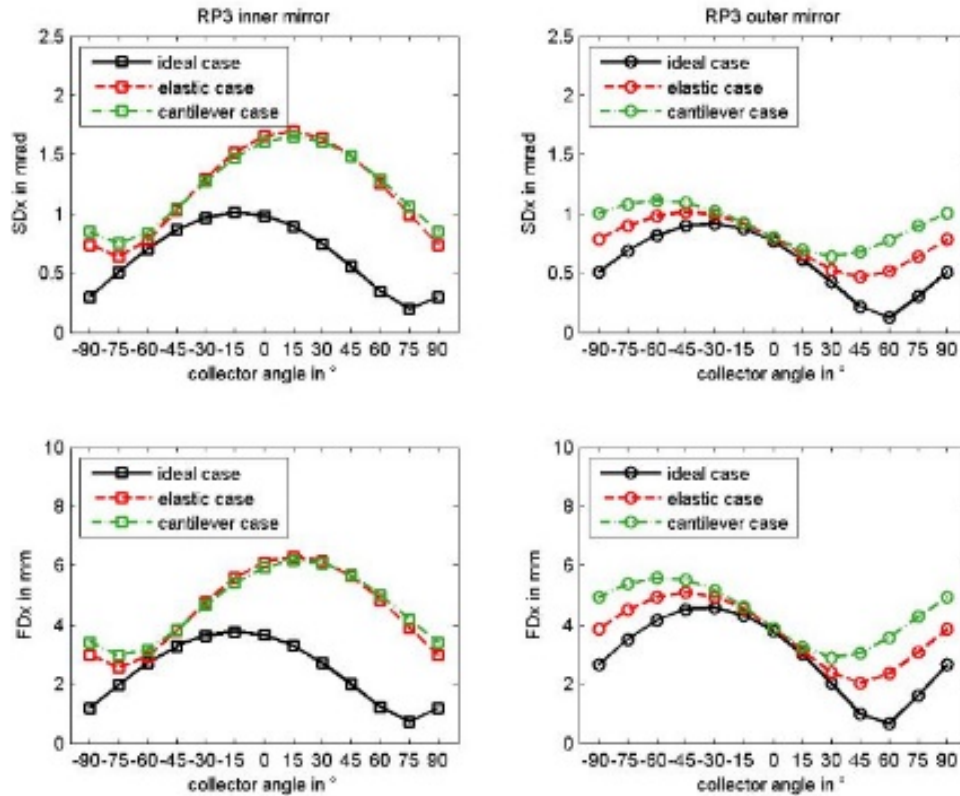


Figure 2.16: RMS slope and focus deviation for outer (right) and inner (left) mirrors that fixed onto ideal, elastic and cantilever PTSC reflector model structure (Meiser et al. 2015).

In another study, ideal, elastic and cantilever PTSC support structures with different constructional designs have been analysed by Meiser et al. (2017). This work was done in order to evaluate and analyse the effect of gravity load on the reflecting sheet using finite element modelling. The results show that the maximum slope deviation in x direction (SDx) is equal to 1.7 mrad. Focusing deviation in x direction (FDx) was found to be 6.3 mm for the inner mirrors of the elastic structure supported model. It was found that the maximum value of SDx and FDx in the outer side of the cantilever structure model was equal to 1.1 mrad and 5.6 mm respectively. As in the previous study, the numerical results of the study need to be validated.

A new method uses three-dimensional data from laser scanners to measure and analyse PTSC surface deformation. Mirror deformation could be due to reflector weight or due to influences from wrong placement or manufacturing processes. Salamanca et al. (2015) recommend using this method when measuring PTSC mirror deformation under operation conditions in a solar power plant.

Based on the above studies, it is necessary to analyse and evaluate the effects of mirror surface weight and the load of the mirror support structure on the system efficiency at the design stage. Furthermore, it is also required to investigate mirror shape during PTSC operation to point out any deviation in the reflecting part.

### **2.2.1.5 Tracking error**

Tracking error is defined as a deviation between the sun position and the normal line on the reflector. In PTSC technology, the tracking system is a main component, which keeps the reflector facing the sun's position during operation time. Therefore, a tracking error could directly influence the PTSC's optical performance.

Zhao et al. (2016) investigated the effects of a tracking error in addition to the effects of receiver installation errors on PTSC performance. The study was performed by coupling the MCRT and CFD software, and simulating different incident angles and constant concentration ratio (CR). Figure 2.17 illustrates the heat flux distribution on the receiver tube outer surfaces under various tracking and incident angle errors. The authors found that the peak of solar heat flux increased slightly and the heat flux was not symmetric on the outer surface of the receiver as the tracking error increased. The authors also investigated the value of the peak flux and its distribution on the receiver wall for a 3 mrad fixed tracking error and various incident solar radiations. The authors found that the increasing incident solar angle leads to rapidly decreasing peak heat flux and flux distribution which result in overheating of the receiver wall. The presented results (influences of tracking error and variation of incident angles on the concentrating heat flux on PTSC receiver tube) should investigate different collector concentration ratios. This is because that the CR factor is a critical parameter in the optical and thermal performances of the PTSC technology.

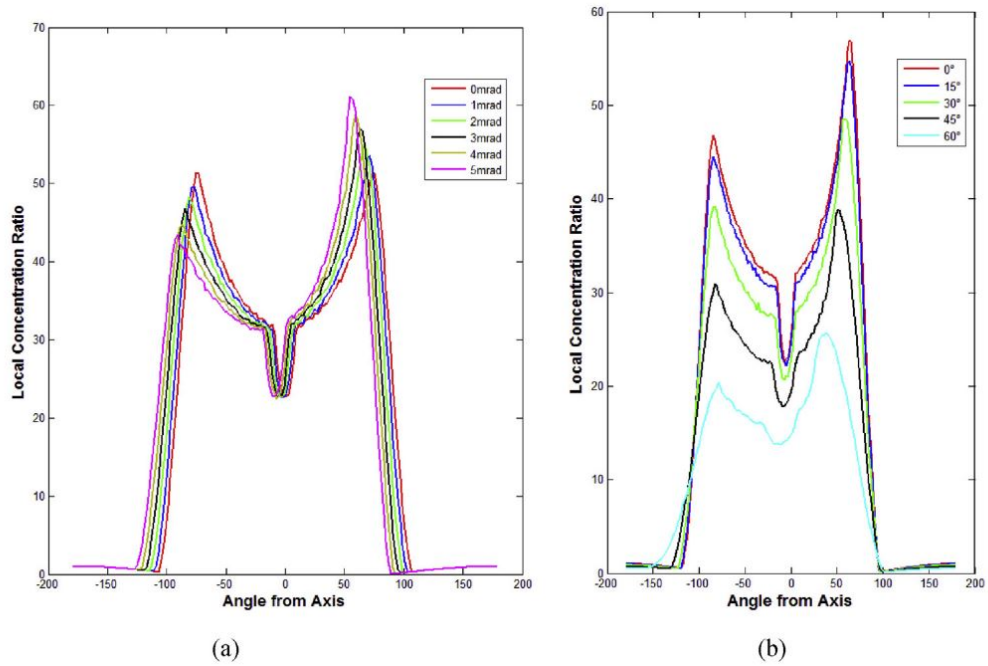


Figure 2.17: The shape of the solar heat flux for tracking errors under (a) CR 20, zero incident angle and various tracking errors, (b) under 3 mrad tracking error CR 20 and various solar incident angles. The non-symmetrical heat flux on absorber tube surface is due to the reflected heat flux being predominantly distributed on one side of the absorber tube because of collector tracking error (Zhao et al. 2016).

The optical performance of a 6 m wide and 1.7 m focal distance of a PTSC has been simulated and analysed through proposing a new analytical method. The new analytical method is summarised by calculating the optical efficiency of each point at the trough solar mirror separately, and then calculating the total efficiency of the PTC system via integrated points of the reflector. The effect of the tracking error in addition to solar radiation incident angles error on the PTSC optical efficiency were investigated in the study, as illustrated in Figure 2.18. The obtained results presented that the collector optical efficiency reduced from 71% to 53% with increasing tracking error from 0 to 12 mrad. This occurred due to misalignment of the focal line from the centre of the absorber tube due to a tracking error. As a result, the reflected sunlight rays do not hit the receiver tube on the proposed area, which can lead to low collector optical performance (Huang et al. 2012). From the study results, it can be noticed that the collector optical performance reduced by 18% due to a  $0.6^\circ$  collector tracking error. This highlights the large influence of this factor (collector tracking error) on deviating reflected solar rays: losing a substantial amount of concentrated radiation energy. Therefore, limiting the PTSC tracking error is very important, especially for this technology that relies on solar tracking.

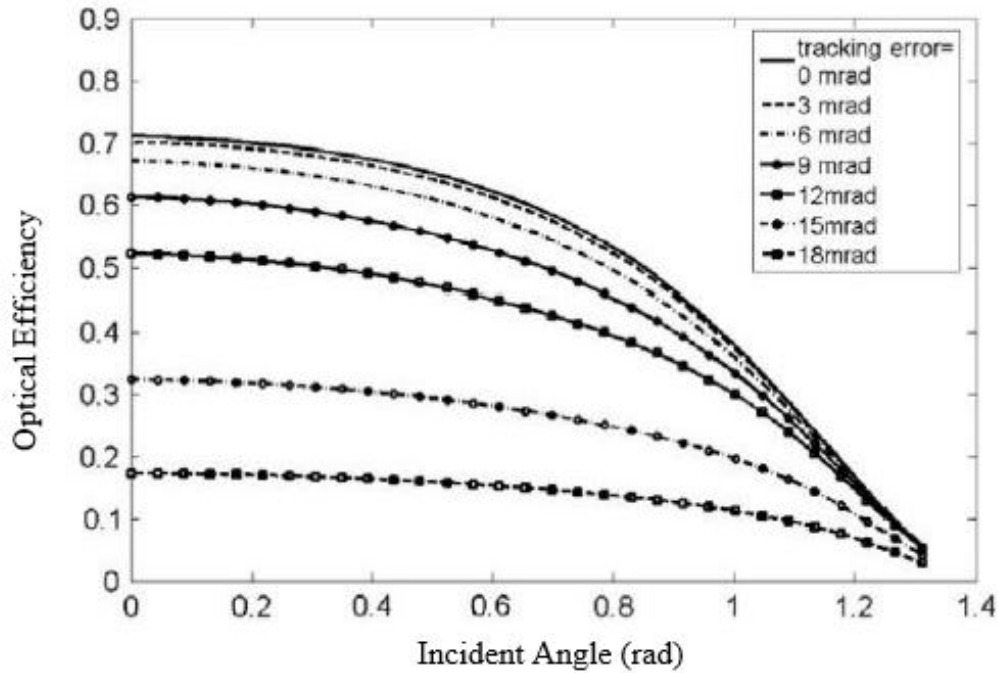


Figure 2.18: Optical efficiency (Y-axis) of a PTSC at different tracking errors (varying from 0 mrad to 18 mrad) and various incident angles (X-axis) (Huang et al. 2012).

Islam et al. (2017) investigated the influence of physical and optical parameters on the optical efficiency of PTSC. Via analysing the effect of tracking errors on the PTSC performance, the results demonstrated that a tracking error more than  $0.6^\circ$  could cause a rapid decrease of the PTSC optical performance as shown in Figure 2.19. This error resulted in a rapid drop of the average of solar heat flux concentration on the receiver tube. This resulted in a rapid reduction of PTSC performance.

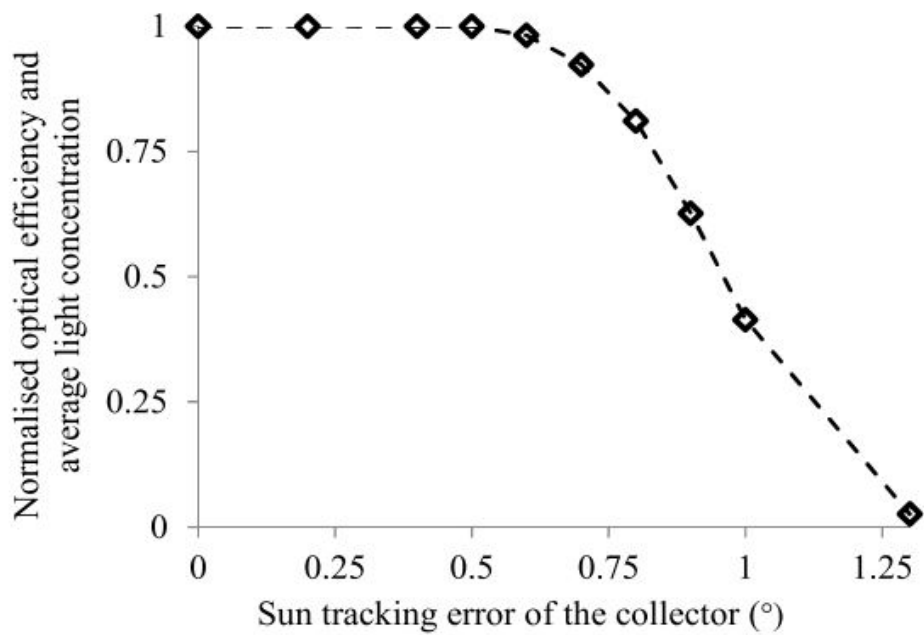


Figure 2.19: Influences of tracking errors varying from  $0^\circ$  to  $1.25^\circ$  on the PTSC optical efficiency (Islam et al. 2017).

### 2.2.1.6 Wind effect

PTSCs are usually located in open terrain where high-speed winds may occur and affect both structure and performance of the PTSC. Thus, the focusing accuracy of a PTSC mirror can be influenced by any deformation that can occur due to wind load. This section presents many analytical and experimental studies that have been carried out to analyse the effect of wind load on PTSC systems.

A two-dimensional numerical study analysing wind velocity effect on a PTSC reflector and its absorber tube was presented by Naeeni and Yaghoubi (2007b). The collector was investigated under various collector tracking angles between  $-30^\circ$  and  $90^\circ$  and various wind speeds between 0 and 16 m/s, as shown in Figure 2.20. This figure shows the investigation cases for the collector under various wind velocities and the magnitude of the wind force. The authors correctly observed that wind load on the collector structure is minimum when the collector is in a horizontal position (at noontime when the collector aperture area level is parallel with wind direction), while the wind load is sharply increased when the collector tracking angle is increased and reaches maximum when it is perpendicular to the wind direction. Tracking collectors

are almost perpendicular to the wind at sunrise and sunset (when the sun is close to the horizon).

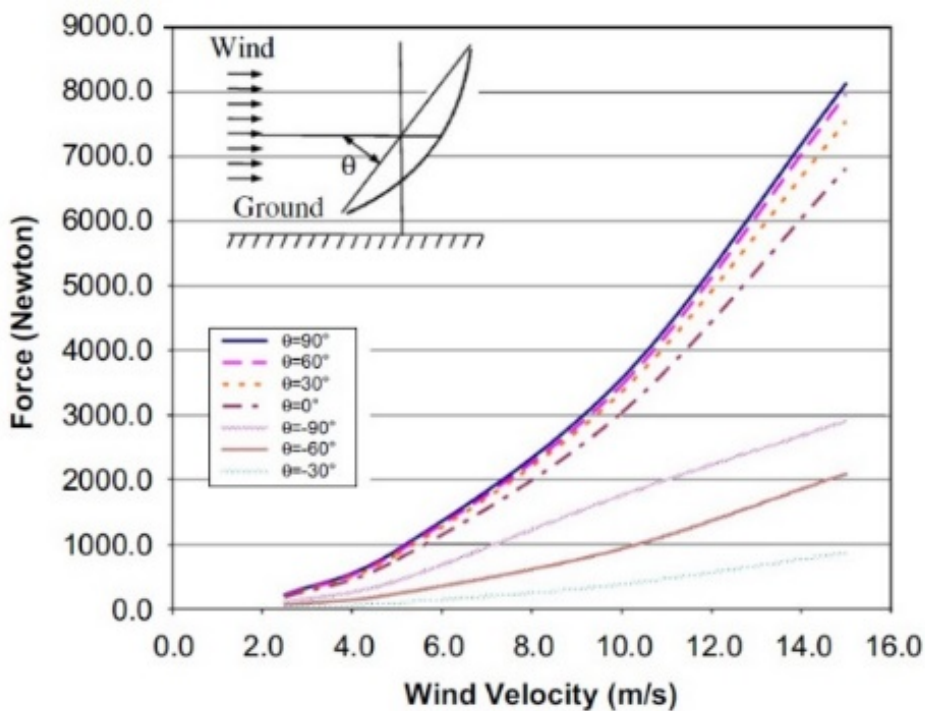


Figure 2.20: Fluctuation of total wind load on the collector aperture area for various collector orientations and wind speeds (Naeni & Yaghoubi 2007b).

A three-dimensional numerical study, a 5.7 m aperture width and 12 m length of a PTSC aperture area was used to analyse and calculate the effect of wind velocity around its structure (Mier-Torrecilla et al. 2014). The simulation results were compared with the experimental data and it was found that the relative mean errors were within 10%, consequently of the similar order as experimental uncertainty. The range of the investigation collector pitch angles were selected to be from  $-30^\circ$  to  $210^\circ$ . It was noticed that the clear difference in the lift force is for angle  $90^\circ$  horizontal position. At this pitch the presence of the back structure especially adjusts the separation point of the flow wind beside the bent surface as displayed in Figure 2.21. The authors found that the wind loads act very strongly along a row of PTSCs, and the PTSC essential support has some impacts on the pitching moments of the modules close to the support. The study would be more valid and useful if it considers the effect of the convective cooling by the wind on the collector receiver tube under the same range of the collector pitch angles, and then evaluate and compare between the wind effect in both aspects (wind load on the reflector and also the receiver tube convective

cooling by the wind) under that range of collector pitch angles. For example, the wind load would be minimum at pitch angle  $90^\circ$  (horizontal) but the receiver tube convective cooling by the wind would be the maximum. The reverse occurs when the collector pitch angle equals  $0^\circ$  or  $180^\circ$  (near sunrise or sunset): the wind load would be maximum, while the receiver tube convective cooling by the wind would be minimum.

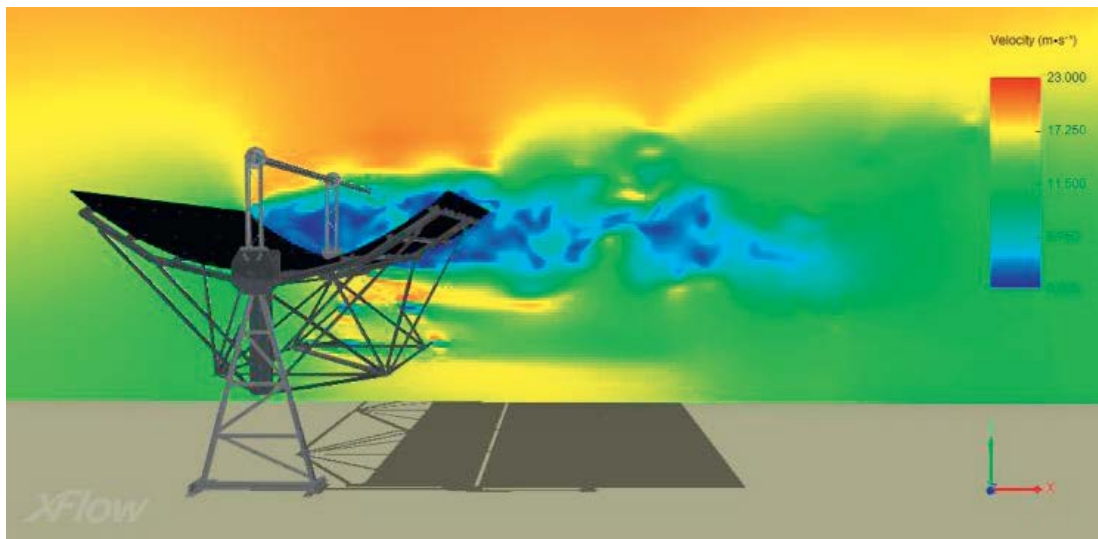


Figure 2.21: Instantaneous wind speed field (Mier-Torrecilla et al. 2014).

A numerical study analysing wind engineering on PTSC efficiency was undertaken by Paetzold et al. (2014) using a three-dimensional simulation via commercial CFD program ANSYS. The authors revealed the influence of wind velocity on both PTSC structure and thermal losses in the receiver tube were due to force convection. The obtained results show that increasing the collector rim angle (making the collector deeper) can lead to increased wind load on the collector structure compared to the shallow trough shape (low rim angle) under normal wind loads. Wind airflow around the absorber tube will decrease with increasing rim angle because the collector shields the absorber tube more. This can result in reducing the thermal losses around the receiver tube and improving the overall PTSC efficiency due to achieving higher temperature. Based on that, it could be important to reduce the receiver heat loss for shallow collectors (low rim angle) by adding insulation, for example.

Hachicha et al. (2014) conducted a numerical analysis of wind speed that affected PTSC structure and leads mainly to increasing heating convection loss around the absorber tube. Three pitch angles of unsteady flow ( $0^\circ$ ,  $45^\circ$  and  $90^\circ$ ) and several PTSC

structures were considered during the study, as shown in Figure 2.22. The results show that the turbulence is strongest when the collector is in the vertical position (sunset and sunrise angles), and weakest when the collector is in the horizontal position (noon time). The authors also noticed that during operation of a PTSC under high wind velocities, strong turbulent fluctuation could occur and that leads to collector structure vibration, especially when the collector aperture area is oriented as the maximum drag obstacle for the wind. This could potentially result in deviating part of the reflected sunlight rays from the receiver tube on the proposed surface area, consequently reducing the collector heat energy gain. Also, this fluctuation could result in the collector structure failing.

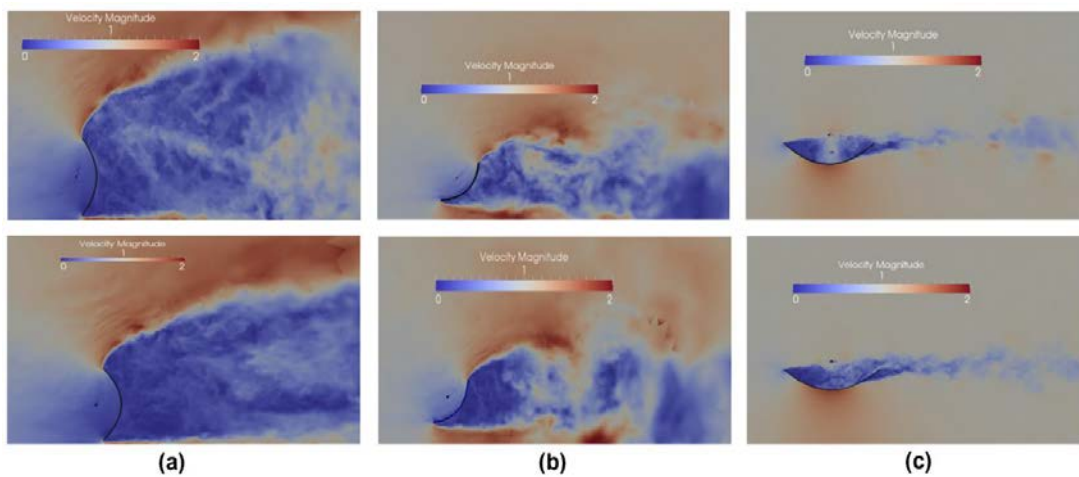
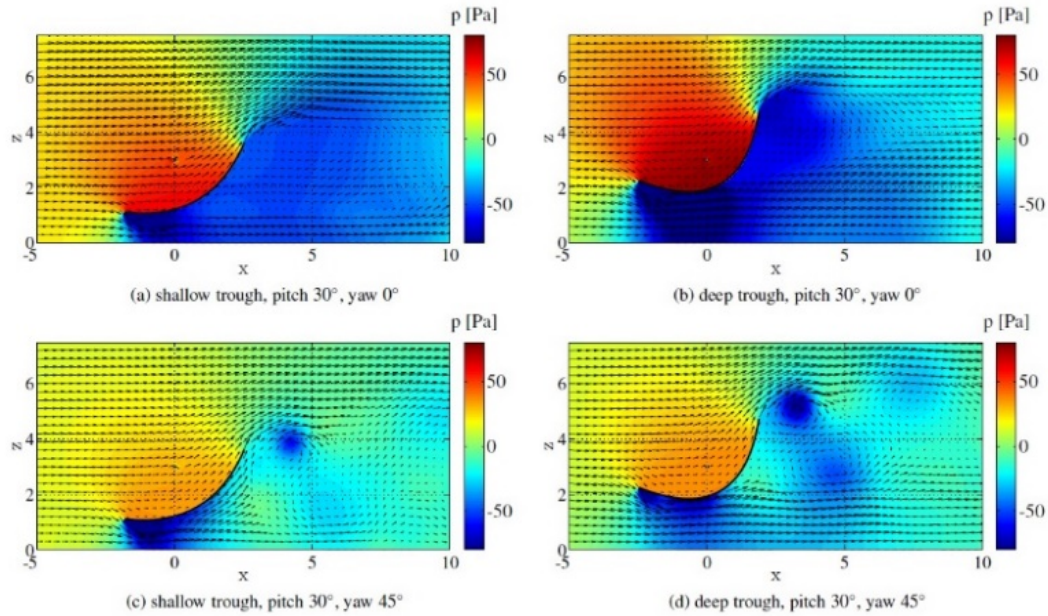


Figure 2.22: Wind velocity distribution around PTSC structure under different collector pitch angles: (a)  $\theta=0^\circ$ , (b)  $\theta=45^\circ$  and (c)  $\theta=90^\circ$ , and under Reynolds number  $3.9 \times 10^5$  (top) and  $1 \times 10^6$  (bottom) (Hachicha et al. 2014).

Because PTSCs are normally can be subjected to high wind load, which impacts the performance of the PTSC solar thermal plant, Paetzold et al. (2015) investigated the effect of wind velocity on the collector structure and performance level. In this study three types of trough collectors under a large range of yaw and pitch angles were analysed. Figure 2.23 illustrates the velocity vector and pressure contour of shallow and deep trough solar collector shapes under various pitch and yaw angles. The obtained results were validated against experimental data. The researchers found that wind velocity around the receiver tube leads to thermal losses due to forced convection, in addition to affecting the collector structure. The study also focused on variation of rim angles and how it influenced both structure and the operation of the PTSC. The study showed that increasing the value of the rim angle can result in

improvement in PTSC thermal performance due to reducing the forced convection, but can also lead to increased wind load on the collector structure due to increased cross-sectional area. However, increasing the rim angle could be also, as in the previous study, cause fluctuations in the reflector structure—especially close to sunrise or sunset—and deviate some of the reflected sunlight from the receiver tube.



*Figure 2.23: Wind load on shallow and deep trough of PTSC, under 30° pitch angle and 0° yaw angle (top row) and 30° pitch angle and 45° yaw angle (bottom row) (Paetzold et al. 2015).*

In another study, Paetzold et al. (2016) undertook numerical work to analyse the wind effects on eight rows of full-scale different parabolic and staggered PTSCs. The authors found that the wind effect on the larger solar field depends on the position of the collector row. The outer rows are normally subjected to the highest wind loads compared to the interior collector rows which are protected from high winds. In addition, the wind aerodynamic pressure on the interior solar collector rows is based on several parameters like collector rim angle (deeper or shallower). Finally, for all the collector shapes it was found that the aerodynamic pressure is significantly lower in the interior of the solar field than in the first line. Based on this, the solar collectors in the first row (first line) should be modified in order to reduce the effect of the wind load on the PTSC performance.

### **2.2.2 PTSC optical enhancement techniques**

The effect of changing the reflector surface (film mirror and glass mirror) of a PTSC, when combined with vacuum receiver tube, were evaluated by Xu et al. (2014). Figure 2.24 illustrates the cross section of the PTSC where film and glass reflectors are used. Experimental data of three typical days at 40° latitude were used for evaluation of the numerical results. The PTSC performance with the glass mirror reflector was higher than that of the system with the film mirror by around 50%. The author recommends using the glass reflector to avoid the optical errors, especially at high latitudes. The proposed solution could be costly. Also, the reflector (usually surrounded by ambient temperatures) concentrates large numbers of incident beam rays towards the collector receiver tube. Therefore, this could produce a high temperature difference between the reflector surface (proposed glass mirror) and the ambient temperature, which could deflect the glass mirror surface or it could reduce the operational life of the proposed reflector. Thus, these aspects should be carefully analysed and evaluated.

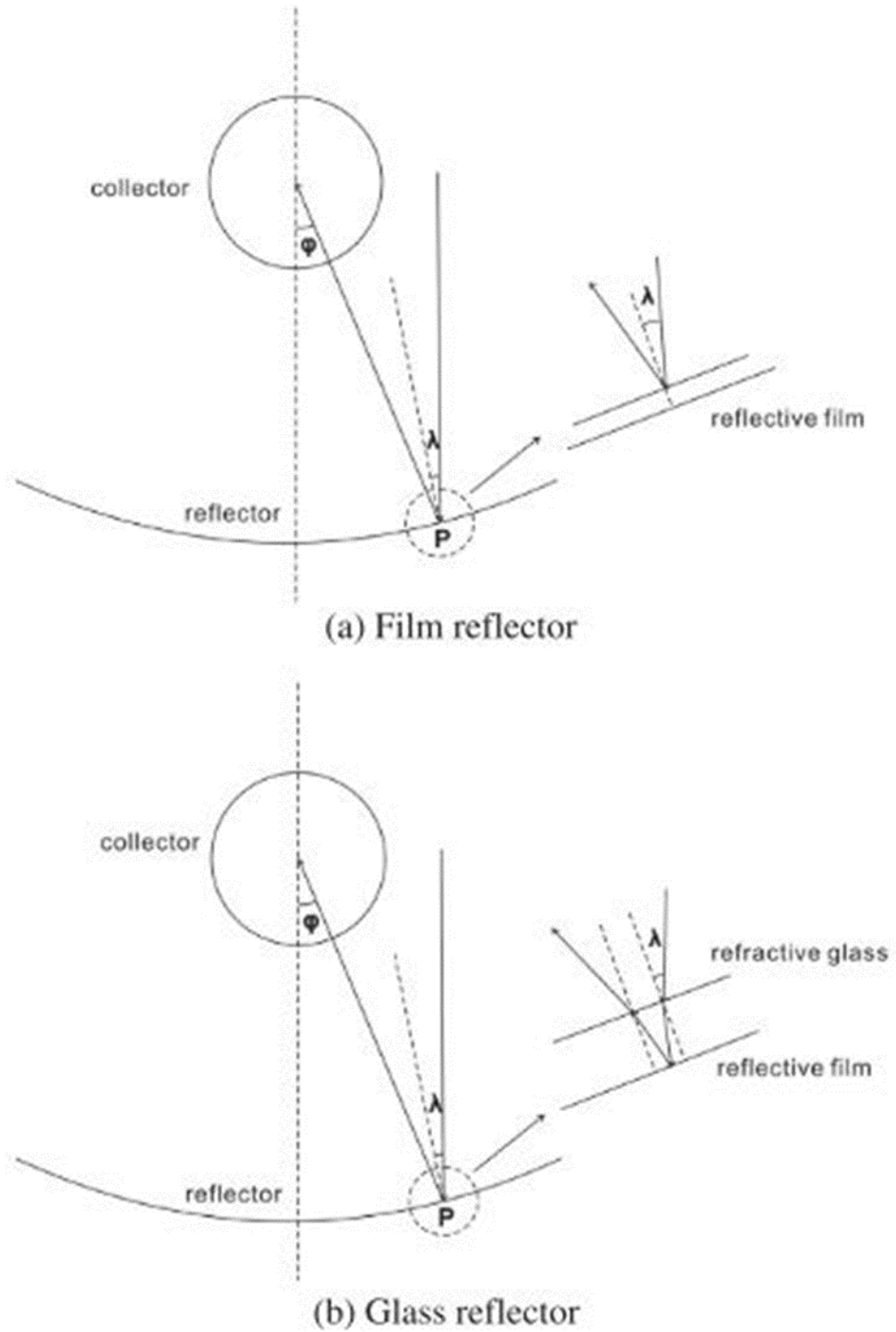


Figure 2.24: Views of cross sections of the glass mirror and film mirror of PTSC reflector with receiver tube (Xu et al. 2014).

light concrete shell prototype of PTSC with target points was designed and manufactured by Forman et al. (2015). The aims of this study are to overcome the disadvantage of the separation between supporting structure and reflecting surface due to using a steel frame as a base for the collector reflector, and also to improve the PTSC optical performance and reduce the effect of structure slope error. “The model consists

of a thin parabolic shell collector made from high-strength concrete to ensure structural stiffness and to serve as substrate for reflection elements simultaneously, all mounted on circular segments of novel rocker bearings. This bearing keeps the shell's centre of gravity horizontally levelled while tracking the sun controlled by an automatic driving system. Though, this kind of bearings causes local tensile stress peaks at the connection between shell and bearings, the prototype primary aims to show the feasibility of the use of concrete for parabolic troughs and therefore consists of geometrically simplified parts appropriate for manufacturing in the frame of this project. Furthermore, it is designed for a limited lifetime. For a serial production additional form optimisation steps minimising local stress peaks are necessary" (Forman et al. 2015).

The concrete model is compared against a steel form as shown in Figure 2.25. It can be seen from the figure that both concrete and steel models have same aperture area dimensions such as rim angle, focal distance and aperture area. The theoretical and experimental results illustrated that the concrete structure resulted in full optical efficiency. Based on the numerical results and due to the highly accurate reflector surface of the light concrete, the author found that using this new structure led to an increase in the collector aperture area and produced more energy. However, one of the bigger challenges with the proposed concrete structure is where a segment of a single reflector or the structure of a collector (which is part of a row of collectors) fails, potentially resulting in costly maintenance. This is due to the proposed structure not being standard (not available commercially). Moreover, a failed part of the reflector structure could require the entire reflector structure to be replaced.

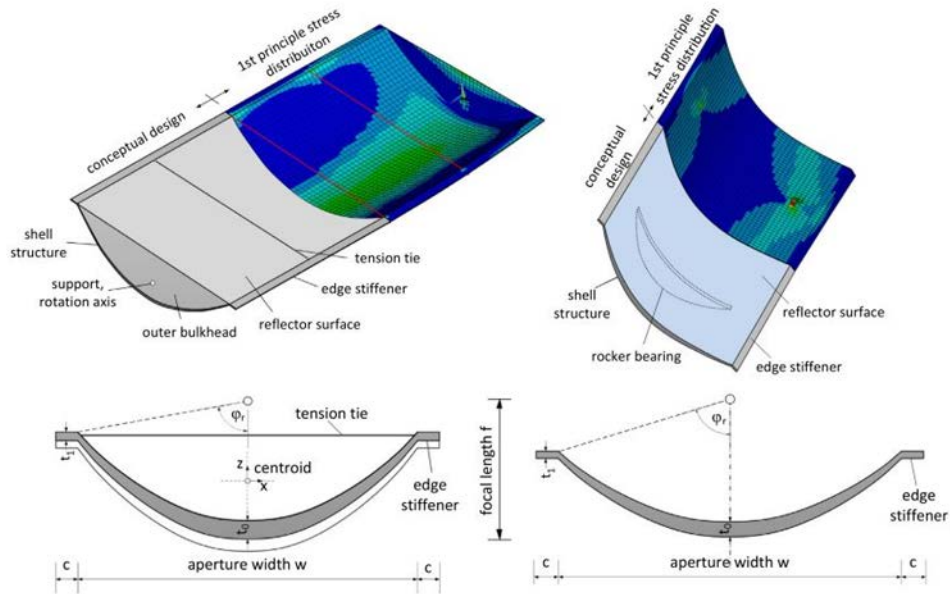
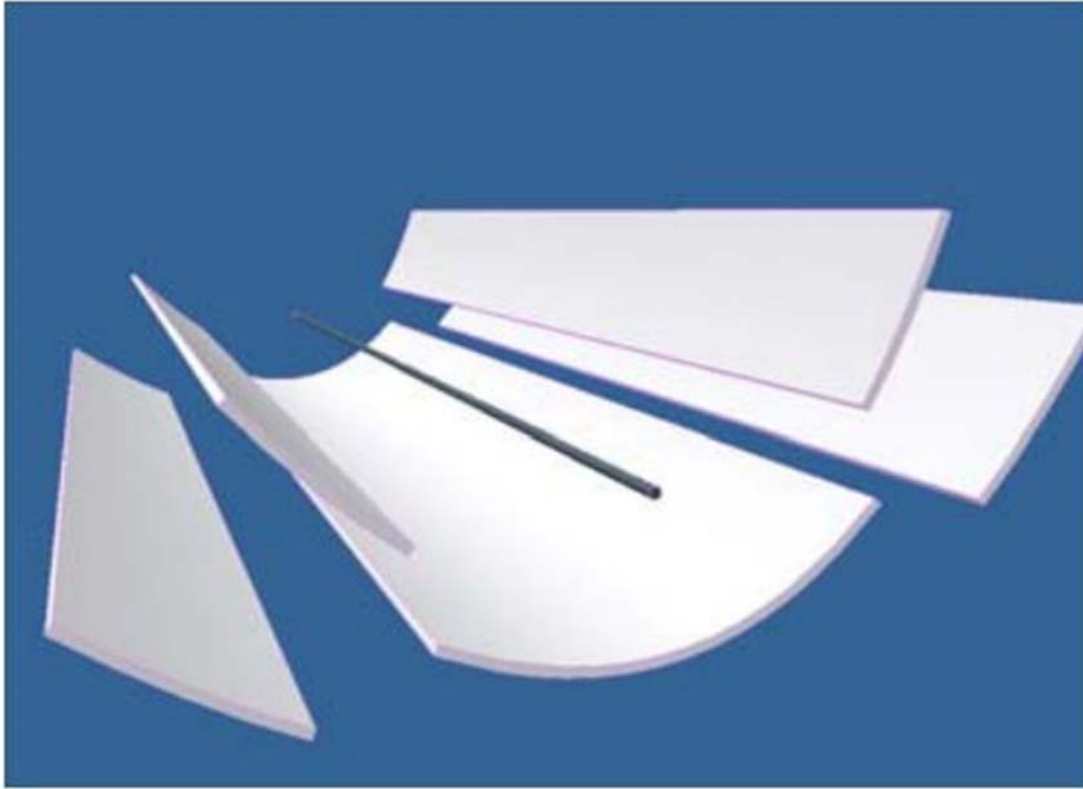


Figure 2.25: Schematic of the PTSC models. The concrete (left) and prototype (right) both have same aperture area dimensions (Forman et al. 2015).

Prahl et al. (2011) proposed an optimising of a line-focussing solar collector with a stationary receiver tube as illustrated in Figure 2.26. This design consists of five panels which are installed to maintain the same relative position to each other. The length of this three-dimensional model is 12 m and the aperture width is 6 m. The authors revealed a cost reduction and efficiency improvement compared to trough solar collector via analysing the new structure of a PTSC under several operation conditions such as wind load and slope reflector accuracy using a finite element method. The results showed that the focus deviation of the reflected solar light from the absorber tube are less than 6 mm (approximately 5% of the absorber tube's diameter) under operating conditions for a collector structure weight of 14 kg per 1 m<sup>2</sup> of aperture area. The 6 mm deviation could deviate some of the concentrating solar radiation, especially for conventional collectors that have a high concentrating ratio. This consequently could reduce energy gain and collector performance. And therefore, based on this outcome, it is necessary to optimise the structure of the proposed design to reduce the solar radiation's deviation (which was 6 mm).



*Figure 2.26: Schematic of the trough collector model consisting of five reflecting panels with 12 m length and 6 m overall aperture width (Prahl et al. 2011).*

## **2.3 Receiver tube thermal loss and enhancement technologies**

This section presents a review of studies of PTSC receiver tube thermal loss, in addition to presenting the techniques that can be employed to improve the PTSC receiver tube heat transfer performance.

### **2.3.1 Convection heating loss of PTSC receiver tube**

The heat collection element (HCE) of the solar collector has a major role in the collection of solar energy. Thus, in order to achieve high solar collector performance, thermal loss should be reduced from this essential element (Singh et al. 2010). Therefore, this section focuses on the reasons behind HCE thermal loss and its influence on PTSC thermal performance. However, few experimental works and limited numerical studies have investigated this part of the PTSC technology.

Wu et al. (2015) carried out an experimental study to investigate the performance of the HCE using different HTF operation temperatures. In this study, molten salt was used as a HTF with 550 °C maximum operating temperature. Using the HTF average temperature compared to the ambient temperature, the HCE thermal loss was

determined. As shown in Figure 2.27, it can be noticed that the HCE thermal loss increased as the average HTF temperature increased. This (increasing receiver heat loss) could have occurred due to the reduction in the HTF absorption of heat—which is due to a reduction in the temperature difference between the absorber tube surface and the HTF. This increased the absorber tube surface temperature, which consequently increased the receiver tube heat loss. Thus, the conclusion from this work is that for the PTSC system that operates with high HTF operation temperatures, their receiver tubes should be modified somehow to reduce convective cooling by the wind from the outside and also protect the absorber tube from thermal strain (which bends the absorber tube) from the inside. This could be achieved, as mentioned before, by adding insulation on the inner surface of the upper part of the receiver tube's glass envelope.

The study also calculated the thermal loss in the joining points of the HCEs and it was noticed that joint points' thermal loss is around 5% of the total HCE thermal loss. It also found that the terminal loss (join points' loss) can reach around 18% without using HCE thermal insulation. The total heat transfer coefficient of the HTF was investigated at different fluid temperatures and Reynolds numbers (Re). It was observed that with increasing HTF temperature, the heat transfer coefficient rose in the range of 600 W/m<sup>2</sup>K to 1200 W/m<sup>2</sup>K as the Reynolds number changed from 14,000 to 32,000.

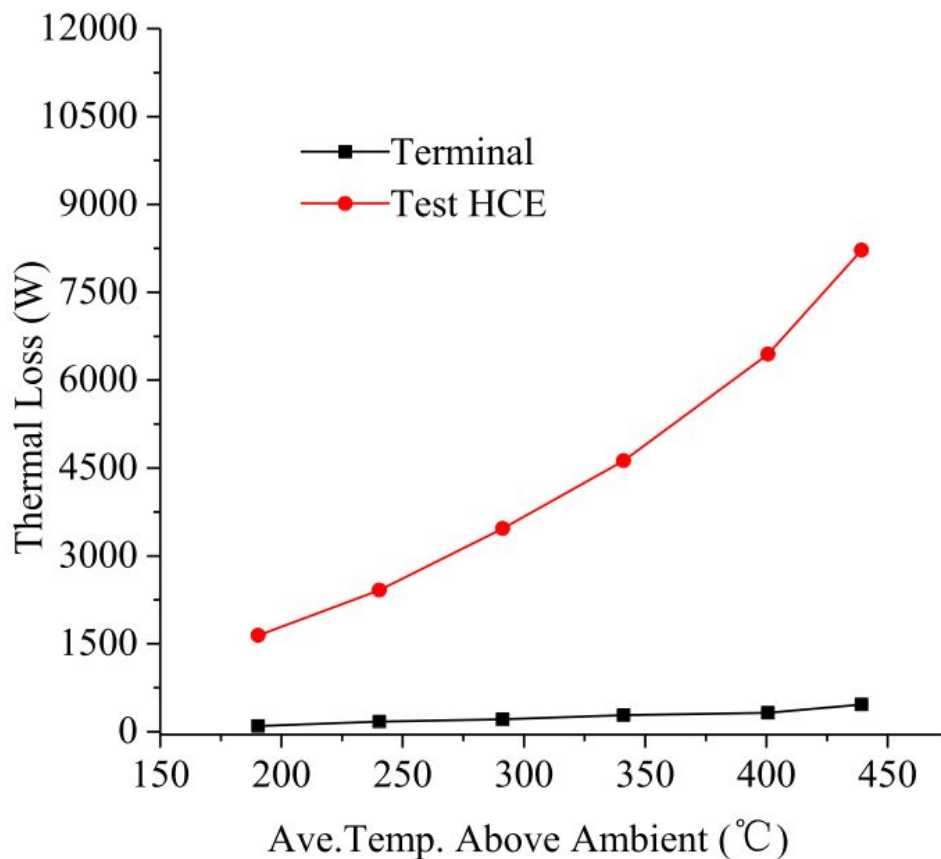


Figure 2.27: Thermal loss of the HCE and end joint points of the receiver tube (Wu et al. 2015).

Under steady and unsteady operating conditions, a two-dimensional heat transfer model was formulated by Heidemann et al. (1992) to calculate the receiver wall temperature of a solar collector. They found that a sudden drop in solar radiation resulted in a very high temperature on the inner side of the absorber tube in a short time. This could be due to the extremely asymmetric temperature field caused by the change of the heat transfer coefficient at the inner surface of the receiver absorber tube and the sunlight rays concentrating at the outer surface of the receiver absorber tube.

The effect of the collector orientation on the average Nu of the HCE in addition to heat transfer loss and wind flow distribution around a PTSC were investigated by Naeni and Yaghoubi (2007a). Figure 2.28 illustrates a PTSC at the Shiraz solar power plant used for the study. It was found that the Nusselt number (Nu) had less influence when wind blew on the convex side because the collector shields the HCE, whereas there is significant sensitivity to wind when it acts on the concave side of the collector aperture area. It was also found that wind flow distribution around the PTSC receiver tube is

completely different from structure flow around the plain tube due to wind boundary layer and PTSC orientations. As mentioned in the previous study, adding insulation into a receiver glass envelope can reduce the receiver's sensitivity to the wind.



*Figure 2.28: Parabolic collector with absorber tube at Shiraz solar power plant (Naeeni & Yaghoubi 2007).*

Optical and thermal analysis of a PTSC were presented by Hachicha et al. (2013) in order to investigate the numerical heat transfer balance of an HCE. Ray tracing and finite volume method technologies were used for the calculation of the solar heat flux distribution on the outer surface of the absorber tube and HCE heat transfer respectively. In the study, the heat loss from the receiver tube was calculated and presented with the absorber tube temperature. Figure 2.29 illustrates the heat loss from an HCE and also it shows the comparison with experimental data. It can be seen from Figure 2.29 that the receiver tube heat loss increased from approximately 40 W/m to 190 W/m as the absorber tube surface temperatures increased from 400 K to 600 K. Based on this receiver tube heat loss, an optimization for the PTSC receiver tube becomes essential, especially for PTSC that have a high CR (which normally results in high absorber tube surface temperatures). In addition, the authors analysed the variation of the glass cover temperature in respect to the temperature of a PTSC

absorber tube. It was noticed that the variation in glass temperature was due to the difference of the glass optical properties at high temperatures and also due to the effect of the anti-reflective coating that was used for the glass cover.

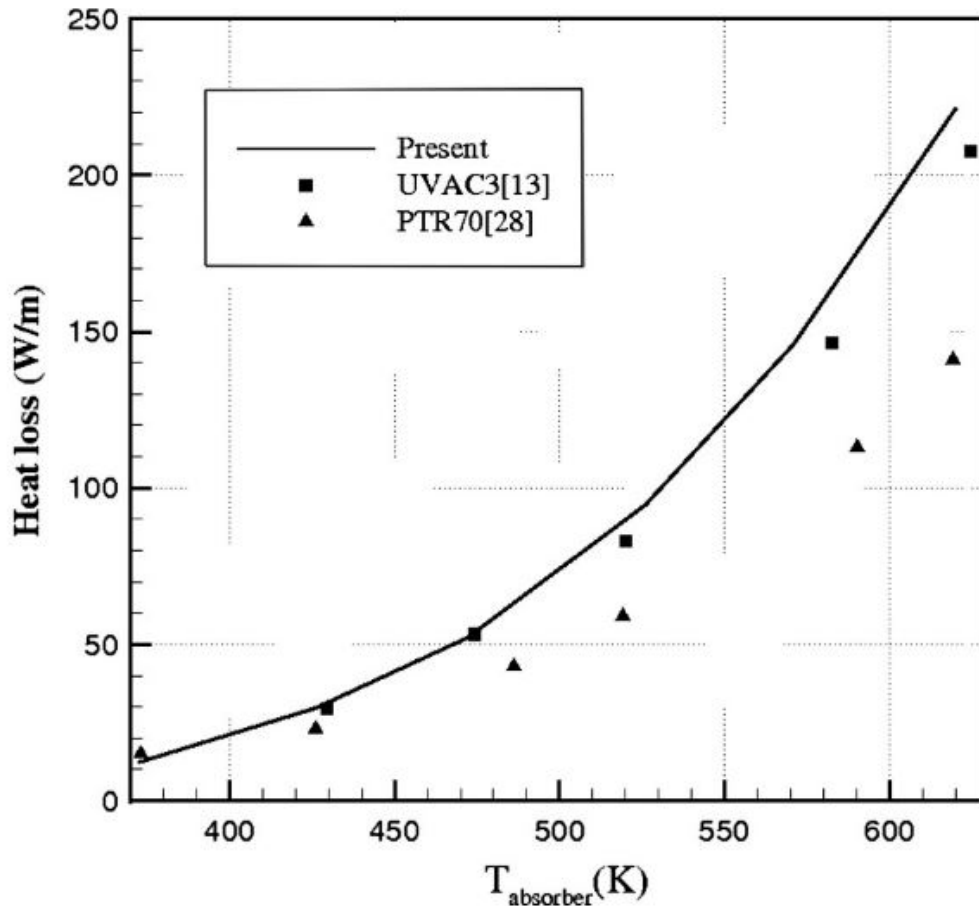


Figure 2.29: HCE heat loss and the absorber tube temperature (Hachicha et al. 2013).

Ouagued et al. (2013) presented a numerical model to estimate the heat loss, temperature and heat gain by of a PTSC device to evaluate the solar system performance in Algerian climate conditions. The major finding of this study was that increasing HTF temperature can lead to increased heat losses and reduce the heat gain of the system. Because it is useful to increase the HTF temperature to amplify the heat gain, appropriate modification of the PTSC receiver tube is required to reduce the receiver tube heat losses, for instance by using insulation.

Heat loss from a non-evacuated PTSC heat collection element was numerically studied by Patil, Panse, et al. (2014). In this study the heat loss from the receiver tube at different surface temperatures was analysed. The study found that the heat loss per unit

length increased by 448% when the average temperature for the HCE temperature rose from 432 K to 690 K (Figure 2.30). It can be seen that the data presented in Figure 2.30 is around 10 times higher than that in Figure 2.29. This is because Figure 2.30 shows the heat loss from the outside of the receiver tube, while Figure 2.29 shows the heat loss from the outside of the absorber tube (from the inside of the receiver tube).

Also, the effect of the external wind velocity on the heat loss from the HCE was also analysed. It can be seen from Figure 2.31 that the heat loss from the heat collection element is constant for variations of the wind speed from 2 m/s to 10 m/s for a constant receiver tube temperature. The lack of effect of wind speed on heat loss above the threshold could be due to the increase of the heat transfer coefficient parameter being balanced by the consequential reduction in outer surface glass cover temperature.

In addition, it can be seen that the heat losses of this element are increased where surface temperature of the absorber tube is increased from 432 K to 691 K. This convection heating loss enhancement is due to the increase in the temperature difference between the glass cover surfaces because of increasing the absorber surface temperature. The effect of evacuated and non-evacuated HCE on the ratio of heat loss was also investigated. The study noted that at lower pipe temperatures, around 432 K, the heat loss from the HCE with a non-evacuated tube is 53% more than that for an evacuated HCE. The loss dropped to around 31% as the absorber HCE temperature increased to be 691 K. Based on the study results, the heat loss for both cases is major and therefore it is necessary to reduce the heat loss, for instance by using insulation, which improves the PTSC technology performance.

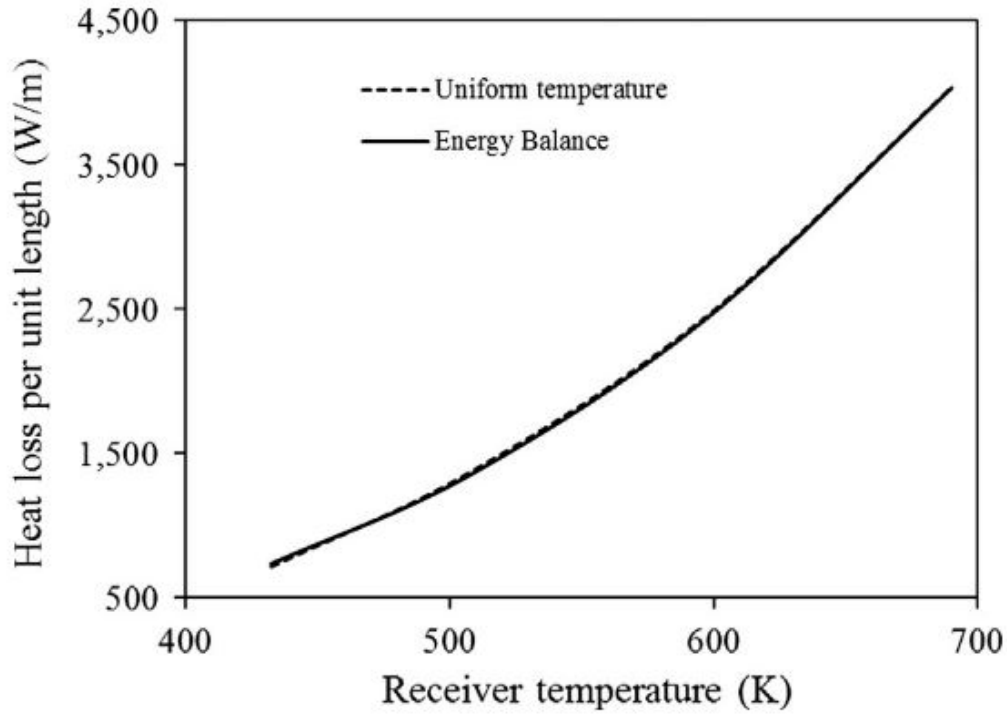


Figure 2.30: Heat loss per unit length for various HCE temperatures (Patil, Panse, et al. 2014).

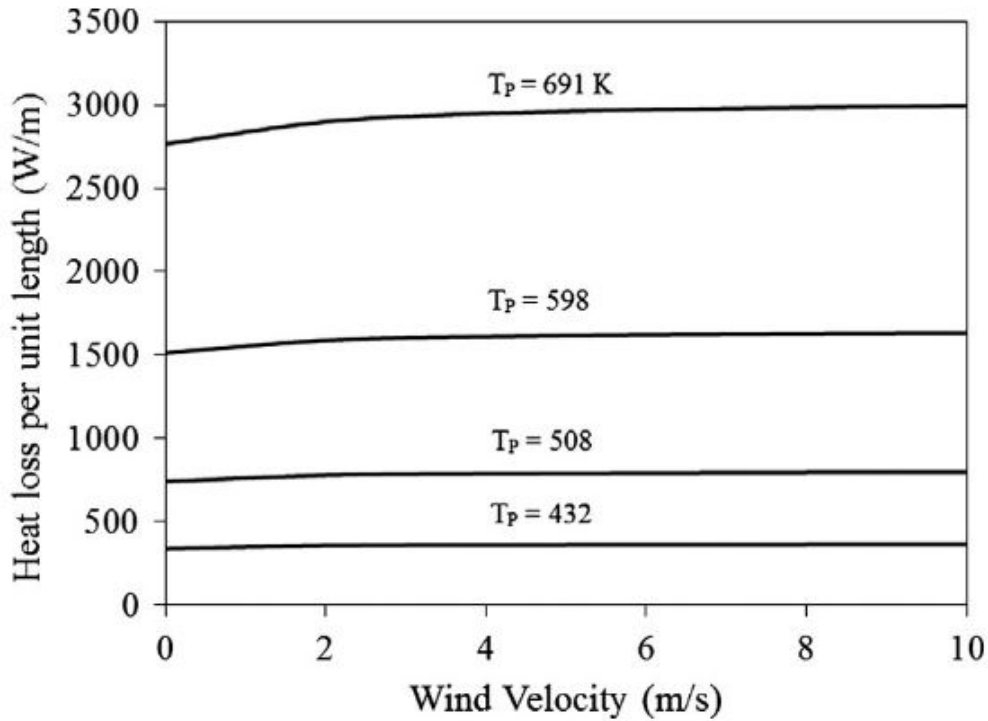


Figure 2.31: Influences of the external wind velocity on the heat loss from the receiver glass envelope for different absorber tube temperatures (Patil, Panse, et al. 2014).

The absorber tube is considered a key component of the PTSC thermal power plant, which has a direct impact on both thermal and economic performance of the solar power station. A simulation study to investigate the connection between receiver tube temperature and heat loss for a high vacuum HCE was presented by Lei et al. (2013). The study found that the heat loss rapidly increased with the increase of receiver tube surface temperature. Obtained results found that the heat loss was around 110, 180 and 270 W/m when the HTF temperature was 300°C, 350 °C and 400 °C respectively. The simulation results revealed that the receiver tube heat loss is not sensitive to the wind velocity between 0 m/s to 2 m/s or ambient temperature in laboratory testing. The rapid increase of the receiver heat loss with the increase of receiver tube surface temperature could be reduced in the case of reducing receiver glass envelope thermal conductivity or, as mentioned above, by adding insulation to the receiver glass envelope.

It is important to note that increasing the collector aperture area to obtain higher temperatures of HTF could result in increased wind effects due to wind load on the structure. This can negatively affect performance levels of the solar thermal plant. For that reason, Paetzold et al. (2014) analysed the wind influence on the PTSC performance of a solar plant. It was found that the wind velocity placed a high load on the collector structure and also created a vortex behind the first collector row, which influenced other rows of collectors. In addition, reduction of focal length (depth of trough) led to rising aerodynamic forces and the pitching moment on the collector surface. On the other hand, a deeper PTSC has a sheltering influence on the HCE, which reduces the thermal loss from the HCE due to forced convection. This point is important as the temperature difference between the ambient air and the HCE increases. In addition, it can also cut down the requirement for an insulated HCE, which has a significant effect on the solar plant cost. Based on that, it is important for shallow collectors (where the receiver tube is outside the rim) to reduce the effects of the wind's convective cooling around their receiver tubes somehow, thereby improving the receiver tube's heat gain.

Navarro-Hermoso et al. (2016) evaluated the heat loss of three different HCEs at different operation temperatures as shown in Figure 2.32. The authors determined heat loss by inserting a high-intensity electric current through the internal receiver to produce Joule heating. The obtained results showed that under 400°C operating

temperature, the heat loss of one 70 mm receiver tube was 225 W/m and the other 231 W/m, while it reached around 322 W/m for the 90 mm receiver diameter.

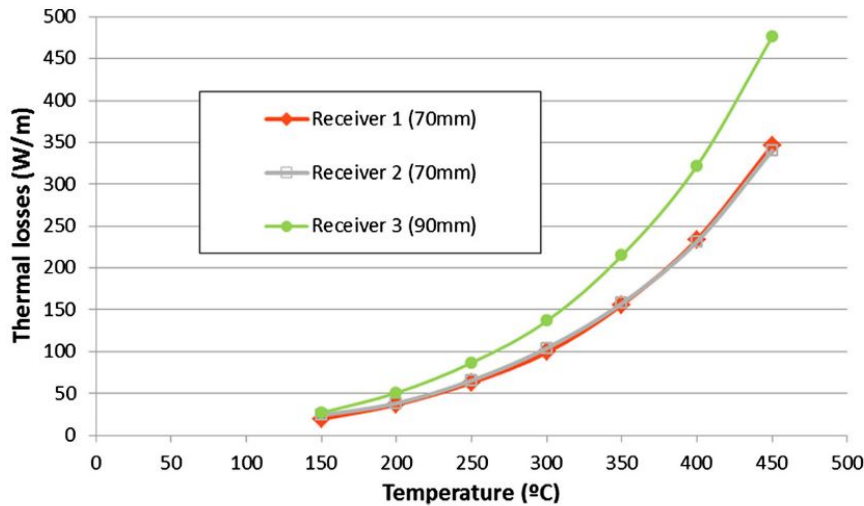


Figure 2.32: Thermal loss of three different diameters of HCE under different operating temperatures (Navarro-Hermoso et al. 2016).

From the above studies, it can be seen that decreasing the receiver tube thermal losses to the surroundings and increasing the heat transfer rate between the absorber tube and the HTF becomes a significant subject for enhanced PTSC performance. Section 2.3.2 is focused on different technologies of convection heat transfer enhancement between receiver tube and heat transfer fluid.

## 2.3.2 Receiver tube enhancement techniques

### 2.3.2.1 Different internal receiver tube structures

In general, the heat transfer performance of a PTSC can be enhanced by modifying the HCE structure to increase the thermal conductivity of the absorber tube and reduce the thermal boundary layer thickness of the fluid. In an experimental study, Chen et al. (2015) designed, manufactured and tested a novel cavity receiver tube for enhancement of PTSC thermal performance. Figure 2.33 shows the cross section of the new design structure. It can be seen from the figure that the new design's absorber tube has internal fins and the surface facing away from the collector has an arc wall that is thermally insulated. The HTF passes between the absorber surface and the arc wall. A glass cover is attached to the bottom of the cavity tube. The obtained results showed that the cavity receiver operated well at medium HTF temperature. They also

revealed that the thermal performance of the system was improved due to using fins and a glass cover in the cavity tube structure. In addition, the authors also investigated the effect of fins on the heat transfer performance between the HTF and the receiver tube. Under the same HTF operating temperature, the results revealed that the receiver temperature was reduced when fins were included to improve the heat transfer (Figure 2.34). This is due to increased areas of the convective heat transfer between the HTF and the surface of the receiver. Therefore, the decrease in the surface temperature is due to the transfer of more thermal energy from the absorber surface to the HTF, which leads to reduced thermal loss from the absorber tube surface to the outdoor environment and improves the thermal performance of the cavity absorbing tube. The results of this study indicated that solar radiation loss due to covering the upper part of the receiver tube by the thermal insulation—thermal insulation blocking aperture area—is much less than the receiver heat gain amount obtained because of the receiver thermal enhancement.

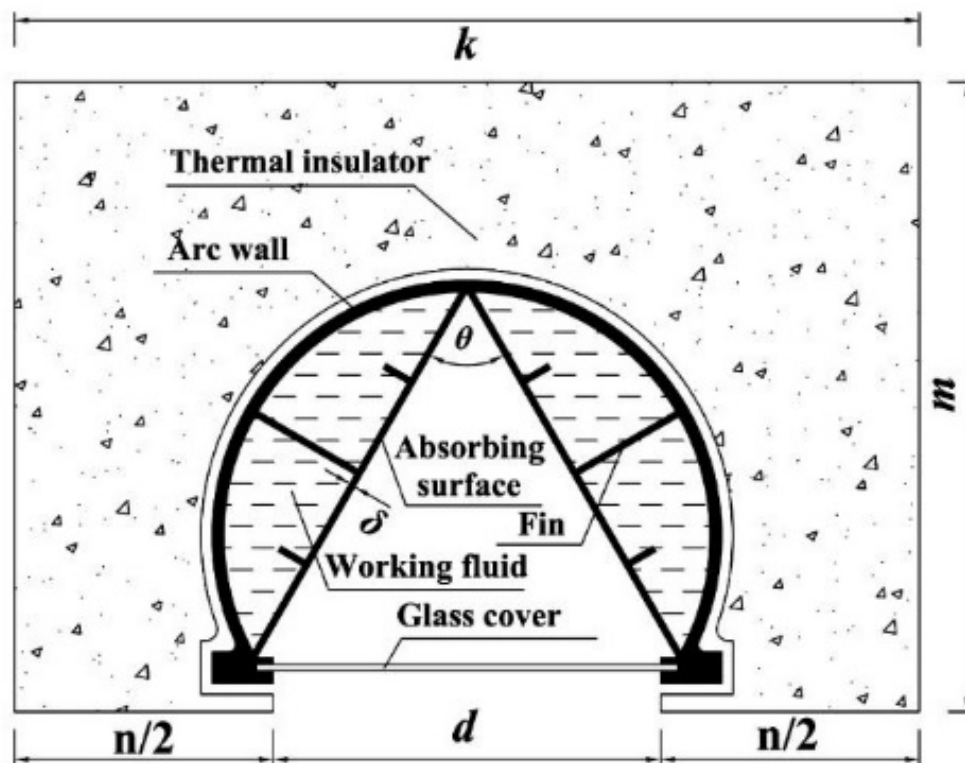


*Figure 2.33: Cross section of the cavity absorber. The glass cover (lower part of the receiver) is exposed to the reflector, thereby receiving the concentrated solar radiation on the absorbing surfaces for transfer to the working fluid; the upper part (facing the incident solar radiation) is insulated (Chen et al. 2015).*

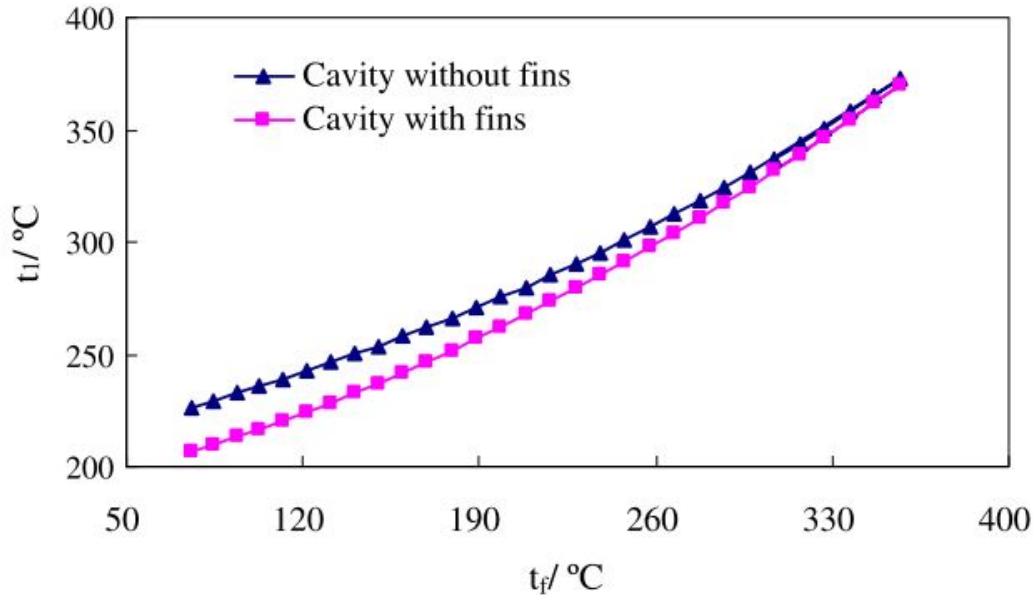


Figure 2.34: Effect of fins on the relationship between the absorber temperature ( $t_1$ ) and HTF temperature ( $t_f$ ) (Chen et al. 2015).

In order to improve the heat transfer in the heat collection element of a PTSC system, Kajavali et al. (2015) modified it and tested experimentally a conventional receiver tube via a new design. The modified absorber tube (the header tube absorber or HTA) consists of three parallel tubes covered by a copper absorber plate 1 mm thick as shown in Figure 2.35. The modified receiver is placed inside a box and the box covered by a glass cover on the bottom and top sides. The purpose of the design is to increase the absorption area of the conventional absorber tube, especially for diffuse solar radiation. The authors compared the efficiency of the modified absorber with the single absorber tube (STA) (a conventional absorber tube) as illustrated in Figure 2.36. The experimental results showed that the modified absorber tube improved PTSC absorption. In addition, it was found that the efficiency value of the HTA is 42.15 %, while for the STA it is 26.7%. The major drawbacks of the proposed design are: firstly, it is the shearing surface area between the upper part of the focal absorber tube surface area (hot surface) and the lower part of the absorber plate (as shown in the Figure 2.35). This can enhance the conduction heat transfer between the surfaces, which reduces the proposed design heat gain. Secondly, even though the modified design can absorb part of the diffused radiation by the absorber plate, this resulted in blocking a significant amount of the primary collector aperture area. This reduced the performance of the

PTSC—which only reflected the normal incident sunlight rays—due to reducing the amount of incident vertical radiation on the primary collector aperture area.

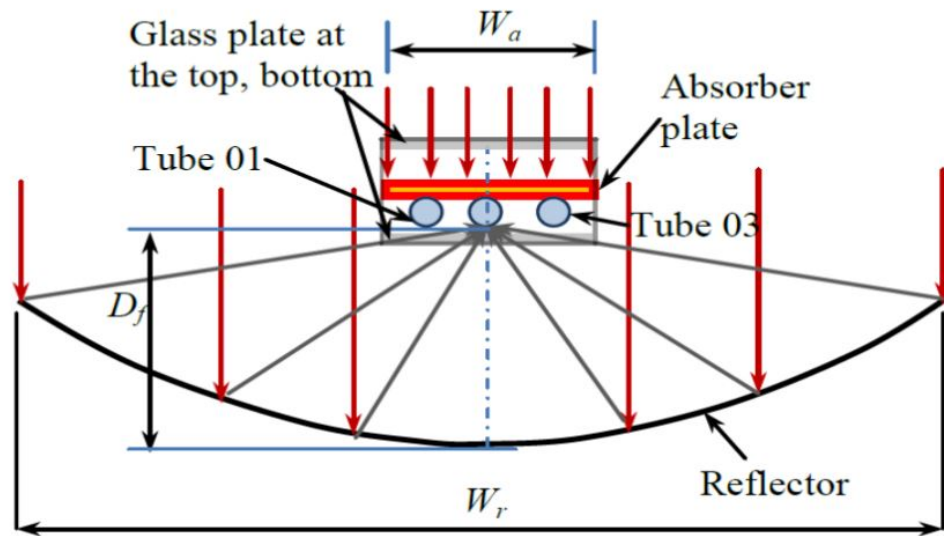


Figure 2.35 Schematic of the alternative receiver tube (HTA) structure, consisting of three absorber tubes placed inside a glass cover. The lower part of the modified receiver tube is subjected to the concentrated solar radiation in addition to diffuse radiation. The upper part (which consists of an absorber plate that covers the three tubes) is subjected to the normal solar radiation (Kajavali et al. 2015).

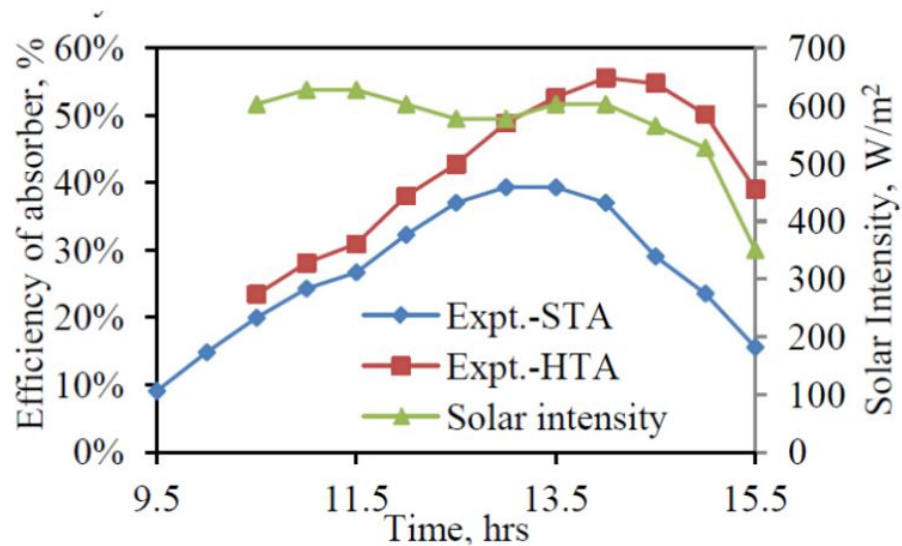


Figure 2.36: Solar intensity data and the efficiency comparison between the single tube absorber (STA) and the header tube absorber (HTA) (Kajavali et al. 2015).

Daniel et al. (2011) undertook a numerical investigation of PTSC receiver tube performance with and without a vacuum shell. The authors used three different HCE geometry structures: a non-evacuated receiver, an evacuated receiver and a vacuum shell receiver, as shown in Figure 2.37. Investigating the sensitivity of the receivers to

external wind conditions ranging from 1 m/s to 5 m/s, the authors examined the geometries under the operating temperature of 250 °C and determined the heat loss of each tube. They found that the non-evacuated tube is more sensitive than the others at the given temperature. In addition, the tubes were analysed under variations of receiver tube surface temperatures from 50 °C to 350 °C and velocities ranging from 1 m/s to 5 m/s, as shown in Figure 2.38. The numerical results showed that the convection and radiation heat loss of the evacuated shell receiver is less sensitive to the outdoor wind velocity than the non-evacuated receiver and found that the evacuated receiver has the lowest heat loss. The authors concluded that the vacuum shell receiver is a simple design that is more flexible and costs a lot less than an evacuated receiver tube. The presented concept of using evacuated shell receiver tubes could be an effective choice for PTSC applications that required high HTF temperatures. However, the proposed structure could be costly and difficult to produce.

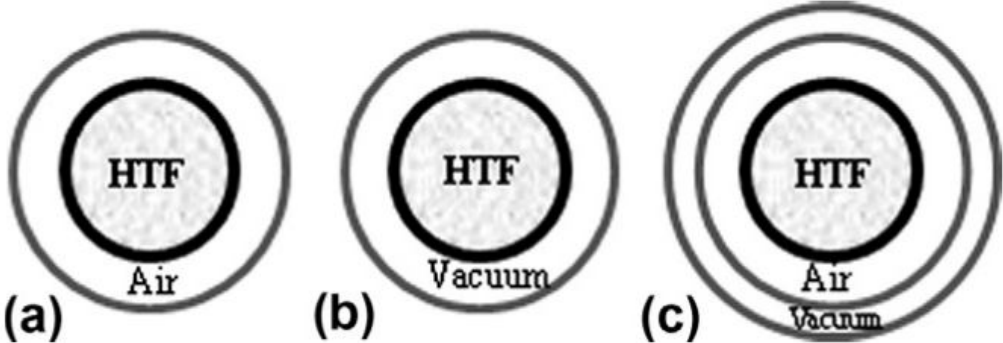


Figure 2.37: Schematic of the receivers (a) non-evacuated, (b) evacuated and (c) evacuated shell receiver (Daniel et al. 2011).

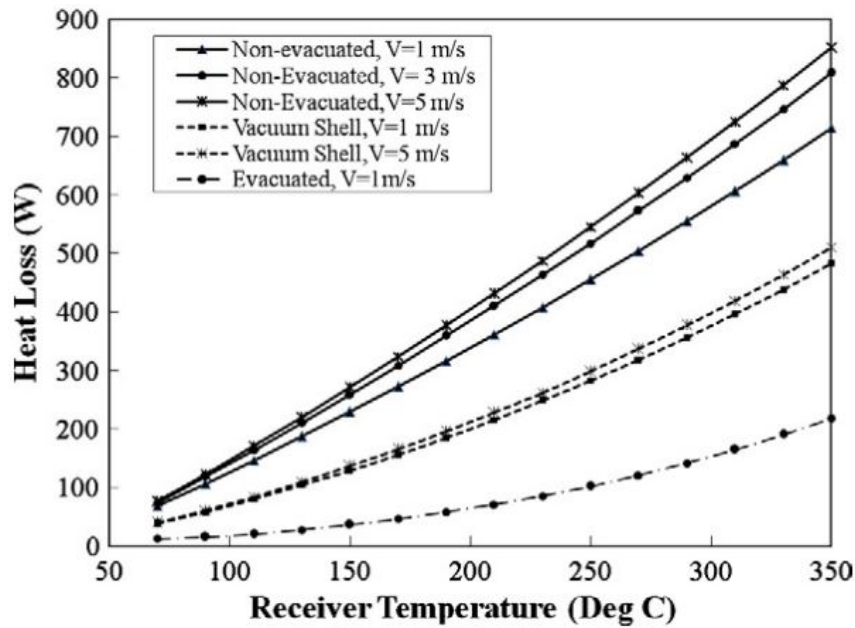


Figure 2.38: Difference of heat loss for three receivers at different temperatures and wind speeds (Daniel et al. 2011).

Cheng et al. (2012) numerically studied a PTSC modified receiver tube for enhanced heat transfer coefficient of the receiver and reducing its convection thermal losses. The modified receiver tube consists of unilateral longitudinal vortex generators inside the collector receiver. The influence of Re and HTF inlet temperature on the HCE thermal performance were investigated. It is noticed that an increasing Re results in decreased receiver wall temperature which leads to decreased convection and radiation external loss. In addition, by increasing the HTF inlet temperature, receiver wall temperatures increased, thereby resulting in increased thermal loss. This is due to the increased temperature difference between the surface wall of the absorber tube and the inner surface of the glass envelope, which consequently increased the radiation loss from the glass cover. Finally, the thermal loss of the new design was reduced by 1.35-12.1% compared to the conventional receiver tube under same operating conditions. The author presented a valid numerical study to reduce receiver tube heat loss, but the economic aspect of this study is missing. This part (financial evaluation) it is required to be considered for any modification for the commercial receiver tubes to evaluate if it is useful commercially.

Heat transfer enhancement of a PTSC absorbing tube by using pin fin array inserts (PFAI) has been numerically analysed by Gong et al. (2017). The details of the tube

structure with the pin fin arrays inserted are illustrated in Figure 2.39. In the study, the MCRT method and finite volume technique were combined to investigate and evaluate the performance of the finned tube. The overall heat transfer performance of the HCE can be increased up to 12.0% when the absorber tube with pin fin arrays inserting was used. Also, the economic aspect for this study is missing.

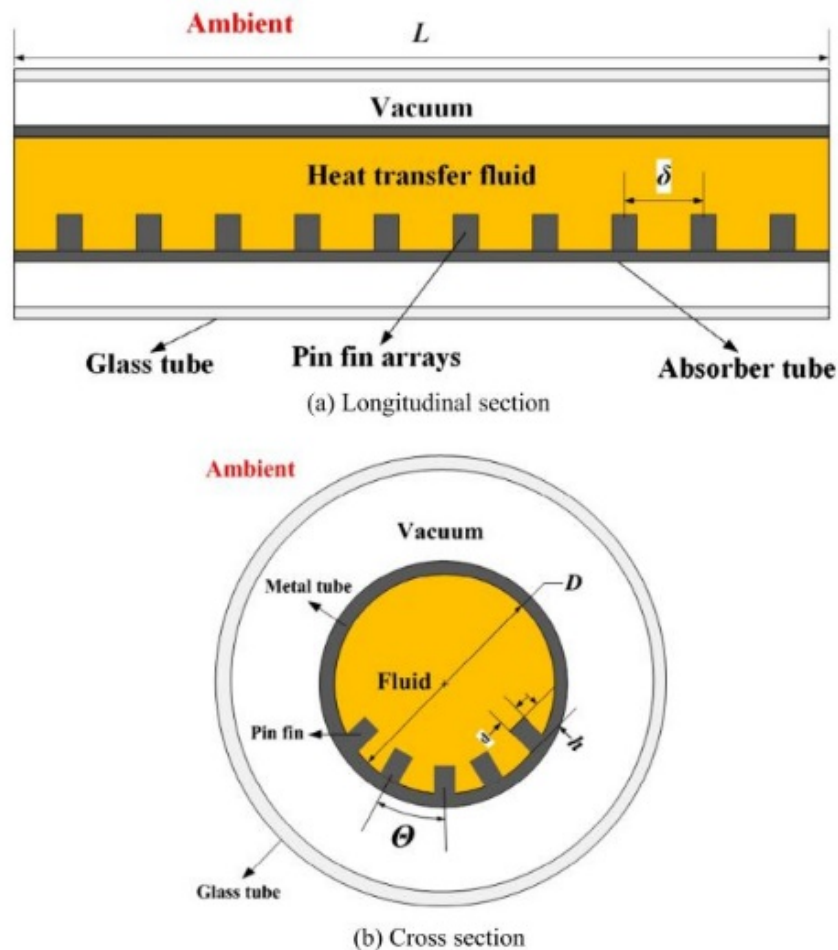
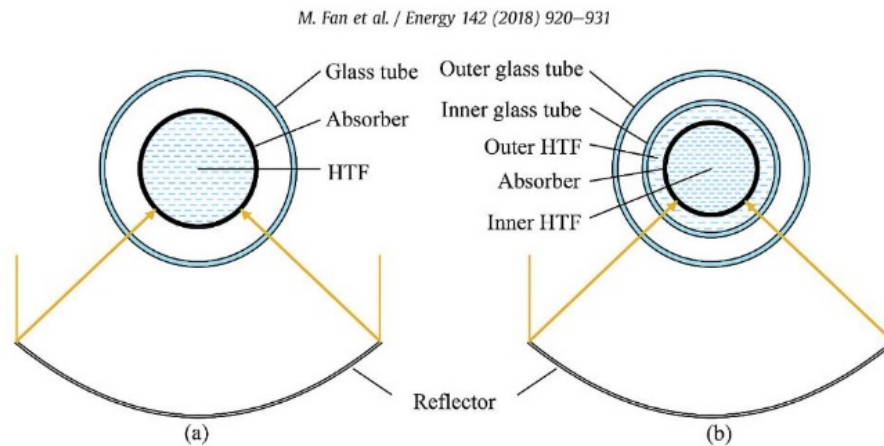


Figure 2.39: Longitudinal and cross section of the structure of the PTSC optimised receiver tube structure with distribution shape of pin fin array inserts (PFAI) (Gong et al. 2017).

Fan et al. (2018) presented a new design of receiver tube to enhance heat transfer (Figure 2.40) by locating the absorber tube inside HTF with twin glass covers. In the study, both the novel receiver tube and the conventional receiver tube were investigated under annular conditions using both air and vacuum. Under normal operating conditions, the PTSC efficiency is higher for the vacuum receiver than the new receiver. However, if the vacuum space is broken due to damage to the external glass tube, the reduction in the PTSC efficiency is between 2.4-4% for the conventional receiver, but only 1.0-2.3% for the novel receiver. Therefore the novel

receiver tube is less sensitive to outdoor conditions. The problem with the proposed design is that the authors did not take into account or estimate the modified design cost and assess the outcome of employing the new design.



*Figure 2.40: Cross section of (a) reflector and conventional receiver and (b) reflector and novel receiver. Yellow lines are the solar rays (Fan et al. 2018).*

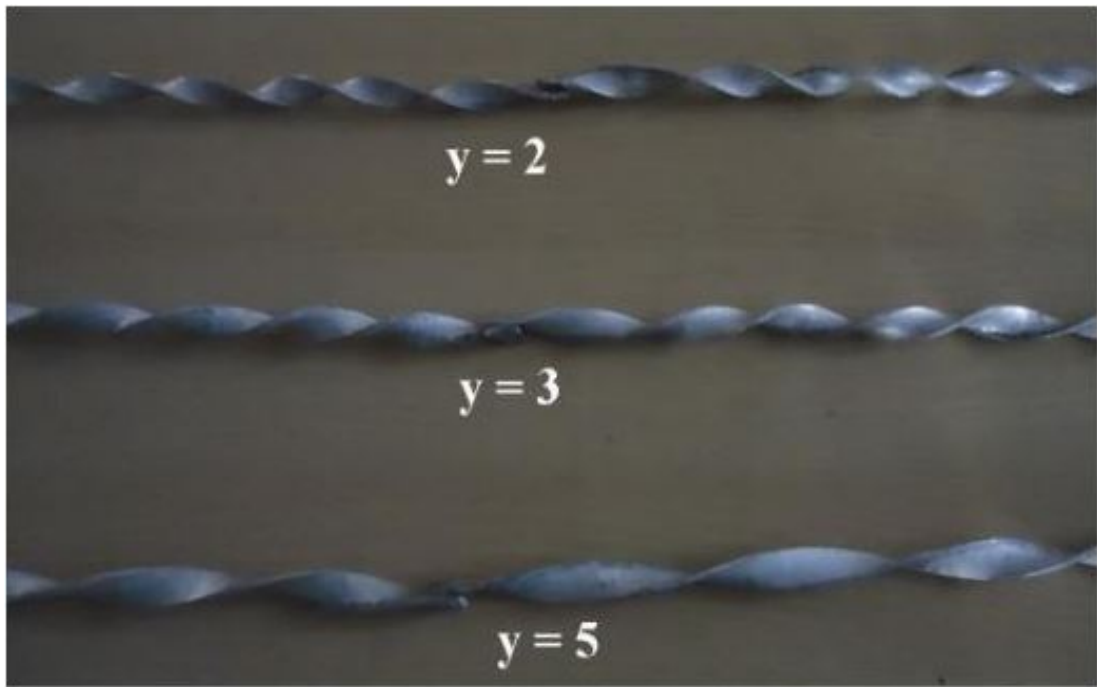
### 2.3.2.2 Segmentations

Further augmentation in HCE heat transfer can be achieved using insert turbulent flow technologies. In other words, increasing the contact area between the inner surface of the receiver tube and the heat transfer fluid can result in an enhanced heat transfer rate inside the receiver tube. This leads to reducing the absorber wall temperature which consequently decreases the natural convection heat loss from the receiver tube.

#### 2.3.2.2.1 Twisted tape insert

A PTSC with a 2 m<sup>2</sup> aperture area, 90° rim angle and 25.46 concentrating ratio has been used for experimental investigation of the effect of plain twisted tape and nails with twisted tape (Figure 2.41) on PTSC performance. Jafar and Sivaraman (2017) noticed that the Nu is higher in the modified absorber tube compared to a conventional tube. That is due to the tape reducing the hydraulic diameter, generating swirl flow through the pipe and better fluid mixing. This produces better heat transfer between the core and absorber wall due to increased temperature between the fluid layers. In addition, the study also found that using nails with twisted tape gives higher efficiency than the plain twisted tape. The Re increased and absorber wall temperature decreased with the decreasing twist ratio. Figure 2.42 shows that PTSC performance increased

by increasing solar radiation and reducing the tape twist ratio. This is because of improved fluid heat transfer and reduced absorber wall temperature, which reduces the convection heat loss from the absorber wall. Using this technology to enhance the PTSC efficiency could positively influence receiver tube performance when employed for the receiver tube of commercial collectors with a high CR. This is because this type of collector produces high HTF temperatures, and the tape can distribute the heat more evenly, which consequently could improve the absorber tube's thermal strain and reduce failures in receiver tubes. However, the major drawback of this technology is that the author did not investigate the effect of the HTF temperatures (which could reach up to 400 °C) on tape thermal strain that could potentially occur. This increases the absorber tube thermal strain (absorber bending).



**(a) Plain Twisted Tape (P-TT)**



**(b) Nails with Twisted Tape (N-TT)**

*Figure 2.41: Plain twisted tape (a) and Nails with twisted tape (b) geometries.  $y$  is the twist ratio of the tape ( $y=H/W$ ),  $H$  is the pitch for  $180^\circ$  rotation of twisted tape (m), while  $W$  represents the width of the twisted tape (m). Nail dimensions equal 11 mm length, 1.5 mm diameter and 3 mm head diameter(Jafar & Sivaraman 2017).*

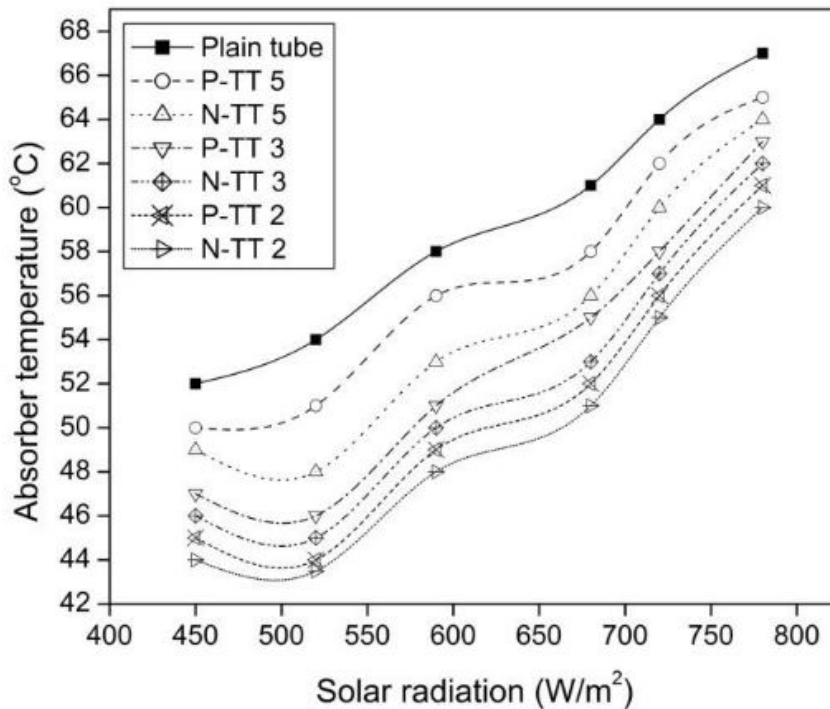


Figure 2.42: Absorber tube wall temperatures for plain and modified absorber tube under various twist ratios ( $Y=2, 3, 5$ ) (Jafar & Sivaraman 2017).

Mwesigye et al. (2013) numerically investigated the influence of twisted tape inserts on both the pressure drop as well as heat transfer of Syltherm-800 HTF in a PTSC absorber tube. For constant  $Re$  turbulent flow and twist ratios of 0.30-2.42, the observed circumferential HTF temperature difference was increased in the absorber tube. Similarly, for an absorber tube with inserts having low twist, increasing  $Re$  caused a considerable decreasing circumferential temperature difference in the absorber tube. A total drop in circumferential temperature difference of 4-76% was found through inserts. This occurred when increased  $Re$  and decreased twist ratio, which increased the  $Nu$ . In the modified absorber tube, the friction factors increase up to 21.8 times compared with a receiver having a plain absorber tube for the range of parameters considered. In addition, it was observed that with increased  $Re$  and decreased twist ratio, the  $Nu$  increased. Also, over the complete range of  $Re$  ( $10,260 \leq Re \leq 320,000$ ) the receiver tube thermal efficiency (ratio of collected energy to the gained energy) was observed to be maximum for the lowest twist ratio and highest width ratio. The increase in  $Nu$  over the range of  $Re$  was a factor of 1.01-3.36 higher than a conventional receiver tube. Similarly, the increases in thermal enhancement and friction factor were 0.74-1.25 times and 1.32-21.8 times respectively.

The influence of perforated louvered twisted tape (LTT) (Figure 2.43) inserts on the convection heat transfer of a PTSC receiver tube with Behran thermal oil used as an HTF was numerically investigated by Ghadirijafarbeigloo et al. (2014). Non-uniform heat flux boundary conditions were employed to the outer surface of the absorber tube and adiabatic conditions were assumed for the end walls of the absorber tube. The friction factor and heat transfer coefficient were calculated for a completely developed turbulent flow. Additionally, with a drop in twist ratio and rise in Re, Nu was increased for louvered twisted tape inserts and normal twisted tape as well. It was found that the best result is achieved when reducing the value of the twist ratio to 2.67 and Re to 5000: heat transfer is enhanced. Again, it is important to consider the influence of the HTF temperatures (which could reach up to 400 °C) on tape thermal strain to ensure that this solution is suitable for this application.



*Figure 2.43: Geometry of the Louvered twisted tape with perforations (Ghadirijafarbeigloo et al. 2014).*

Correspondingly, for heat transfer enhancement in a PTSC system, an absorber tube with twisted tapes and molten salt HTF were numerically studied by Chang et al.

(2015). The authors presented the effects of twisted tape clearance ratios and twist ratios in their study. It was found that heat transfer enhancement occurred when the twist ratio reduced from 41.7 to 2.5 and clearance ratio reduced from 1 to zero.

In order to investigate the thermal performance of a PTSC receiver tube with a twisted tape insert, a thermodynamic model system was numerically established by Jaramillo et al. (2016). The values of Re and twist ratio that were studied were 1350-8350 and 1-5 respectively. The study found that where Re=1350 and twist ratio=1 the maximum value of Nu was 3.5. In addition, it also showed that when the twisted tape insert was employed in the receiver tube, the total heat loss coefficient was cut down to about 1.5%.

In order to present a significant heat transfer enhancement of a PTSC absorber tube, friction factors and thermal performance, Bhuiya et al. (2016) investigated and assessed the heat transfer performance of turbulent flow in a heat collector element by inserting helical tape at higher Re. The authors used twist ratios of 1.88, 3.13, 4.69, 6.41 and 7.81. The main results of the study indicate that helical tape has a significant improvement on the friction factor and absorber heat transfer compared to a plain tube. The authors noticed that with decreasing twist ratio, the heat transfer, friction factor and PTSC thermal performance increased. Additionally, the value of the friction factor and Nu for the absorber tube with helical tape was higher than those in the conventional absorber tube. Analysing the thermal strain for the helical tape under a high-range of HTF operation temperature is missing in addition to the analysis of the economics of this modification.

Based on the experimental results of an LS-2 receiver on an AZTRAK experimental platform, a numerical investigation was carried out by Song et al. (2014). In this numerical simulation, helical screw tape with different twist ratios was inserted into the receiver tube. Through various operation parameters and using Dowtherm A as an HTF, the relative enhancements of the PTSC were determined with and without inserts. In addition, maximum outer surface temperature of the receiver tube and heat loss were also examined. Under operating conditions with volume flow rate of 0.11 L/s and inlet fluid temperature of 373 K, the study illustrated that the heat loss from the plain receiver surface tube was six times more than the receiver with the insert. In addition, when the volume flow rate was increased to 0.6 L/s, the pressure dropped by

a factor of 23 for the receiver with inserts, but only a factor of 4 for the plain receiver. As mentioned above, the analysis of the thermal strain for the helical screw tape under a high-range of HTF operation temperature is missing in addition to the analysis of the economics of this modification.

#### **2.3.2.2.2 Porous geometry insert**

The influence of applying copper foam inside a PTSC absorber tube in addition to studying the effect of mass flow rate volume on PTSC efficiency were experimentally investigated by Jamal-Abad et al. (2017) using a PTSC with 1.28 m<sup>2</sup> aperture area and 90° rim angle. The porosity of copper foam was 0.9 and the pore density was 30 pores per inch. The tests were carried out under different volumes of fluid mass flow rate (from 0.5 to 1.5 kg/min). The results illustrated that inserting metal foam in a PTSC receiver has a positive impact and leads to enhanced PTSC efficiency due to improvement of the thermal conductivity and increase in the value of Nu and friction factor as well. In addition, it also revealed that lowering the mass flow rate of the HTF results in reducing PTSC system performance. The limitation of this study is that the author also did not investigate the performance of inserting material under high HTF temperatures, such as 400 °C, that can be achieved by increasing the HTF inlet temperature. And then the effect of inserting the material on performance, under the influence of the HTF hot domain, can be analysed.

Using commercial CFD software, a three-dimensional numerical model of a PTSC with 2 m of porous disc receiver length was used by Kumar and Reddy (2009) for analysing PTSC performance. Therminol VP-1 was used as the working fluid in this investigation. The influence of several parameters such as HTF, receiver dimensions and solar radiation concentration on PTSC efficiency were also investigated. In addition, distance between discs, height of the disc and different heat flux conditions were carried out for receiver thermal analysis. The simulation results illustrated that with increased distance between the discs, Nu and the drag coefficient decrease and this structure enhances the heat transfer coefficient of the modified absorber compared to a plain receiver. The author successfully simulated the porous receiver, but the simulation results did not validate with experiments or other numerical studies. In addition, this modified receiver is probably costly to produce, which could potentially reduce its commercial opportunity.

The same authors numerically analysed the influence of porous foam on HCE performance. Water and therminol oil were used as the HTF in the study. A three-dimensional simulation was carried out using the CFD software Fluent to evaluate the best pattern. The receiver tube and the porous medium are made from stainless steel and the porous medium contains 57 longitudinal holes in a staggered pattern with 100 mm length, as shown in Figure 2.44. When installing the porous block inside the receiver tube, the dimensions of the inside diameter of the absorber tube and the outside diameter of the porous medium are equal. The flowrate of both water and therminol oil varied from 0.5 to 1 L/s. The investigation revealed that using a porous disc receiver resulted in a lower pressure drop compared to the solid disc receiver because of less resistance. It also found that the HCE with half vertical porous disc and bottom inclined porous disc provided the highest heat transfer augmentation efficiency of 13.5% and 31.4% with the use of water and therminol oil as HTF respectively (Kumar & Reddy 2012). As mentioned above, the proposed design appears to be costly and the author did not evaluate the commercial aspects of this design.

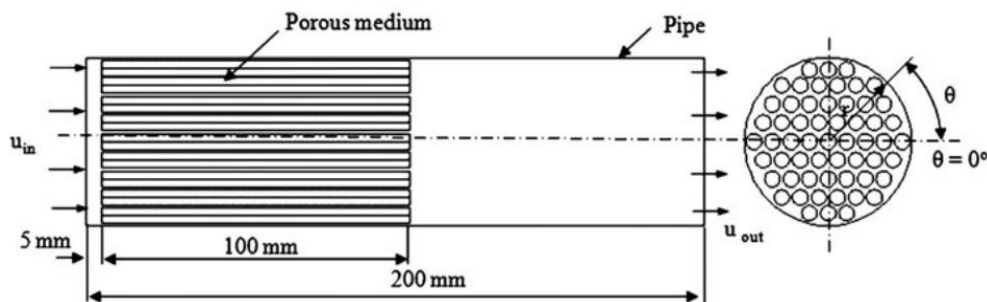


Figure 2.44: Schematic of modified absorber tube by porous medium along the length of the HCE (Kumar & Reddy 2012).

Different HCE structures have been numerically investigated in three dimensions to evaluate the absorber tube with different configurations of porous inserts. Reddy and Satyanarayana (2008) presented a numerical study to investigate several porous finned receiver tubes of a PTSC using CFD software. Square, triangular, trapezoidal and circular shapes are the various shapes of porous fins that were used in the simulation to evaluate the HCE performance. In addition, the natural convection heat transfer loss with mass flow rate and for various absorber tube configurations were also investigated as presented in Figure 2.45. The study found that under a 6.4 kg/s mass flow rate and 1.7 kPa pressure difference parameters, the PTSC heat transfer enhancement due to

the trapezoidal and square porous fins were 13.8% and 21% respectively. It is also found that convection natural heat loss from the circular absorber tube is higher than from the enhanced absorber tube. However, the proposed design of the various porous fin receivers could result in a rapid drop in PTSC efficiency under cloudy weather (when concentrating solar radiation on the absorber tube surface is reduced, and as a result the HTF temperature becomes higher than the absorber tube temperature), which potentially increases the receiver tube heat losses.

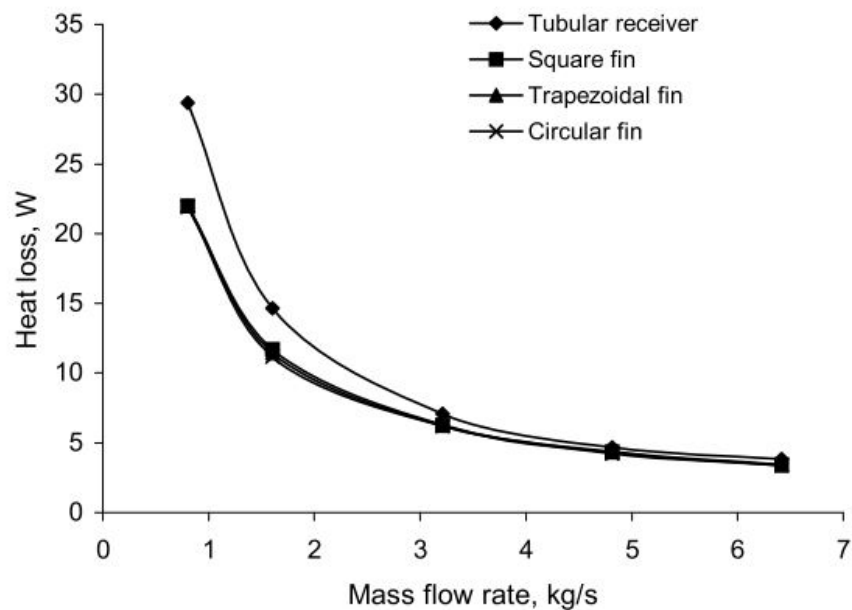


Figure 2.45: Heat loss of various absorber tube configurations under different mass flow rate values (Reddy & Satyanarayana 2008).

A numerical study was undertaken by Wang et al. (2013) to investigate the effect of inserting foam inside the absorber tube in order to enhancement heat transfer between the inner surface of the absorber tube and the heat transfer. The numerical simulation structure included inserting metal foam inside a collector absorber tube as illustrated in Figure 2.46 and Figure 2.47. The authors analysed the influence of top and bottom layout, porosity and geometrical structure (H) on heat transfer. It was found that the maximum absorber tube surface temperature decreased by about 45%, resulting in reduced thermal stress. In addition, the numerical study found that with constant H and layout the porosity influence on the absorber thermal performance is less than the effect of the geometrical structure (H) under porosity and layout constant value. By comparing with the clear absorber tube, it is also found that the optimum thermal

performance is reached when  $H=0.75$  (metal foam placed at the top of the absorber tube). It appears that the author did not consider the additional cost of the modified receiver tube and also did not investigate the modified receiver tube under the high collector concentrating ratio. However, the new design could be more suitable for a PTSC that operates at moderate HTF temperatures.

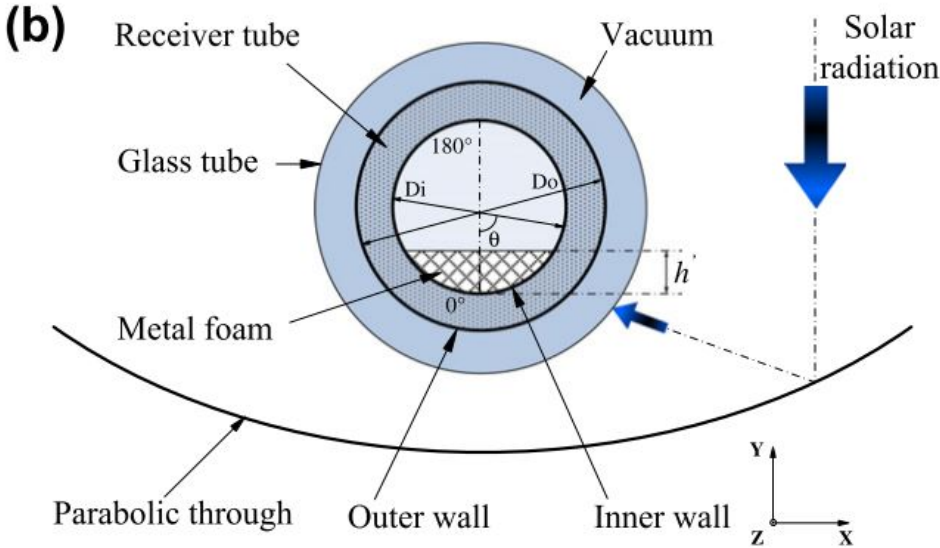


Figure 2.46: Cross section of the absorber tube with the metal foam insertion (Wang et al. 2013).

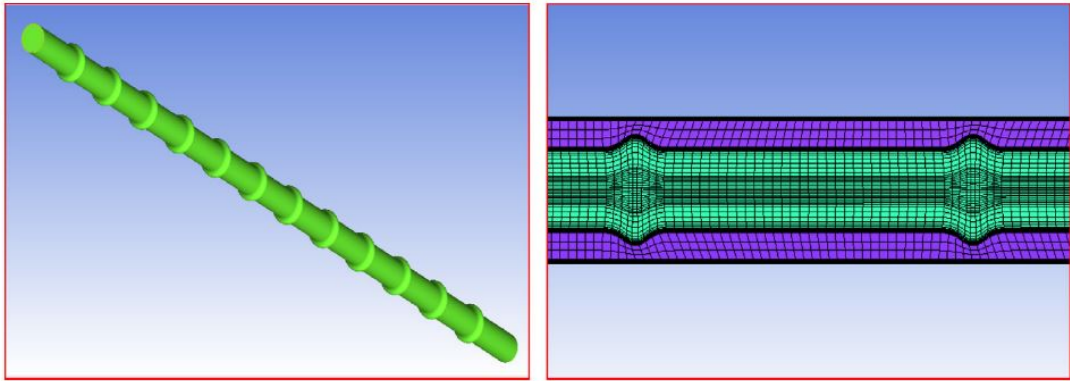
Type	$h'/D_i=0$	$h'/D_i=0.25$	$h'/D_i=0.5$	$h'/D_i=0.75$	$h'/D_i=1$
Series 1					
Series 2					

Figure 2.47: Absorber tube section with the metal foam layout (Wang et al. 2013).

**2.3.2.2.3 Corrugated receiver**

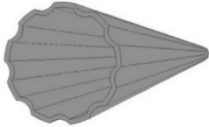
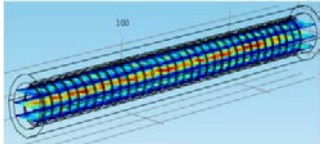
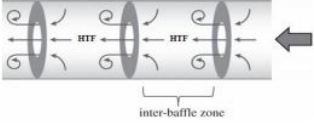
For improving PTSC heat transfer and enhanced thermal performance, an absorber tube was numerically investigated by Fuqiang et al. (2016). Figure 2.48 presents the schematic modified absorber tube with its convex corrugated pipe. The numerical results found that the temperature distribution on the modified absorber tube glass cover was more uniform. Additionally the thermal stress deformation is relatively

smaller compared to a conventional tube. Therefore, the new design improved the absorber tube thermal performance. Finally, it was observed that the heat transfer enhancement is about 8.4% and the maximum thermal strain can be reduced by around 13.1%. As mentioned above, the proposed design appears to be costly and the author did not show any commercial evaluation to this design.



*Figure 2.48: Mesh section and 3D view of the corrugated absorber tube (Fuqiang et al. 2016).*

### 2.3.2.2.4 Other studies

No	Structure	Authors	Enhancement technology details	Findings
1	-	(Ghasemi et al. 2013)	PTSC receiver tube with two porous segmental rings	<ul style="list-style-type: none"> <li>Heat transfer coefficient increase with decreased distance between two segmental rings.</li> </ul>
2		(Benabderrahmane & Benazza, 2017)	PTSC receiver tube with dimpled absorber tube	<ul style="list-style-type: none"> <li>Enhanced heat transfer performance.</li> <li>Reduced HCE temperature slope.</li> </ul>
3		(Diwan & Soni 2015)	Absorber tube with wire coil inserts	<ul style="list-style-type: none"> <li>Increased turbulence inside the HCE.</li> <li>Convective heat transfer increased</li> </ul>
4		(Benabderrahmane et al. 2016)	PTSC receiver tube with baffle inserts	<ul style="list-style-type: none"> <li>High Nu and friction factor compared with plain tube.</li> </ul>

				<ul style="list-style-type: none"> <li>• Nu increased with increased baffle thickness and decreased distance between the baffles.</li> </ul>
5		(Xiao et al. 2014)	V-cavity receiver tube with rectangular fin structure	<ul style="list-style-type: none"> <li>• Due to the triangular receiver shape, the sun rays reflected repeatedly.</li> <li>• High outlet HTF temperature and lower heat loss than absorber without fins.</li> </ul>
6		(Mwesigye et al. 2014b)	Receiver tube with circular plate inserts	<ul style="list-style-type: none"> <li>• HCE temperature gradients are reduced with the use of circular plate inserts.</li> <li>• The modified thermal efficiency rises by between 1.2% and 8%.</li> </ul>

## **2.4 Summary of the project**

The literature review has provided a brief overview about the parabolic trough solar collector (PTSC) technology structure, components and its operation (section). It then focused on two main challenges for efficient PTSC operation—optical and thermal losses—in addition to technologies to enhance the optical and thermal performances.

### **2.4.1 PTSC Optical loss**

The main causes of the PTSC optical loss were discussed in section 2.2.1. The PTSC optical studies determined that there are two main sources for deviating the reflected solar radiation in this technology. The first source is errors in the PTSC geometry, such as the supported structure's accuracy, reflector and receiver tube misalignments. The second source is wind changes, which vibrates the collector structure, especially under high wind conditions. The effects of wind sharply increase as the collector is oriented to face the wind, creating the maximum drag area. This results in a high total load on the PTSC aperture area, which usually has an aperture of 6 m width and 100-150 m length (Lüpfert & Ulmer 2009; Christian & Ho 2010; Huang & Han 2012; Salamanca et al. 2015; Paetzold et al. 2016; Simonović et al. 2016; Zhao et al. 2016; Fraidenraich et al. 2017; Islam et al. 2017; Meiser et al. 2017).

This chapter then analysed the optical enhancement technologies (section 2.2.2) that have been devised to reduce the PTSC optical loss. All of those studies are only numerical optimization, and they showed a clear optical improvement. However, the major drawbacks of these studies are: for some, it is costly to produce the modification, while for others it is difficult to implement the modification to a real application due to their physical structure.

It can be concluded that, regardless of the reasons for the collector optical loss (by deviating reflected sunlight rays from hitting the collector's focal line), this loss resulted in not only losing some of the concentrating radiation, but it also resulted in asymmetry in the concentrating radiation on the absorber tube surface area. This could potentially result in overheating the absorber tube surface (producing thermal stain), which can reduce the receiver tube's operational life. Therefore, the PTSC optical loss is a major challenge to this solar technology and it requires a new modification to reduce its optical loss and improve the PTSC performance.

It is proposed to reduce the optical losses by using a secondary parabolic reflector. This element can help to catch most of the deviated solar rays from the receiver tube and reflect them on the upper part of the collector absorber tube irrespective of the source of the sun rays' deviation (either due to structure misalignment or due to wind variations). This also could reflect some of the absorber tube's radiative loss onto the upper part of the absorber tube surface, potentially reducing the absorber tube thermal stress as well.

To test whether a secondary reflector fulfils this objective, a PTSC heating system is designed, consisting of two identical collectors so that any modification to a collector can be compared to a control. A secondary mirror is attached to one of the collectors to test its effect; since this secondary mirror blocks direct sunlight from the absorber tube, a secondary reflector without a mirror is directly compared to the secondary mirror. The design process for this system is detailed in Chapter 3, with results of the tests presented in Chapter 4.

In addition, in order to overcome the large drag under high wind conditions—especially when the collector aperture area is vertical to the wind direction (during periods close to sunrise and sunset)—a fixed case for the conventional PTSC system is proposed. This design configures the conventional PTSC length (axis) to be parallel with the East-West orientation (instead of North-South) and permanently angles the collector aperture area based on the latitude of a site (this setup of the fixed case is the standard for PV solar panels). Such a design enables the structure to be much more rigid than is possible for a tracking system, so this design would reduce the instances of solar radiation from being misdirected from the primary collector and missing the receiver tube in two ways. Firstly, the drag force on the collector is reduced (so there is less force deflecting the primary collector from its designed shape and target orientation). Secondly, the structural support for the primary collector could be designed to be much stronger, reducing the deflection for a given drag force. To compensate for the tracking error caused by the primary collector being oriented for midday at the equinox, a secondary collector could increase the efficiency of the system significantly.

To test the possibility of using a fixed configuration, in the current study a new test methodology is proposed: to orient the PTSC axis in the North-South direction and use the tracking system to aim the collector aperture area at the sun throughout the day.

The noon time of the test simulates the sun's position at noon at the equinox, while the test time of 10 am represents noon at the winter solstice and 2 pm simulates noon at the summer solstice.

#### **2.4.2 PTSC thermal loss**

In terms of the PTSC thermal loss, this chapter also presented heat losses from the receiver tube due to forced convection—convective cooling by the wind (section 2.3.1). The HTF temperature (due to flowing through the PTSC receiver tube) reaches up to 400 °C, which increases the glass cover temperature. Therefore, radiation and forced convection heat transfer losses accrue due to the significant difference between the outer surface temperature of the glass envelope and the ambient temperature (Padilla et al. 2011; Hachicha et al. 2013; Lei et al. 2013; Wu et al. 2014; Navarro-Hermoso et al. 2016; Prahel et al. 2017). Moreover, it is also noticed that the bottom part of the receiver tube is normally exposed to concentrated sunlight, whereas the upper part of the receiver is subjected to normal direct solar radiation. This potentially leading to thermal deformation which bends the receiver tube and breaks the glass cover (Mwesigye et al. 2014a; Wu et al. 2014; Gong et al. 2017).

The previously-developed PTSC receiver tube enhancement technologies are valuable and present a clear improvement for the receiver performance by reducing the thermal loss (section 2.3.2). However, some of these studies have major drawbacks such as being costly and difficult to produce. Also, in attempting to remedy one challenge, some studies have created different problems, such as enhancing absorber tube conductive heat loss; enhancing absorber tube thermal strain; or producing thermal expansion (for tape inserts), especially for porous geometry inserts.

It can be concluded that the forced convection heat loss reduces the receiver tube heat gain and this significantly influences the PTSC thermal performance. In addition, under normal operation, the reflected sunlight concentrates on the bottom part of the receiver tube. As a result, the heat flux distribution on the absorber tube surface is highly non-uniform, which results in a high temperature gradient that produces thermal strain. This thermal strain is also a major challenge for this solar technology. And therefore this technology is required a new thermal modification to reduce receiver

tube thermal losses and also the absorber thermal strain, which thereby improve the PTSC performance.

To overcome the receiver tube's thermal challenges it proposed to add annular thermal insulation to the inner surface of the upper part of the receiver tube glass envelope. The consequent reduction in conduction heat transfer across the receiver glass envelope wall reduce the outer surface temperature of the glass envelope, reducing the convective cooling by the wind. Moreover, this annular insulation can create a hot air domain around the upper portion of the receiver absorber tube. Therefore, this thermal enhancement can also reduce the absorber tube thermal stress (consequently the thermal deformation) that occurs due to non-uniform concentrating solar flux on the absorber wall.

To test whether the annular insulation fulfils this objective, 3D simulations of three different insulated and non-insulated receiver tube designs are performed. The cross-sections of the receiver tubes are circular, parabolic and hybrid (circular-parabolic shape). The insulated and non-insulated versions of the receiver tubes are directly compared for different wind speeds. The design, methodology and testing conditions are detailed in Chapter 5, with results of the numerical tests presented in Chapter 6.

Thus, the modified receiver tube not only can reduce the PTSC optical losses and limit the convective cooling of PTSC receiver tube caused by the wind, but it also could effectively improve the distribution of both the solar heat flux and also the temperature distribution on the upper part of the absorber tube wall. By achieving this aim, there is an economic benefit by producing more heat due to the improvement of optical and thermal performances of the PTSC technology, in addition to improving the operational life of the receiver tubes.

# Chapter 3 **Experimental structure and instruments of solar heating system**

## **3.1 Introduction**

This chapter presents the solar heating system that was designed, manufactured and assembled for investigating the influence of a secondary reflector on a parabolic trough solar collector's performance. The proposed technology aims are to reduce the PTSC optical loss (section 2.2.1), which can be achieved by reflecting the deviated sunlight rays on the upper part of the collector absorber tube. Also, this optical enhancement could reduce the absorber tube thermal strain that could occur due to the high concentration of the solar radiation on the lower part of the absorber tube surface area. Therefore the receiver operation life could be enhanced due to this optical enhancement. Figure 3.1 illustrates the main components of the solar heating system that was built on the University of Southern Queensland (USQ) site. The heating system consisted of two symmetrical collectors, with one of the collectors used as a control (solely with the conventional primary collector) while the second one was modified by attaching a secondary reflector above its absorber tube and sharing the same focal line. The secondary reflector consisted of a mirrored reflecting sheet glued onto the inner surface of an opaque parabola.

This chapter presents the details of the design and manufacturing stages of each component in the system, commencing with the key component: the two reflectors and corresponding mounting structure. The support structure for the reflectors, including seasonal tracking structure (base and support of the seasonal tracking system), are then illustrated in detail. This provides a suitable testbed as proof of concept.

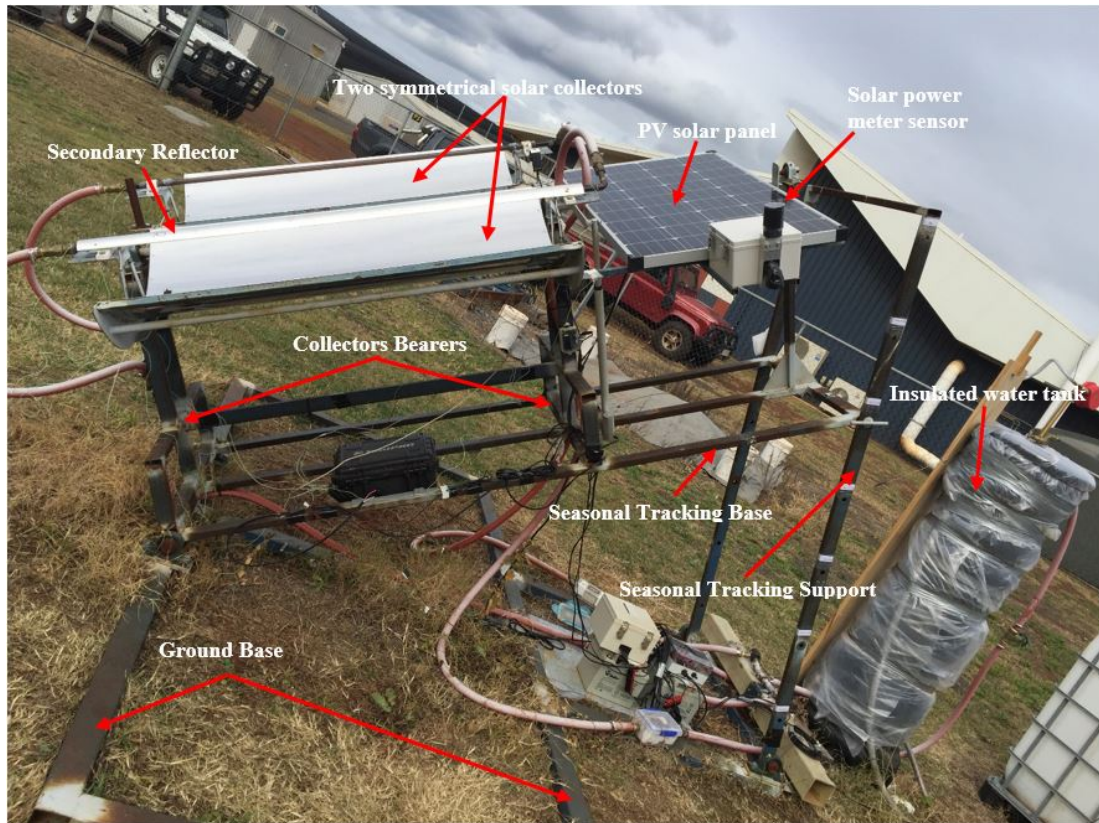


*Figure 3.1: The experimental solar heating system installed on site.*

### **3.2 Collector reflector (mirror)**

Several parameters should be considered for choosing a suitable mirror sheet to use as a reflector. Principally, the material must have high reflectivity with minimal absorption. In addition, it must have high resistance to the outdoor environment conditions such as humidity that could oxidise the reflecting sheet and reduce both its reflectivity and its operating life. Therefore, a super mirror made of stainless steel grade 316 was selected due to its high reflectivity. It was created using high-speed buffing and a special rouge, with subsequent buffing (Rimex Metals Australia 2018)

The design of the entire system was centred around this element due to its expense (capital and transportation costs) and the time required for its delivery. The operating limitations of the USQ workshop cutter size (MatCam water jet) further constrained the dimensions of the mirror. Therefore, this element is considered as a starting point for the whole heating system design process and all other components' sizes were designed based on the size of the mirror sheet.

The mirror sheet (1550 mm × 1200 mm × 2 mm) was cut in half to produce two mirrors of dimension 775 mm (arc of the reflector aperture area which produces 700 mm of the reflector aperture width) × 1200 mm (length the reflector aperture area), as shown in Figure 3.2.



*Figure 3.2: Super mirror stainless steel grade 316 (left) and the installed mirrors of the solar heating system (right), consisting of two symmetrical parabola collectors.*

### 3.3 Structure of the reflector support frame

The reflector (mirror) support frame is considered one of the most important parts of the proposed solar heating system. Accuracy of its design, manufacturing and assembly can significantly affect PTSC performance. Figure 3.3 shows the 2D schematic of the two symmetrical reflectors.

The geometry of the reflector support frame is defined by (Mwesigye et al. 2016):

$$Y = 0.25 \times X^2 \times F^{-1} \quad (1)$$

Where Y is the height of the reflector frame, X is the half aperture width ( $W = 2X$ ) of the frame and F is the focal distance of the frame aperture area.

Based on the constraints of Eq. (1), in order to design a parabola trough shape, two of the collector formula variables should be selected and then the third variable is determined. Therefore, the dimensions of each mirror sheet are 700 mm × 1200 mm (width and length (L) of collector aperture area). This produces a collector width of 2X. In addition, the focal length of the collector aperture area (F) is a function of the collector aperture width and rim angle as defined by (Chafie et al. 2016):

$$F = W / 4 \tan (\theta_i/2) \quad (2)$$

The collector rim angle ( $\theta_r$ ) was chosen to be  $80^\circ$  as presented by (Günther et al. 2011). Therefore, after obtaining the aperture width (due to mirror sheet dimension) and focal distance (from Eq. 2), the third variable (Y) can be determined by Eq. (1). Table 3.1 shows the dimensions and details of the designed collector.

A sheet of galvanised steel ( $3 \times 200 \text{ mm} \times 2400 \text{ mm}$ ) was used to manufacture the structure of the reflector support frame due to its resistance to external weather conditions. This was carried out by a Computer Numerical Control (CNC) machine after being programmed with a Creo 3.0 software reflector frame design file. As shown in Figure 3.4, two symmetrical collector structure pieces were designed. The mirror sheets were bent onto the reflector frame and fixed by pins every 100 mm. In addition, each reflector support frame has a tiny base; one used as a tracking sensor base, while the other one is used as an alignment indicator base.

Table 3.1: Dimensions of the proposed collector.

Item	Value
Aperture length (L)	1.2 m
Aperture width (W)	0.7 m
Rim angle ( $\theta_r$ )	$80^\circ$
Concentration ratio (CR)	11.7
Aperture area	$0.84 \text{ m}^2$
Focal distance (F)	0.208 m

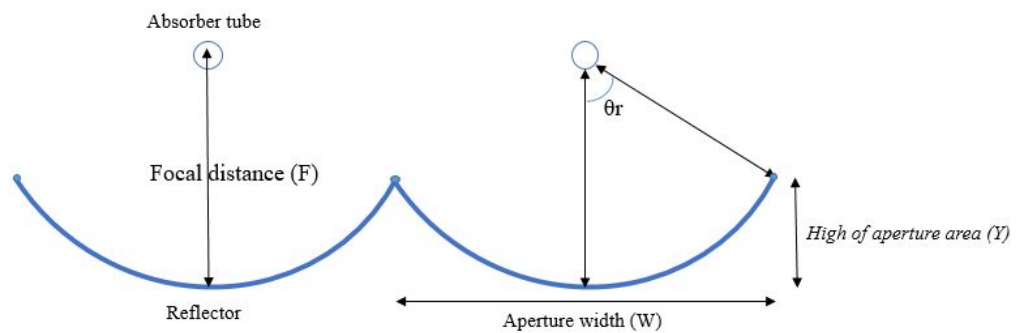
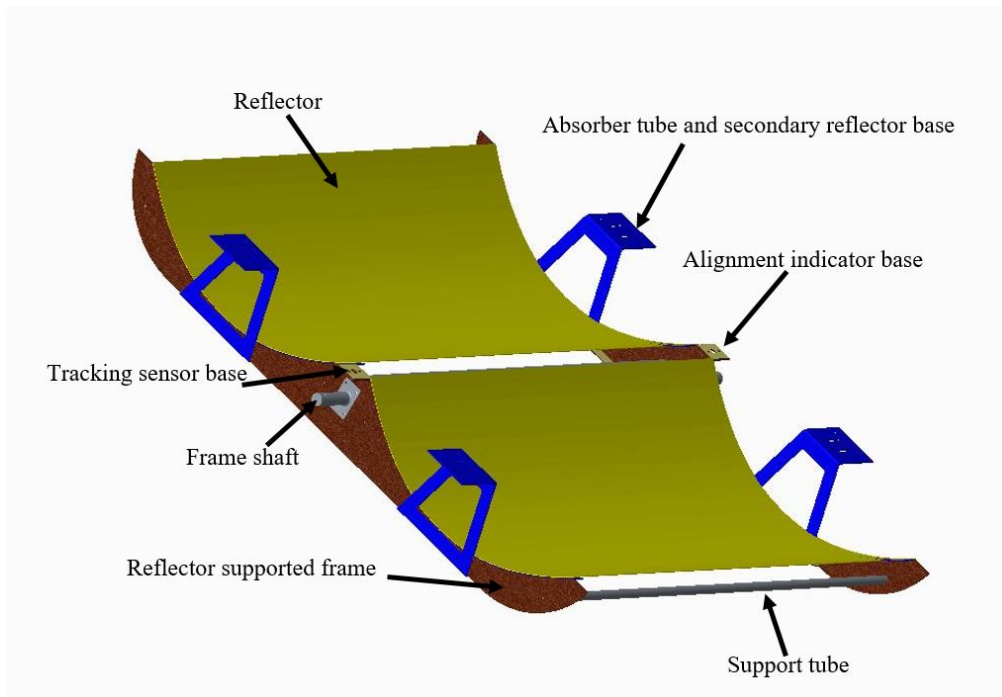


Figure 3.3: Plans of the symmetrical primary reflectors,  $\theta_r$  is the rim angle of the aperture area.



*Figure 3.4: Primary collector structure showing the mounting of the mirrors (reflector), pivot for hourly tracking (frame shaft) and mounting supports for the absorber tube and secondary reflector (blue components), alignment indicator and tracking sensor.*

### **3.4 Main parts of collector base**

This section is focused on the whole structure of the PTSC heating system base, shown assembled in Figure 3.5. The parts are the ground base, seasonal tracking base, seasonal tracking support and collector bearers. This structure is designed to serve several purposes. Not only does it bear the system, but it also enables the sun's path to be tracked throughout the day and the system to be reoriented to account for the change in the sun's elevation during the seasons as well.

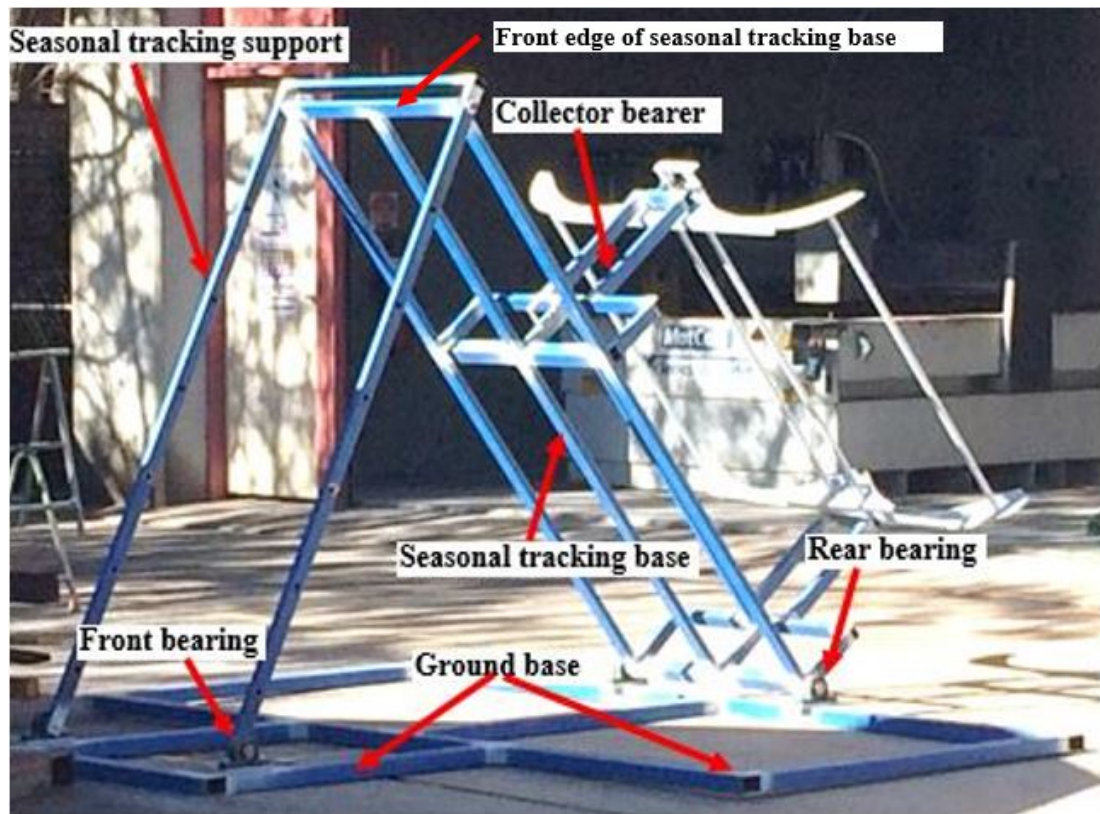


*Figure 3.5: The assembled support structure for the mirrors.*

Figure 3.6 illustrates the structure of the collector bearer. The main purpose of this component is to support the collector frame. It can be seen from this figure that the bearing in the top of the collector bearer is used to mount the collector frame. These bearings allow the collectors to rotate  $150^\circ$  around the horizontal axis to track the sun from sunrise to sunset. The distance between the collector bearers is equal to the collector length. When the collector rotates, it has 100 mm clearance from the support beam between the bearers (coloured blue). This clearance allows the collector to rotate  $360^\circ$ . This range of rotation is also used for maintenance purposes and gives it flexibility for increasing the east-west tracking domain. In addition, as illustrated in Figure 3.6, the collector bearers placed on the seasonal tracking base are used to track the sun path during the seasons (also illustrated in Figure 3.4). The rear edge of the seasonal tracking base is provided by two pins. These pins are used to mount the rear edge of the seasonal tracking base by the ground base (through the rear bearings). The front edge of the seasonal tracking base is mounted with the seasonal tracking support (U tool) from the other side (see Figure 3.4).

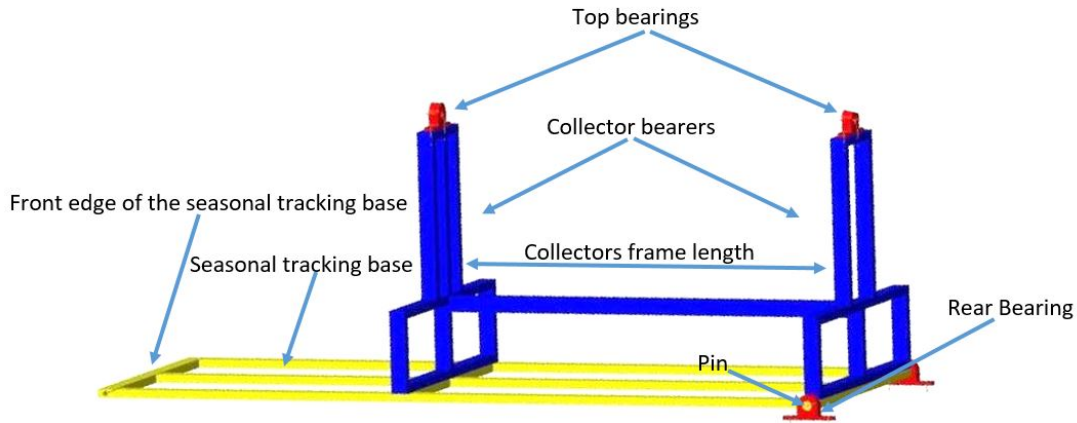


Figure 3.6: Bearer parts of the collector structure.

Another part in the collector foundation is the seasonal tracking support. Figure 3.7 shows the structure of this component. A rectangular hollow tube with cross-section dimensions of 50-25-1.6 mm was used to manufacture this part. This component was designed and manufactured to be a support base for the collector body by mounting the seasonal tracking base by the seasonal tracking support (see Figure 3.5). This part is also used for seasonal tracking.

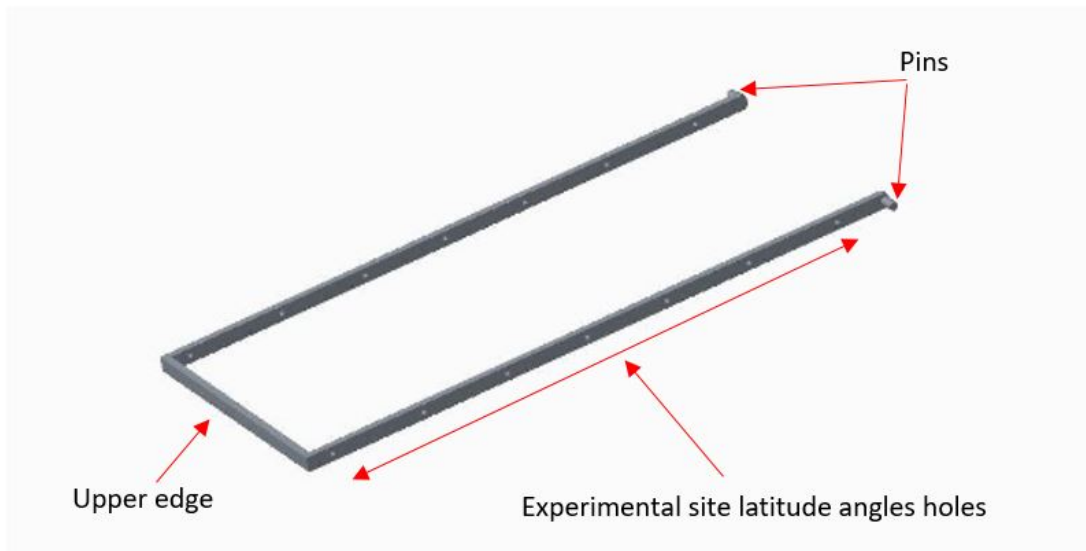
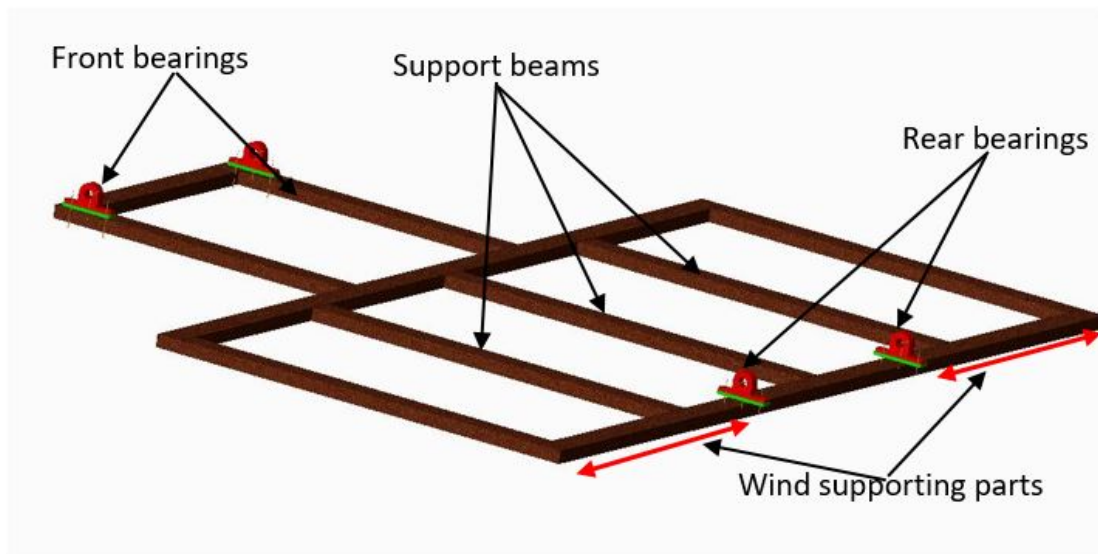


Figure 3.7: Seasonal tracking support (U tool) has a number of holes for tilt angles. Pins are used to mount this component onto the front bearing of the ground base. Holes are used to mount the seasonal tracking base onto the seasonal tracking support to adjust the collector seasonal angle.

The last part is the ground base of the system, a major bearer for the whole heating system (except the insulated water tank). Figure 3.8 illustrates the structure of the

system ground base. It consists of rectangular frames welded together to support the weight of the collector structure and also support against lateral wind load. A rectangular hollow tube with cross-section dimensions of 75-50-2 mm was used to manufacture this base. Four bearings are attached at either end of the base. The front bearing is used to mount the seasonal tracking support onto the ground base (see Figure 3.5). As can be seen from Figure 3.6, the rear bearing houses are used to mount the seasonal tracking base onto the ground base.



*Figure 3.8: Heating system ground base. Front bearings used for mounting the seasonal tracking support, and rear bearings used for mounting the seasonal tracking base.*

### **3.4.1 Secondary parabola (SP)**

The secondary parabola (SP) is designed and manufactured based on the same trough formula (Equation 1). Figure 3.9 shows the cross section of this geometry. The purpose of this component is to be a secondary reflector (SR) for the primary reflector (after a mirror sheet is glued to the inner surface of the SP). Figure 3.10 shows the primary reflector and SR that share the same focal distance. Using the SR can reflect most of the deviated reflected solar rays, which occur due to wind load or geometry misalignment of the primary collector, back to the absorber tube. The focal line of the SP is the same focal line of the primary collector (sharing same absorber tube) as shown in Figure 3.10. The rim angle of the SP is  $90^\circ$  which means it is suitable to use with a PTSC that has a rim angle of up to  $90^\circ$ . Based on the specific secondary dimensions that are presented in Table 3.2, an aluminium tube with dimensions of 70 mm outer diameter, 64 mm inner diameter and 1400 mm length was cut into two parts

along the length of the tube. Figure 3.11 shows the cross-section of the aluminium tube in addition to the sections that were utilised as the secondary parabola. These parts almost match the shape of the proposed secondary parabola as illustrated in Figure 3.12; only the very edges of the secondary reflector significantly deviate from the theoretical shape.

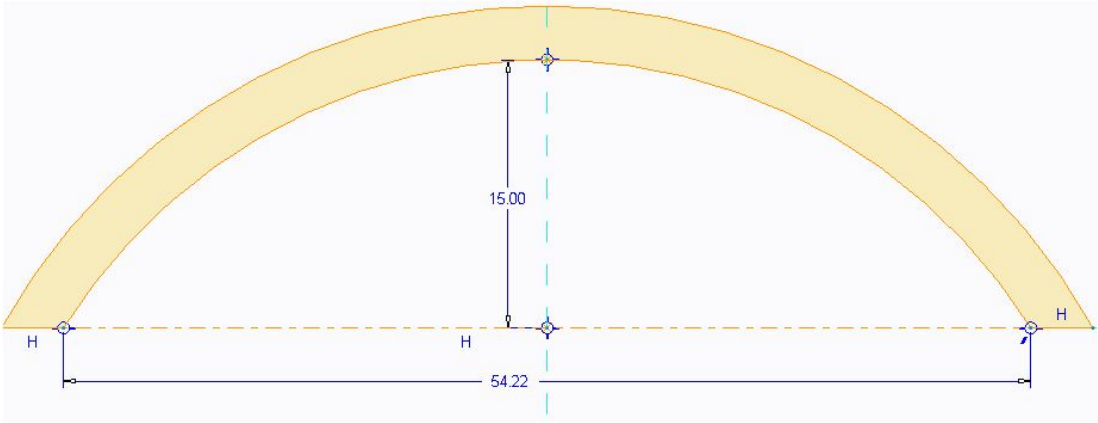


Figure 3.9: Cross section of the secondary parabola (SP).

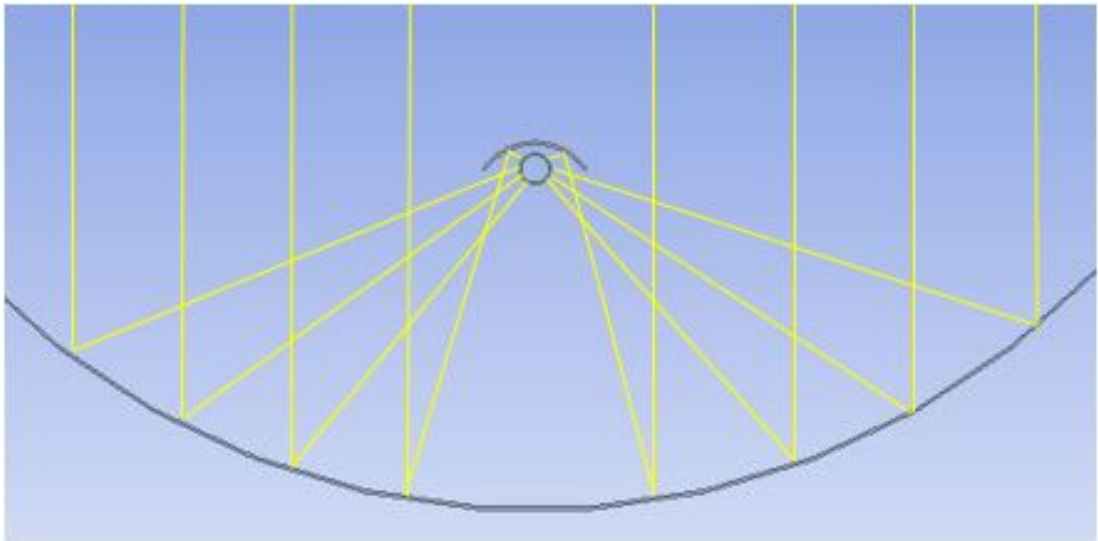


Figure 3.10: Schematic of the primary and secondary reflectors in operation.

Table 3.2 Secondary reflector dimensions

Item	Value
Aperture length	1.2 m
Aperture width	0.06 m
Rim angle	90°
Aperture area	0.072 m <sup>2</sup>
Focal distance	0.015 m

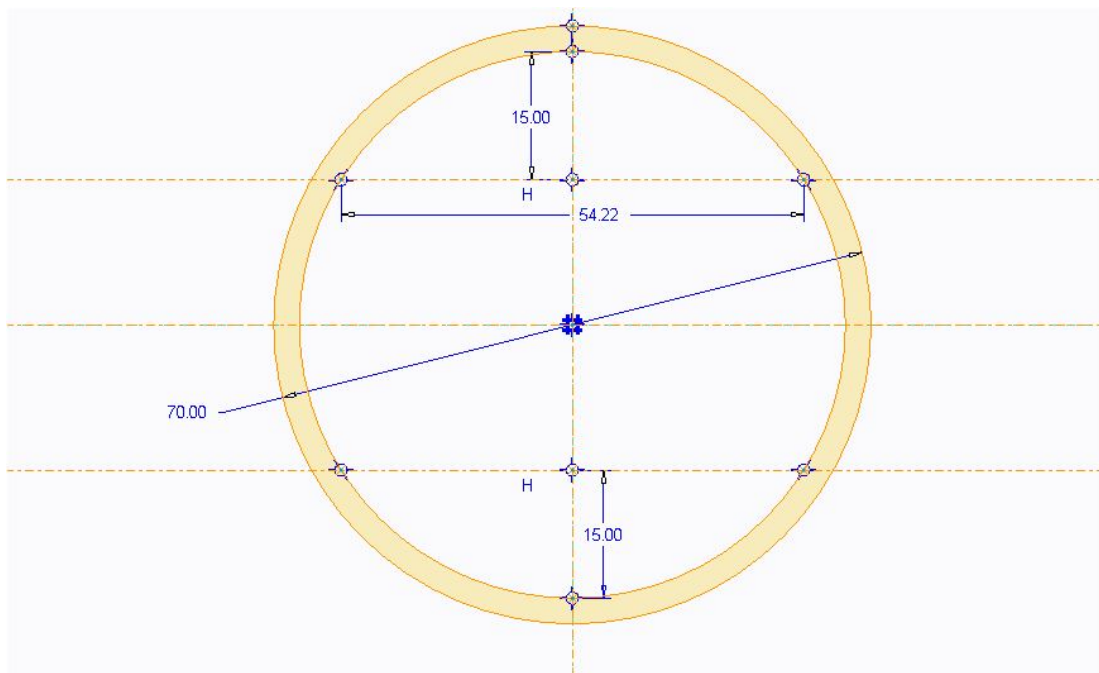
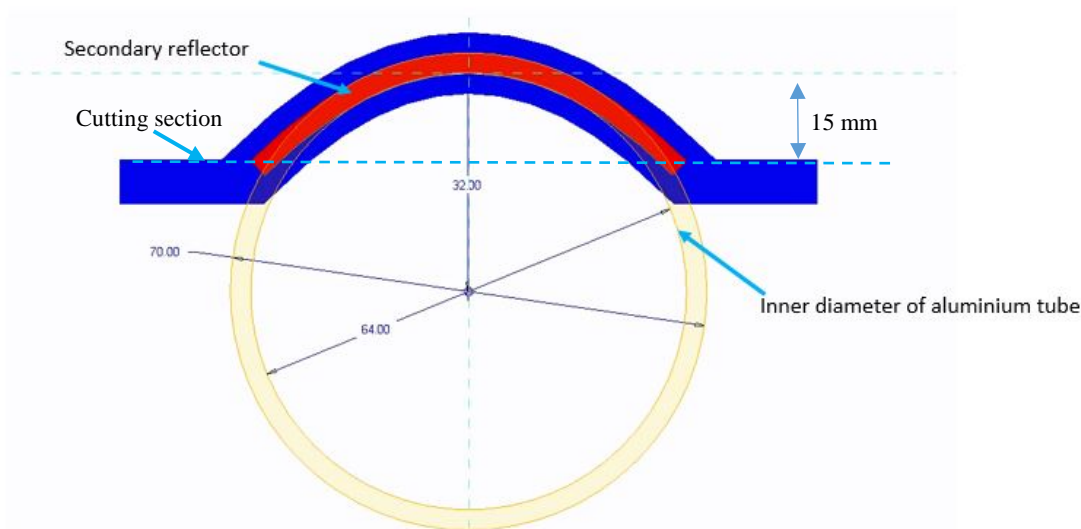


Figure 3.11: Cross section of aluminium tube used to create the two secondary parabolas with focal length 15 mm. The segments of aluminium tube used for the secondary parabolas were cut a focal length from the top/bottom as indicated.



*Figure 3.12 Comparison of actual secondary reflector shape (from Figure 12) and theoretical shape (red colour).*

A mirror sheet called reflective solar film is used as the mirror due to its high reflectivity, which can reach up to 97% reflective rate. This sheet is glued onto the inner surface of one SP to use as a secondary reflector. This component consists of a secondary parabola (SP) with mirror film (SPM). The other secondary parabola (cut from another segment of the aluminium tube) was painted black. This component is called secondary parabola painted black (SPB). The finished SPM and SPB are shown in Figure 3.13. The aim of using the SPB is to operate both primary collectors under same aperture areas (both of them lose the same areas due to utilising the SPM and SPB). In addition, the black paint also helps to avoid any reflecting that could occur due to the inner surface of the aluminium tube segment (SP). This could affect the accurate measurement of the collector's performance. Figure 3.14 shows the SPM and the SPB before installing on the primary collectors of the heating system. The secondary reflector was mounted on the upper part of a wooden block and its upper surface was shaped according to the inner shape of the secondary reflector (Figure 3.15).



*Figure 3.13: Geometries of secondary parabola with mirror film (SPM) (upper) and secondary parabola painted black (SPB) (lower).*



*Figure 3.14: Heating system and the SPM and SPB before installation.*

### 3.4.2 Heat collection element

The possibility of minimising the PTSC intercept factor ( $\gamma$ ) is increased with increasing value of collector concentration ratio (CR), that is based on the absorber diameter and collector aperture width. This is because the ratio of absorber tube diameter to the collector aperture width is very small. For example, in a solar thermal plant using PTSC the collector aperture area is approximately 6000 mm while the absorber diameter is 70 mm (CR approximately equal to 30). Therefore, the possibility of the reflected solar rays' deviation is raised and can be clearly observed.

In the current heating system, to obtain a CR equal to 20 (suitable for heating applications), an absorber tube with a diameter of 10 mm is required. This is based on the above CR and due to the collector aperture width which equals 700 mm. However, using this absorber tube, with diameter 10 mm and length 1200 mm, will produce geometric misalignments due to the flexibility of the absorber tube. Therefore, in the current design, a copper tube with  $\frac{3}{4}$  inch diameter and 1.4 m length is used as an absorber tube for the solar collector (Figure 3.15). This element is placed along the focal line of the primary collector and secondary reflector (which share a common focal line). In order to reduce conduction thermal loss from the absorber tube onto the support frame, a wooden block was used to mount the absorber tube. The wooden block is designed to house the absorber tube, while the secondary reflector is mounted on its upper surface.

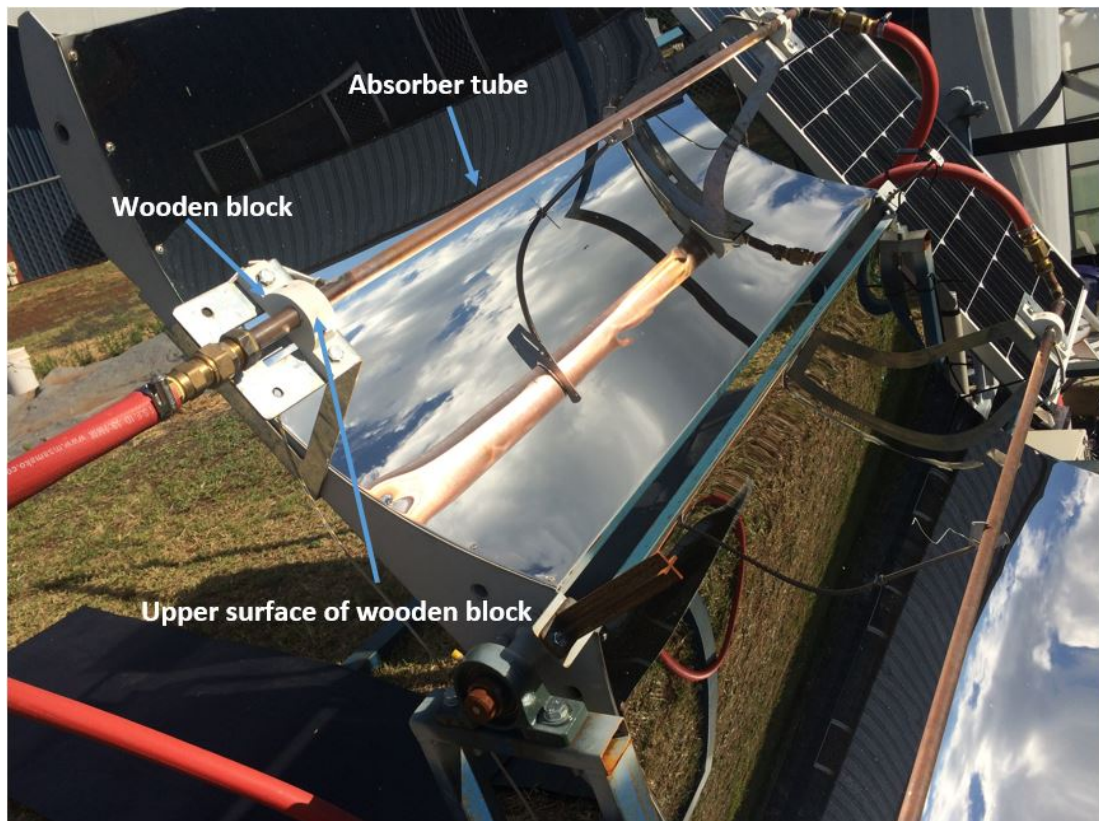


*Figure 3.15: Wooden block is acting as absorber tube housing and secondary parabola support.*

### **3.5 Tracking system**

A parabolic trough collector geometry reflects or focuses normal incident solar radiation. Therefore, this type of solar collector works by using a tracking system that adjusts the collector plane during the day to be in line with the solar radiation. A single-axis auto tracking system is normally used for PTSCs that are used in solar thermal plants and industrial heating applications.

In the current experimental work, the tracking system consists of an hourly and seasonal tracking system. Figure 3.16 shows the hourly and the seasonal tracking of the heating system. The hourly tracking is an auto tracking system, which is a single-axis solar track run by a 12 VDC motor (actuator motor). Stroke length, max push and linear speed of the actuator motor were selected based on the range of the collector angle tracking ( $15^{\circ}$ - $165^{\circ}$ ) and the collector frame weight. Figure 3.17 shows the main dimensions and angle range of the auto tracking system.

The seasonal tracking system consists of a seasonal tracking support (U tool) and a seasonal tracking base as shown Figure 3.16. The seasonal tracking support has holes

that were made and distributed based on the tilt angles of the USQ site (Table 3.3). The seasonal tracking can be carried out manually by mounting the seasonal tracking base on the seasonal tracking support at the appropriate angle. Via the hourly and seasonal tracking systems, collectors can track the sun's location in the sky so that the solar rays have a normal incidence on the collectors' aperture areas, and are reflecting to the receiver tube.

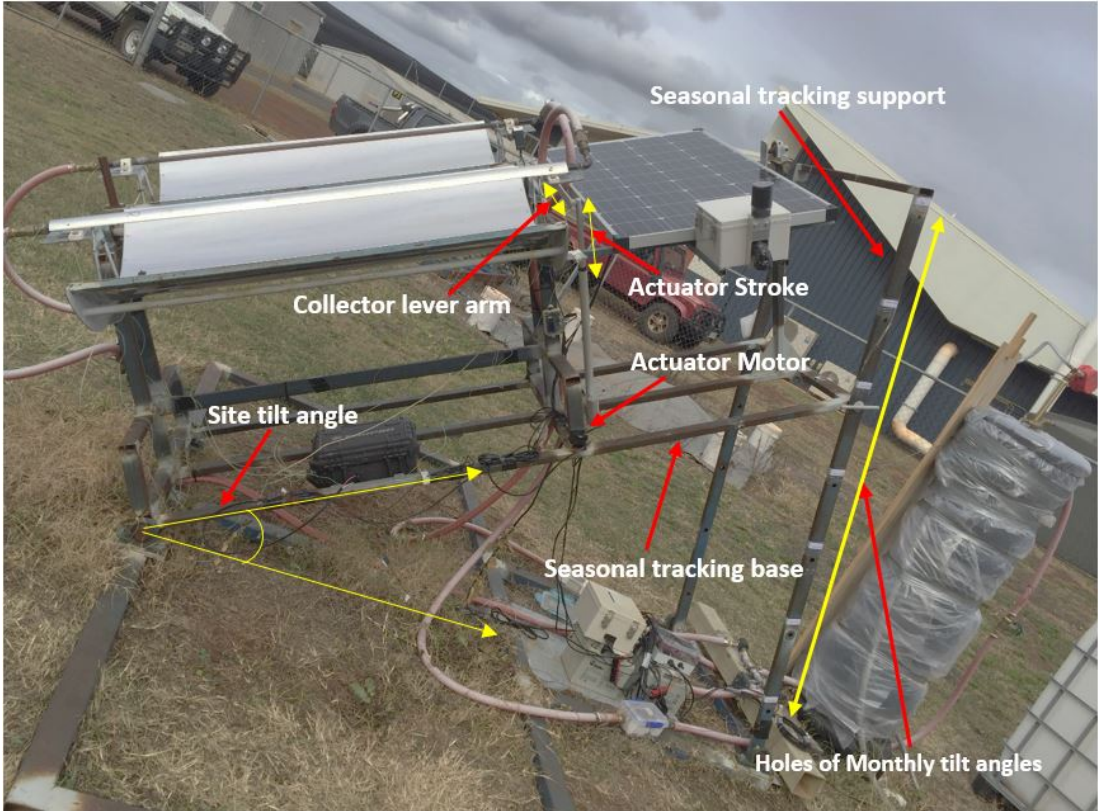


Figure 3.16: Hourly and seasonal tracking system of the collectors.

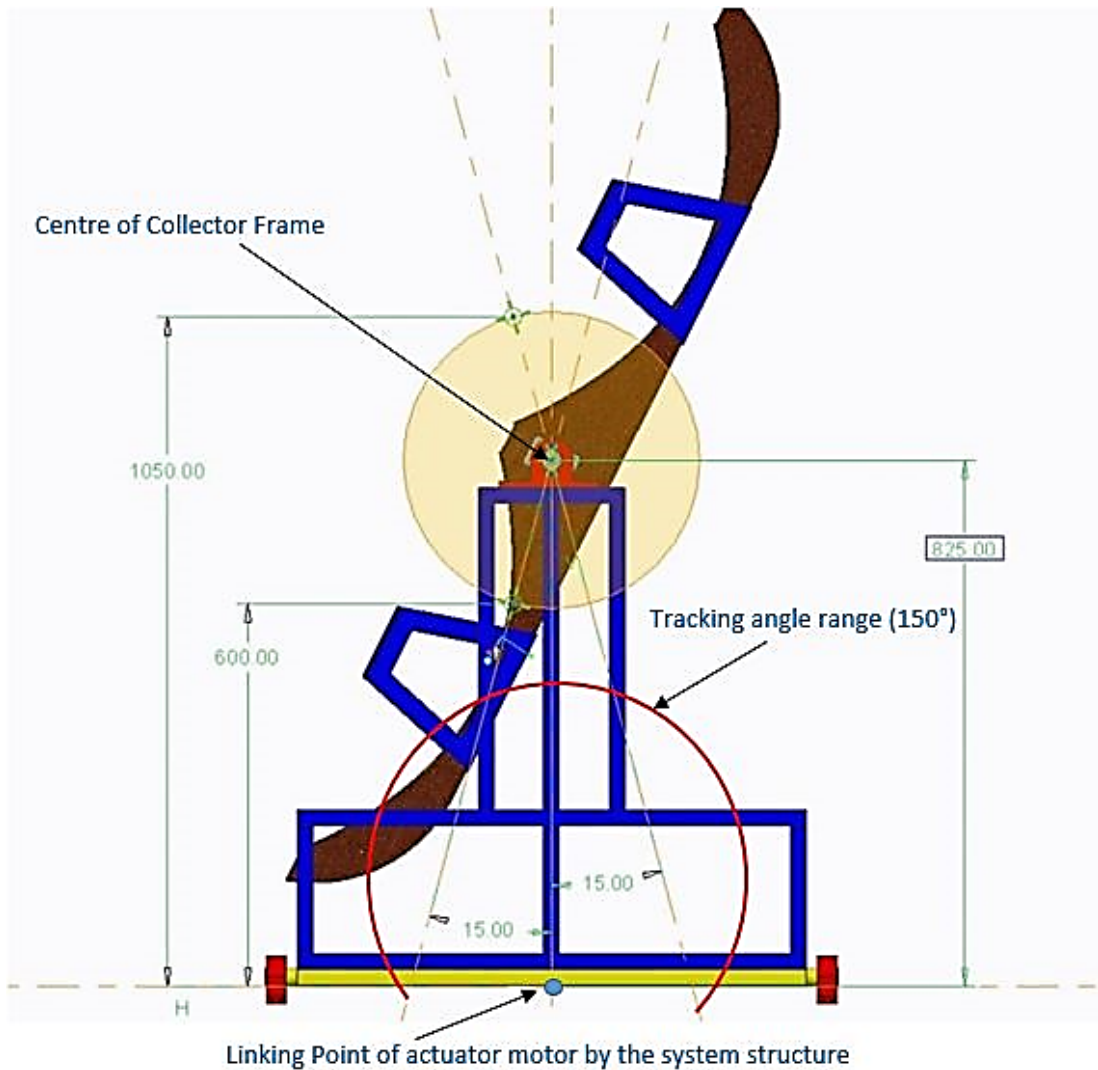


Figure 3.17: Dimensions of the motor actuator and range of tracking angles.

Figure 3.18 illustrates the base frame of the PV solar panel. This base was welded to the reflector support frame so that it tracked with the collector. In addition, a solar power meter box was attached to the PV solar panel base, which keeps the solar power meter sensor aligned with the collector plane to measure the normal incident solar radiation. After assembly, the collector components were painted with silicone epoxy to protect the prototype structure from oxidation.

Finally, to ensure checking collector tracking accuracy and alignment, the collector indicator was designed and manufactured as shown in Figure 3.19. This figure shows the structure and dimensions of this component placed on the alignment indicator base (shown in Figure 3.4). Ensuring that the alignment ribs cast no shadows on its base provides accurate tracking.

Table 3.3: Optimum tilt angle of solar collector by month

<b>Month</b>	<b>Jan</b>	<b>Feb</b>	<b>Mar</b>	<b>Apr</b>	<b>May</b>	<b>Jun</b>
Optimum Tilt angle	78°	70°	62°	54°	46°	38°
<b>Month</b>	<b>Jul</b>	<b>Aug</b>	<b>Sep</b>	<b>Oct</b>	<b>Nov</b>	<b>Dec</b>
Optimum Tilt angle	46°	54°	62°	70°	78°	86°

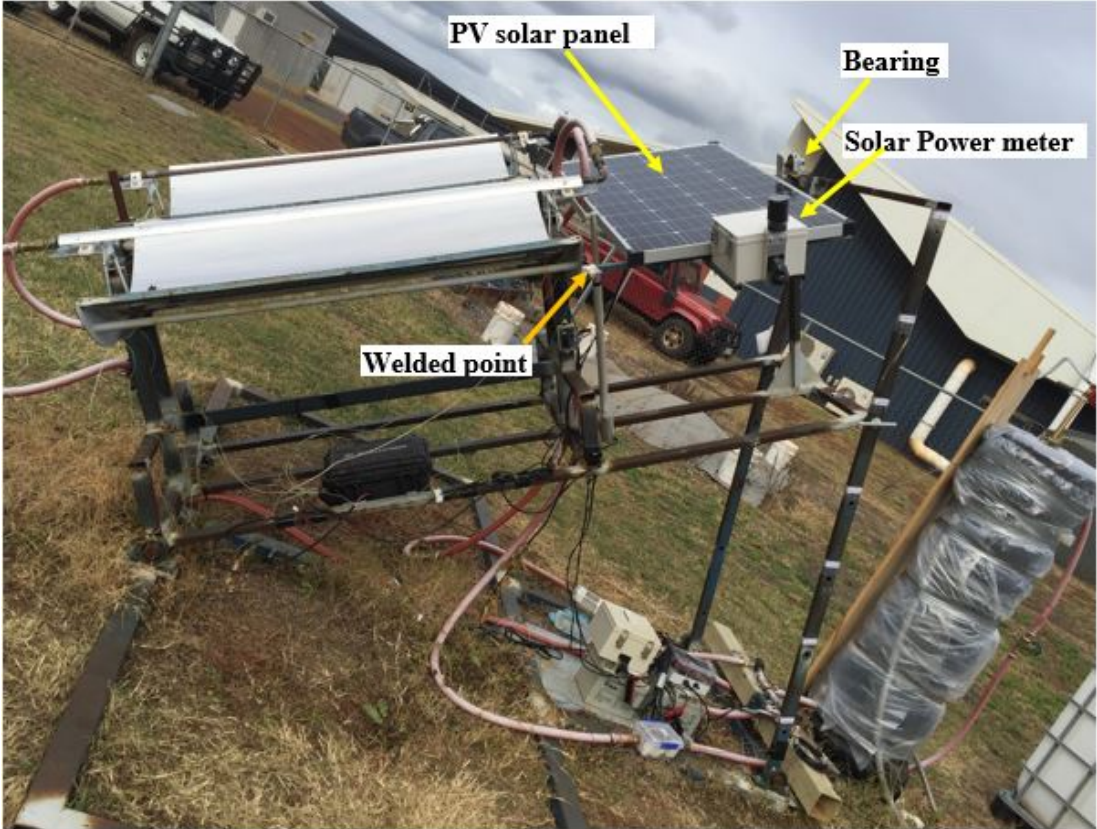
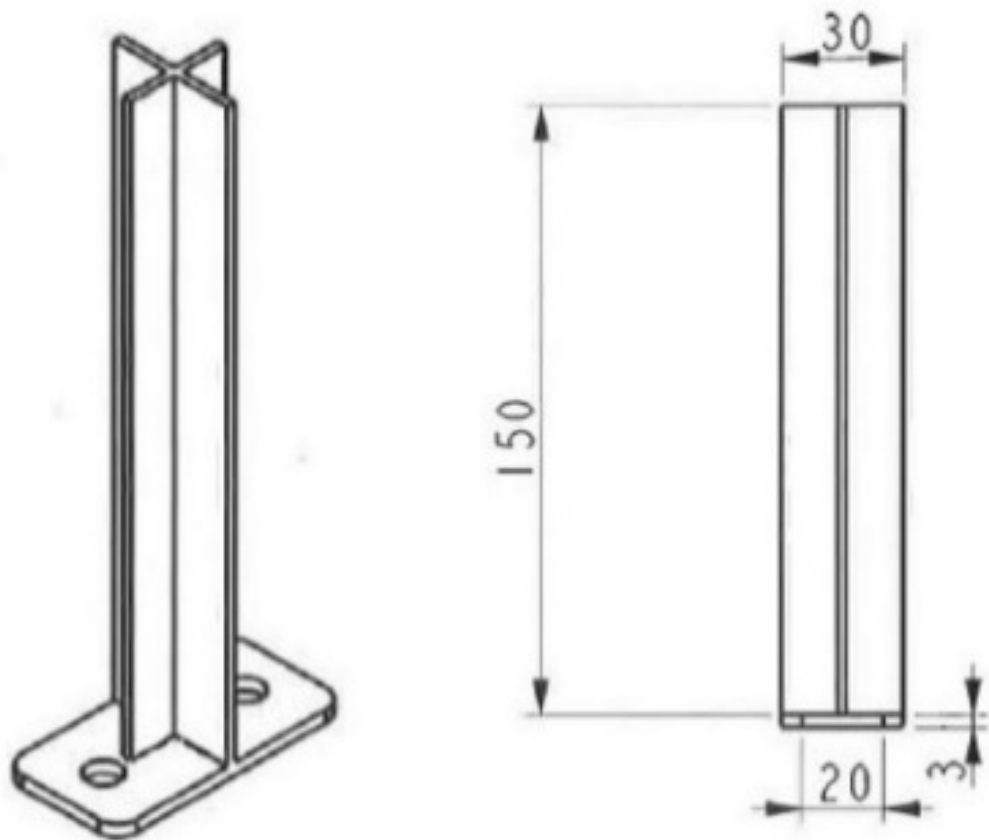


Figure 3.18: PV solar panel installation, showing its mounting points onto reflector support (welded point) and bearing. Also shown is the solar meter box (contains the solar power meter).



*Figure 3.19: Structure body of the collector indicator.*

### **3.6 Storage tank**

The storage tank is an essential part which contains the HTF (water) to be supplied to the heating system. The size of the storage tank in the current design was chosen to be 135 litres (1400 mm height and 350 mm diameter). Figure 3.20 shows the storage tank of the heating system before being covered by the thermal insulation.

A galvanised steel plate with dimensions of 2400 mm length, 1200 mm width and 3 mm thickness was used for manufacturing the storage tank. Three levels on the tank's wall were selected for placing temperature sensors. The temperature sensor sites are (starting from tank base) 200 mm, 1000 mm and 1200 mm. The aim of these sensors is to measure the water temperature at different locations. The location of the sensors is presented in Figure 3.21. Water is fed into the top of the tank via a tap (Figure 3.20). The tank also has a pressure gauge to measure its pressure and a safety valve to release any high pressure which might occur. The HTF inlet point of the tank is at 1.2 m from

its base, while the outlet HTF point is at 0.2 m from the tank base. Earthwool insulation was used to insulate the exterior of the water tank.



*Figure 3.20: Storage water tank before installing the thermal insulation, showing sites of water temperature sensors and zoomed on the tank cover showing the safety valve, pressure gauge, water tap and sight glass with hexagonal head.*

### **3.7 Pumps and water cycles**

In the experimental project, due to the low concentrating ratio of the designed collector, which produces little heat (the HTF inlet temperature could not increase more than 2 °C as the HTF flowrate equal 0.06 litre per second). Therefore water is the best option to be used as an HTF in this heating system: it has a high specific heat value in addition to being cheap, readily available and safe. The HTF (water) was actively circulated through the solar heating system by using a solar water pump. The selection of a suitable solar water pump is based on several principles. First of all, the HTF operation temperature varies between 0°C and 80°C, while the surface of the components could reach 50°C (due to it being subjected to the solar radiation). Secondly, the required range of the HTF water flow rate is between 0.06 and 0.07

kg/sec, which causes turbulent flow due to dimension of the absorber tube inner diameter (Re range between 5046 and 5887). Moreover, lower flow rates could produce a high HTF temperature, which could affect some of the system components like plastic pipes. On the other hand, increasing the HTF flow rate more than that range could make it difficult to observe the increase in HTF temperatures because of the low collector concentrating ratio and also because of the small collector aperture area. Finally, one of the project aims is to run all required instruments by solar energy, hence the selection of a solar water pump that can deliver for all the above operation conditions. Therefore, a 12 VDC micro solar pump that works with a fluid temperature range between 0°C and 100°C was selected. The solar pump circulates HTF inside a closed water cycle (Figure 3.21). The heating system was provided by three solar pumps. One of them was used for circulating water between the collectors and the tank; the second solar pump can be used for circulating water between the tank and an external load, such as a swimming pool (potential future work); the third one is installed as a redundant backup.

The solar pump pumps the water through the pipe and then it is split using Y connection to send HTF to each collector. Each collector has a water valve to be able to control the flow rate separately. Each collector has a water temperature sensor at the start and the end of the absorber tube to measure the HTF temperature at the start and the end of the absorber tube. Then the flow rate of each collector is measured separately by a flow meter device. Then the outlet collector pipes reconnect and there is also another HTF valve to control the overall flow rate before the HTF returns to the tank.

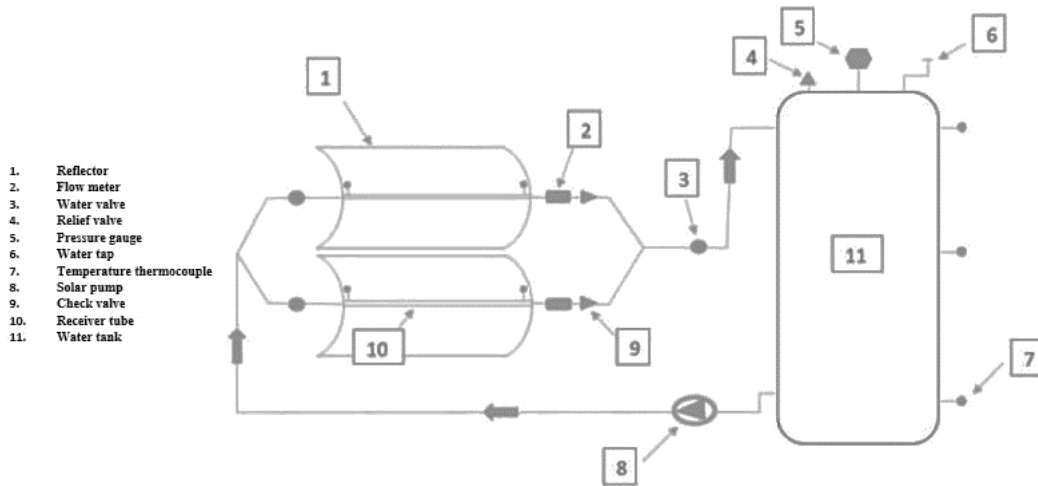


Figure 3.21: Diagram of the solar heating system.

### 3.8 Electronic Control System

The solar heating system is monitored and regulated by an electronic control system, as illustrated in Figure 3.22. The main operational components of the system are three solar pumps which are used to circulate the heat transfer fluid (each of the solar pumps also had its own isolation switch) and an electro-mechanical sun tracking device. The design of this system is made more complex by the need for it to operate standalone with no connection to mains power. To accomplish this, the system has two main sub systems: the generation and storage of electrical energy needed to power the complete control system and the control and monitoring sub system, including the pump controller, solar tracker and data acquisition unit.

The generation system utilises two 120 W solar panels. These are connected to a solar charge controller incorporating a maximum power point tracker (MPPT) in order to extract the maximum power from the solar cells for the given conditions. The controller provides 12 VDC power to the control and monitoring sub system. Excess power is then used to charge the two 32 Ah deep cycle lead-acid batteries. In optimum weather conditions, the maximum output power of the panels is far in excess of the requirements of the system. This allows the batteries to be kept in a good state of charge overnight (to avoid the temperature data logger device losing the recording data) or on cloudy or overcast days where the output from the solar cells is insufficient to power the system. The solar charge connector continuously monitors the condition of the batteries. In the event of an extended period of low solar output or a fault within



experimental system, the solar power meter model SPM-1116SD is used to measure the normal solar radiative flux. In addition, the solar meter box is mounted to the collector frame in such a way that it is always in the collector aperture plane during tracking tests. This way the solar power meter can measure the normal solar radiations on the collector. The solar logger has an option to measure and record the solar data during the operating periods on an SD card. The accuracy of this device is better than  $\pm 10 \text{ W/m}^2$ , according to the specifications. In addition, during the test of the stationary experimental cases when the collectors are fixed to the sun's midday position, the solar data is obtained from the stationary solar power meter of the USQ P Block weather station.

### **3.9.2 Temperatures measurement**

One of the essential parameters in the solar heating system is measuring the HTF temperature accurately. Thermocouples were installed at different locations in the water cycle and storage tank. These sensors provide a temperature logger device with HTF temperature data, which is used to calculate collector performance and also storage energy in the water tank. Two types of thermocouple type K are employed in the current project. The first one is a thermocouple type K with an operating temperature of  $-30^\circ\text{C}$  to  $480^\circ\text{C}$ . The length of the temperature sensor is 12 mm. This type of sensor is used especially for measuring HTF temperatures at the inlet and outlet of the collector's absorber tubes by making a hole that is threaded based on the sensor's thread.

The other type of thermocouple is an Uxcell K-type 50 mm long probe, used for measuring HTF water temperature in the storage tank due to its length. Water tank temperatures are measured at three levels. Figure 3.21 shows the sensors' distribution in the water tank and also shows the sensors' location at the collector's absorber tube. All sensor wires are linked to a temperature data logger device. The sensors are calibrated before assembly stage by using a thermometer; they are also checked regularly during operating periods to make sure that they are still working properly during operation time.

### **3.9.3 Flow meter measurement**

The range of HTF flow rate, HTF operation temperature and outdoor operation conditions are the main parameters that are considered when selecting the proper mass flow rate devices. In the current work, a turbine digital flow meter with a flow meter range from 10 L/min to 120 L/min with measurement accuracy  $\pm 1\%$  was used in the solar heating system. The devices are calibrated by timing the filling of a beaker, with the device's accuracy confirmed to be within  $\pm 1\%$ . In addition, the flowmeter device has an option for user calibration that can be used to adjust flowrate measurement accuracy, which is based on manual calibrating data. The flowrate devices were installed in the outlet pipe of each collector.

### **3.9.4 Data recording**

A 12-channel temperature data logger (LU-BTM-4208SD) is used for recording all thermocouple data and saving the data every five minutes. This device has options for displaying the data and also recording the data on an SD card and the data logger is capable of sampling up to 1 Hz. The environmental conditions like air temperature, wind speed and solar radiation data were recorded every five minutes by the USQ P Block weather station that is located near the experimental site. During stationary tests, solar radiation data is collected by the USQ weather station, while during tracking tests, the solar data logger device is used to provide solar radiation data. The instruments can measured each second, but it setup to measure and save the data for each 5 minutes according to the weather station to do the calculations.

### **3.10 Installing the solar heating system on the selected site**

Several factors were considered in order to select a suitable site for installing the solar heating system. One of these factors was the test operation time. While it is possible to take readings between 8 am and 4 pm because the test site is clear from any shadows (trees or buildings), to be sure of no interference from the surroundings, the measurements used here were recorded between 9 am and 3 pm for tracking tests and between 10 am and 2 pm for fixed tests. In addition, there should not be any building or any other reflecting surfaces close to the experimental site. A fence is also required to avoid interruptions to experimental tests. After selecting a suitable site, the ground should be adjusted to be level. It is also necessary to determine the north-south axis by

using a compass tool to locate the collector in the right direction to track the sun during operating daylight hours.

For the solar system, a wide available area was selected, located in the P5 compound of USQ (Figure 3.23). This area is clear of any building or tree shadow during the test operation hours and it has a fence and other facilities like a water source. The ground was adjusted and checked by a level. The north-south axis was determined before installing the collector system. After that, the solar heating system components were assembled using a forklift. The system's ground base was installed first. Then the collector structure base was installed by linking it with the ground base by the housing bearings and linked with the seasonal tracking base by pins. Then the collector's body structure was joined to the vertical bearers via housing bearings.



*Figure 3.23: The site of the experimental prototype at USQ Toowoomba.*

# Chapter 4 Experimental tests of the PTSC optical and thermal performance

## 4.1 Introduction

The aim of this chapter is to present the experimental results investigating the effect of a secondary mirror (section 3.4.1) on PTSC performance under real weather conditions. The experimental tests were classified into two main stages, which are tracking and fixed stages, as illustrated in Figure 4.1. The tracking stage adjusts the collector plane during the day to be in line with solar radiation (tracking the sun's path throughout the day from sunrise to sunset). During the fixed stage tests, the collector plane was aimed at the noon sun position for the entire test; more details can be found in sections 4.5 and 4.6.

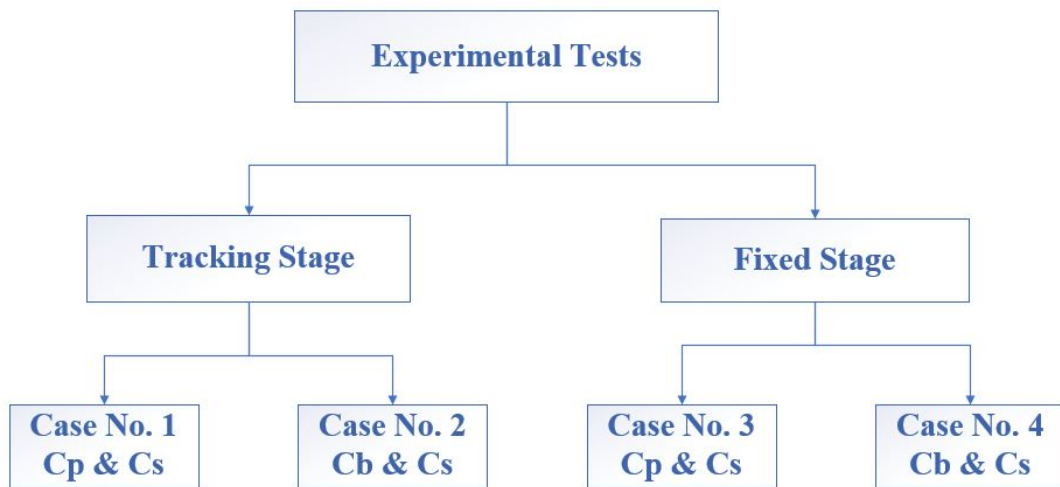


*Figure 4.1: Flowchart of the stages and cases of the experimental tests of the PTSC heating system. The tracking stage is the hourly tracking. The fixed stage is when the collector is aimed at the sun noon position. Cp is the primary collector (normal design), Cs is the primary collector with secondary parabola mirror (SPM), Cb is the primary collector with secondary parabola painted black (SPB).*

## 4.2 System Verification

As mentioned in Chapter 3, the heating system consists of two identical collectors with the same design and materials (section 3.3). Before starting each experimental test, the two identical collectors were tested (under the same water flow rate) to check the

similarity between the collectors. As expected, the performances of the two identical collectors have a negligible difference.

Before each experimental test, several steps were adopted for checking some aspects of the heating system. The first step was to clean the reflectors of dust. The second step was checking the water flow rate of each collector separately to ensure they were equal and the flowmeters were calibrated. This was done by opening the outlet pipe of each collector (downstream of the flow meter) and timing the duration for the water to fill a five-litre measuring bucket. The third step was checking the accuracy of the tracking system. This was done by casting a shadow on the auto tracking sensor (hourly tracking system), which caused the collector's orientation to deviate from aiming at the sun. The shadow effect was subsequently removed from the tracking sensor, and then the auto tracking system adjusted the collector orientation to aim at the sun position again. Finally, the water level in the water tank was also checked before each test.

In addition, the accuracy of the water temperature sensors was regularly checked before starting each case of the experimental study. This was done by placing the sensors in graduated glass beakers with thermometers and comparing the readings.

### **4.3 Configuration of experimental cases**

The experimental tests of the tracking and fixed stages consisted of four cases. In each case of the experiment, the pair of identical primary collectors was set up differently from each other to investigate some phenomenon. The aim of case 1 in the tracking stage and case 3 in the fixed stage was to compare between the  $C_p$  (standard design) and  $C_s$  (modified design) under outdoor conditions during tracking and fixed stages (sections 4.5.1 and 4.6.1). For cases 1 and 3 the configuration, as shown in Figure 4.2, can be summarised by setting up one of the primary collectors with the secondary parabola with mirror film (SPM); this configuration (primary collector and SPM) is called  $C_s$ . The other primary collector of these cases was set up without a secondary parabola (SP). This configuration is called  $C_p$ .

In cases 2 and 4 the experimental operation retains the  $C_s$  geometry. The other primary collector uses a secondary parabola painted black (SPB), as shown in Figure 4.3. This configuration is called  $C_b$ . The aim of case 2 in the tracking stage and case 4 in the

fixed stage is to compare the two identical collectors under SPM and SPB configurations. In cases 2 and 4, both identical primary collectors lost the same amount of direct solar radiation because the same amount of each collector aperture area is blocked by the secondary parabola. Both of the primary collectors are influenced by same effect of wind distribution on their absorber tubes due to utilising the SPM and SPB, because both SPM and SPB have the same dimensions and shape (same geometry), which make the same shape around the upper part of the absorber tube of each collector. Therefore this assisted to present the effect of the secondary mirror on the PTSC performance during the tracking and fixing stages. More details can be found in sections 4.5.2 and 4.6.2.

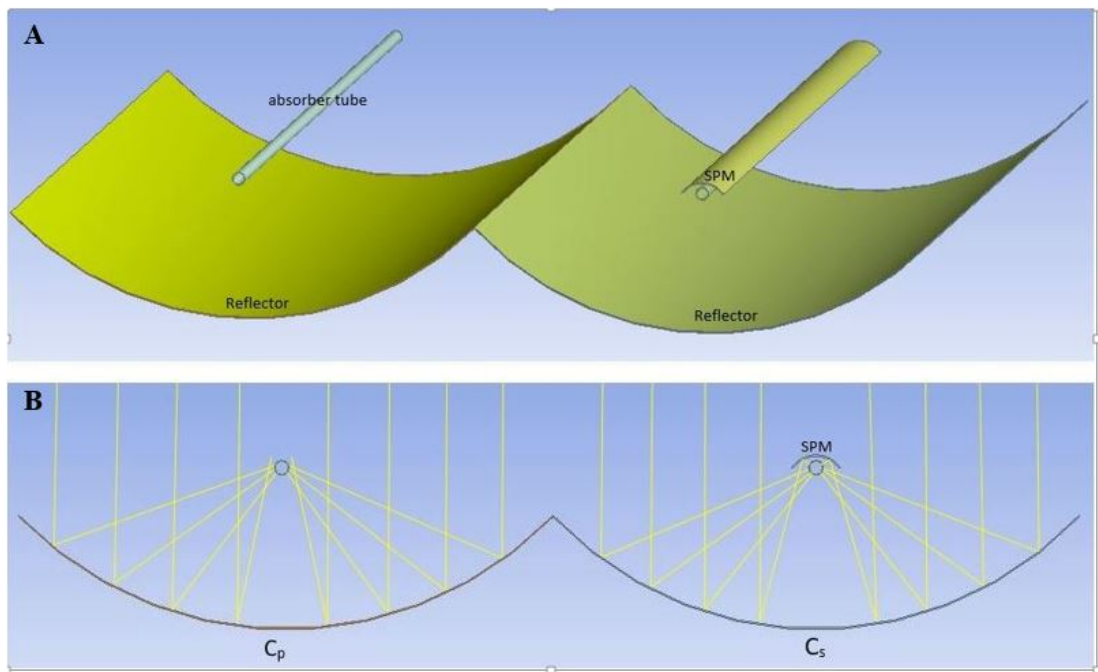


*Figure 4.2: Schematic of  $C_p$  and  $C_s$  configurations for cases 1 and 3.  $C_p$  is the primary collector,  $C_s$  is the modified design and SPM is the secondary parabola mirror. A is the 3D structure; B is the 2D structure; yellow lines are the solar rays, with some deviation from the absorber tube due to geometry misalignment.*

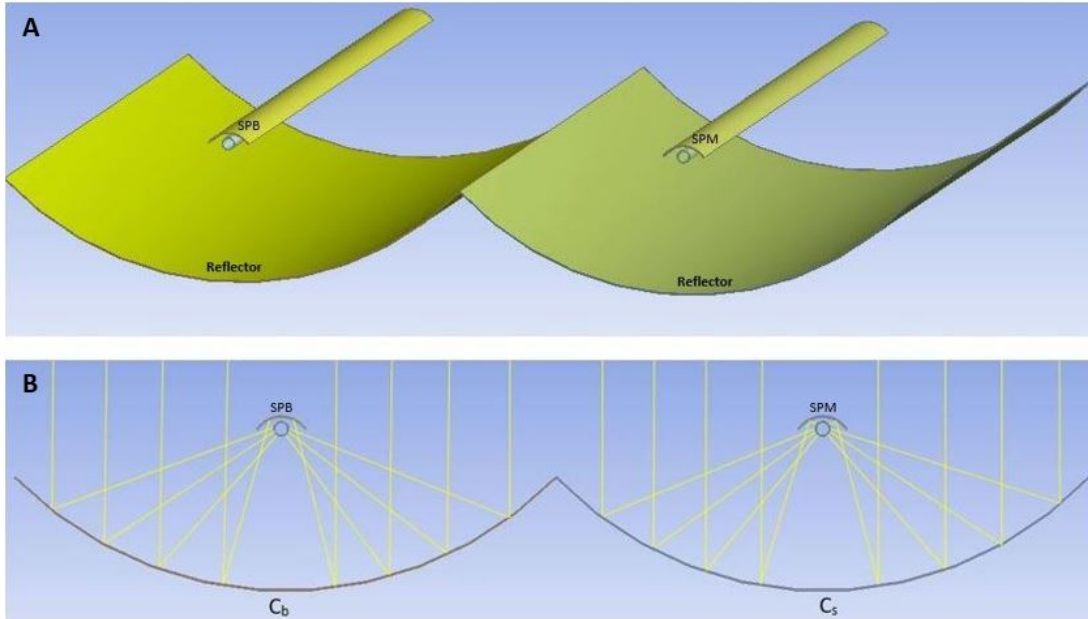


Figure 4.3: Schematic of  $C_b$  and  $C_s$  configurations for cases 2 and 4.  $C_b$  is the primary collector with the black secondary parabola (SPB),  $C_s$  is the modified design and SPM is the secondary parabola mirror. A is the 3D structure; B is the 2D structure; yellow lines are the solar rays, with some deviation from the absorber tube due to geometry misalignment.

#### 4.4 Solar collector thermal efficiency

Many factors can influence the optical efficiency of the PTSC and consequently reduce its performance. Some of these factors related to the collector components' optical properties are (Zhu & Lewandowski 2012):

$$\eta_o = \rho\tau\alpha\gamma \quad (1)$$

where  $\rho$  is the primary reflector (mirror) reflectance,  $\tau$  is the receiver glass envelope transmissivity,  $\alpha$  is the absorber tube surface absorptivity and  $\gamma$  is the collector intercept factor. The intercept factor is defined as the ratio between the amount of radiation hitting the absorber tube and the amount of radiation hitting the reflector. The value of the intercept factor is also affected by several parameters: reflector surface profile (mirror slope), tracking error, absorber's alignment and reflector's alignment. Moreover, the outdoor effect of wind load (dynamic load) is an external factor that has significant influence on the collector intercept factor value. This factor leads mainly to vibration in the reflector structure and, as a result, the reflected solar rays deviated from hitting the collector receiver tube which results in reducing its optical efficiency (Stynes & Ihas 2012).

Reducing collector optical efficiency basically results in reducing the useful heat gain ( $q_u$ ) due to some of the concentrating solar heat flux being deviated from the strike the collector receiver tube (deviated reflected solar rays). Consequently, the daily average collector efficiency ( $\eta_{th}$ ) could be reduced (Mwesigye et al. 2016):

$$\eta_{th} = \dot{m} \times C_p \times \left( \frac{\sum_{i=1}^n T_{out} - T_{in}}{\sum_{i=1}^n I_{beam} A_c} \right) \quad (2)$$

In Equation (2),  $\dot{m}$  is the HTF mass flow rate which equal 0.06 kg/s, measured by the turbine digital flow meter that presented in section 3.9.3),  $c_p$  is the specific heat of the HTF and  $T_{inlet}$  and  $T_{outlet}$  are the inlet and outlet temperatures of the HTF which measured by thermocouples type K at the inlet and the outlet of the collector absorber tube (presented in section 3.9.2).  $I_{beam}$  is the normal solar radiation flux that calculated by the solar power meter (SPM-1116SD) during tracking cases, and by stationary solar power meter of the USQ P Block weather station during fixed cases (presented in section 3.9.1). The  $A_c$  is the collector aperture area which equal 0.84 m<sup>2</sup> and n is the total number of the tests during the day (Mwesigye et al. 2016).

#### 4.5 Results of tracking stage

The aim of this stage is to present the effect of the wind velocity fluctuations (wind change) on the collector's performance while the collector is tracking the sun (this wind effect has previously been observed: section 2.2.1.6). Also, this stage of the study presents the effect of tracking errors on PTSC performance. Tracking errors usually occur because of collector vibration, which occurs due to the partly cloudy weather, when the tracking system searches for the brightest point (this tracking error effect also has been observed in the previous studies presented in section 2.2.1.5). The other aim of this stage is to investigate the effect of the SPM on the collector's performance during the tracking stage. Therefore, in this tracking stage the PTSC is oriented parallel to the north-south axis to track the sun's path throughout the day from sunrise to sunset. The range of the tracking angle is 15°-165° and the tracking period is between 9 am and 3 pm. This period was selected due to there being no building or tree shadows during that period of tests across the year.

### 4.5.1 Effect of adding secondary mirror (case 1)

The aim of case 1 is to investigate the effect of adding a secondary mirror to the primary collector. The experiment was conducted by comparing the modified design (Cs) with the other primary collector (Cp) during the tracking stage (Figure 4.4).

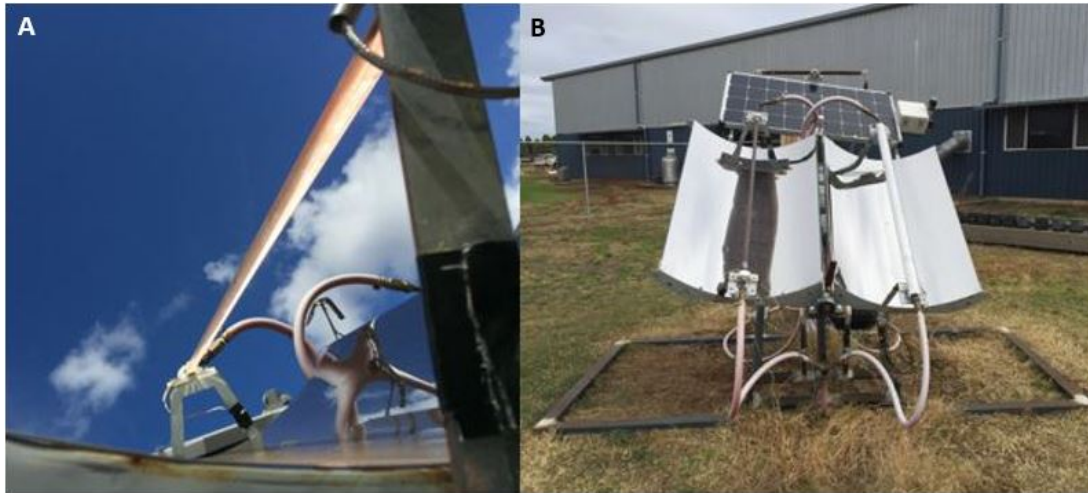


*Figure 4.4: Experimental setup of case 1 for the tracking stage and case 3 for the fixed stage. A is the concentrating solar radiation on the absorber tube of the primary collector. B is the structure of Cp (on the left) and Cs (on the right).*

#### 4.5.1.1 Wind speed and solar radiation of the outdoor experimental tests

Because PTSC performance can be highly sensitive to weather conditions, wind speed and solar radiation data for the experimental heating system tests are presented first.

Two tests were conducted in the same week. From Figure 4.5 it can be seen that the wind velocity during the first test had fluctuations between 2 m/s and 6 m/s and the average wind speed slightly increased between 9 am and 11 am and then remained relatively constant. In addition, during the second test, using the same system operating parameters as before, the wind velocity was fluctuating between 0.5 and 5.5 m/s and the average slightly increased throughout the day from just below 2 m/s to almost 4 m/s. From this figure, it can be seen that the wind velocity fluctuation during both tests and its average value during the first test was higher than during the second test by approximately 2 m/s before midday, with the difference between the wind speeds decreased to around 0.5 m/s at the finish. In both cases, large vibrations in the apparatus were observed when there was significant wind.

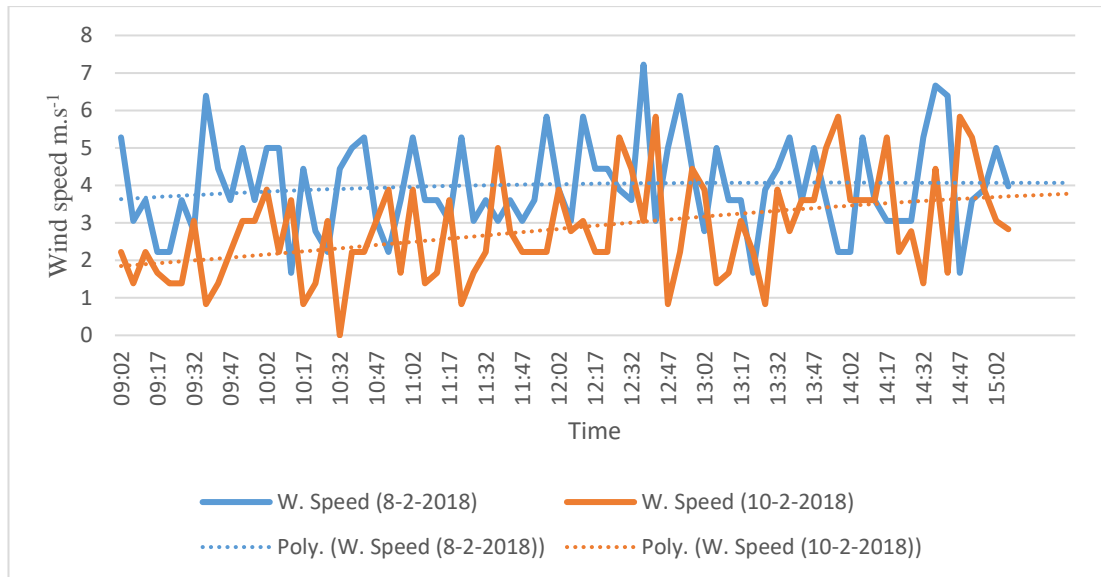


*Figure 4.5: Variation of wind velocities during first and second tracking tests of Cs and Cp during case 1. The third-order polynomial lines are the general trends of the variations during the day*

Figure 4.6 shows the solar radiation striking the Cs and Cp during the tests of case 1. It can be seen that the solar radiation during the first test fluctuated between  $150 \text{ W.m}^{-2}$  and  $1300 \text{ W.m}^{-2}$  because the sky was partly cloudy during the tests. When a cloud passed over the collector a system tracking error occurred because partly cloudy weather makes the PTSC tracking system search for a bright spot (PTSC tracking system operates based on solar sensors linked to the collector actuator motor), which may not be in the direction of the sun. During the second test, the solar radiation fluctuated between  $1000$  and  $1150 \text{ W.m}^{-2}$  and it sharply decreased between  $9.47$  am and  $10.02$  am to be  $300 \text{ W.m}^{-2}$ . This demonstrated that the weather was almost clear during the second test with minimal clouds during that period.

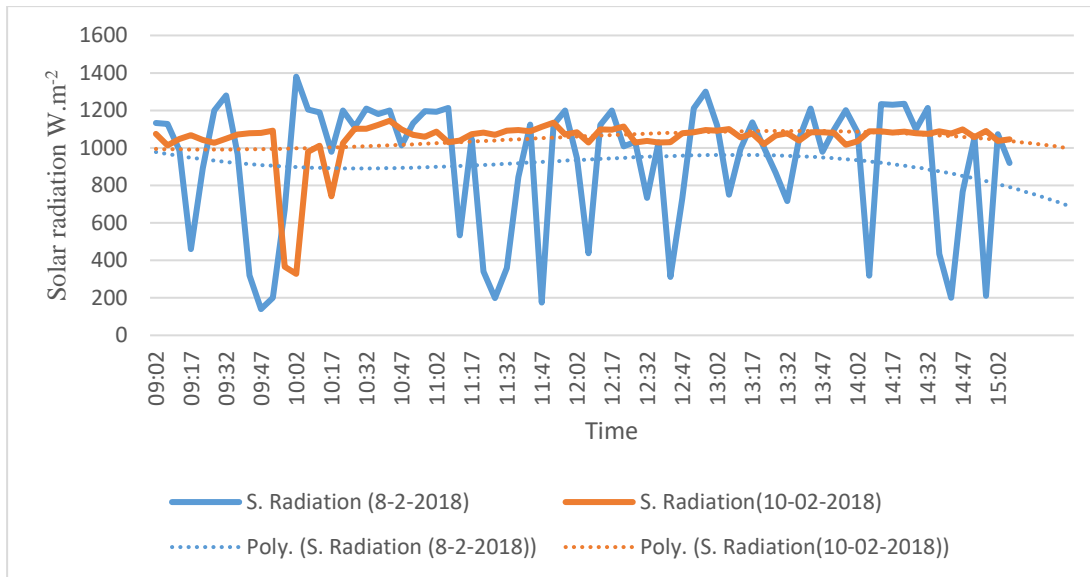
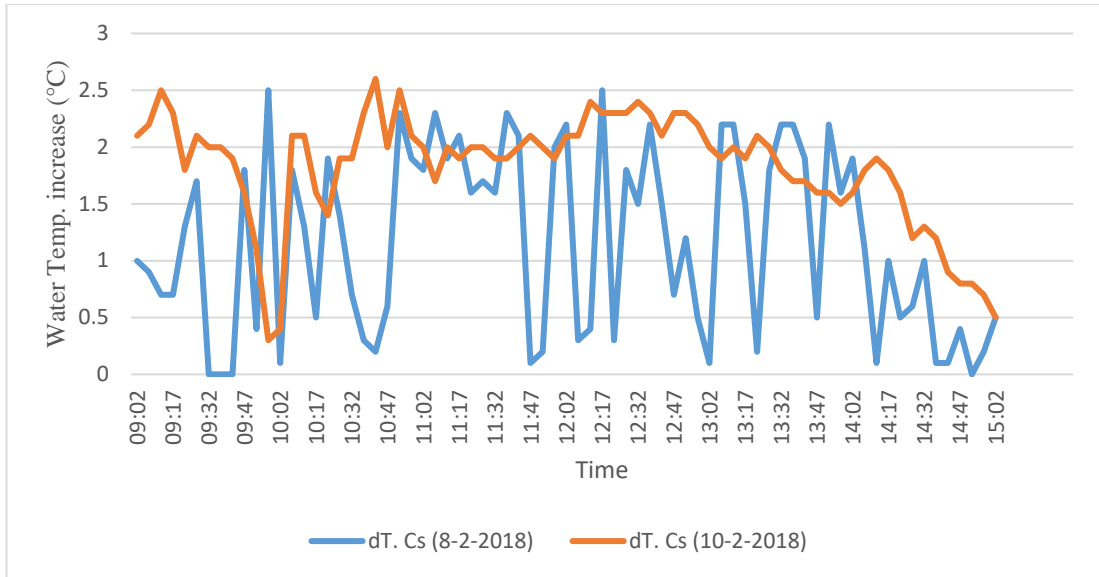


Figure 4.6: Measured data of solar radiation during first and second tracking tests of  $C_s$  and  $C_p$  of case 1. The third-order polynomial lines are the general trends of the variations during the day

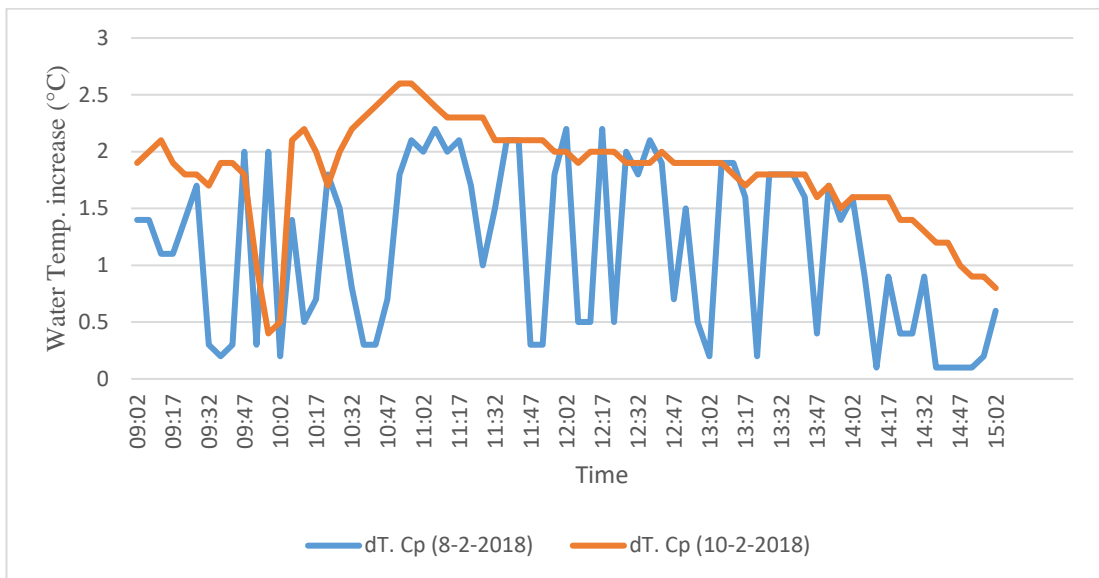
#### 4.5.1.2 Water temperature increase

HTF temperature difference is an essential parameter of solar collector performance in addition to the solar radiation. Changes in HTF temperatures give information about the profile of collector performance. Hence, in this section the  $C_s$  and  $C_p$  HTF temperatures are illustrated.

Figure 4.7 displays the increase in HTF temperatures from the inlet to the outlet during the first and second tests of case 1. It can be observed that the HTF temperature increase for both configurations fluctuated more during the first test due to the partly cloudy weather. During the second test, the HTF temperature difference was relatively constant from start time until the finish, except the period between 9.32 am and 10.02 am due to some large clouds passing over.



(A)



(B)

Figure 4.7: Water temperature increase from the inlet to the outlet of Cs (A) and Cp (B) during tracking tests of case 1.

### 4.5.1.3 Efficiency of modified collector (Cs) and primary collector (Cp)

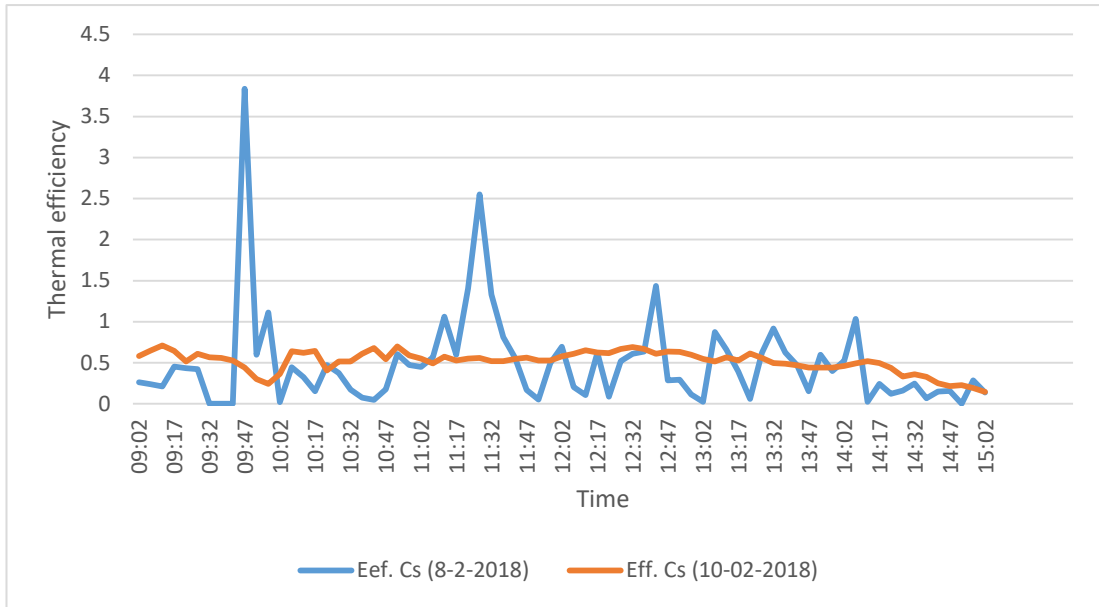
The performances of Cs and Cp for the above weather conditions are illustrated here.

Figure 4.8 illustrates Cs and Cp efficiency during the first and second tests of case 1 of the tracking stage. During the first test, it can be seen that the average of the

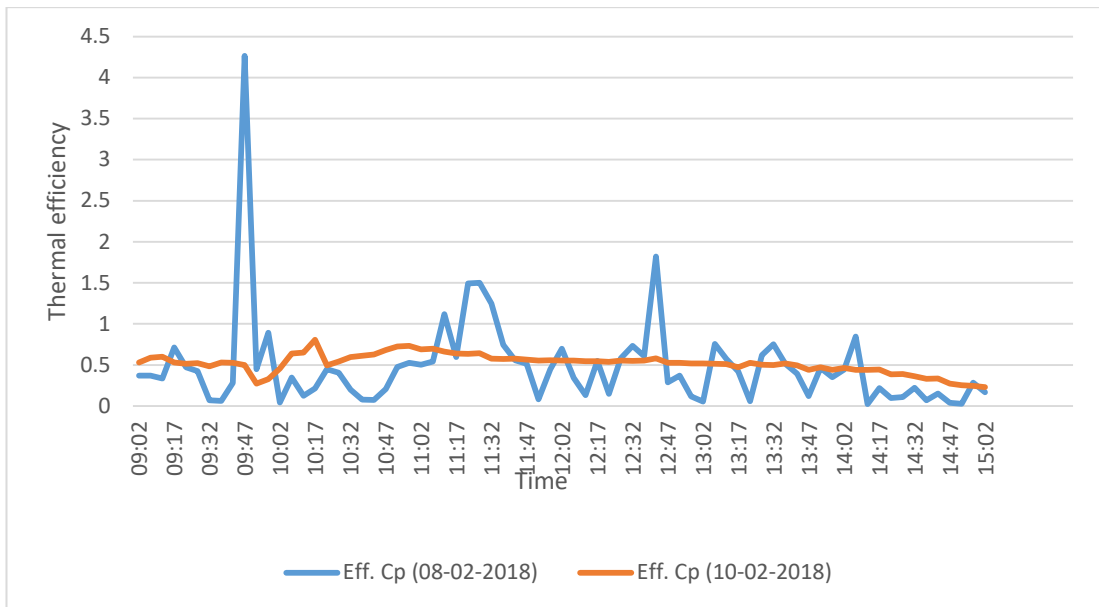
efficiency of both collectors was approximately 0.5 all morning and then reduced to zero during the afternoon. It can be seen that the average value of efficiency for both collectors was maximum at midday, while it was lower at the beginning and at the end. That could be due to the orientation of the collector aperture area and the effect of the wind load. As mentioned before, the optical error increased due to increased wind load. This occurred before and after midday when the collector's orientation caused the collector to present a larger area to the wind. The minimum wind effect was at midday when the collector aperture area presented the smallest profile to the wind. This phenomenon also noticed in other studies (Naeeni & Yaghoubi 2007b), that presented in section 2.2.1.6.

Considering the second test, it can be observed that the collectors' performance also slightly fluctuated between 9 am and 10 am due to partly cloudy weather. This is because the electric motor searches for the brightest spot, which is not necessarily the direction of the sun— which produced system tracking errors, as observed in section 2.2.1.5. When the weather is clear, the tracking error is constant. Therefore the average value of the collectors' performance was maintained at a relatively constant value. In general, the average value of the collectors' efficiency was also lower at the start and at the end of the tests, as in the first test. The reduction in the efficiency could be due to the increased wind velocity and also because of the orientation of the collector during that period, facing the wind direction. Consequently, during both tests, it was found that the wind load, especially before and after midday, led to vibration in the structure of the collectors (Naeeni & Yaghoubi 2007b), and therefore it resulted in increased deviation of the reflected solar rays, which reduced the collectors' performance.

Furthermore, During both tests it was noticed that there are some points of the  $C_s$  and  $C_p$  performances that reached more than 100%. That is because of thermal lag in the absorber tube. Indeed, clouds dropped the values of the solar radiation suddenly at those points and at the same period the fluid was still absorbing some heat from the hot absorber tube wall. Based on the overall thermal efficiency (Eq. (2) section 4.4), the reducing ratio of the solar radiation value is higher than the reducing ratio of HTF temperatures difference, which resulted in reaching the collector efficiency more than 100% at that experimental point.



(A)



(B)

Figure 4.8: Experimental performance of Cs (A) and Cp (B) during first and second tracking tests of case 1.

#### **4.5.1.4 Performance comparison of modified collector (Cs) and primary collector (Cp)**

Figure 4.9 displays the average of the first and second tests and the corresponding curve fits. It can be seen that the average efficiency of both collectors is relatively equal. This is despite the Cp operating with whole collector aperture area ( $0.84 \text{ m}^2$ ), while Cs aperture area was blocked by SPM area ( $0.072 \text{ m}^2$ ). This indicated that the performance of Cs is improved due to the SPM because it operated with less reflecting aperture area, but has relatively similar Cp efficiency. In addition, for most of the afternoon it can be observed that the Cs performance is higher than the Cp performance. Finally, the overall average efficiency of Cs and Cp during the tests of case 1 was  $44.94\% \pm 0.04\%$  and  $44.55\% \pm 0.04\%$  respectively, and therefore Cp efficiency equals 99% of the Cs efficiency.

In the current design, the SPM blocked around 8.5% of the primary collector aperture area (the width of the SPM in the current design equals 0.06 m, and the collector aperture width equals 0.7 m, and therefore the ratio of the SPM blocking area is 8.5% of the primary collector aperture area), which influenced the amount of the incident direct solar radiation on the primary collector.

For larger PTSC systems (commercial PTSC system) where its CR could reach up to 30, the influence of the secondary reflector's blocking area in the PTSC commercial size can be neglected. This is because the ratio of the SPM blocking area in the commercial collectors will be very small (approximately 1%) compared to the collector aperture area. This is because the width of the SPM in the conventional system will be not more than 0.119 m, because the inner diameter of the conventional receiver glass envelope is not more than 0.119 m (the SPM placed on inner surface of the upper part receiver tube glass envelope, thus the SPM width equals the area of the inner surface of the upper part of the conventional receiver glass envelope). Moreover, the collector aperture width reaches up to approximately 6.5 m.

Therefore, for the big CR (as in commercial collectors), it a substantial difference in using the secondary reflector is anticipated. This is because the secondary reflector will have a smaller effect on the primary collector aperture area and the primary collector will still have a high solar concentration, and it also means that the high

potential energy that misses the receiver tube can be collected by the secondary reflector.

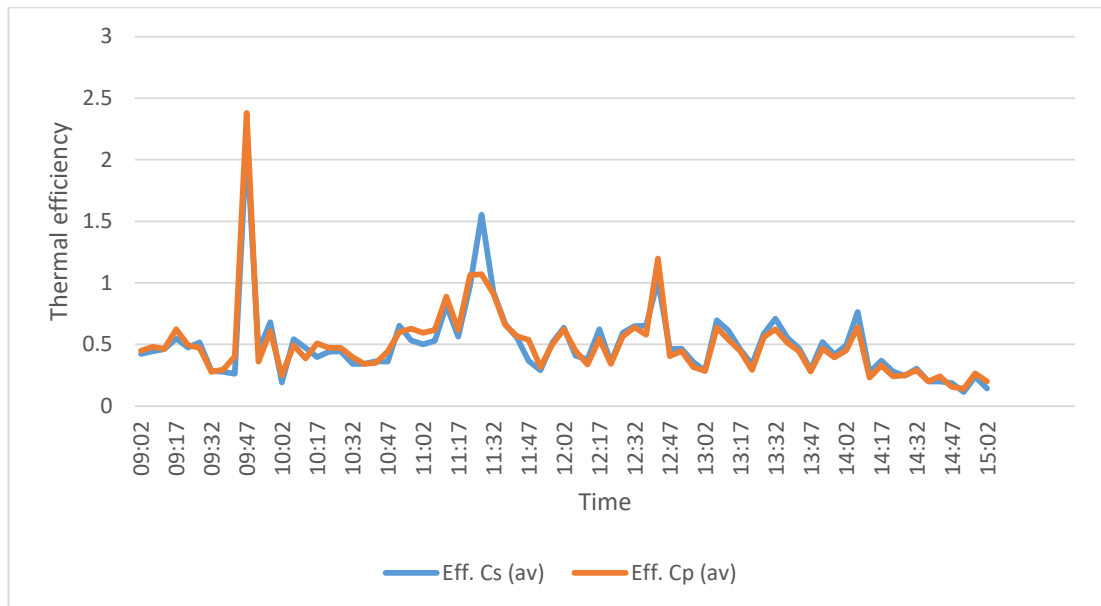


Figure 4.9: Overall average efficiency data of the two days of the Cs and Cp during tracking tests of case 1.

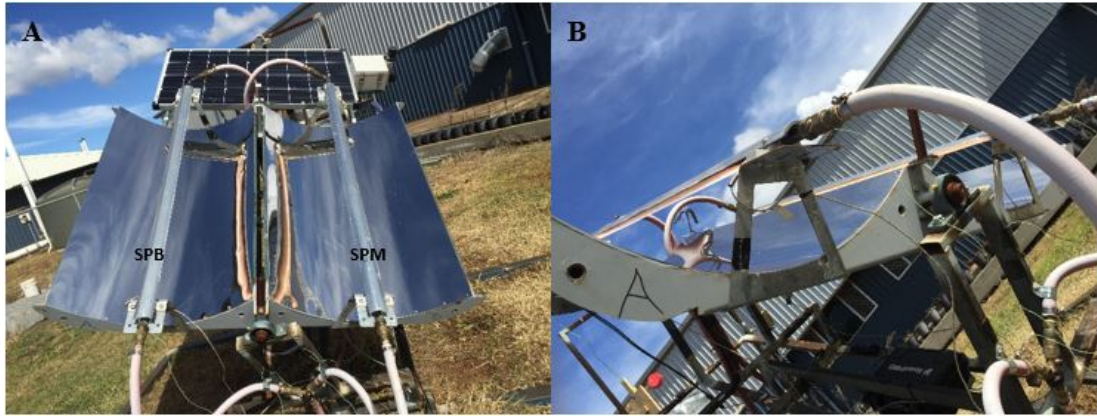
Table 4.1 displays the Cs and Cp gained energy during other tracking experimental tests of case 1. The table also presents the ratio of the Cp energy gained and the Cs energy gained. It can be seen that most of the Cs energy gained was relatively higher than the Cp energy gained. This is due to the optical enhancement of the SPM geometry on Cs performance.

Table 4.1: Daily gained energy for the Cs and Cp configurations during 20 days of experimental tests (Case 1). The Ratio is the ratio of Cp to Cs.

<b>No</b>	<b>Test date</b>	<b>Cs Energy gained (MJ)</b>	<b>Cp Energy gained (MJ)</b>	<b>Ratio (%)</b>
1	8-2-2018	6.38	6.28	98.4
2	10-2-2018	10.02	9.99	99.7
3	18-3-2018	5.79	4.66	80.4
4	19-3-2018	7.01	6.25	89.1
5	22-4-2018	7.67	7.42	96.7
6	23-4-2018	10.54	9.42	89.3
7	24-4-2018	8.08	7.78	96.2
8	25-4-2018	7.95	6.49	81.6
9	26-4-2018	11.72	10.71	91.3
10	27-4-2018	8.5	7.91	93.0
11	24-5-2018	7.08	6.73	95.0
12	25-5-2018	4.20	3.40	80.9
13	19-7-2018	10.21	9.87	96.6
14	20-7-2018	1.96	0.85	43.3
15	21-7-2018	11.51	10.6	92.0
16	22-7-2018	11.97	11.01	91.9
17	23-7-2018	10.64	10.12	95.1
18	24-7-2018	11.83	9.51	80.3
19	25-7-2018	11.66	9.78	83.8
20	26-7-2018	10.74	8.68	80.8

#### 4.5.2 Effect of adding secondary mirror (Case 2)

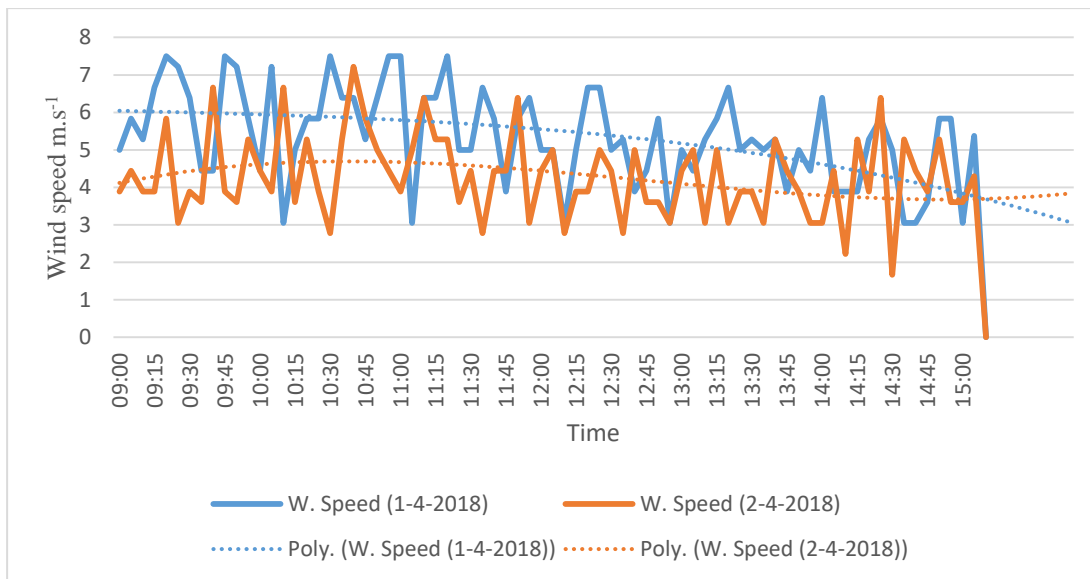
The aim of case 2 is also to investigate the effect of adding a secondary mirror (SPM) to the primary collector during the tracking stage. In this tracking case the investigation is done by comparing the performance of the Cs with the performance of the Cb, as shown in Figure 4.3 and Figure 4.10. The structure of the Cb consists of a primary collector with a secondary parabola painted black (SPB). As mentioned before (section 4.3), this structure assists to clearly show the effect of the secondary reflector (SPM) on the Cs. This is because both primary collectors lost the same reflection area (both are receiving the same amount of solar radiation) and the wind load distribution on each absorber tube is same for both collectors because both the SPM and the SPB have the same shape.



*Figure 4.10: Experimental setup of case 2 for the tracking stage and case 4 for the fixed stage. SPM is the secondary parabola with mirror sheet; SPB is the secondary parabola painted black. A is the structure of the Cb and CS; B is the concentrating solar radiation on the absorber tube of the collectors.*

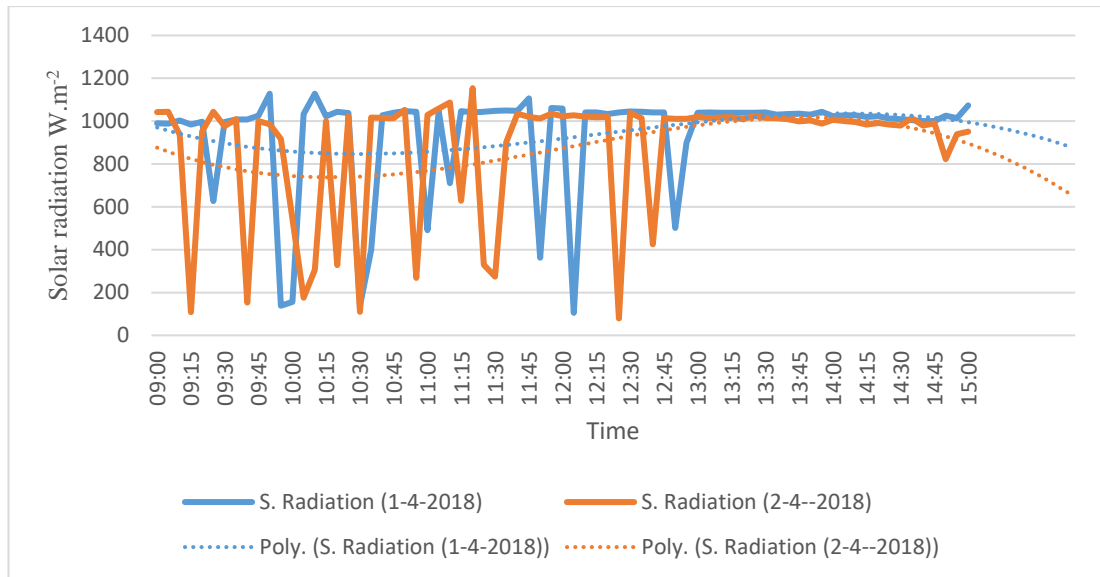
#### **4.5.2.1 Wind speed and solar radiation of the outdoor experimental tests**

Figure 4.11 shows the variation of wind velocity during the experimental tests of case 2. During the first test, the wind velocity fluctuated between 3 m/s and 7.5 m/s and the average velocity was around 5.3 m/s. Also it is clear that the wind speed at the beginning of the test was relatively higher than at the finish. During the second test on the following day, using the same system operating parameters as before, the wind velocity fluctuated between approximately 2.5 m/s and 6.5 m/s during the test period and the average wind velocity was approximately 4.2 m/s. It can be seen that the wind velocity was changing during both tests and the wind speed was higher during the first test than during the second test.



*Figure 4.11 Variation of wind velocities during first and second tracking tests of Cs and Cb during case 2. The third-order polynomial lines are the general trends of the variations during the day*

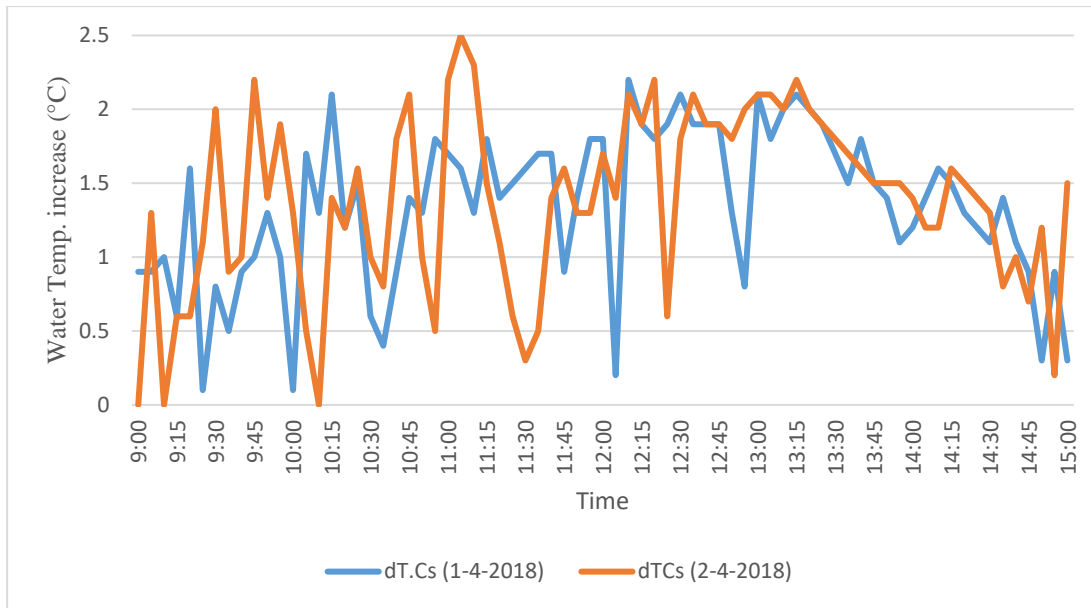
Figure 4.12 presents the solar radiation hitting the Cs and Cb during the experimental tests of case 2. It can be seen that the solar radiation during the first test fluctuated between approximately 100 W/m<sup>2</sup> and 1050 W/m<sup>2</sup> from 9 am until 1 pm due to partly cloudy weather. After 1 pm, the sky became clear and therefore the solar radiation maintained a relatively constant value of around 1050 W/m<sup>2</sup> from 1 pm until finishing at 3 pm. During the second test on the following day, the solar radiation was similar, with similar levels of solar radiation varied over the same period and then kept relatively constant during the same period of the afternoon. However, the solar radiation during the first test was slightly higher than during the second test on average, due to fewer variations in the morning.



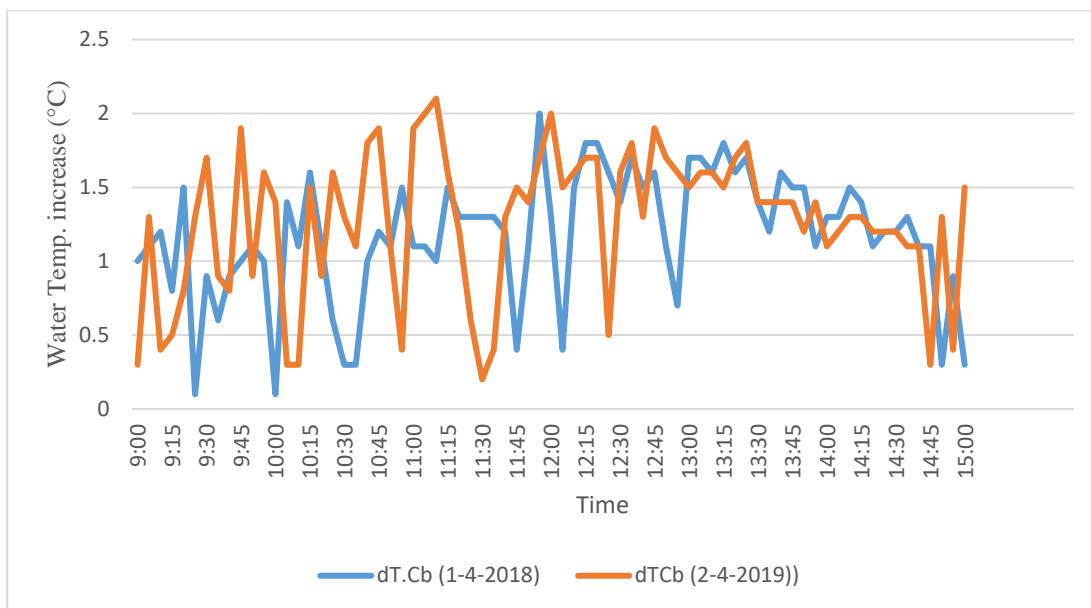
*Figure 4.12: Measured data of solar radiation during first and second tracking tests of Cs and CP of case 2. The third-order polynomial lines are the general trends of the variations during the day*

#### **4.5.2.2 Water temperature increase**

Figure 4.13 shows the values of the HTF temperature increase from the inlet to the outlet of the Cs & Cb during the first and second tracking tests of case 2. It can be seen that temperature increase fluctuated in both collectors, especially between 9 am and 1 pm due to partly cloudy weather and windy conditions during the tests. This resulted in reduced amounts of solar radiation received by the absorber tubes and reduced temperature increase. There was less variation between 1 pm and 2 pm because of the clear sky. The temperature increase was higher as a result.



(A)



(B)

Figure 4.13 Water temperature increase from the inlet to the outlet of Cs (A) and Cb (B) during tracking tests of case 2.

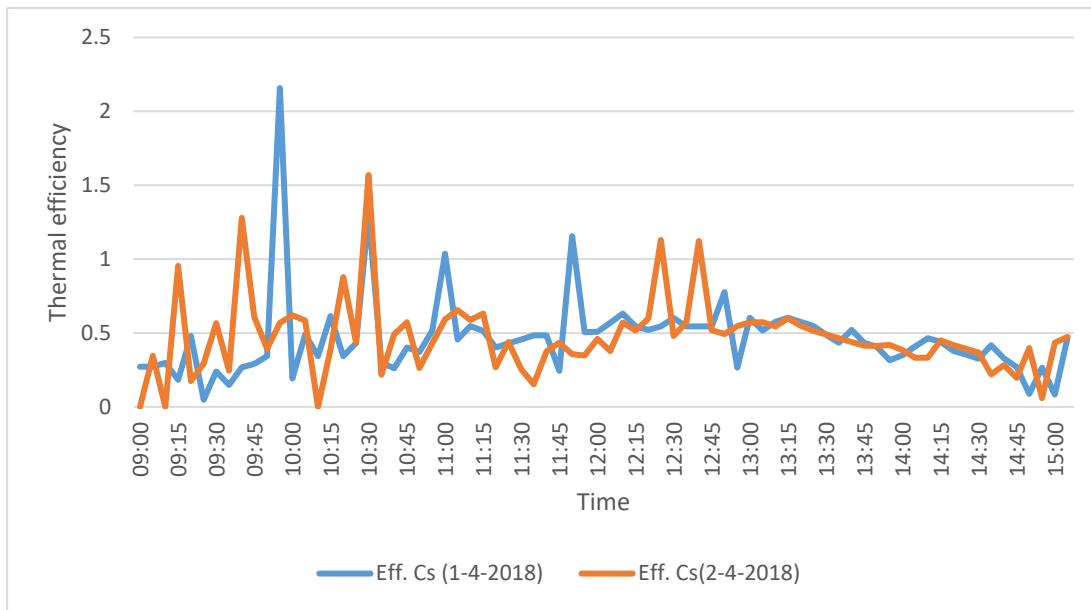
#### 4.5.2.3 Efficiency of modified collector (Cs) and primary collector with SPB (Cb)

In this section, the performance of Cs will be presented. Figure 4.14 presents the experimental efficiency of both collectors during the tracking stage of case 2. It is clear that the Cs efficiency [Figure 4.14 (A)] fluctuated significantly between 9 am and 1 pm

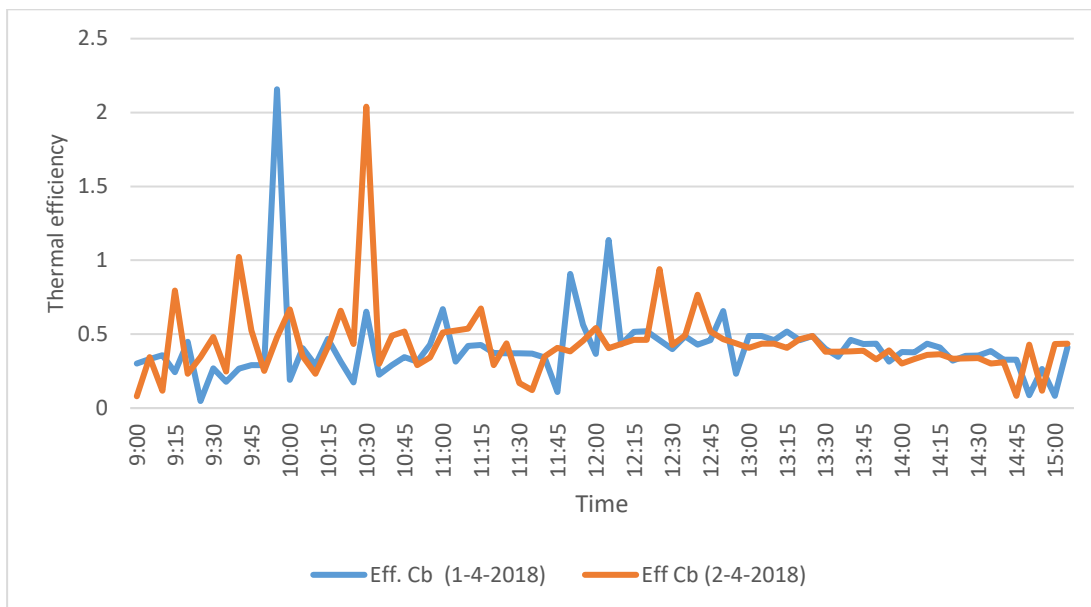
due to partly cloudy weather during that period, and fluctuation was lower from 1 pm until the end of the test because of the clear weather during that period. Moreover, during both tests it was noticed that there are some points of the Cs and Cb performances also reached more than 100%. As it mentioned in section 4.5.1.3, this occurs due to the receiver tube's thermal lag. In addition, during the period between 9 am and 12 noon, it can be seen that there is a clear difference between the average performances of the Cs during both tests. That was due to the effect of wind velocity, which was higher during the first test than during the second test, which led to vibration of the collector structure and led to deviating reflected solar radiation, this effect of wind change was also observed in other studies that are presented in section 2.2.1.6 (Hachicha et al. 2014; Mier-Torrecilla et al. 2014; Paetzold et al. 2014; Paetzold et al. 2015; Paetzold et al. 2016). Therefore, the daily average efficiency of the Cs was approximately  $42.6\% \pm 0.03\%$  due to it being windier and cloudier during the first test, while during the second test it reached around  $43.19\% \pm 0.03\%$ . It can be noticed that the Cs efficiency reduced by about 1%, which is because of the effect of SPM that helps to reduce the effect of collector vibration, due to wind load, by reflecting the deviated solar rays back towards the collector absorber.

In Figure 4.14 (B) the performance of the Cb during the same time periods from 9 am to 3 pm is illustrated. From this figure it can be seen that the shapes of the Cb efficiency curves are similar to the shapes of the Cs efficiency curves because both tests had the same weather conditions. However, the daily average efficiency of the Cb was approximately  $37.35\% \pm 0.03\%$  and  $39.68\% \pm 0.03\%$  during the first and second tests respectively, which is less than the Cs performance. This is because of the optical losses due to wind speed fluctuations.

By focusing on the first test (windy test), a clear difference of 5% can be seen between the Cs and Cb efficiencies, which is due to the deviation of the reflected solar radiation because of wind fluctuation (section 2.2.1.6). During the second test, the difference between the Cs and Cb is roughly the same as in the first test. This is because the partly cloudy weather increased the tracking errors (during the searching for the brightest spot). The above differences (during windy and partly cloudy weather) illustrate the positive influence of the secondary mirror on the solar collector which works effectively, under those weather conditions, by reflecting the deviated solar radiation onto the absorber tube.



(A)



(B)

Figure 4.14: Experimental performance of Cs (A) and Cb (B) during first and second tracking tests of case 2.

#### 4.5.2.4 Performance comparing of the modified collector (Cs) and the primary collectors with SPB (Cb)

In this section, Cs and Cb efficiency and energy gained is compared and presented in order to show the influences of SPM on PTSC performance.

Figure 4.15 shows the overall average efficiency from the two days of the Cb and Cs tests during case 2. The efficiency value for each collector was lower at the start and finish. One of the main causes for that is the operation errors that result due to wind load on the collector aperture area. It reached maximum load especially earlier than 11 am and later than 1 pm, because the collector's orientation caused the collector to present a larger area while the wind load decreased at noon (Naeeni & Yaghoubi 2007b). Through comparing both curves, it can be easily seen that there is a clear difference between the overall average performances of Cs and Cb. Based on the efficiency calculations, it was found that the overall average value of Cs efficiency reached approximately  $42.92\% \pm 0.03\%$ , while the overall average value of Cb efficiency only reached around  $38.52\% \pm 0.03\%$ —which is equal to 89% of the Cs efficiency. This is because of the influence of SPM on Cs performance by reflecting the concentrated solar radiation which was deviated from the absorber tube due to weather conditions during the first and second tests.

During windy days, the wind load led to a vibration of the collector structure, which led to a deviation of the reflected solar radiation from hitting the absorber tube (as observed in section 2.2.1.6). In addition, during partly cloudy weather there is also an increase in the number of reflected solar rays which are deviated. This is due to increasing electrical motor steps searching for brighter spots, leading to increased tracking errors (as observed in section 2.2.1.5). Tracking error influence on collector performance could be doubled during windy and cloudy conditions. Therefore, under these weather and operating conditions, the secondary parabola with mirror film (SPM) reversed the deviation of some of the reflected solar radiation. This increased the solar flux around the absorber tube and, as a result, its improved the heating process in the solar system.

The efficiency improvement of the Cs collector is relatively low (5%) compared to the Cb under windy and partly cloudy weather because of the experiment's small geometry, which limits the collector aperture area (width and length of the collector). The aperture area of the experimental model is  $0.84 \text{ m}^2$  (aperture width of the experimental model is 0.7 m and the length 1.2 m, while the aperture area for the PTSC row in solar thermal plant is approximately  $900 \text{ m}^2$  (aperture width for the solar thermal plant PTSC is approximately 6 m and the length 150 m) (Fernández-García et al. 2010). This means the effect of wind load (collector vibration) in the PTSC solar

plant and commercial collector is much higher than that in the current experimental model. Therefore, employing this technology (SPM) for the PTSC of the solar thermal plants at sites that have relatively high wind velocity, will notably improve the solar plant performance. This would make viable those sites which have sufficient average solar radiation (at least 2000 kWh/m<sup>2</sup>/year) (Trieb et al. 2009), but the wind velocity is too high for conventional PTSC solar thermal plants. Therefore, utilising this technology (SPM) can assist in attracting solar thermal investments for constructing PTSC solar plants at windy sites.

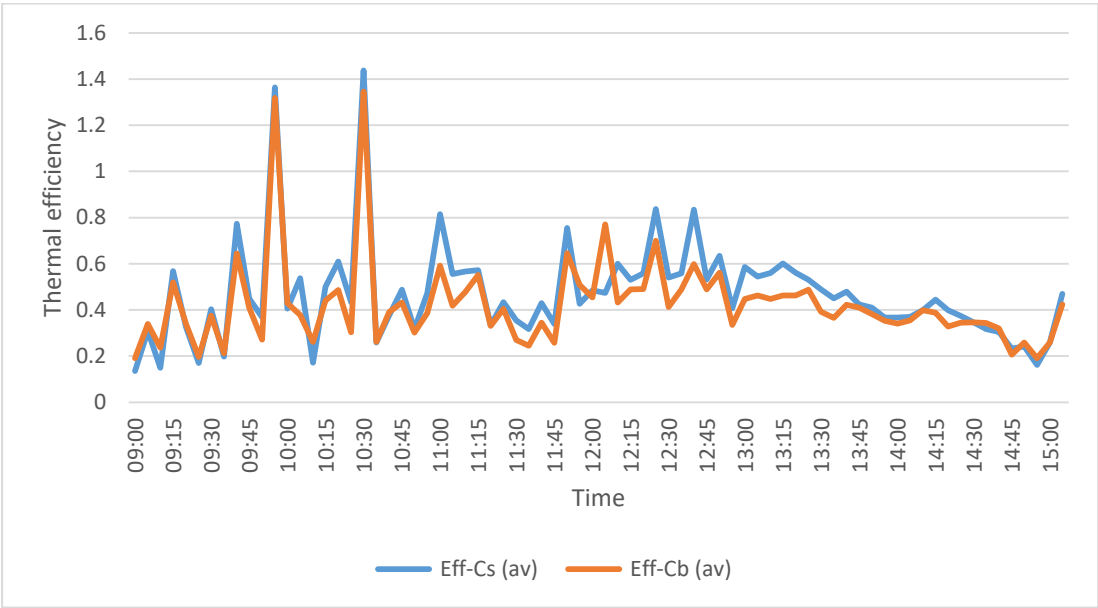


Figure 4.15: Overall average efficiency data of the two days of the Cs and Cb during tracking tests of case 2.

Table 4.2 illustrates the amount of gained energy for Cs and Cb during the experimental tests of case 2. It also presents the ratio of the energy gained by Cb to the energy gained by Cs. It is clear that the energy of Cs that was gained during the first and second tests were higher than the average energy of Cb. This is due to the influence of SPM on Cs performance.

Table 4.2 Daily gained energy for the Cs and Cb configurations during 20 days of experimental tests (Case 2). The Ratio is the ratio of Cb to Cs.

<i>No</i>	<i>Test date</i>	<i>Cs Energy gained (MJ)</i>	<i>Cb Energy gained (MJ)</i>	<i>Ratio (%)</i>
1	12-3-2018	4.74	3.38	71.3
2	1-4-2018	7.38	6.46	87.5
3	2-4-2018	7.6	6.98	91.8
4	12-4-2018	6.59	4.92	74.6
5	13-4-2018	8.42	8.01	95.1
6	8-6-2018	3.28	2.58	78.6
7	9-6-2018	4.24	3.68	86.7
8	10-6-2018	8.83	8.30	93.9
9	24-8-2018	5.79	4.75	82.0
10	25-8-2018	5.93	5.22	88.0
11	27-8-2018	9.73	7.80	80.1
12	28-8-2018	9.45	8.61	91.1
13	29-8-2018	10.17	9.12	89.6
14	31-8-2018	9.54	9.05	94.8
15	1-9-2018	8.66	6.78	78.2
16	3-9-2018	7.73	7.16	92.6
17	4-9-2018	5.06	4.04	79.8
18	5-9-2018	4.4	3.49	79.3
19	7-9-2018	8.23	7.85	95.3
20	12-9-2018	10.09	9.32	92.3

#### 4.6 Results of fixed stage

The experimental results of cases 1 and 2 of the tracking stage (section 4.5) presented the effect of the wind speed fluctuation on collector performance. It has been found that the wind velocity fluctuation has a major influence on PTSC optical performance that leads to vibrations of the collector structure and, therefore, it results in reduced thermal efficiency (as noticed in section 4.5). There are sites that have annual average direct normal solar irradiation of more than 2000 kWh/m<sup>2</sup>/year, which is suitable to construct PTSC technology (Trieb et al. 2009), but they experience high wind velocity during many periods of the year. Therefore, it could be useful to use the PTSC technology with the SPM in the fixed state instead of the tracking state. Figure 4.16

shows the orientation of the PTSC for fixed setup during the seasons of a year. The length of the parabola solar collector is aligned parallel with the east-west direction and the collector aperture area is oriented based on a site latitude angle (as done for the PV solar panel setup). The sun's path throughout the day will be across the collector length during the equinox period. The only optical losses at that particular season are collector end losses, which could be neglected for long collectors. The maximum deviation of reflected solar radiation will be during the summer and winter seasons, due to the solar radiation falling obliquely on the solar collector. Using the SPM technology can reduce the effect of the deviated solar radiation in addition to reducing the wind effect around the collector receiver tube, which results in improving the optical and thermal performances of the PTSC.

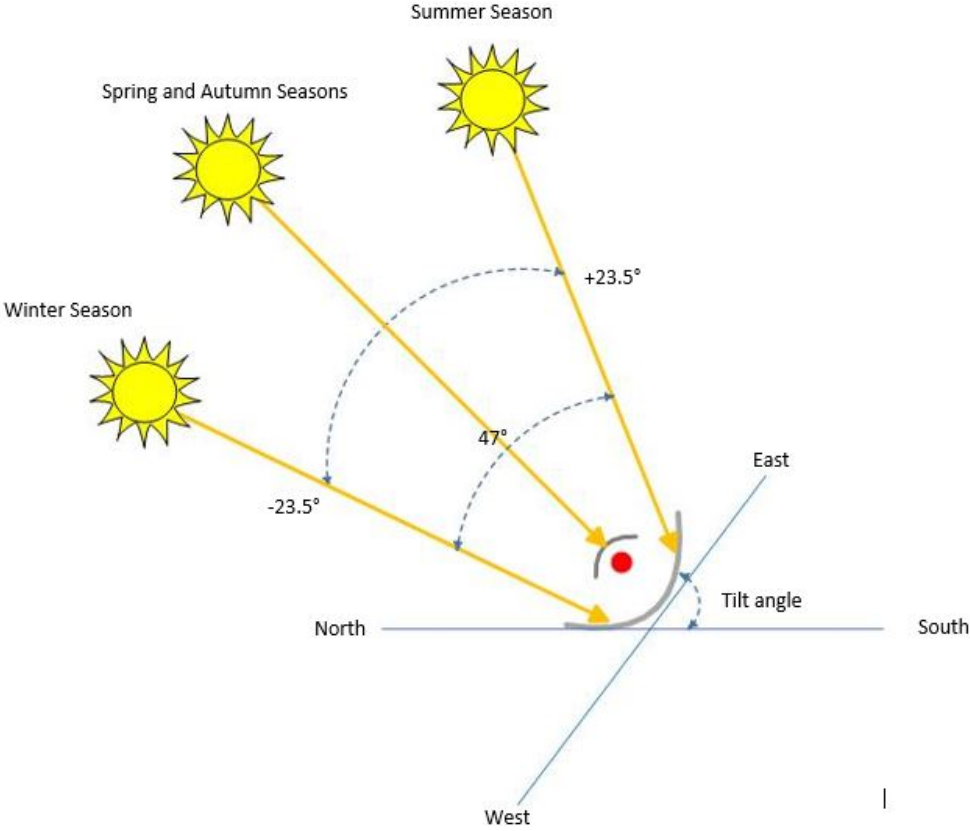


Figure 4.16: PTSC orientation during the year for the fixed operation.

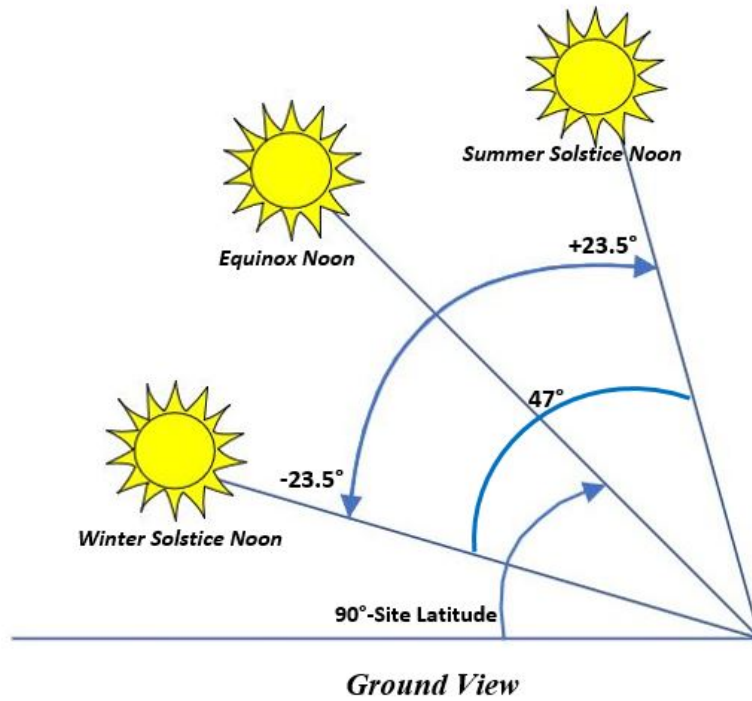
Employing this setup (fixed PTSC) at windy sites can lead to several important improvements. In terms of structural stability, the drag force caused by the wind will be much lower in the fixed case and therefore it will be more stable than the tracking

structure because it is mounted directly to the ground via a fixed structure, while the tracking structure is mounted on the actuator motor. In terms of solar radiation loss, the PTSC in the fixed structure will lose some of the normal incident solar radiation due to the SPM aperture area, but it will gain more solar radiation because of the reflection of the SPM and also because it is more stable than the tracking system at windy sites. In terms of the financial aspect, this structure is simple and less complicated compared to the PTSC with a tracking system, which requires a complicated tracking system and additional structural support from the PTSC to the actuator motor and then to the ground. Therefore, it could be very convenient to use the PTSC technology with the SPM in the fixed state instead of the tracking state at windy sites.

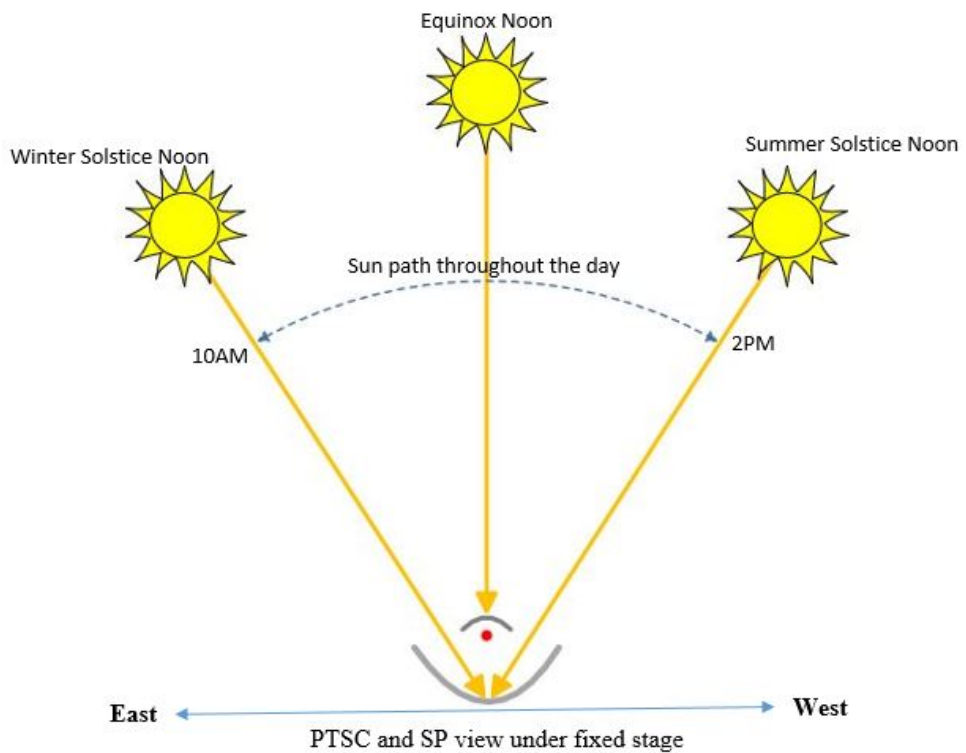
In this section, the experimental tests of the fixed stage (cases 3 and 4) are presented. This unique PTSC testing method simulates the sun's path throughout the seasonal solstice noon angles by orienting the collectors to align with the sun's noon position on the day of the test and disabling the tracking mechanism throughout the test. To ensure the orientation was correct, the tracking mechanism was used the day prior to the test to align the collectors at noon; the tracking mechanism was then disabled. Figure 4.17 (A) represents the seasonal noon angles for a site which varied between approximately  $-23.5^\circ$  and  $+23.5^\circ$ . Figure 4.17 (B) represents the daily fixed orientation of the PTSC during the whole tests of the fixed stage. It also shows the range of the incident sunlight angles during the day. One hour of the test in the fixed stage is equivalent to a  $15^\circ$  change in the seasonal sun path and therefore the total hours of the experimental tests should be 3.13 hours (which is equivalent to  $47^\circ$  seasonal sun solstice noon angles). The period from 10 am to 2 pm is slightly outside what is actually required, but illustrates what really happened. During the fixed tests, the vertical direction (midday) simulated the equinox noon sun position, 10 am represented winter solstice noon, while 2 pm simulated summer solstice noon.

For the current experimental setup, the deviation of the reflected sunlight for a fixed structure (equivalent to a large tracking error) will be larger during the morning (winter solstice noon) and afternoon (summer solstice noon) since it will not be directly oriented towards the sun, but this can be compensated for by the SPM. The accuracy of collector orientation to the sun noon angle throughout the day during fixed tests to accurately simulate the equinox noon orientation is achieved by adjusting the seasonal

tracker. The accuracy of the orientation was checked by the collector alignment indicator.



(A)



(B)

Figure 4.17: Seasonal noon sun angles for a site and the orientation of the PTSC during the fixed stage. A is ground view of seasonal noon angle when installed in practice. B is the fixed orientation of the PTSC during the experimental tests of cases 3 and 4 for the fixed stage.

### 4.6.1 Effect of adding secondary mirror (case 3)

The aim of case 3 is to investigate the effect of adding a secondary mirror to the primary collector (Cs) during the fixed stage. This is done by comparing the performance of the modified design (Cs) with the performance of the primary collector (Cp). Figure 4.2 and Figure 4.4 show the configuration of the collectors for this case.

#### 4.6.1.1 Wind speed and solar radiation of the outdoor conditions

Figure 4.18 shows the wind velocity during the first test and also during the second test of case 3. It can be observed that the wind velocity fluctuated during both tests. During the first test, the wind speed fluctuated between approximately 0 m/s and 4 m/s and the average speed during the test was 1.76 m/s. During the second test, it can be seen that the wind velocity fluctuated between approximately 3 m/s and 7 m/s and the average value of the wind velocity was approximately 4.98 m/s, which is significantly higher than during first test.

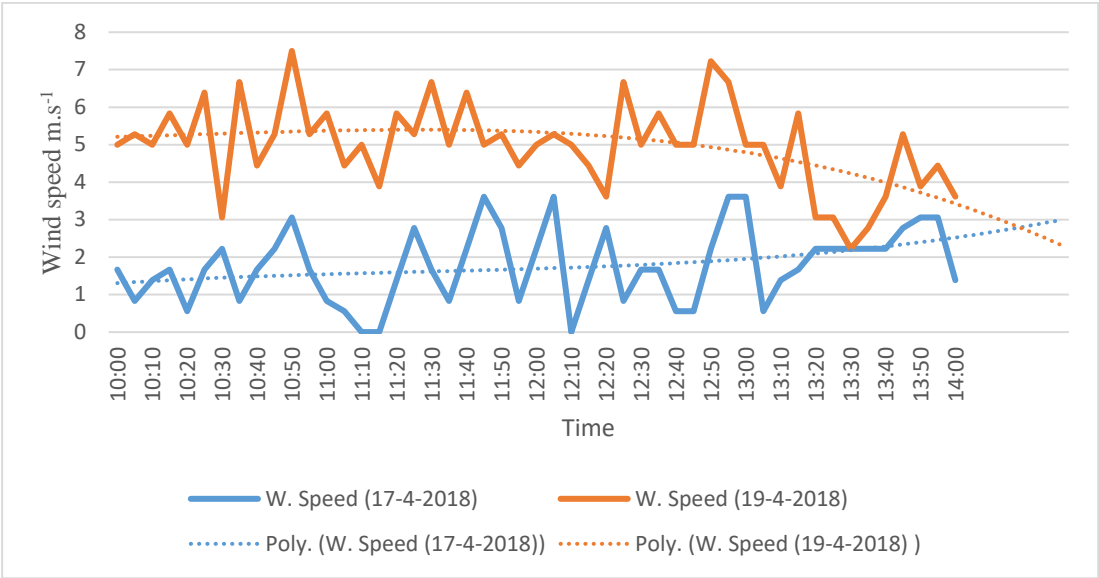


Figure 4.18: Variation of wind velocities during first and second fixed tests of Cs and CP of case 3. The third-order polynomial lines are the general trends of the variations during the day.

Figure 4.19 displays insolation that hit the collectors during the first and second tests of case 3. It can be seen that the solar radiation was slightly lower at the beginning and at the end, and reached up to 800 W/m<sup>2</sup> at midday. The weather was relatively clear during the first test, but there were some cloudy spells during the second test, as evidenced by brief falls in the insolation. The average solar radiation during the first

day was higher than in the second day:  $756.7 \text{ W/m}^2$  and  $700.1 \text{ W/m}^2$  for the first and second tests respectively.

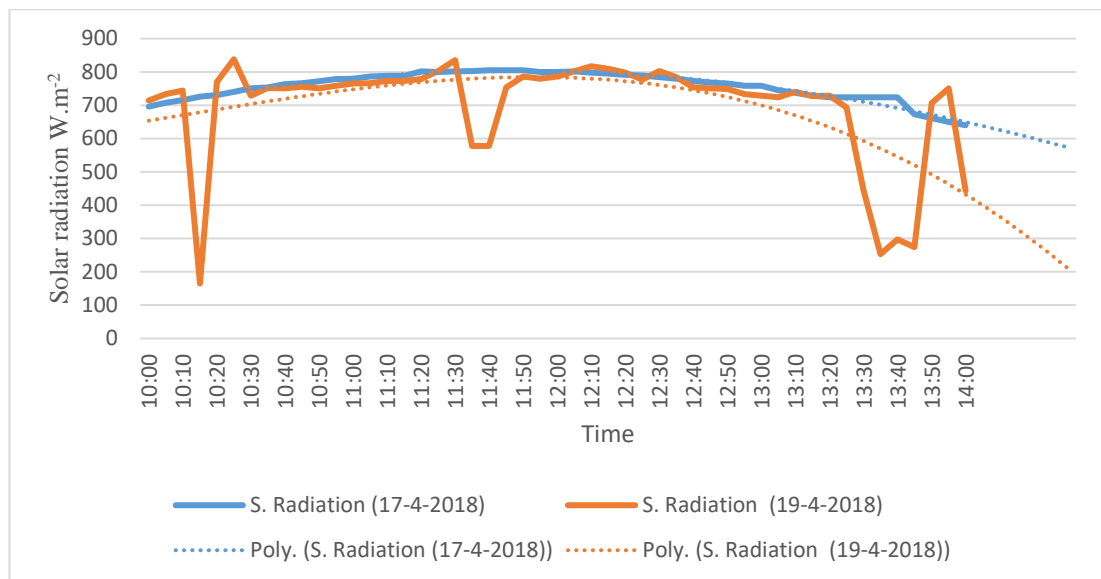
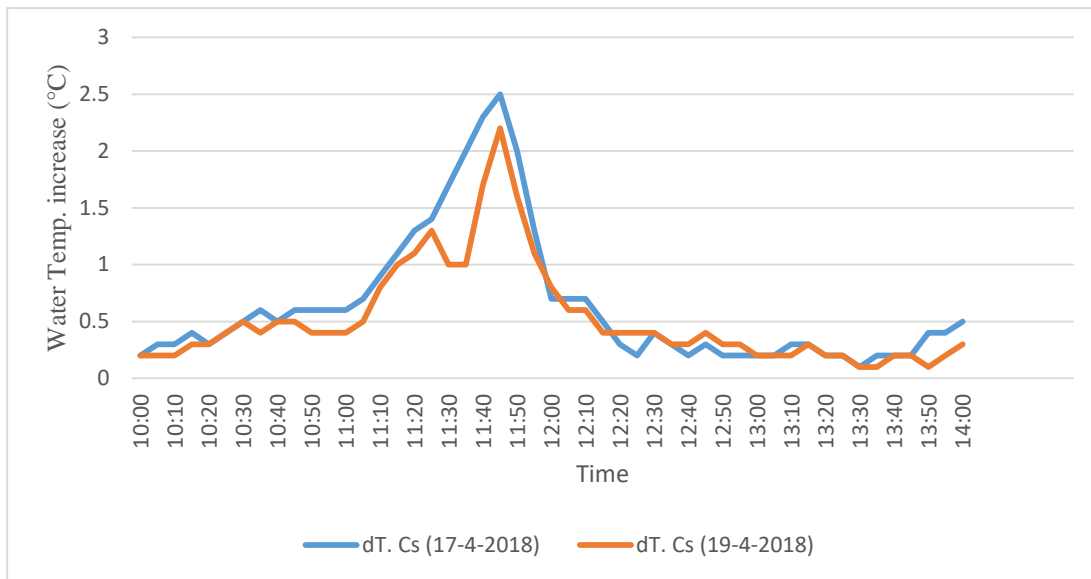


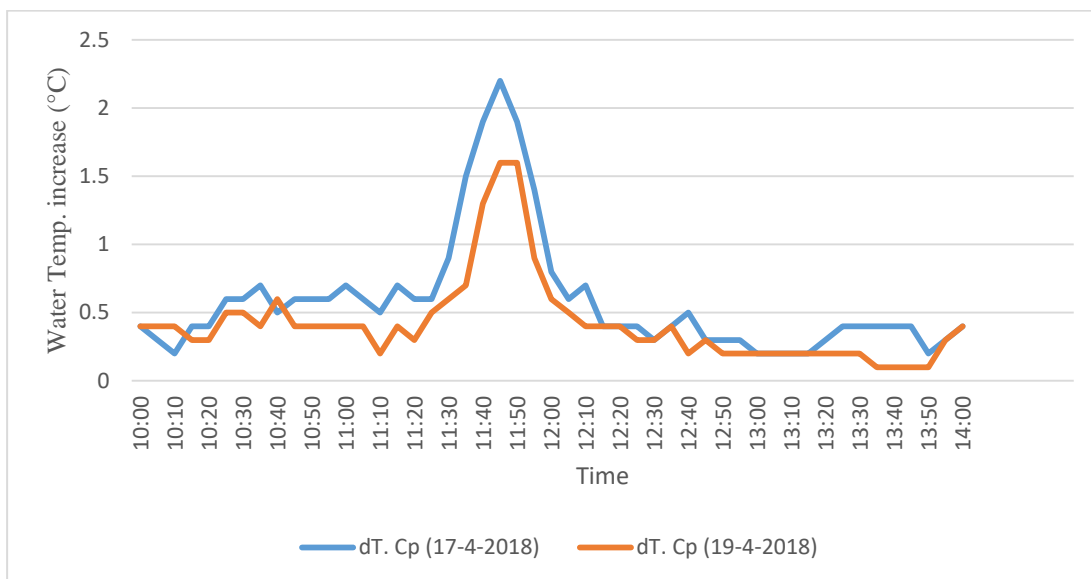
Figure 4.19: Measured data of solar radiation during first and second fixed tests of Cs and CP of case 3. The third-order polynomial lines are the general trends of the variations during the day

#### 4.6.1.2 Water temperature increase

Figure 4.20 shows the fluid's temperature increase from the inlet to the outlet of the collectors during the first and second tests of case 3. By comparing Figure 4.20 (A) and Figure 4.20 (B), it can be seen for both tests that the average water temperature increase around noon for Cs is higher than the average water temperature increase of Cp. The Cs fluid's temperature increase was improved for longer than in Cp due to the influence of the SPM that assisted to reflect the deviated concentrating solar radiation onto the surface of the absorber tube, and therefore the HTF temperature increased.



(A)



(B)

Figure 4.20: Water temperature increase from the inlet to the outlet of Cs (A) and Cp (B) during fixed tests of case 3.

#### **4.6.1.3 Efficiency of the modified collector (Cs) and the primary collector (Cp)**

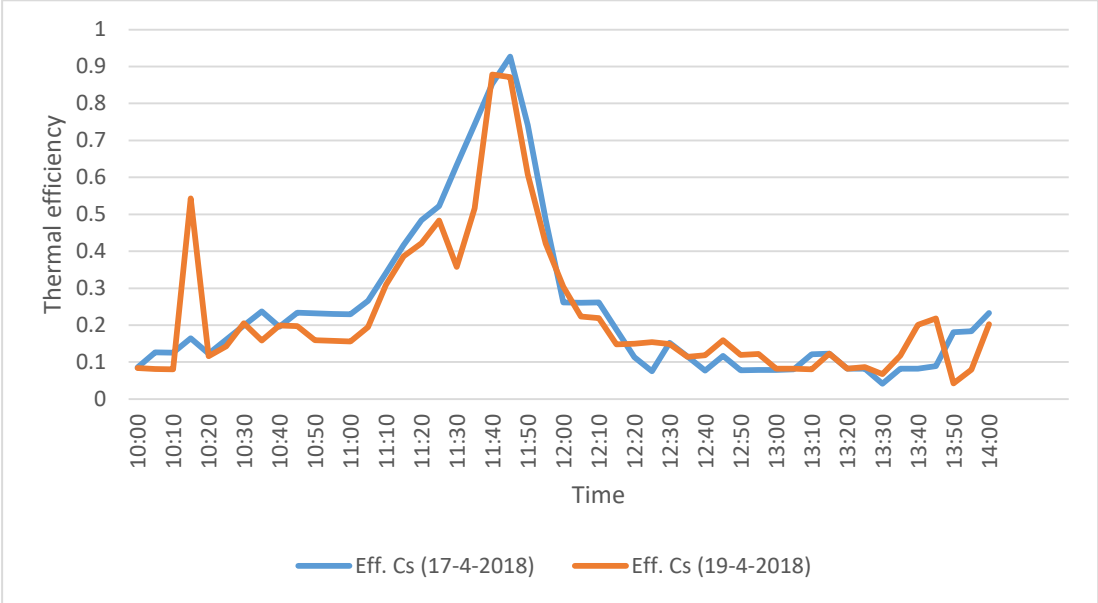
In this section, the efficiencies of Cs and Cp for case 3 are presented to analyse their performances. Figure 4.21 shows the annual midday average efficiency of both collectors during the experimental tests of case 3.

From Figure 4.21 (A) it can be seen that the values of Cs performance during both tests are relatively similar due to the weather being clear. In addition, it can be seen that the efficiency of Cs was approximately 10% between 10 am and 11.10 am and also between 12.10 pm and 2 pm. That was due to solar rays falling in an oblique direction on the collector, which causes a misalignment between the reflected solar rays and the necessary trajectory to strike the absorber tube. Therefore it results in reduced system performance. Also, it can be seen that the Cs performance during the second test was elevated suddenly at several points before and after midday. This is because some clouds appeared during those periods, which resulted in thermal lag. It also can be observed that the Cs performance curves during both tests reached around 0.9 between 11.40 am and 11.50 am. That was due to solar beams falling relatively vertically on the collector aperture area and therefore the solar beams were reflected directly towards the absorber tube. The annual midday average efficiency value for Cs during the first and second tests was  $25.12\% \pm 0.02\%$  and  $22.36\% \pm 0.02\%$  respectively. This difference is due to the changed weather conditions: the second day was partly cloudy and significantly windier.

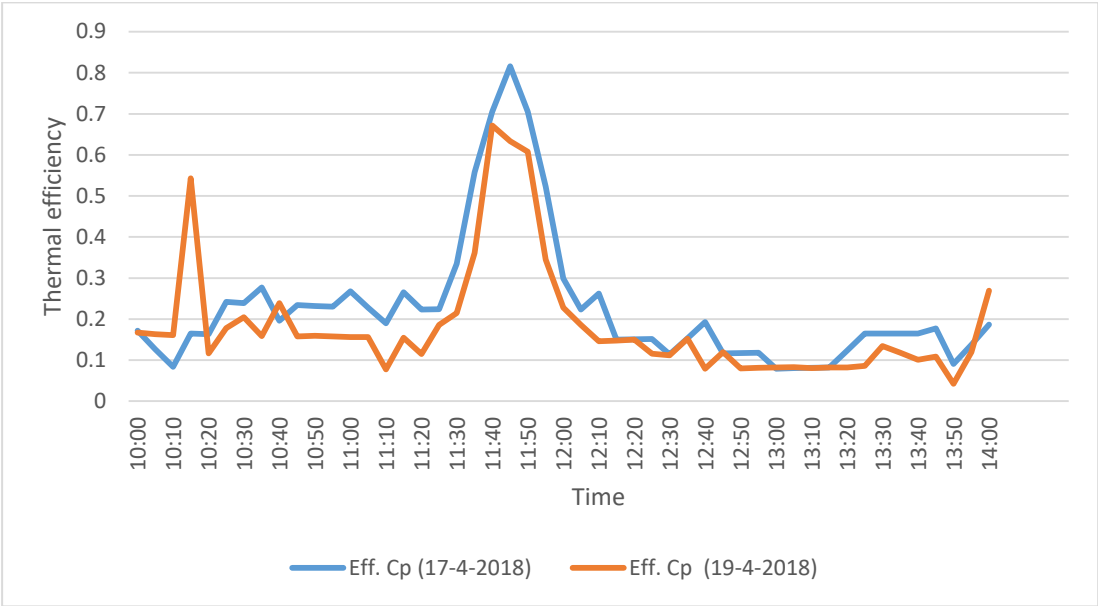
Figure 4.21 (B) presents the annual midday average efficiency for Cp during the first and second tests of case 3. A clear difference can be seen between Cp performances during both tests, which is more notable between 10.20 am and 12.10 pm. This is due to increasing wind velocity during the second test, which increased the absorber heat loss in addition to vibrating the collector. The annual midday average efficiency for Cp during the first and second tests was  $23.18\% \pm 0.02\%$  and  $17.92\% \pm 0.02\%$  respectively. As mentioned above, this is due to the weather conditions.

From the tests of both days, it can be seen that even though the Cs operated with less aperture area, due to SPM area, its efficiency is higher than the efficiency of the Cp, which operated with full aperture area. This clearly shows the ability of the SPM to reflect the deviated reflected sunlight onto the absorber tube and improve the collector

efficiency. This also shows the need to utilise this geometry for PTSC during the fixed stage even under normal weather conditions.



(A)



(B)

Figure 4.21 Experimental annual midday average performance of Cs (A) and Cp (B) during first and second fixed tests of case 3.

#### **4.6.1.4 Performance comparison of the modified collector (Cs) and the primary collector (Cp)**

Figure 4.22 shows the overall annual midday average efficiency for the Cs and the Cp from the two days of the experimental tests of case 3. It can be seen that the lowest efficiency values of both collectors are before and after the midday period. This was due to oblique angles of the falling solar rays (reducing the irradiance) which, when reflected, missed the absorber tube and that resulted in reduced solar heating of the system. In addition, it can be seen that the efficiency of both collectors reached maximum values during the midday period because of the collectors being closely aligned with the solar rays during that period to match the parabolic alignment.

However, it can also be seen that there is a clear difference in efficiency values and also in the period when the efficiency was improved (around midday). For Cp, the optimal period was approximately equal to 30 minutes, between 11.30 am and 12 pm, and the overall annual midday average efficiency value of the Cp collector is  $20.55\% \pm 0.02\%$ . For Cs, the optimal period was approximately 50 minutes, between 11.10 am and 12 pm and the overall annual midday average efficiency of the Cs collector was  $23.74\% \pm 0.02\%$ —the Cp efficiency was 86% of the Cs efficiency. The difference between Cs and Cp efficiencies is slightly more than 3% even though the Cs aperture area was blocked by the SPM's area ( $0.072 \text{ m}^2$ , around 8.5% of the Cs aperture area). That presents a positive effect for the SPM on the PTSC performance under stationary tests due to reflecting the deviated solar radiation on the absorber tube.

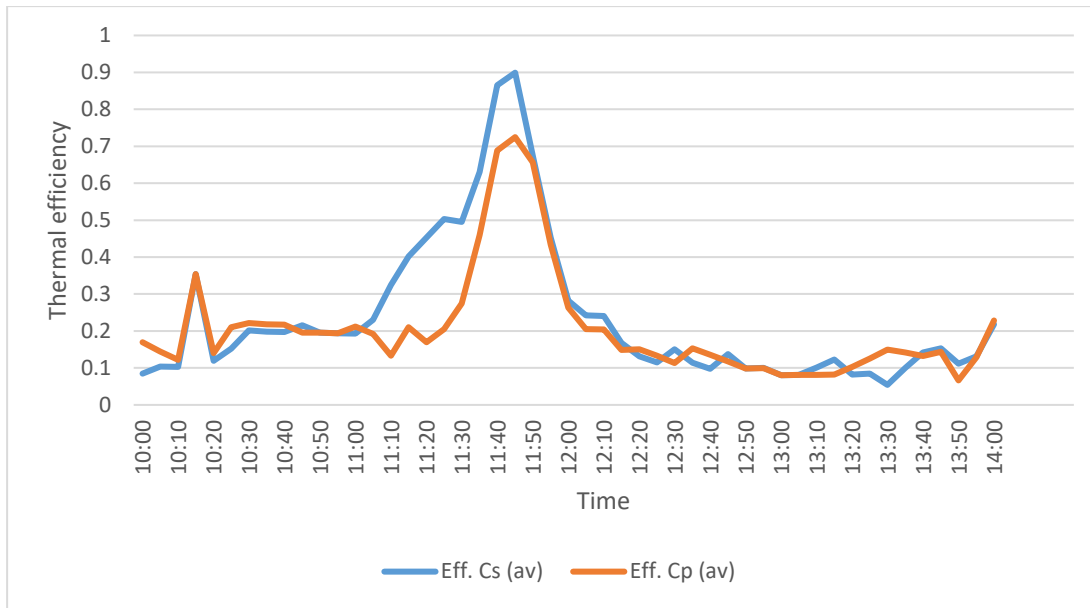


Figure 4.22: Overall annual midday average efficiency data of the Cs and Cp during fixed tests of case 3.

#### 4.6.2 Effect of adding secondary mirror (case 4)

The aim of case 4 was to investigate the effect of adding a secondary mirror (SPM) to the primary collector during the fixed stage. This was done by comparing the performance of Cs with that of Cb (Figure 4.3 and Figure 4.10). As mentioned before, the Cb is a primary collector with a secondary parabola painted black (SPB); this latter geometry (primary collector and SPB) called Cb. Adding the SPB geometry to the Cp assisted to observe the effect of the SPM on the Cs performance, as mentioned in section 4.3.

##### 4.6.2.1 Wind speed and solar radiation of the outdoor conditions

Wind speeds associated with the first and second Cs and Cb tests of the fixed stage are presented in Figure 4.23. While the behaviour is similar, with the morning being windier than the afternoon, the wind velocity during the first test was slightly higher than during the second test.

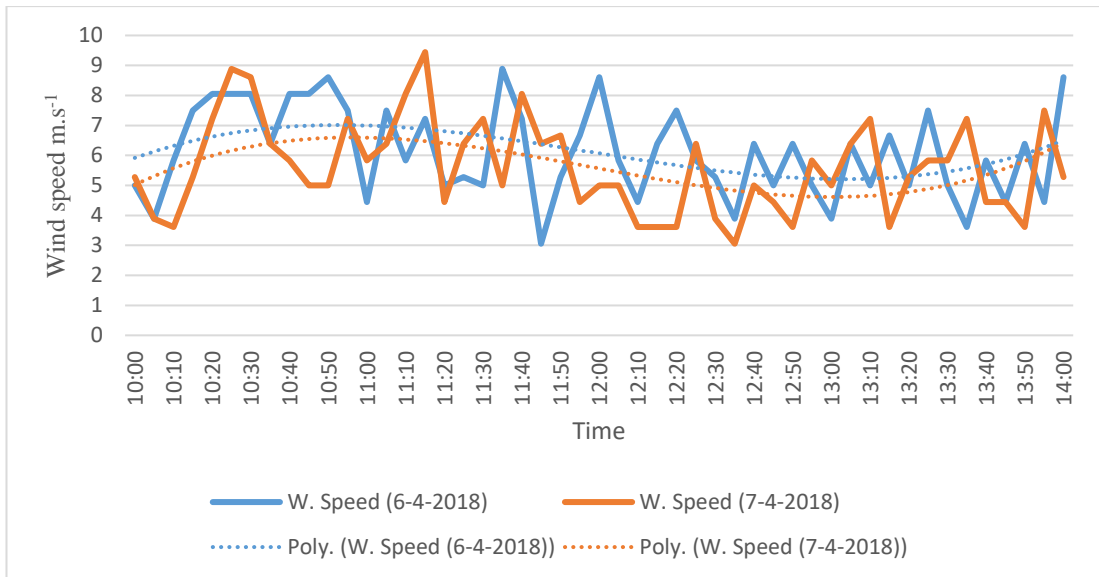


Figure 4.23: Variation of wind velocities during first and second fixed tests of the  $C_s$  and  $C_b$  during case 4. The third-order polynomial lines are the general trends of the variations during the day

Figure 4.24 displays the solar radiation striking the collectors during the tests of case 4. It can be seen that the solar radiation was relatively constant during the first test, which indicated that the weather was clear except briefly in the afternoon. Also, it can be noticed that the solar rays were reduced to approximately  $200 \text{ W.m}^{-2}$  during some periods after midday due to clouds. The average solar data at midday was approximately  $900 \text{ W.m}^{-2}$  while it reduced at the beginning and at the end times during the first test. During the second test there was a partly cloudy sky, especially during the afternoon.

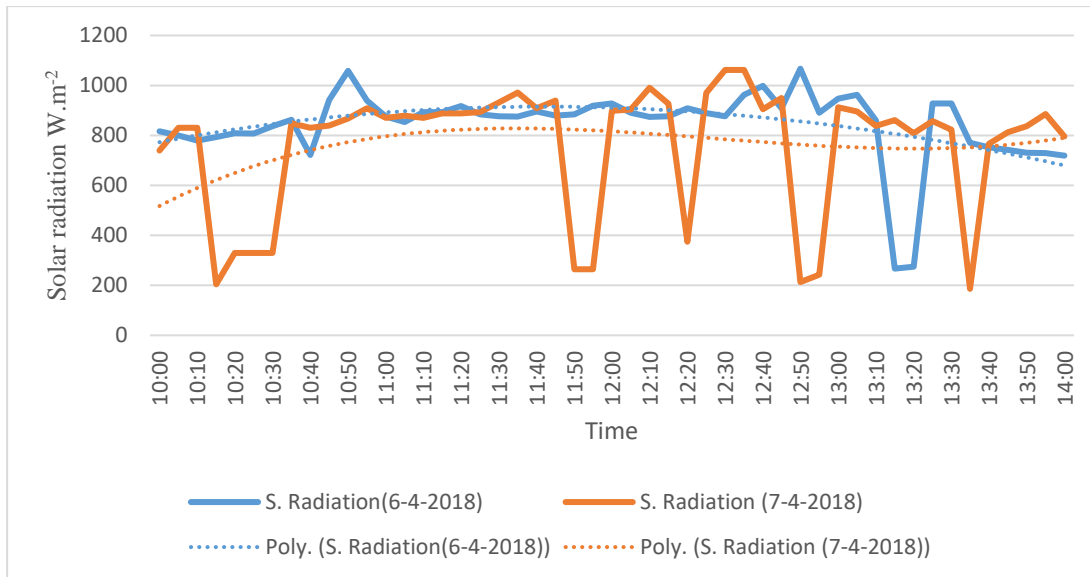
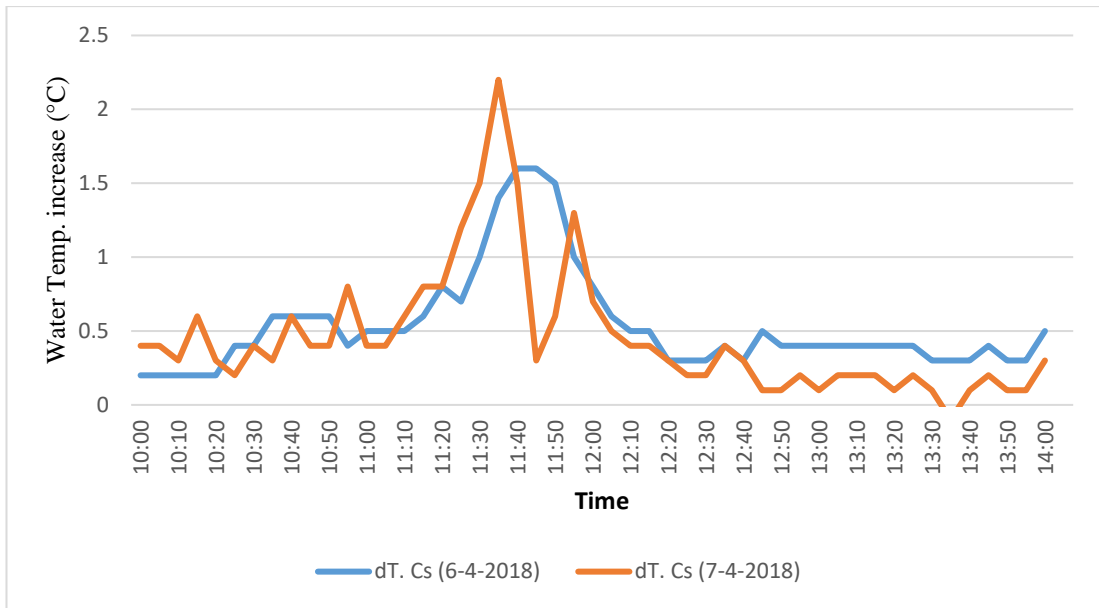


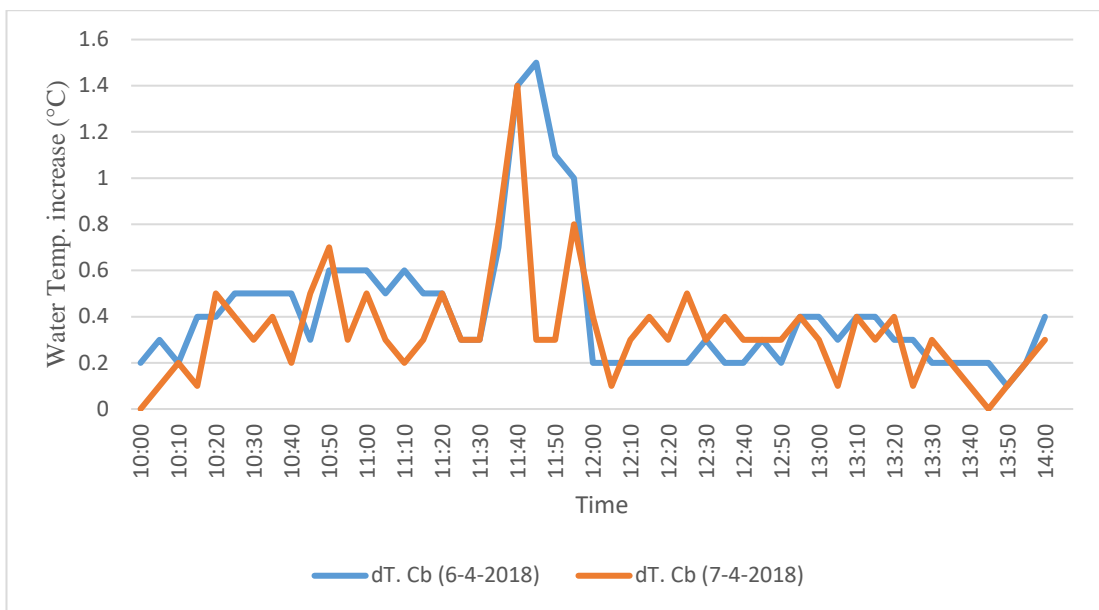
Figure 4.24: Measured data of solar radiation during first and second fixed tests of Cs and Cb of case 4. The third-order polynomial lines are the general trends of the variations during the day

#### 4.6.2.2 Water temperature increase

Figure 4.25 presents the values of the fluid's temperature increase from the inlet to the outlet of Cs and Cb during the tests of case 4. It can be seen that the average value of the Cs water temperature increase difference was around 0.9. The average value of the Cb water temperature increase difference was around 0.7. The addition of the SPM in Cs increased the period when a large temperature increase was produced, and also intensified the heat transfer to the water. This is due to the effect of the SPM, which captured some of the deviated solar rays during that period and reflected them again to the absorber tube. Also, as can be seen from the solar radiation data (provided by the USQ weather station), the weather during the second test was slightly cloudy, and therefore the passage of some clouds could affect the solar radiation data records (recorded every 5 min). This means it could be there was cloud during 4 minutes but at the recording time it becomes sunny.



(A)



(B)

Figure 4.25: Water temperature increase from the inlet to the outlet of Cs (A) and Cb (B) during fixed tests of case 4.

#### 4.6.2.3 Efficiency of the modified collector (Cs) and the primary collector with SPB

In this section, the annual midday average performance of the Cs and Cb of case 4 are presented. Figure 4.26 displays the experimental simulation of the annual midday

average efficiency of the Cs and Cb performances during the first and second tests of case 4.

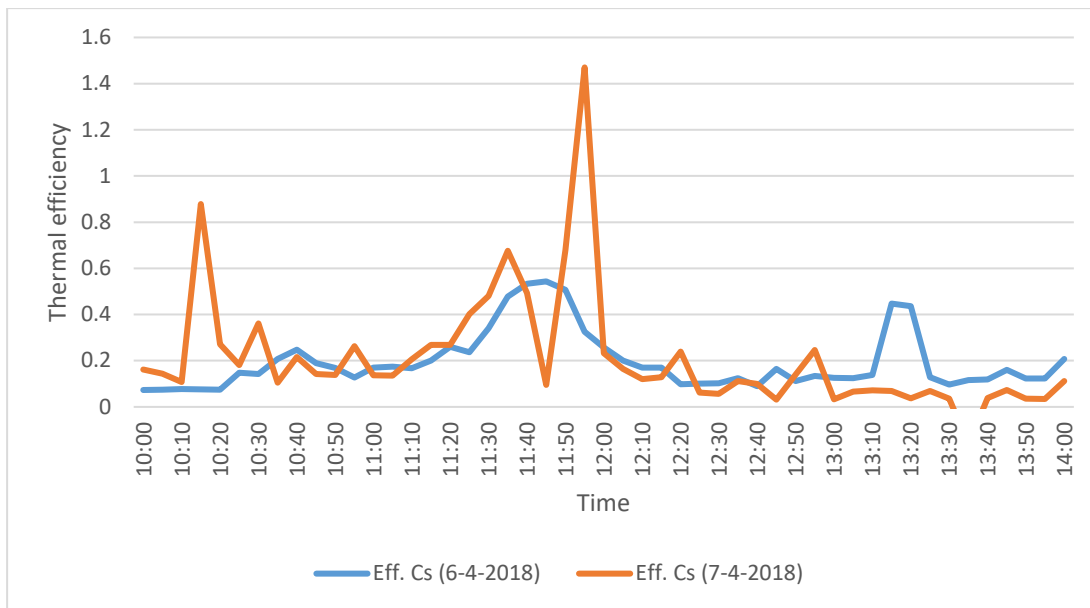
From Figure 4.26 (A) it can be seen that the performance of the Cs during the first test was relatively low before and after midday, and the average value of the Cs performance during that period was around 10% because the collector was fixed to the midday alignment. Therefore, the solar radiation fell obliquely on the collector aperture area during that period, and therefore it reflected out of the SPM's range, so missed the absorber tube. This severe deviation reduced the optical performance of the Cs. In addition, the wind velocity also had an effect on the solar rays' deviation due to vibration of the collector structure, but it is much less than that seen in the tracking cases due to the small cross-section area of the PTSC exposed to the wind. It can be noticed that the efficiency of the Cs increased sharply during the midday period due to the solar radiation relatively falling normally on the Cs aperture area during that time. This resulted in reflecting the solar rays directly toward the absorber tube and heating the HTF efficiently. Furthermore, during some periods it can be seen that the Cs performance suddenly increased while the solar rays were falling in an oblique direction and. This was due to weather conditions, which were partly cloudy, resulting in reduced solar radiation. Meanwhile, the HTF temperature difference decrease was small compared with the solar rays' reduction, which led to an increase of the collector efficiency based on the PTSC thermal efficiency formula.

The figure also presents the annual midday average performance of the Cs during the next test. It can be observed that the Cs performance also fluctuated in different periods of time due to cloudy weather during the test. During some periods, the efficiency of Cs reached more than 100%, which was due to the thermal lag phenomenon.. As mentioned above, this was due to reducing the solar radiation ratio at these times due to partly cloudy weather, and at the same time the water continued heating from stored heat from the absorber tube wall. Finally, the annual midday average efficiency of the Cs during the first and second tests was  $18.99\% \pm 0.02\%$  and  $17.88\% \pm 0.02\%$  respectively.

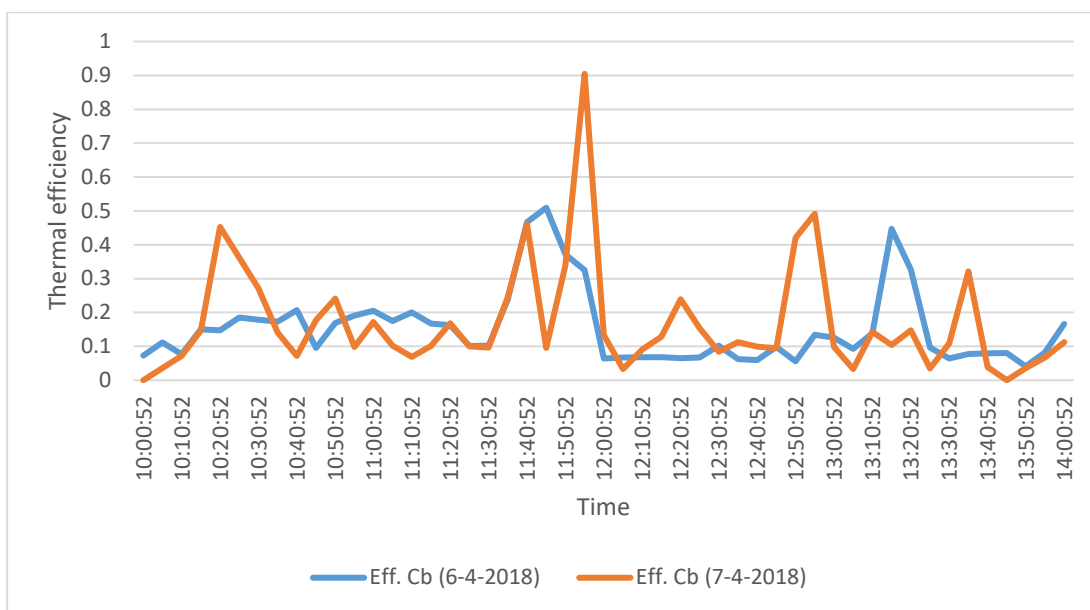
Figure 4.26 (B) displays the annual midday average performance of the Cb during the same test period from 10 am to 2 pm. It can be seen that the Cb performance is similar to the Cs performance. However, the annual midday average efficiency of the Cb

during the first and second tests was  $14.67\% \pm 0.02\%$  and  $13.23\% \pm 0.02\%$  respectively.

This significant difference in annual midday average efficiency (despite the small collector aperture area and also the tests only simulating midday for a season) demonstrates the impact of the SPM in a fixed orientation.



(A)



(B)

Figure 4.26: Experimental annual midday average performance of Cs (A) and Cb (B) during first and second fixed tests of case 4.

#### 4.6.2.4 Performance comparison of the modified collector (Cs) and the primary collector with SPB (Cb)

Figure 4.27 shows the overall annual midday average performances of the Cs and Cb data from the two days of the experimental tests of case 4 under the same weather conditions such as solar insolation and wind velocity. It can be seen that both collectors

have similar performance values away from midday. This is due to the solar radiation falling in an oblique direction on the collectors during those periods and therefore it was reflected away from the absorber tubes, even out of the SPM operation scope of the Cs collector. It is apparent from the performance of Cb that there was a short period before midday when the PTSC was aligned correctly, thereby producing regular efficiency. The extended period of improvement in the Cs demonstrates that the SPM captured a significant number of deviated solar rays (caused by the solar misalignment). During the period when the PTSC was aligned, the SPM produced a significantly higher efficiency (Cb equal approximately 75% of Cs overall annual midday average efficiency), which indicates that even during the aligned period, there were a significant number of deviated solar rays.

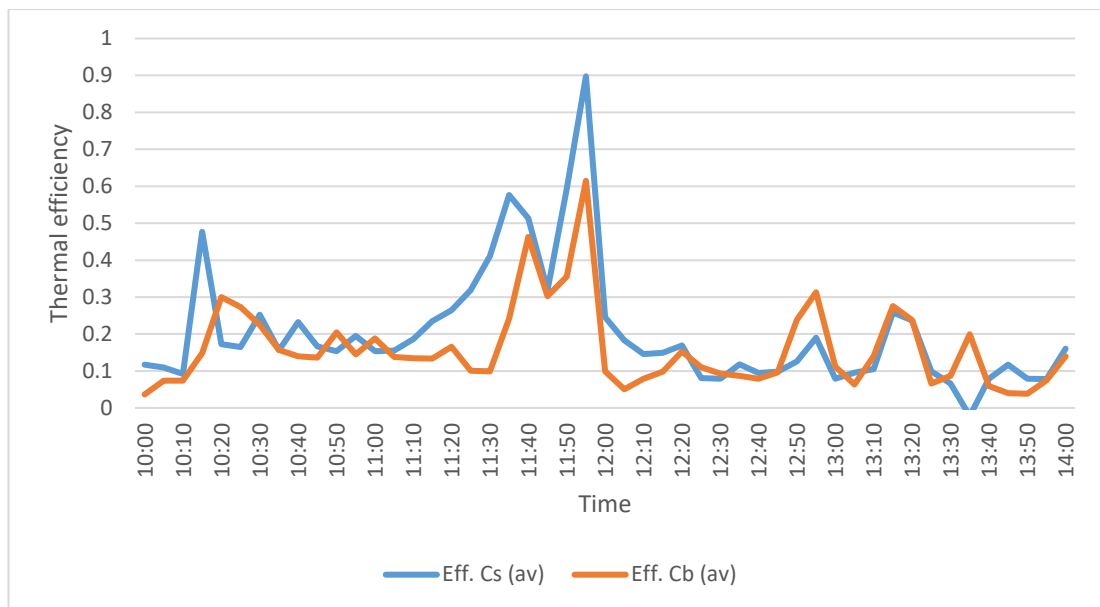


Figure 4.27: Overall average annual midday efficiency data of the Cs and Cp during fixed tests of case 4.

#### 4.7 Effect of modified collector for different seasons

The final test compared the performance of the primary collector (Cp) and the modified collector (Cs) during tracking tests (Figure 4.2) for different ambient temperatures to assess how their performance changes for different seasons of the year. Days that have similar average values of solar radiation and wind speed, but different ambient temperatures, were selected for that purpose, as presented in Table 4.3.

Table 4.3 Overall average performance of Cs and Cp during tracking tests at different times of the year for similar solar radiation and wind speed but with different ambient temperatures.

<i>Month</i>	<i>S. Radiation (W.m<sup>-2</sup>)</i>	<i>W. Speed (m.s<sup>-1</sup>)</i>	<i>Ambient Temp. (°C)</i>	<i>Average Eff. of Cs (%)</i>	<i>Average Eff. of Cp (%)</i>
February	1045.9	2.8	28.56	51.78	51.84
May	1045.9	3.9	18.92	50.64	50.44
July	1098	3	10.99	47.36	46.23
September	1081.8	2.2	17.81	49.05	48.83

From Table 4.3 it can be seen that efficiency for both collectors is similar, with Cs slightly higher for all months except February, when it was slightly lower. Therefore the Cs efficiency is always effectively higher than the Cp efficiency because the Cs aperture area is less than the Cp aperture area by around 8.5% due to the SPM blocking the Cs aperture area. The SPM's reflection of the deviated solar rays towards the absorber of the Cs overcame the effect of its blocking area.

The average efficiency is clearly linked to the ambient temperature, with summer (February) producing the best performance. Winter (during July) produced the worst performance, due to the radiative loss, but also the highest efficiency improvement for the Cs (approximately 2%). This indicated the capability of the SPM for reflecting some of the absorber tube radiative loss in addition to deviated sunlight rays. Spring (September) was slightly worse than autumn (May), which is possibly due to deterioration of the mirror surface due to its exposure to the elements throughout the year.

## **4.8 Summary**

### **4.8.1 Outcomes of the optical enhancement experimental investigations.**

It has been found that both PTSC tracking errors (which are increased during windier periods and partly cloudy weather) and wind changes have a significant negative effect on the PTSC optical efficiency. This is because both lead to increasing the deviation

of the reflected solar rays from collector absorber tube (as also observed in sections 2.2.1.5 and 2.2.1.6). Therefore, utilising the SPM has a clear positive effect on PTSC performance by reflecting the deviated solar rays back to the absorber tube. In order to investigate the effect of the SPM on the solar collector, two configurations were used.

The first configuration is the Cs and Cp configuration (section 4.3), which was done to compare between the modified collector (Cs) and primary collector (Cp) (case 1). Even though the Cs has less aperture area due to the SPM geometry, the experimental results showed that its performance was slightly higher than the Cp performance during normal weather conditions. This difference is slightly increased under windy and cloudy weather. The second configuration is the Cs and Cb configuration (section 4.3), where the Cb is the primary collector with a secondary parabola painted black. This setup (case 2) was carried out in order to compare the collectors with a similar geometric structure. In this case, each collector lost the same amount of its aperture area, due to both having secondary parabola geometry. Therefore, this case presented the net positive effect of the SPM especially on windy and cloudy days.

Due to the finding that wind fluctuation has a clear effect on the collector performance during tracking tests, a fixed stage (new test methodology) for the PTSC system was carried out to propose a viable alternative design (section 4.6).. The aim of this stage was to investigate the PTSC average performance for midday throughout the year and to investigate the effect of the SPM under this experimental simulation. The experimental simulation results of the PTSC revealed that the SPM not only improved the PTSC performance during the fixed tests, but it also prolonged the improvement period. Therefore, using this technology (SPM) could assist in employing the PTSC system at windy sites.

The performance of the PTSC in different seasons was explicitly investigated by selecting different days throughout the year that have different ambient temperatures, but similar solar radiation and wind speed (section 4.7). It was found that the effect of the SPM was strongest during cold weather, which means this component (SPM) supplied additional heating energy when it was most needed: while the outdoor conditions and also the supplied HTF were coldest.

Based on the above, it can be seen that under environmental conditions like windy and partly cloudy weather, and geometry misalignments (as also observed in sections 2.2.1.1 and 2.2.1.2), which all increase deviating reflected solar rays, the utilisation of an SPM is required to enhance the PTSC optical performance.

It must be noted that improving PTSC optical performance, due to utilising SPM, results in increasing HTF temperatures. This HTF increasing temperature could enhanced the receiver tube heat loss (convection cooling by the wind and radiation heat transfer), especially if the collector's concentrating ratio is higher (section 2.2.1.3). Therefore, the blocking area of the SPM geometry (optical enhancement) will be employed to improve the PTSC receiver tube thermal performance. This is explored in Chapter 5 and Chapter 6.

#### **4.8.2 Optical enhancement evaluation**

In terms of the optical enhancement, the optical solution (secondary reflector) has effectively improved the PTSC performance. This because the secondary reflector reduces the PTSC optical loss by reflecting the deviated solar radiation—irrespective of the source of the solar rays' deviation (either due to structural misalignment or due to wind changes)—towards the upper part of the absorber tube. The other reason is that the secondary reflector also reflects some of the absorber tube radiative heat loss onto the upper part of the absorber tube. Both reasons not only improve the PTSC performance but also improve the absorber tube operation life due to reducing the absorber tube thermal stress that occurs due to the non-symmetrical concentration of reflected solar radiation on the absorber tube surface. In contrast, all of the presented studies of optical enhancements (section 2.2.2) focused on reducing effect of one factor of optical loss, such as structural misalignment (Forman et al. 2015), receiver misalignment (Prah et al. 2011) and reflector errors (Xu et al. 2014).

Moreover, for the economic aspect, the presented optical solution is simple and not require any modifications for the PTSC components like reflector or receiver tube structures. On the other hand, the presented optical enhancement studies (section 2.2.2) are complicated and required modification of the standard design for the PTSC system which makes them costly and not attractive solutions commercially.

# Chapter 5 Alternative Receiver Tube CFD Model

## 5.1 Introduction

In Chapters 3 and 4, an experimental work was undertaken to decrease the optical loss of a parabolic trough solar collector, which was achieved by using a secondary parabolic mirror (SPM) placed above the upper surface of the absorber tube, as seen in Figure 5.1. Although this secondary reflector blocked normal sunlight from striking the upper half of the absorber tube surface (due to the dead zone), there was a net increase in PTSC performance. This is due to capturing the solar rays reflected from the primary reflector which missed the absorber tube and reflecting them towards the absorber tube. In addition, some of the radiative heat loss from the upper surface of the absorber tube is reflected back to the absorber tube.

Chapters 5 and 6 focus on the possibility of utilising the dead zone of the SPM (Figure 5.1) to enhance the thermal performance of the PTSC system. The proposed utilisation of the dead zone is by adding a thermal insulation material on the inner surface of the upper half of the glass envelope. The inner surface of the insulation layer (facing the absorber tube) has the same shape and dimensions as the SPM geometry (presented in section 3.4.1), as illustrated in Figure 5.2. The figure shows the 2D mesh structure of several alternative receiver tubes, each consisting of a glass envelope surrounding the absorber tube (more details in section 5.3). The upper portion of the glass envelope for the parabolic and hybrid receiver tubes is a parabola shape, which is same design as the SPM structure. The lower part of the parabolic receiver tube glass envelope is symmetrical, while the hybrid receiver tube is a circular shape. The circular receiver tube consists of an absorber tube covered by a circular glass envelope.

The proposed utilisation of the dead zone is by adding a thermal insulation material on the inner surface of the upper half of the glass envelope, as can be seen in Figure 5.2. The inner surface of the insulation layer (facing the absorber tube) has the same shape and dimensions as the SPM geometry. The thermal insulation reduces the conduction heat transfer loss across the upper part of the glass envelope wall by reducing the temperature of the outer surface of the glass envelope.

Some commercial receiver tubes used for supplying hot water and industrial heating applications are non-evacuated. Despite evacuated receiver tubes having higher operating efficiencies, these tubes have higher capital and maintenance costs (see section 1.3). Therefore, the non-evacuated receiver tube is adopted, with the space between the glass envelope and the absorber tube of the proposed receiver tubes filled with air.

The width of the glass envelope in all the designs is equal to the width of the SPM. Therefore, inserting thermal insulation can create a thermal enhancement to ameliorate the drawback of utilising SPM (Al-Ansary & Zeitoun 2011; Chandra et al. 2017). The combination of the designs studied experimentally and numerically in this thesis could provide a new method to reduce the overall optical and thermal loss in a parabolic trough solar collector system.

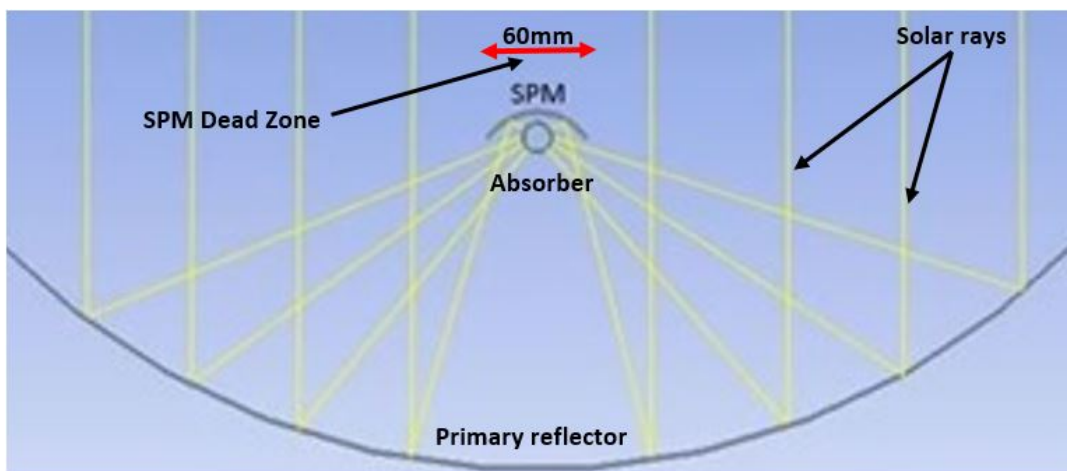


*Figure 5.1: 2D structure of the experimental setup: absorber tube, secondary parabolic mirror (SPM), primary reflector and dead zone (produced due to employing the SPM).*

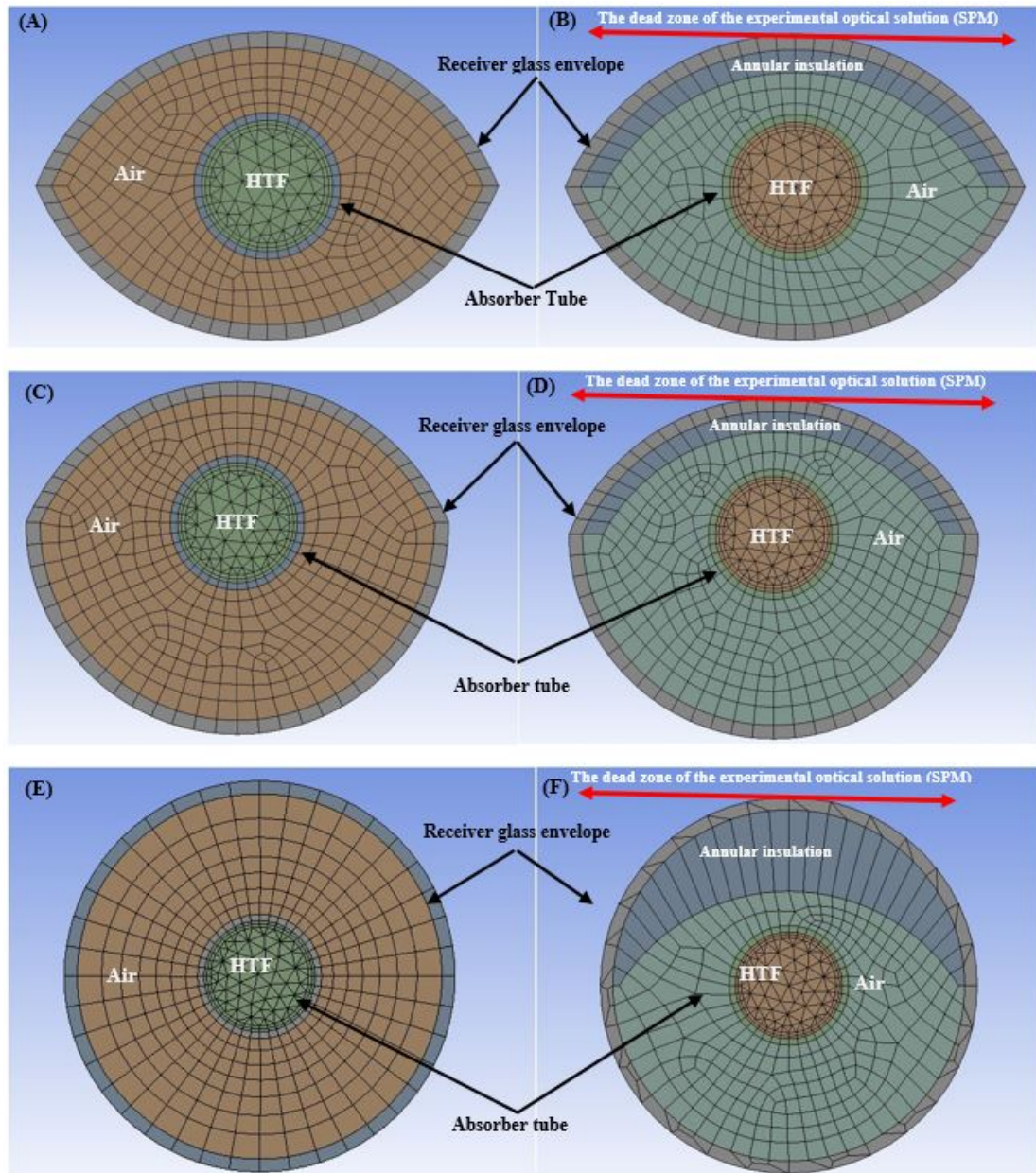


Figure 5.2: Non-insulated (first column) vs insulated (second column) cross-section area of the proposed receiver tubes. The first row represents the parabolic receiver tubes. The second row represents the hybrid receiver tubes. The third row represents the circular receiver tubes. “SPM dead zone” is the same width as the SP.

## 5.2 Solar heat flux calculation

The numerical study focusses on the effect of thermal insulation on the PTSC performance for various wind speeds. Therefore, it is necessary to apply solar radiation as an input energy to the PTSC system. Fluent is not able to accurately simulate the parabolic mirror reflection because this software represents curves using line segments. Therefore, reflections from curved surfaces, like parabolic mirrors, cannot be accurately simulated by this software. To properly capture the reflection from a

curved mirror (an infinite number of reflection angles that converge at the mirror's focal point) requires specialised software. Therefore SolTrace software (designed by the National Renewable Energy Laboratory, or NREL), an optical modelling tool, was used here to simulate the parabolic mirror reflection for normal incident solar rays. It operates based on the MCRT method, by randomly sampling a large number of solar rays and tracing their paths as they reflect off the reflector and are (potentially) absorbed by the absorber tube. More details about the calculation steps of the solar flux by the SolTrace software and its methodology (MCRT method) are described in detail in (Wendelin et al. 2013).

The optical properties of the PTSC components are presented in Table 5.1. To produce an accurate heat flux map and reduce the optical simulation errors, the total number of solar rays was  $10^6$ . The effect of sun shape error in addition to the geometry components errors was considered in the optical simulation in order to present an accurate simulation that simulated errors of outdoor conditions, like sun shape and components misalignments.

*Table 5.1: Optical properties of the PTSC components.*

Component	Absorptivity	Reflectivity	Transmissivity	Slope error (mrad)	Specularity error(mrad)
Absorber	0.04	0.04	0	0.02	0.02
Glass cover	0.015	0.015	0.97	0.02	0.02
Reflector	0.04	0.96	0	0.95	0.2

Figure 5.3 shows the 3D model of a parabolic trough solar collector (built by the SolTrace software) that consisted of the reflector (mirror) and the receiver tube. The solar rays are represented by the yellow lines, with the incident rays the vertical lines, and the reflected rays then strike the receiver tube. In this simulation  $1000 \text{ W.m}^{-2}$  was selected to be the solar flux.

Because each point along the length of the absorber tube is statistically equivalent, the statistical error is reduced by subsequently averaging the flux along the length of the absorber tube, with the result presented in Figure 5.4. This averaged flux profile was then imported to Fluent as a heat flux boundary condition for the absorber tube wall (Figure 5.5).

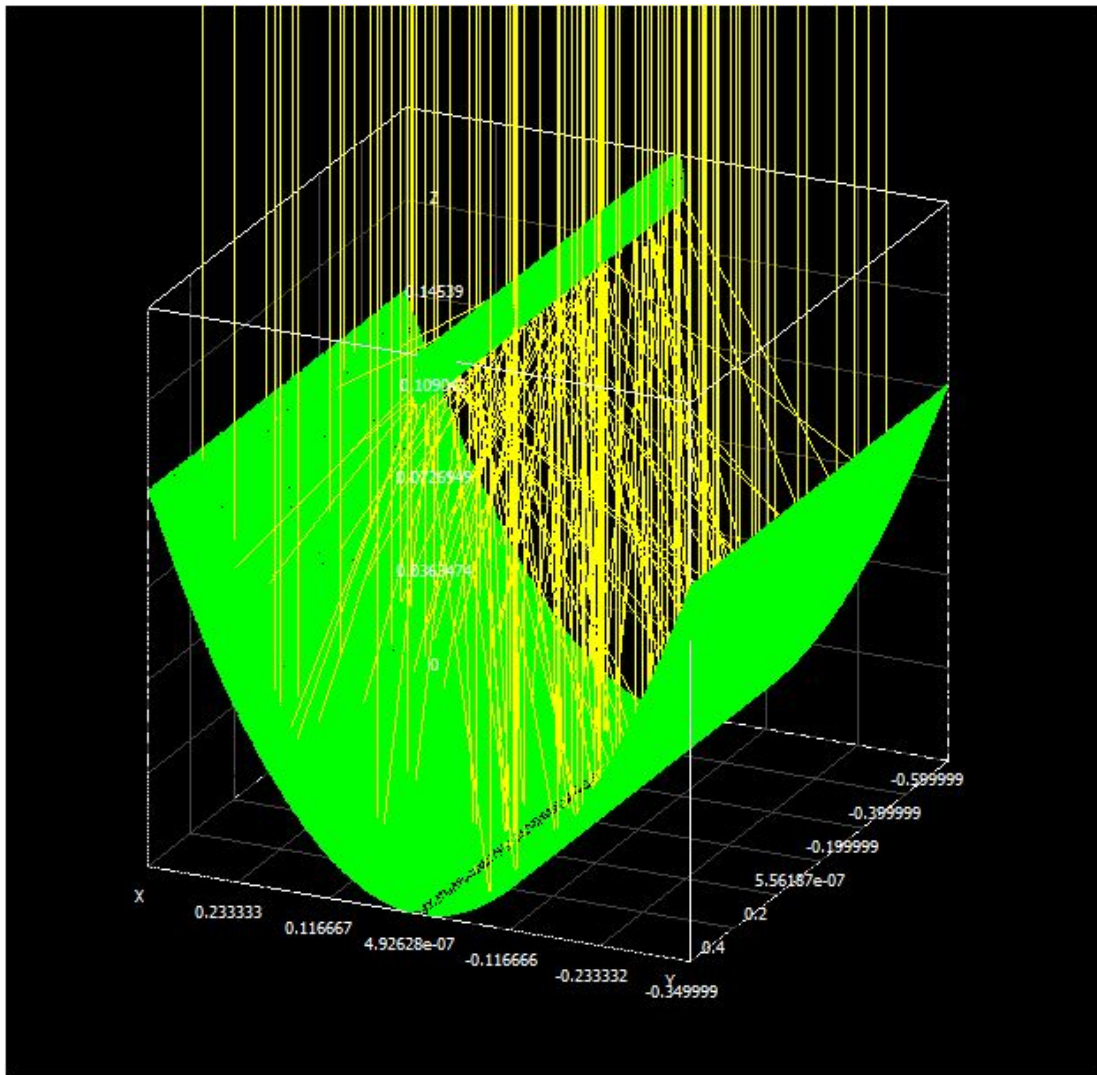
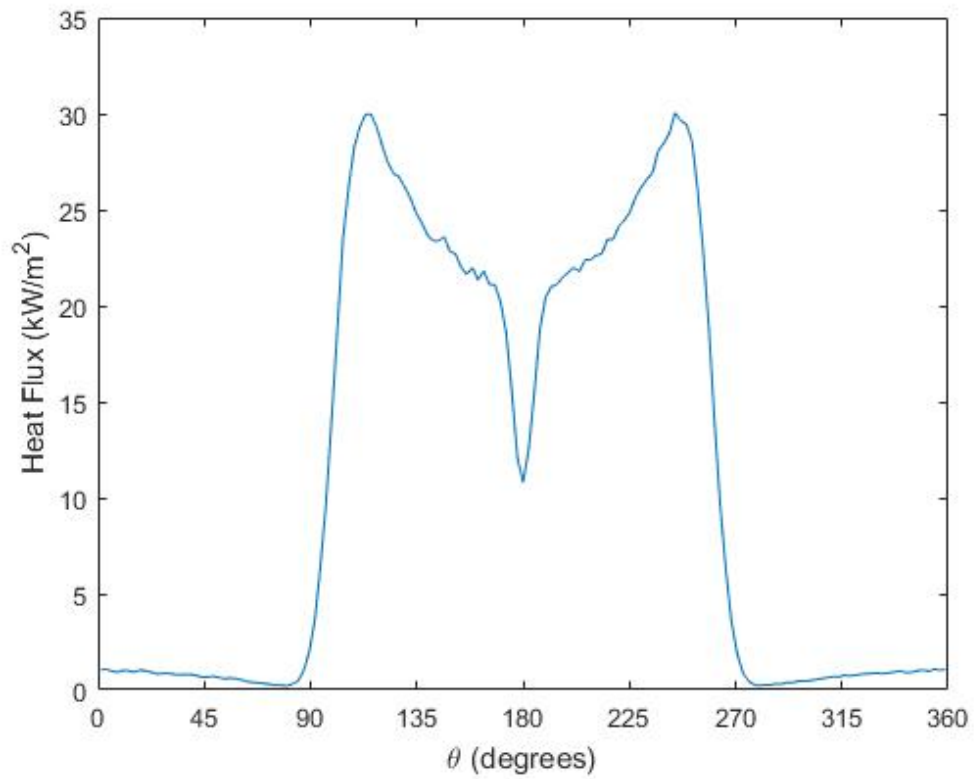


Figure 5.3: SolTrace 3D diagram of the incident solar radiation (yellow collar) reflecting off the PTSC system and onto the receiver tube.



*Figure 5.4: Average flux distribution of the incident solar rays (insolation of 1000 W.m-2) around the absorber tube circumference, calculated by averaging the Figure 4 flux distribution along the absorber length. The X-axis shows the absorber tube's circumference; 0° is the top of the absorber.*

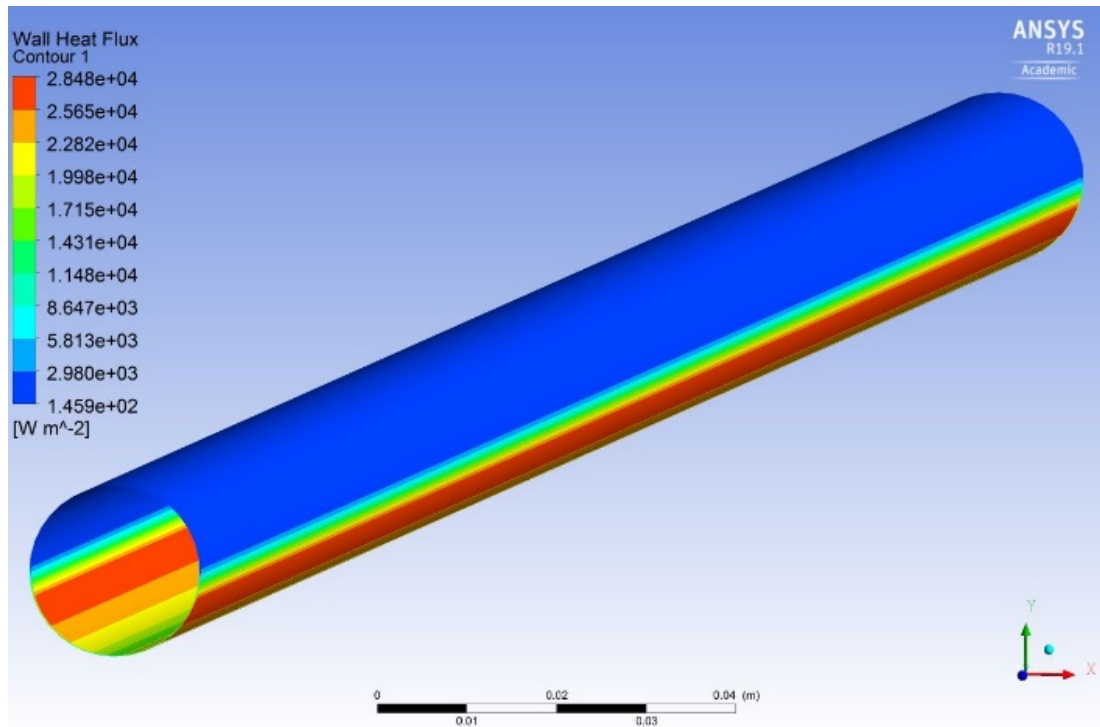


Figure 5.5: Fluent presentation of the solar heat flux distribution on the collector absorber tube from the profile in Figure 5.4.

### 5.3 Physical model of the alternative receiver tube.

Even though evacuated receiver tube is efficient, it is costly, equal to approximately 30% of the total material of the PTSC solar thermal field (Wu et al. 2014). In addition, its replacement cost is expensive due to its required advanced technology for installation (Patil, Panse, et al. 2014) Although the non-evacuated receiver tube efficiency is less than the evacuated receiver by around 10% (Sandeep & Arunachala 2017), it is less expensive and therefore it is used for supplying hot water. In addition, it is employed in some industrial solar technologies (Kearney 2007; Fernández-García et al. 2010).

Utilising thermal insulation on the inner surface of the upper portion of the receiver tube glass envelope could lead to keeping the temperature of the hot air, especially around the upper portion of the absorber tube, relatively high compared with a non-insulated receiver tube. This is because the thermal insulation restricts cooling with the glass envelope, which is exposed to the wind. This could additionally enhance the heat distribution around the outer surface of the absorber tube, reducing the thermal deformation in this element that occurs due to focusing solar heat flux on the lower part of this element, especially with a PTSC that has a large concentrating ratio.

In addition, inserting insulation in this way could also help to reduce the glass envelope heat loss to the environment. This is because the thermal insulation reduces conduction heat transfer across the glass envelope wall, which reduces the outer surface temperature of the glass envelope. All of these effects can lead to improving the receiver tube's thermal performance and increasing its operational life as well.

In this section, the alternative receiver tubes and geometrical specification of PTSC models are presented, which are designed based on the experimental model as presented in Table 5.2. Figure 5.7 demonstrates the structure and the main components of each alternative receiver tube. The absorber tube is made of copper, with the same dimensions as the experimental absorber tube, and is surrounded by a parabolic glass cover. The width of the glass cover is the same as the experiment's SPM (the dead zone). Borosilicate is typically used for producing the PTSC commercial receiver tube glass envelope (Amina et al. 2016; SCHOTT 2019) and therefore it is selected here. Glass wool is selected for the insulation layer due to its low thermal conductivity (Chandra et al. 2017). The insulation is attached on the inner surface of the receiver glass cover. The annular space between the absorber and the glass cover for the insulated and non-insulated alternative receiver tubes are non-evacuated.

*Table 5.2: Geometrical values of the PTSC experimental model and the alternative receiver tube materials used in this numerical work.*

<b><i>Parameter</i></b>	<b><i>Value</i></b>	<b><i>Parameter</i></b>	<b><i>Value</i></b>
Aperture area	0.84 m <sup>2</sup>	Reflector	Super Mirror Stainless Steel (316 grade)
Aperture length	1.2 m	Absorber tube material	Copper
Aperture width	0.7 m	Glass material	Borosilicate
Focal length	0.208 m	Heat transfer fluid	Water
Rim angle	80°	Insulation material	Glass wool
Inner absorber diameter	0.01701 m	Insulation conductivity	0.04 W/m.K
Outer absorber diameter	0.01905 m	Concentrating ratio	11.4

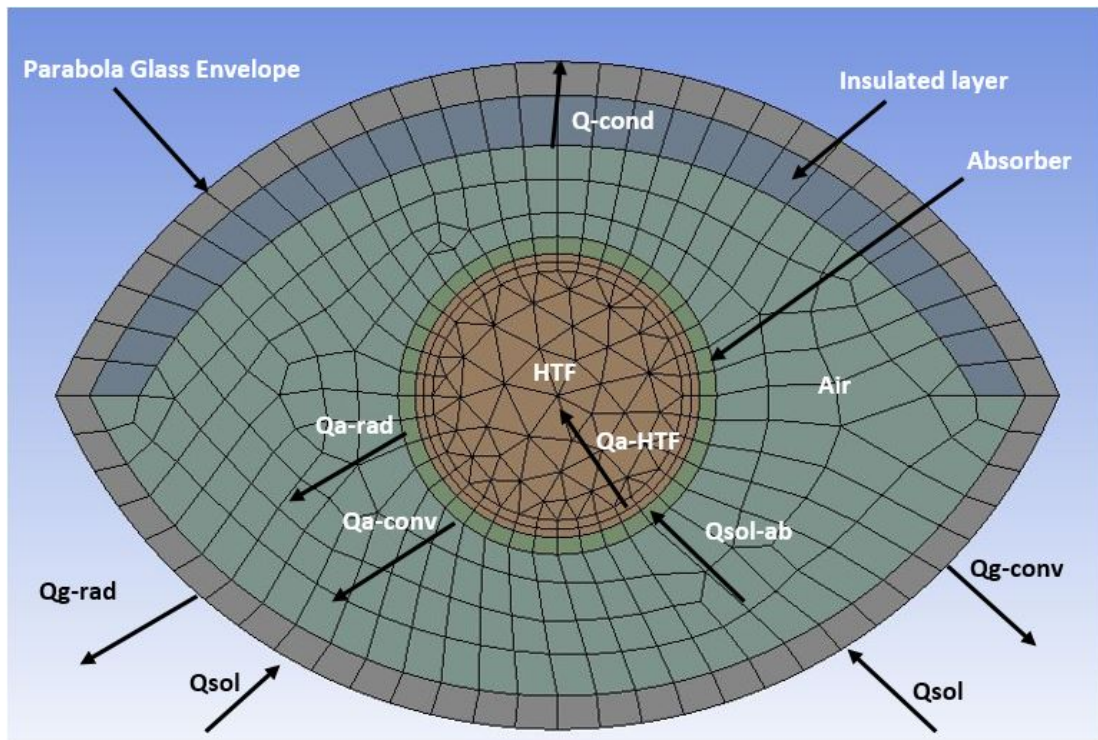


*Figure 5.6: Cross-section area of parabolic receiver tube showing the absorber tube, parabolic glass envelope, thermal insulation and the heat transfer behaviours. Air fills the space between absorber and glass cover; water used as HTF.*

Figure 5.6 also shows the heat transfer components of the receiver tube. In detail, the input energy (radiation solar energy) passes through the glass cover wall, due to its transmissivity, and strikes the absorber tube surface. The absorber tube absorbs most of the solar radiation energy due to its high absorptivity and low reflectivity. Due to the high temperature difference between the outer side and inner side of the absorber tube wall, the absorbing heat is transferred across the absorber tube wall by conduction towards the HTF, and then convection heat transfer from the inner surface of the absorber tube heats the HTF.

Due to the temperature differences between the outer surface of the absorber tube (hotter surface) and inner surface of the receiver glass envelope (colder surface), convection and radiation heat transfer normally occur between these surfaces. Consequently, this resulted in creating a high temperature difference between the inner and the outer surfaces of the receiver glass envelope wall, and therefore conduction heat transfer across the glass cover occurred. Subsequently, this ended by increasing the glass envelope outer surface temperatures, which raised the convection and radiation heat transfer losses from the glass envelope to the outer environment.

Figure 5.7 illustrates the longitudinal and cross-section mesh of the insulated and non-insulated parabolic receiver tubes, as an example for the 3D receiver tube geometry that was used in the CFD simulation.

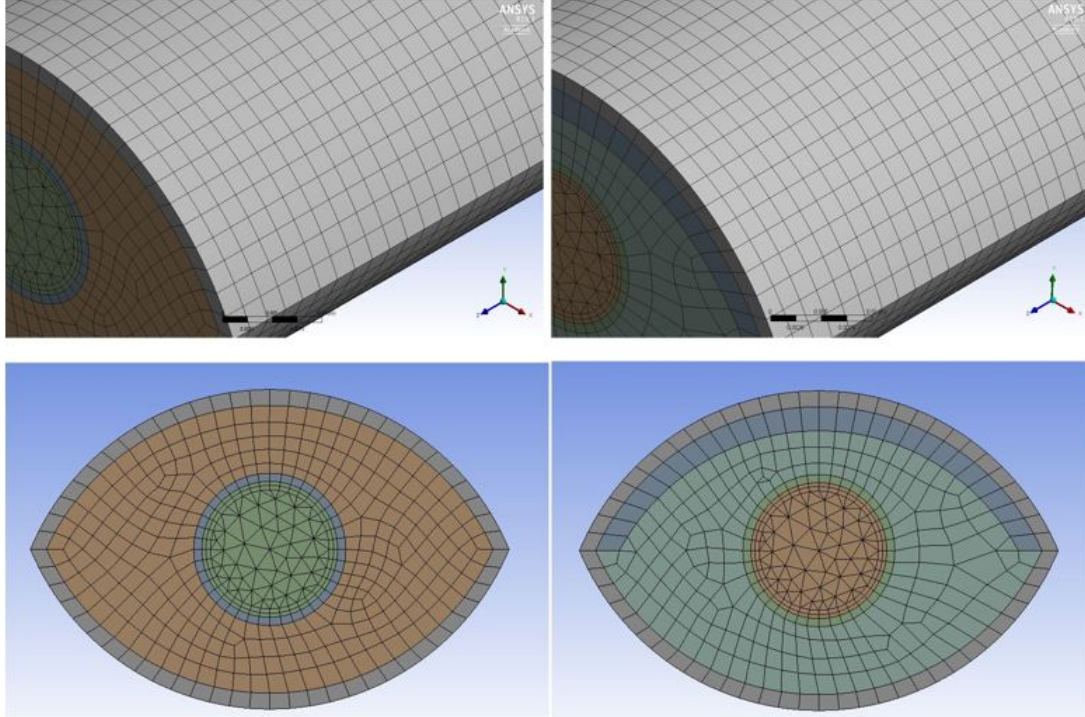


*Figure 5.7: Longitudinal and cross-section mesh of the non-insulated and insulated parabolic receiver tubes of the PTSC.*

#### 5.4 Heat transfer analysis

This section presents the basic theory for assessing the heat transfer model for the proposed receiver tube, as illustrated in Figure 5.6 (Cengel 2010; Duffie & Beckman 2013; Bellos et al. 2017; Chang et al. 2017).

The thermal efficiency ( $\eta_{th}$ ) of the receiver tube is the ratio of the useful heat gain ( $Q_u$ ) to the input solar heat flux energy ( $Q_i$ )

$$\eta_{th} = \frac{Q_u}{Q_i} \quad (1)$$

Because the receiver tube is subjected to constant solar heat flux, the useful heat gain is:

$$Q_u = h_F(\pi D_{ai}L)(T_{aa} - T_{Fa}) \quad (2)$$

In this form,  $D_{ai}$  is the inner diameter of the absorber tube,  $L$  is the length of the absorber tube,  $T_{aa}$  is the average temperature of absorber tube inner surface,  $T_{Fa}$  is the HTF mean temperature, and  $h_F$  is the convective heat transfer coefficient.

The convective heat transfer coefficient ( $h_F$ ) is a function of the inner diameter of the absorber tube, HTF thermal conductivity ( $k_F$ ) and Nusselt number:

$$h_F = \frac{K_F Nu}{D_{ai}} \quad (3)$$

In this equation,  $K_F$  is the HTF thermal conductivity, based on the properties of water at the HTF average temperature. Because the HTF is fully developed turbulent flow in a smooth receiver tube, therefore the  $Nu$  is given by the following expression (Gnielinski 1976):

$$Nu = \frac{(f/8) Re Pr}{1.07 + 12.7 (f/8)^{0.5} (Pr^{2/3} - 1)} \quad \left( \begin{array}{l} 0.5 \leq Pr \leq 2000 \\ 3 \times 10^3 < Re < 5 \times 10^6 \end{array} \right) \quad (4)$$

In Eq. (4),  $f$  is the friction factor which can be calculated using (Petukhov 1970):

$$f = 0.184 Re^{-0.2} \quad (5)$$

The Reynolds number is calculated by:

$$Re = \frac{4\dot{m}}{\pi D_{ai} \mu_F} \quad (6)$$

where  $\dot{m}$  is the HTF mass flow rate and  $\mu_F$  is the HTF dynamic viscosity (determined using the average of the HTF temperature).

Convection and radiation heat transfer were considered between the outer surface of the glass envelope and the surrounding external environment. Therefore, the total heat transfer loss is obtained from:

$$Q_{total} = \pi D_{hg} L h_w (T_{og} - T_{amb}) + \varepsilon \pi D_{hg} \sigma (T_{og}^4 - T_{sky}^4) \quad (7)$$

where  $D_{hg}$  is the hydraulic diameter of the receiver tube's glass envelope,  $h_w$  is the convective heat transfer coefficient, which is a function of wind speed ( $u_w$ ) and is given by the following expression (Cheng et al. 2012; Bellos et al. 2017):

$$h_w = 4u_w^{0.58} D_{hg}^{-0.42} \quad (8)$$

where  $T_{og}$  is the temperature of the outer surface of the glass envelope,  $T_{amb}$  is the ambient temperature (set to 300 K),  $\varepsilon$  is the glass envelope emissivity,  $\sigma$  is the Stefan-Boltzmann constant,  $T_{sky}$  is the sky temperature which is given by (Swinbank 1963; Chaabane et al. 2015; Bellos et al. 2017):

$$T_{sky} = 0.0552T_{amb}^{1.5} \quad (9)$$

*Table 5.3 Dimension and parameter properties used in numerical simulation.  $T_{amb}$  is the ambient temperature,  $T_{sky}$  is the sky temperature,  $D_{hg-P}$  is the hydraulic diameter of the glass envelope for the parabolic receiver tube,  $D_{hg-H}$  is the hydraulic diameter of the glass envelope for the hybrid receiver tube and  $D_{OD-C}$  is the outer diameter of the circular receiver tube.*

<b>Parameter</b>	<b>Value</b>	<b>Parameter</b>	<b>Value</b>
$T_{amb}$	300 K	$D_{OD-C}$	0.06 m
$T_{sky}$	286.82 K	$L$	1.2 m
$D_{hg-P}$	0.0414 m	Borosilicate conductivity ( $K_g$ )	1.2 W/m.K
$D_{hg-H}$	0.053 m	Specific heat ( $C_p$ )	800 J/kg.K

## 5.5 Mesh independence

A mesh independence test was conducted to ensure the numerical results are independent of the grid. For each design of the study, several meshes were investigated with different numbers of elements. Table 5.4 shows the results of the grid independence test for the insulated and non-insulated receiver tube designs. For each configuration, the results for the case with the most elements are independent of the mesh; these meshes were used in all simulations. Finally, it can be seen that the cells' distribution of the air domain do not influence the accuracy of the numerical results.

Table 5.4 Number of mesh elements and the calculation of useful heat gain for the insulated and non-insulated of the proposed receiver tubes.

Insulated Parabolic Receiver Tube			Non-Insulated Parabolic Receiver Tube		
Case	Mesh Elements	Useful heat (W)	Case	Mesh Elements	Useful heat (W)
1	394378	588.12	1	374422	579.73
2	394637	587.56	2	391741	576.35
3	405095	586.96	3	394097	575.92
4	406805	585.57	4	399310	579.719184
5	415553	585.56	5	403214	579.71
Insulated Hybrid Receiver Tube			Non-Insulated Hybrid Receiver Tube		
Case	Mesh Elements	Useful heat (W)	Case	Mesh Elements	Useful heat (W)
1	364582	875.01	1	399234	882.93
2	383698	878.34	2	392087	876.82
3	394417	865.58	3	404505	883.58
4	403597	888.15	4	404777	883.60
5	405085	888.15	5	434387	883.61
Insulated Circular Receiver Tube			Non-Insulated Circular Receiver Tube		
Case	Mesh Elements	Useful heat (W)	Case	Mesh Elements	Useful heat (W)
1	469326	885.22	1	469601	885.54
2	477998	884.53	2	469801	883.59
3	482842	890.38	3	476125	893.57
4	484878	893.64	4	477832	893.61
5	505820	893.64	5	502299	893.61

## 5.6 Boundary conditions

This section presents the boundary conditions (BC) and assumptions that were adopted in the numerical simulation for all the simulations. For the heat transfer fluid (HTF), the inlet mass flow rate value and its inlet temperature were considered to be 0.06 kg/s and 300 K respectively, while the outlet BC is defined to be Outflow to ensure fully developed conditions occurred (Kaloudis et al. 2016; Gong et al. 2017). The lower

portion of absorber tube surface received concentrating solar reflected flux due to it facing the reflector side. The concentrated solar heat flux calculated from SolTrace was applied on the absorber tube's outer surface (Chandra et al. 2017). Due to the outer surface of the glass envelope being surrounded by external environmental conditions, a mixed thermal boundary conditions option was selected to combine convection and radiation BC. The wind heat transfer coefficient ( $h_w$ ) around the receiver glass cover was calculated by Eq. (8) and the sky temperature ( $T_{sky}$ ) was calculated by Eq. (9) The Reynolds number inside the absorber tube is higher than 4000 in all cases, thus the HTF flow rate is turbulent in all cases. Finally, the two ends of the alternative receiver tube were treated as adiabatic walls. PTSC receiver tube ends are normally wrapped with insulation material to reduce the heat transfer losses.

### **5.7 Setup of the numerical model**

The receiver tube model was analysed by Computational Fluid Dynamics (CFD) software Fluent 19.1. Conduction, convection and radiation heat transfer as well as gravitational forces were considered in the solution. To also solve the model heat transfer, the energy model was also considered. The realisable k-epsilon turbulent model with the enhanced wall treatment was used (Kalogirou 2012; Xu, L. et al. 2014). The surface to surface (S2S) radiation model was used, so the components of the receiver tube (absorber tube, glass cover and insulation) were considered to be grey and diffuse surfaces. The coupled solution method was used for coupling pressure and velocity (Patankar & Spalding 1983), and weighted body force was considered for pressure discretisation. The second order upwind method was selected for momentum and energy, while the first order upwind method was used for all other equations (Cheng et al. 2012; Wu et al. 2014). The absolute convergence criterion achieved by the solutions is approximately  $10^{-4}$ .

### **5.8 Model validation**

The PTSC experimental model of this thesis was used to validate the numerical models. The dimensions of the PTSC's components are listed in Table 5.2. The results of the CFD validation (Figure 5.8) revealed a good agreement with the experimental results, because the difference between the numerical and experimental HTF outlet temperatures was relatively constant for all the validation tests. It is clear that the CFD results are higher than the experimental results by approximately  $1.4^{\circ}\text{C}$  for all the

simulation cases, which can be seen also from Table 5.5. The difference between the CFD results and the experimental results was due to the limitations of Fluent. For instance, Fluent could not apply both solar radiation and convection heat transfer on the outer surface of the absorber tube at same time, as it occurred in the experimental tests.

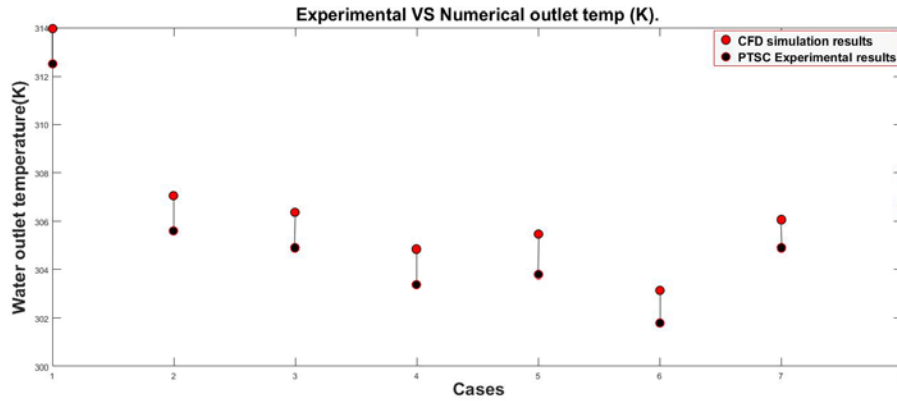


Figure 5.8: Numerical results of the CFD model vs experimental results of the PTSC heating system. X axis cases refers to the cases in Table 5.5

Table 5.5 CFD results vs experimental results in addition to testing environment conditions. Volume flow rate equal to  $0.06 \text{ L.s}^{-1}$ . SR is the solar radiation ( $\text{W.m}^{-2}$ ),  $T_{amb}$  is the ambient temperature ( $^{\circ}\text{C}$ ), and WS is the wind speed ( $\text{m.s}^{-1}$ ).  $T_{in}$  is the inlet temperature ( $^{\circ}\text{C}$ ),  $T_{out}$  is the outlet temperature ( $^{\circ}\text{C}$ ). %T is the percentage increase in the raised temperature computed by the simulations compared to the experiments.

Case	Date of experimental test	SR ( $\text{W.m}^{-2}$ )	$T_{amb}$ ( $^{\circ}\text{C}$ )	WS ( $\text{m.s}^{-1}$ )	$T_{in}$ ( $^{\circ}\text{C}$ )	$T_{out}$ (experimental results)	$T_{out}$ (numerical results)	%T
1	26/04/2018	1127	297.1	2.2	310.4	312.5	313.96	69.5
2	20/05/2018	1107	290.7	4.4	303.5	305.6	307.06	69.5
3	21/05/2018	1134	291.2	2.78	302.8	304.9	306.35	69
4	22/05/2018	1127	289.6	5	301.3	303.4	304.86	69.5
5	23/05/2018	1084	292.3	2.78	301.9	303.8	305.46	87
6	14/07/2018	1142	284.7	2.78	299.6	301.8	303.15	61.3
7	17/07/2018	1115	290.7	2.32	302.5	304.9	306.06	48.3
8	18/07/2018	1119	290.9	5	304.5	306.6	308.06	69.5

## 5.9 Summary

In this chapter, details of insulated and non-insulated alternative receiver tubes were presented. These receiver tube models are simulated for convection cooling by the wind in Chapter 6 to evaluate the effect of the thermal insulation on the receiver tube collection efficiency. In order to evaluate the accuracy of the simulation model, selected experimental results (in addition to their testing conditions, as per Table 5.5),

were simulated using Fluent. The simulation results show a good agreement with the experimental results. The tests were completed for a range of wind speeds to evaluate the effect of the thermal insulation on the receiver tube efficiency.

# Chapter 6 Analysing effects of thermal insulation on alternative receiver tube performance

## 6.1 Introduction

The purpose of this chapter is to study and analyse the effect of thermal insulation on PTSC receiver tube performance (Figure 5.2) for three different receiver tube designs. The first design is the circular receiver tube, for which numerical results of insulated and non-insulated designs for variation wind speeds are analysed and presented. The temperature distribution of the receiver tube components governs the system heat transfer to reveal the thermal insulation effect on the domain temperature distribution and thermal performance. The results for the hybrid and parabolic receiver tubes are similarly presented, then all three designs are compared.

## 6.2 Circular receiver tube

### 6.2.1 Glass envelope and annular domains temperatures distribution

Figure 6.1 shows the cross-sectional temperatures of the glass envelope wall, insulation layer and air domain for the insulated and non-insulated circular receiver tube at both ends and middle of the receiver tube for the extreme values of wind speed. Appendix A contains the equivalent results for intermediate wind speeds. From these figures it can be seen that the receiver temperature distribution is strongly influenced by the concentrated solar heat flux on the absorber wall, as observed in other studies (Bellos et al. 2017; Chandra et al. 2017; Mwesigye & Meyer 2017). Therefore, the lower half of the tube cross section is much hotter than the upper half. The temperature distribution in the axial direction is almost constant along the receiver tube length, which follows the trend of the absorber tube, this phenomenon was also found in other studies (Kaloudis et al. 2016; Mwesigye et al. 2016; Gong et al. 2017).

It can also be seen that the air domain temperature is much higher than absorber tube wall and HTF temperatures, which could be due to several reasons. One of the reasons is that the air domain ends are insulated (closed domain) and the thermal transmissivity between the air domain and outer surface of the absorber tube is very limited. However, inside the absorber tube, the HTF flows and therefore it absorbs a substantial amount of heat from the tube wall. This high heat absorption is because the thermal transmissivity between the HTF and the inner surface of the absorber wall is much higher than that between the air domain and outer surface of the tube. The other reason is that under the same supplied heat flux, the air's thermal energy capacity is much lower (due to it having very low density and also lower specific heat) compared to thermal energy capacities of the absorber tube (copper material) and HTF (water) and therefore the air domain temperature is increased significantly.

Comparing between insulated and non-insulated designs, it can be easily identified that the air in the insulated design is much hotter than in the non-insulated design. This difference is because of the low thermal conductivity (0.04 W/m.K) of the insulation material (glass wool) compared to the thermal conductivity of the glass envelope material (around 1.2 W/m.K). This insulation layer reduced conduction heat transfer across the glass cover wall, which reduced the glass cover outer surface temperature and ultimately reduced forced convection heat transfer between the outer surface of the glass envelope and the outer environment. This reduction in heat losses kept the insulated annular air domain around 70 °C higher than in the non-insulated design. This hot air domain increased the absorber tube's outer surface temperature, which enhanced the conduction heat transfer across the absorber wall. Therefore, it transferred more heat to the HTF. This resulted in improving the insulated receiver tube's thermal performance.

When the wind speed varied from 1.5 m/s to 6.5 m/s, the temperature distribution of the air domain and the glass envelope of the non-insulated receiver tube changed significantly. This is due to the conductivity of the glass envelope, which enhanced the conduction heat transfer across the glass wall, and, as a result, the convection heat loss (due to increasing wind speed) on the envelope outer surface increased. However, the insulated layer limits the influences of wind speed variation.

The reduction in temperature of the receiver glass envelope and its air domain due to increased wind speed was very limited for both the insulated and non-insulated receiver tube. This is due to two main reasons. The first reason is the low value of the current collector concentrating ratio ( $CR = 11.7$ , while for a commercial collector the  $CR$  reaches up to 30), which made the concentrating solar radiation on the absorber tube (in the current project) relatively low. Therefore, this produced a low temperature for the receiver tube outer surface—which created a small temperature difference between the receiver tube and outdoor conditions—and, as a result, the receiver thermal loss was small and therefore the receiver tube temperature reduction was very limited. The second reason is that the receiver tube is short (1.2 m) and its outer diameter is small (0.06 m) compared by conventional receiver tube dimensions (that has outer diameter 0.125 m and length of each row of collectors reaches up to 150 m). Therefore (in the current project) this produced a small outer surface area of the receiver tube glass envelope—which was exposed to the wind effect—and therefore the heat loss is small, which resulted in limiting the observation of the effect of the insulation.

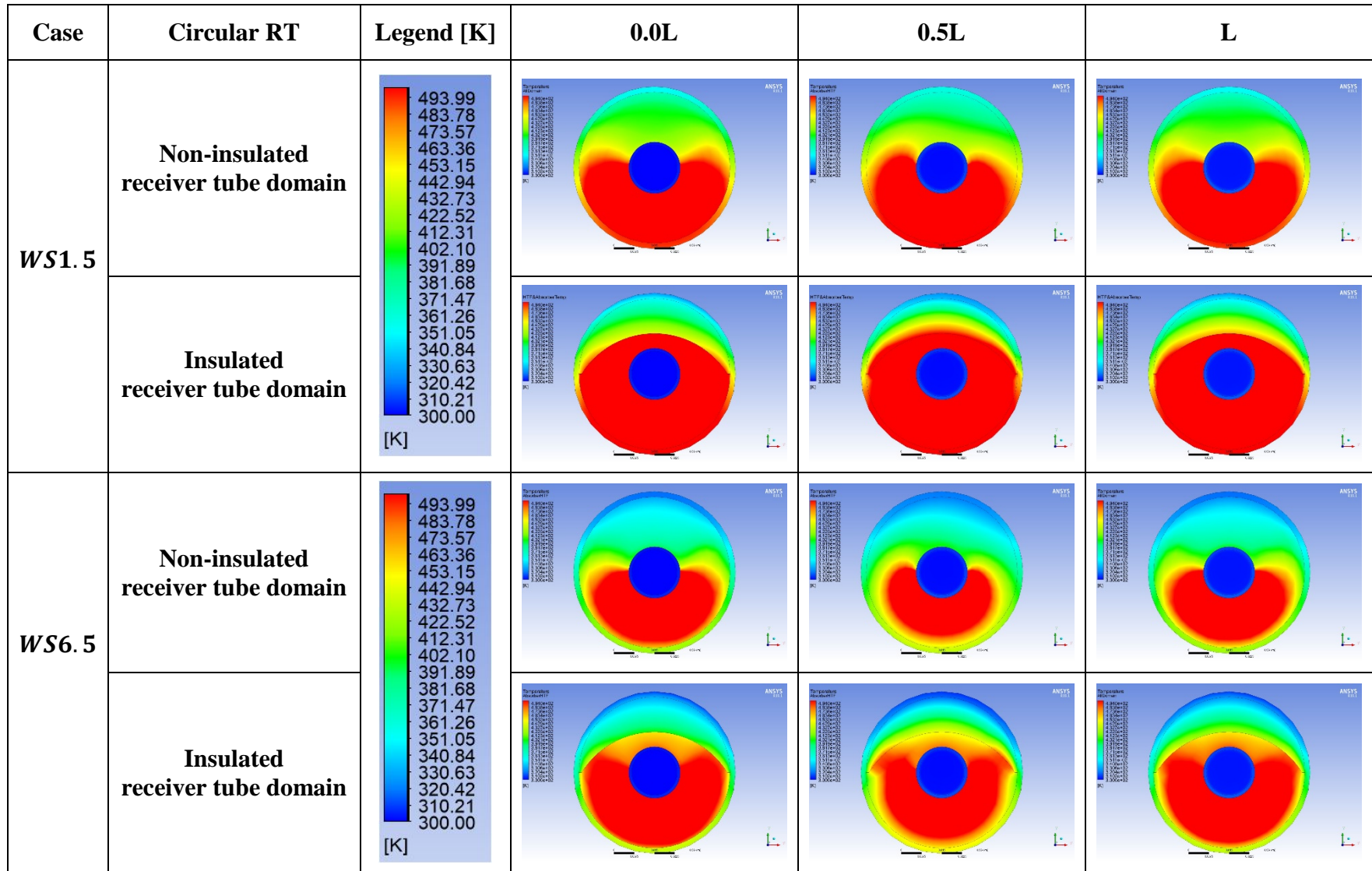


Figure 6.1: Temperature distribution of annular air and glass envelope domain of non-insulated and insulated circular receiver tubes (shapes E and F in third row in figure 5.2) for smallest and largest variation wind speed (WS): 1.5 m/s and 6.5 m/s. Results are shown for different stations along the tube (0.0L, 0.5L and L).

## 6.2.2 Temperature distribution of the absorber tube and HTF domains

Figure 6.2 presents the temperature distribution of the absorber tube wall and HTF cross section area at both ends and the middle of the insulated and non-insulated receiver tube for the smallest and largest wind speed variation (1.5 m/s and 6.5 m/s). These simulations are undertaken under constant values of solar heat flux ( $1000 \text{ W.m}^{-2}$ ), water volume flow rate ( $0.06 \text{ L.s}^{-1}$ ) and ambient air temperature (300 K). Unsurprisingly, the absorber tube wall is hotter at the bottom than the top, owing to the solar heat flux distribution. It can also be observed that the absorber wall temperature is increased along the axial direction, as also noticed in other studies (Kaloudis et al. 2016; Gong et al. 2017). . This is because the HTF becomes hotter as it flows through the absorber tube, so the thermal energy supplied by the absorber tube's wall decreases for the same HTF temperature rise.

For the HTF temperature distribution, it was observed that the HTF temperature increased along the absorber tube length due to absorbing solar heat flux that was supplied along the absorber pipe. The HTF is hottest towards the bottom because it is heated directly by the lower part of absorber wall (where the reflected solar flux is concentrated). Because the HTF domain is heated by convection heat transfer from the hot wall, the temperature in the centre of the fluid domain is less than temperature at the peripheral layers.

The obtained results show that the insulation layer slightly increases the fluid's average temperature and the absorber tube's inner surface temperature. The absorber wall temperature is almost constant under variation of wind velocity and increasing wind velocity does not make a clear difference. As mentioned above, that is due to the low value of the collector's CR and its small surface area.

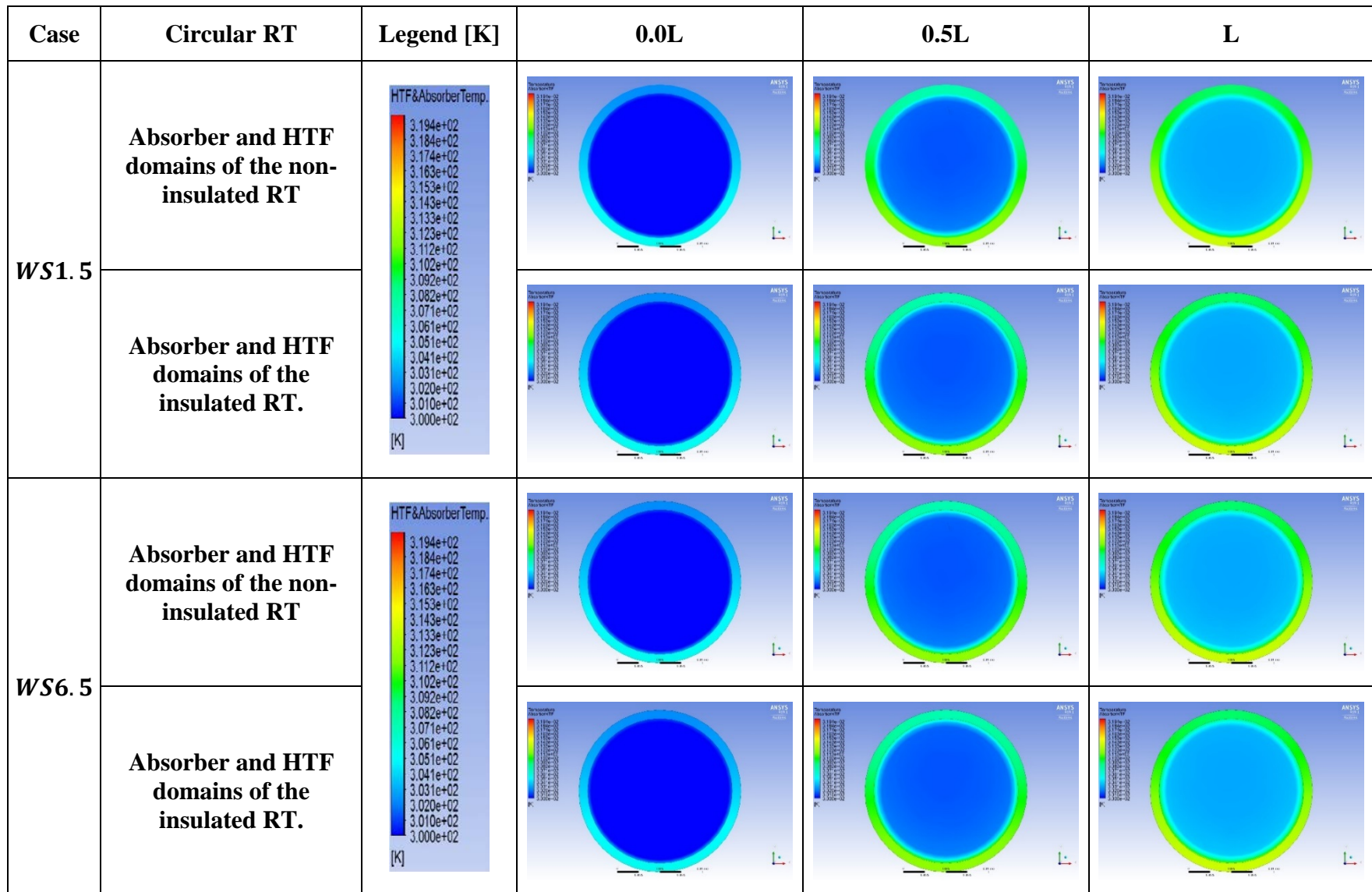


Figure 6.2 Temperature distribution of absorber tube wall and HTF domain of non-insulated and insulated circular receiver tube for smallest and largest variation wind speed (WS): 1.5 m/s and 6.5 m/s. Results are shown for different stations along the tube (0.0L, 0.5L and L).

### 6.2.3 Outer surface of glass envelope average temperature

Figure 6.3 shows the average temperature over the outer surface of the glass envelope for the insulated and non-insulated receiver tubes for various wind speeds. All case tests were conducted under constant values of water volume flow rate ( $0.06 \text{ L.s}^{-1}$ ), HTF (water) inlet temperature (300 K) and solar heat flux ( $1000 \text{ W.m}^{-2}$ ). Increasing wind speed caused both insulated and non-insulated receiver tube glass cover average temperatures to decrease due to the effect of forced convection, this glass temperature reduction due to increasing wind speed was also observed in another study (Patil, Panse, et al. 2014).

In addition, it can be also seen that the insulation decreases the glass cover temperature, particularly at lower wind speeds, due to reduced conduction losses across the glass wall. As wind speed increases, the temperatures for the two designs converge because the heat losses on the bottom surfaces (which are not insulated in either configuration) become much higher than the heat losses on the top surfaces, so the effect of the insulation is weaker.

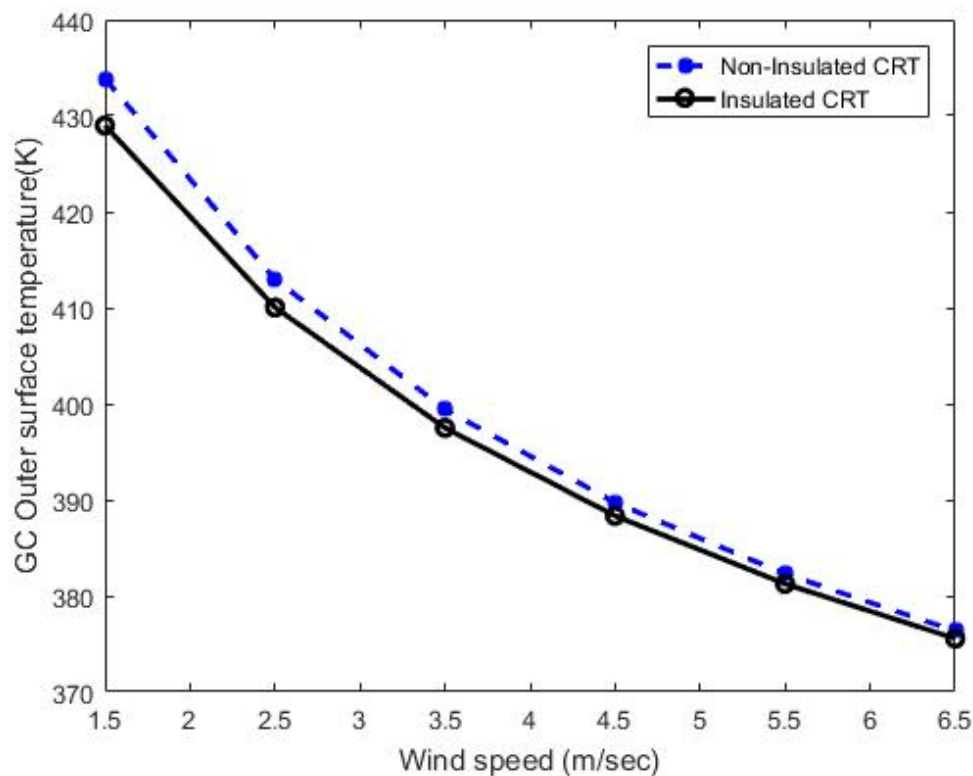


Figure 6.3: Glass cover outer surface temperature for the insulated (black) and non-insulated (blue) circular receiver tube with wind speed variation and constant solar heat flux ( $1000 \text{ W.m}^{-2}$ ), water volume flow rate ( $0.06 \text{ L.s}^{-1}$ ), ambient and HTF inlet temperatures ( $300 \text{ K}$ ).

### 6.2.4 Average temperature difference between absorber tube and HTF

The average temperature difference between the absorber tube wall and the HTF is an essential parameter for determining useful heat gain, heat loss and receiver tube efficiency (section 5.4)

Figure 6.4 shows that the average temperature difference between the inner surface of the absorber tube and the HTF for both designs is not affected by wind velocity. This is mainly due to the low thermal transmissivity between the enclosed air (that directly affected by the W.S.) and absorber tube outer surface limiting the effect of any change in the air temperature on the absorber wall temperatures

By comparing both designs it can be seen that the average temperature difference of the insulated case is higher by around 0.04%. As mentioned previously, the insulated material reduces the influence of the forced heat transfer convection around the

insulated receiver tube, which reduces the cooling effect of wind speed across the glass cover wall. Therefore, the air domain temperature of the insulated receiver tube remains relatively higher compared with the non-insulated design. This kept the outer surface absorber wall hotter which relatively enhanced the conduction heat transfer across the absorber wall towards the HTF. Finally, this increased the HTF's useful heat gain and also reduced the heat loss of the insulated receiver tube.

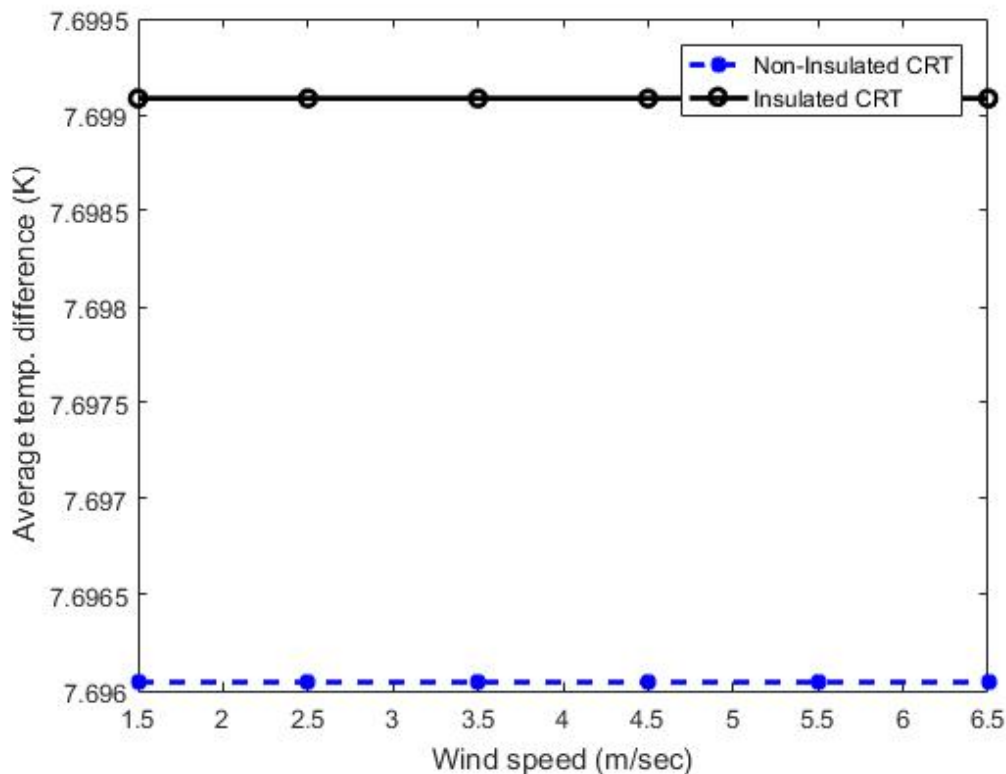


Figure 6.4: Average temperature difference between inner surface of the absorber tube and the HTF for the insulated (black) and non-insulated (blue) circular receiver tubes' collecting efficiency with wind speed variation and constant solar heat flux ( $1000 \text{ W.m}^{-2}$ ), water volume flow rate ( $0.06 \text{ L.s}^{-1}$ ), ambient and HTF inlet temperatures ( $300 \text{ K}$ ).

## 6.2.5 System heat transfer

Figure 6.5 shows the insulated and non-insulated receiver tubes' heat loss to the environment for variations in wind speed. It can be seen from the figure that both designs have relatively constant heat loss under various wind speeds. This trend of constant receiver heat loss under varying wind speed is also observed in section 2.3.1, as illustrated in Figure 2.31 (Patil, Panse, et al. 2014). Besides that, this trend of constant receiver heat loss for different wind velocities was also observed in another study's figure 3 (Daniel et al. 2011). As mentioned previously, this is not only because

of the constant supplied heat flux ( $1000 \text{ W.m}^{-2}$ ) and the low CR, but also due to the short length of the receiver tube (1.2 m) and small outer diameter (0.06 m),, which means there is a very small receiver outer surface area (compared to the commercial receiver tube with dimensions 7.8 m length and 0.115 m outer diameter) (García-Valladares & Velázquez 2009) exposed to the wind. In addition, the insulation has slightly reduced the insulation receiver tube heat loss.

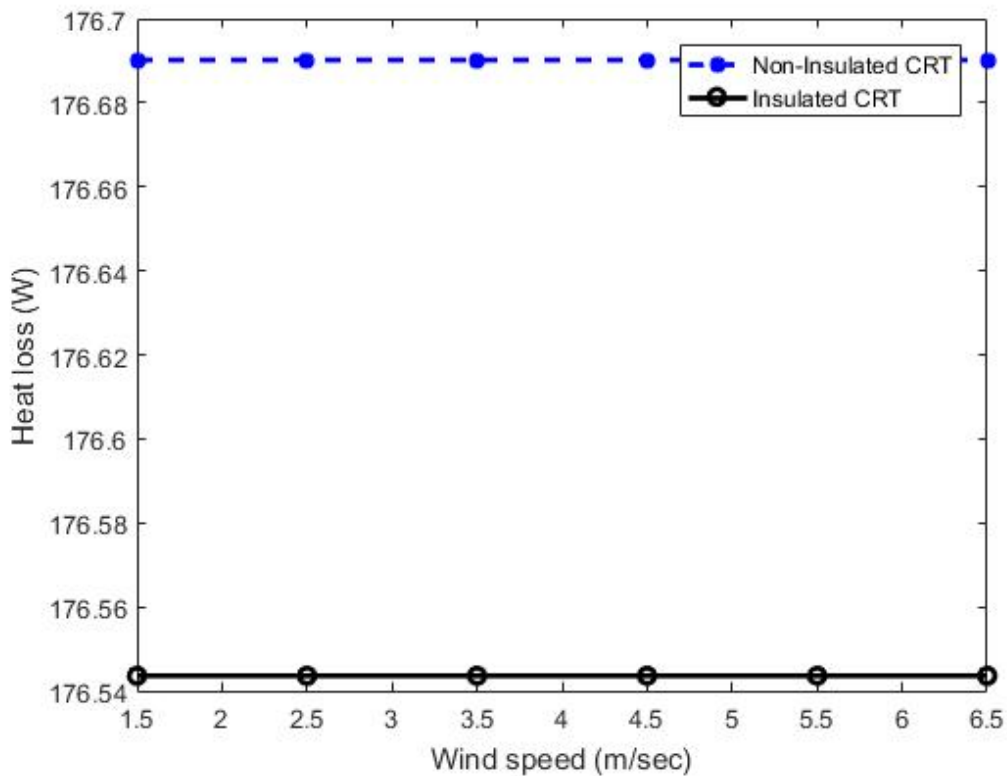


Figure 6.5: Heat loss of the insulated (black) and non-insulated (blue) circular receiver tubes under effect of wind speed variation and constant solar heat flux ( $1000 \text{ W.m}^{-2}$ ), water volume flow rate ( $0.06 \text{ L.s}^{-1}$ ), ambient and HTF inlet temperatures (300 K).

Figure 6.6 shows the receiver tube collecting efficiency for both designs. As expected, the collecting efficiency of both receivers is relatively constant due to the constant value of the heat loss for variations of wind speed. In addition, as anticipated, the insulated receiver tube collecting efficiency is higher than that of the non-insulated receiver. This difference is mainly due to the glass wool insulation effect which reduces the outer glass cover temperature of the insulated receiver. This results in reducing the heat loss that occurs due to convection and radiation between the outer surface of the glass cover and the environment (Hachicha et al. 2013; Wu et al. 2015; Navarro-Hermoso et al. 2016). The minor enhancement in the modified receiver

(insulated receiver) is due to the low collector concentration ratio, which results in low absorber wall temperature, air and glass cover temperatures. And also, as mentioned before, it is due to the small receiver tube surface area.

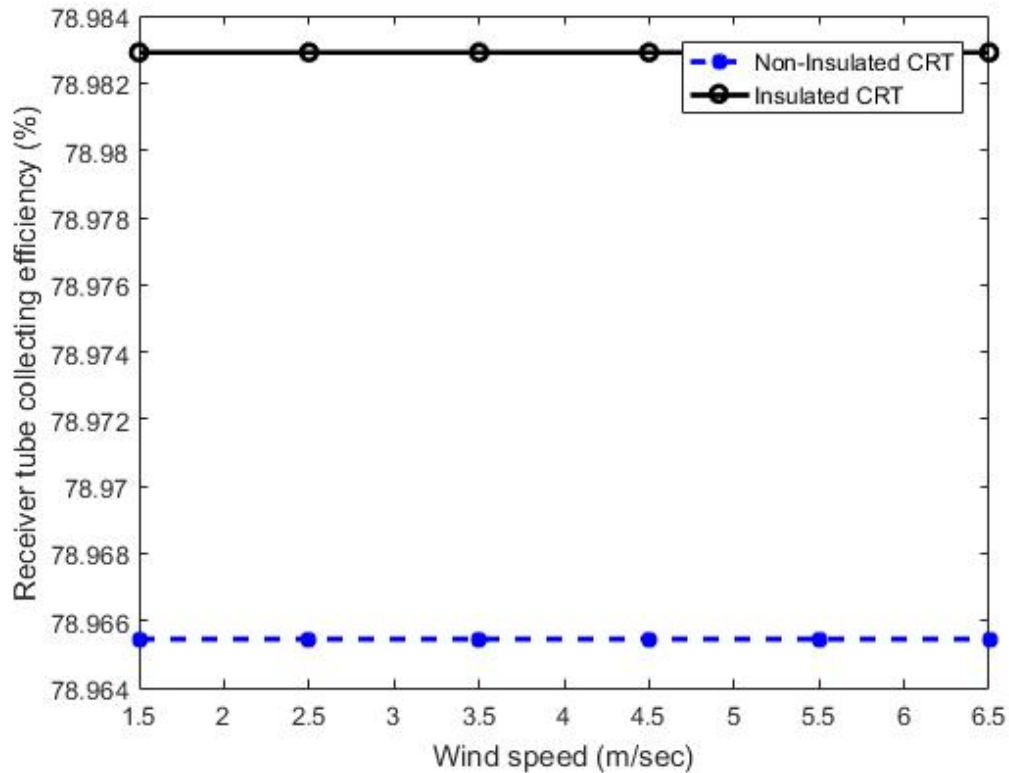


Figure 6.6: Insulated (black) and non-insulated (blue) receiver tubes' collecting efficiency with wind speed variation and constant solar heat flux ( $1000 \text{ W.m}^{-2}$ ), water volume flow rate ( $0.06 \text{ L.s}^{-1}$ ), ambient and HTF inlet temperatures ( $300 \text{ K}$ ).

### 6.3 Hybrid and parabolic receiver tubes

In order to investigate the possibility of utilising other new designs of PTSC receiver tubes and evaluating their performances against the performance of the circular receiver tube, hybrid and parabolic receiver tubes have been designed (as presented in Figure 5.2) and investigated.

The hybrid receiver is created by adjusting the upper portion of the circular receiver tube glass envelope to match the shape of the secondary reflector (section 3.4.1 includes all details of the secondary reflector).. This design sets the upper part of the circular glass envelope (the standard design) to be the shape of the secondary reflector (SPM) (see Figure 5.2). This could produce a simple method for inserting a thermal insulation layer on the inner surface of the receiver glass envelope

instead of adjusting the insulation itself to be the secondary parabolic shape, as done for the circular receiver. In addition, this design could also produce a more rigid structure for the insulation layer than in the circular design, because the insulation layer profile is the same the shape as the upper portion of the glass envelope.

The parabolic receiver tube is designed by adjusting the lower portion of the hybrid glass cover to also be parabolic. In this design, both the lower and the upper parts of the glass cover are symmetrical to make this receiver tube have a symmetrical cross-section as is done for circular, rectangular or elliptical metal tubes. Just like the hybrid design, it also has the advantage of the parabolic upper portion of the glass envelope that is useful for insertion of the insulation layer and the rigid structure of the insulation shape. The width of the glass cover receiver of the hybrid and the parabolic are equal to the width of the secondary reflector (dead zone—section 3.4.1), as in the circular receiver tube. This helps to utilise the SPM's dead zone (the experimental optical enhancement) to improve the thermal performance of these receivers.

### **6.3.1 Annular air and glass envelope domain temperature distribution**

Figure 6.7 and Figure 6.8 show the cross-sectional temperatures of the glass envelope's air domain at both ends and the middle of the insulated and non-insulated hybrid and parabolic receiver tubes for the smallest and largest wind speed variation (1.5 m/s and 6.5 m/s). Appendices B and C also show intermediate wind speeds. As in the circular receiver case, the investigations for both receivers are performed for constant values of solar heat flux ( $1000 \text{ W}\cdot\text{m}^{-2}$ ), water volume flow rate ( $0.06 \text{ L}\cdot\text{s}^{-1}$ ) and ambient air temperature (300 K). The same general behaviour (temperature distribution, temperature difference between insulated and non-insulated designs and the limited effect of wind speed) as the circular receiver tube can be seen for the hybrid and parabolic receiver tubes. However, the asymmetry in the hybrid receiver tube causes the temperature distribution to be non-uniform compared to both the parabolic and circular receiver tubes. The parabolic receiver tube temperature distribution profile is different to the circular receiver tube temperature profile because the parabolic shapes produce dead corners which have a lower contribution to natural convection and are relatively far from the hot absorber tube.

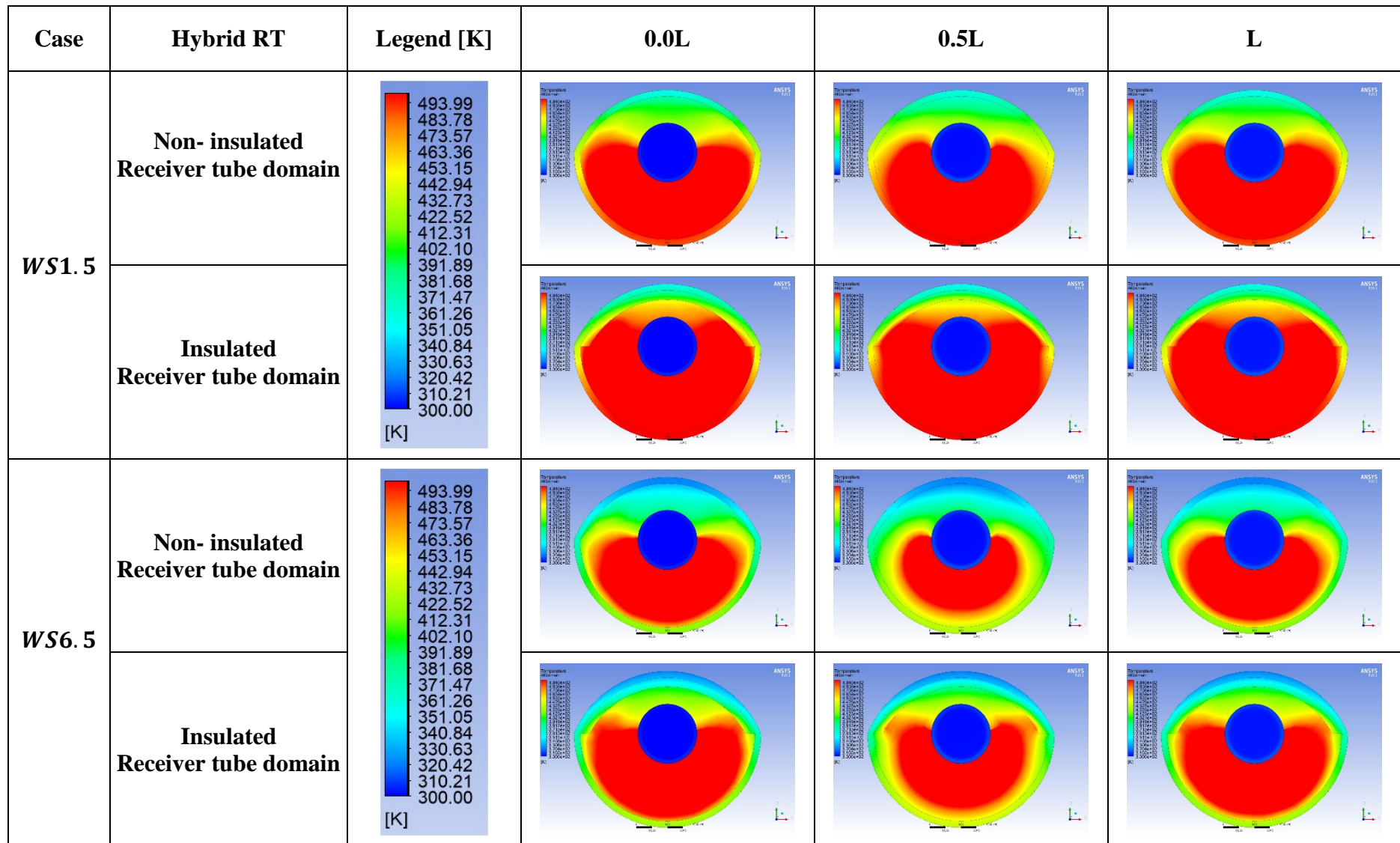


Figure 6.7: Temperature distribution of annular air and glass envelope domains of non-insulated and insulated hybrid receiver tubes (shapes C and D in the second row in figure 5.2) for smallest and largest variation wind speeds (WS): 1.5 m/s and 6.5 m/s. Results are shown for different stations along the tube (0.0L, 0.5L and L)

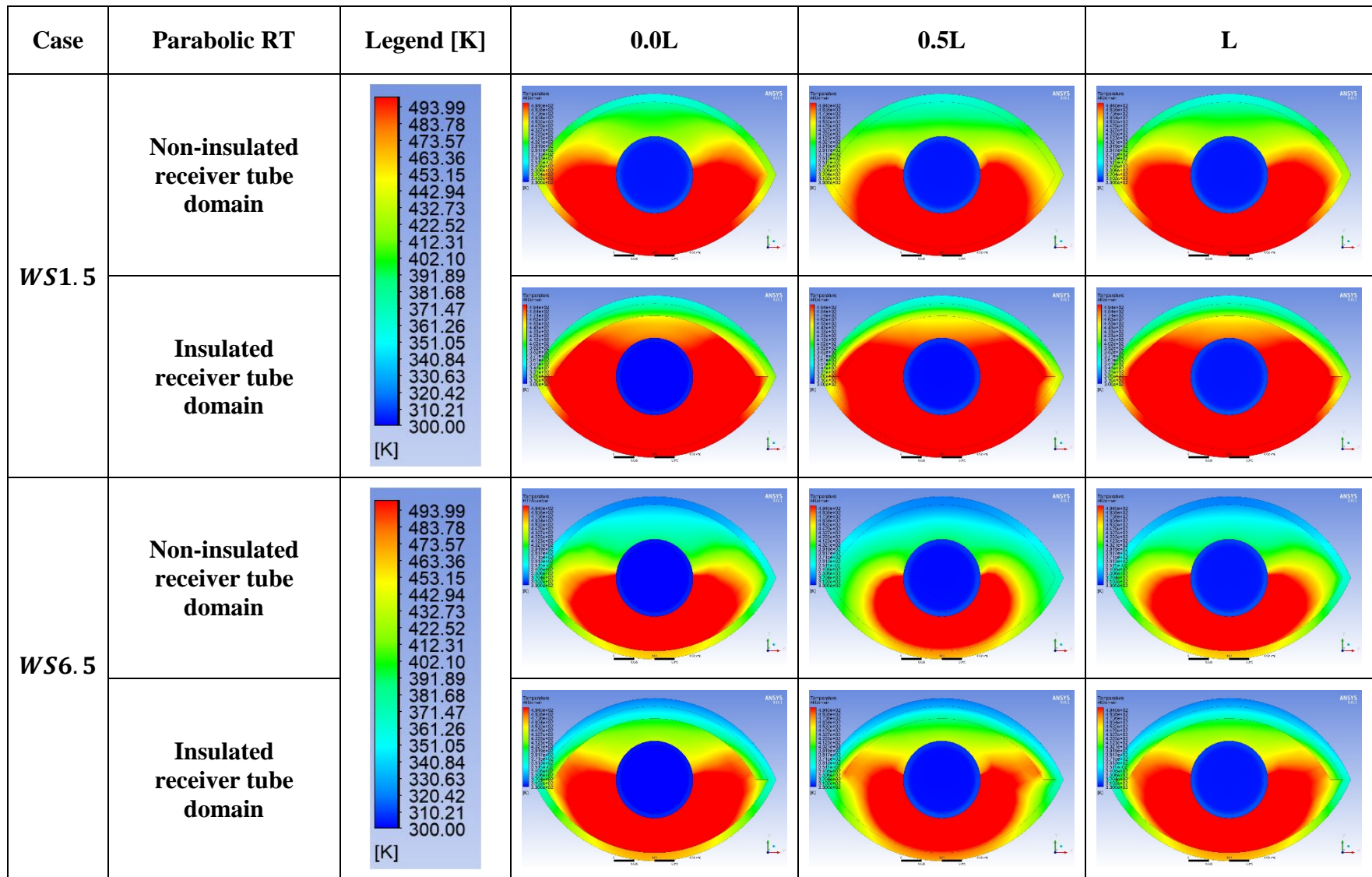


Figure 6.8: Temperature distribution of annular air and glass envelope domains of non-insulated and insulated parabolic receiver tubes (shapes A and B in the first row in figure 5.2) for smallest and largest variation wind speeds (WS): 1.5 m/s and 6.5 m/s. Results are shown for different stations along the tube (0.0L, 0.5L and L)

### **6.3.2 Absorber tube and HTF domains temperature contour of the hybrid and parabolic**

Figure 6.9 and Figure 6.10 present the temperature distribution of the absorber tube wall and the HTF of the hybrid and parabolic tubes at both ends and the middle of the receiver tube length for the smallest and largest wind speed variation (1.5 m/s and 6.5 m/s). As in the circular receiver case, the investigations for both receivers are performed for constant values of solar heat flux ( $1000 \text{ W}\cdot\text{m}^{-2}$ ), water volume flow rate ( $0.06 \text{ L}\cdot\text{s}^{-1}$ ) and ambient air temperature (300 K). As can be seen from the figures, the same general behaviour and temperature distribution profiles as the circular receiver tube can also be seen for the hybrid and parabolic receiver tubes.

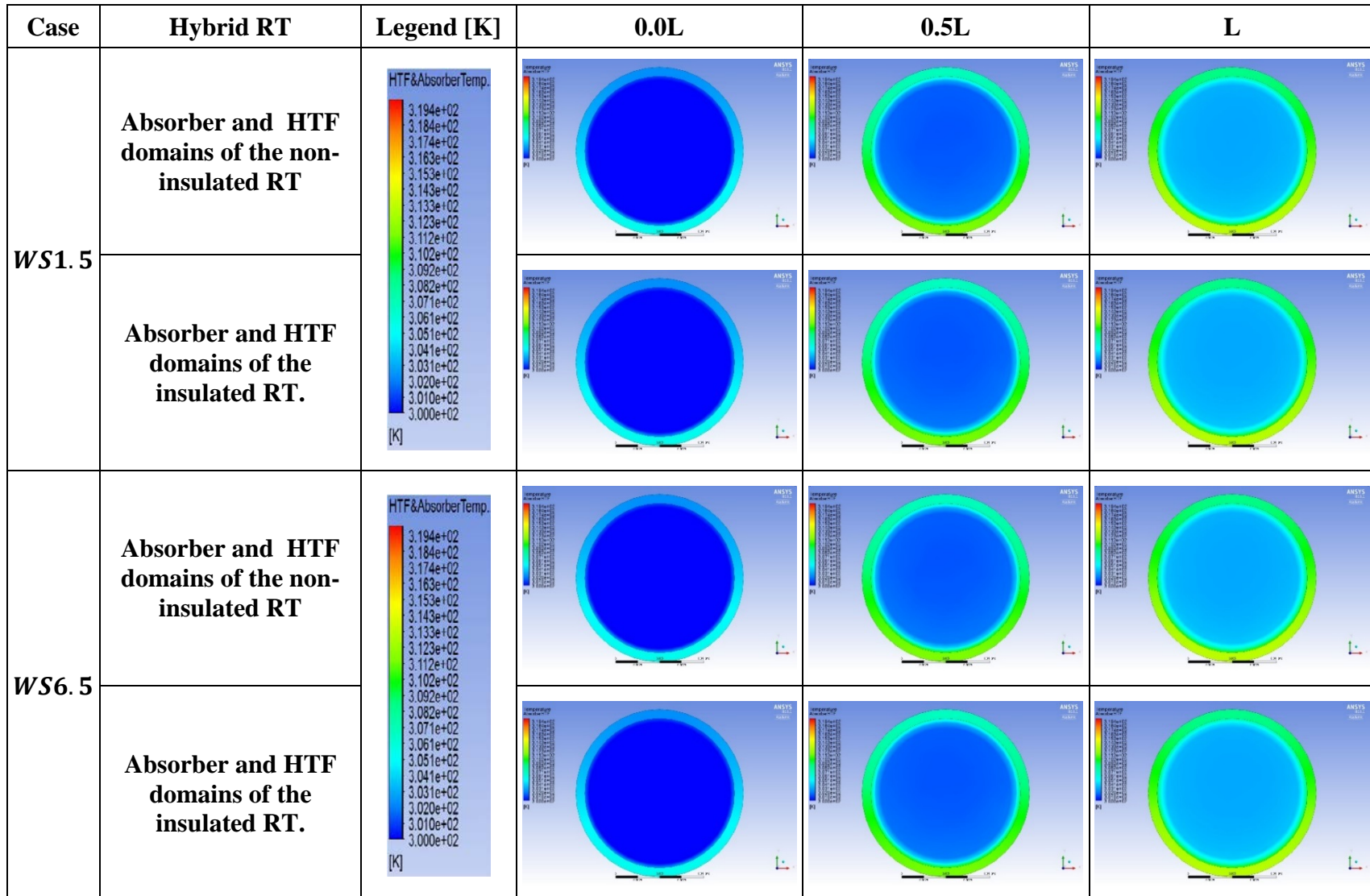


Figure 6.9: Temperature distribution of absorber tube wall and HTF domain of non-insulated and insulated hybrid receiver tubes for smallest and largest variation wind speeds (WS): 1.5 m/s and 6.5 m/s. Results are shown for different stations along the tube (0.0L, 0.5L and L).

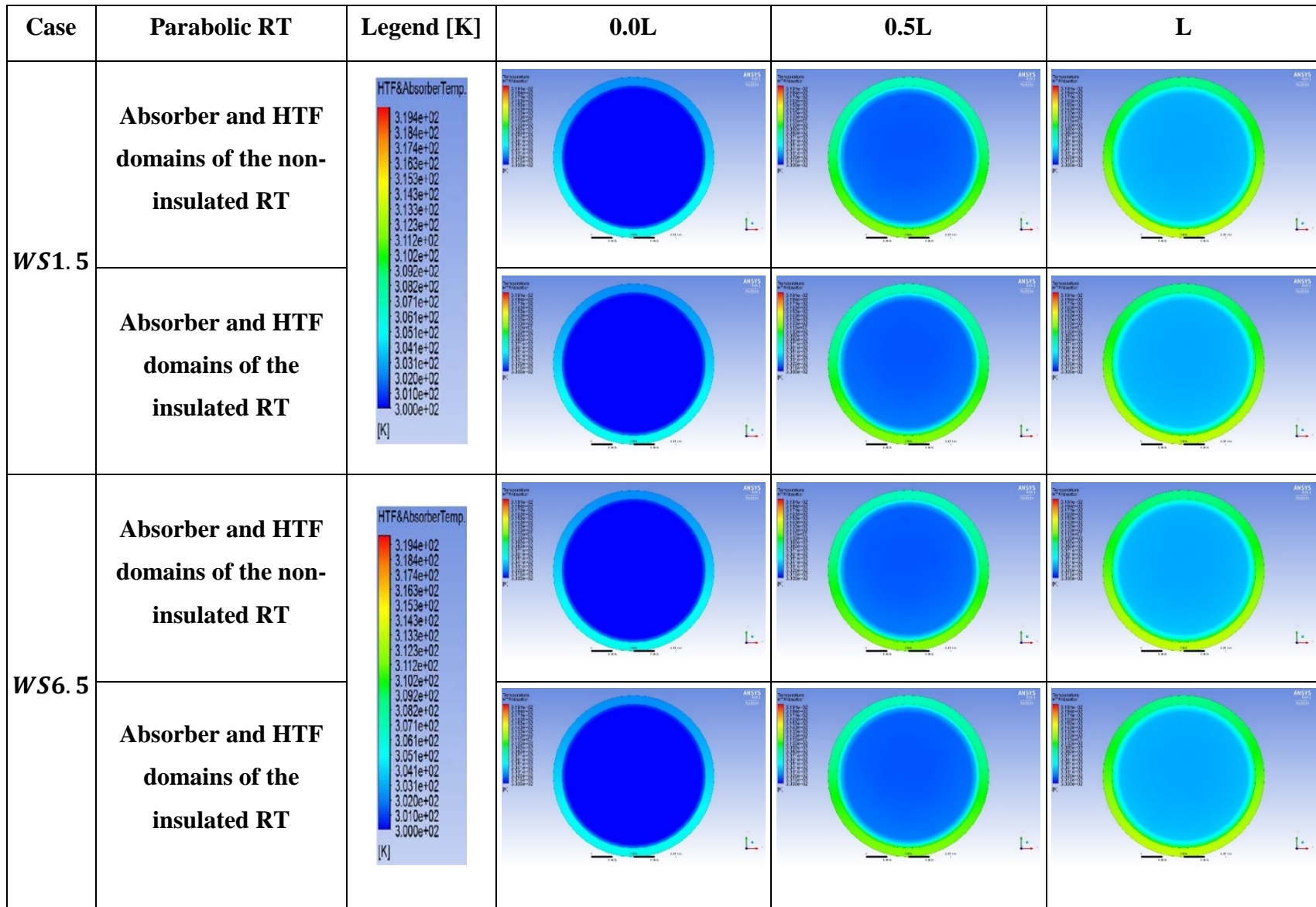


Figure 6.10: Temperature distribution of absorber tube wall and HTF domain of non-insulated and insulated parabolic receiver tubes for smallest and largest variation wind speeds (WS): 1.5 m/s and 6.5 m/s. Results are shown for different stations along the tube (0.0L, 0.5L and L).

## **6.4 Comparing between the three types of the receiver tubes**

### **6.4.1 Glass cover temperature**

Figure 6.11 shows the glass cover temperature of the three types of receiver tubes under variations of wind velocity. It can be seen that the hybrid and parabolic glass covers' temperatures reduced as wind speed increased, similarly to the circular design. In addition, it can be seen that circular design produced the lowest glass envelope temperatures, while the parabolic design produced the highest. That is due to the different hydraulic diameters of the glass envelopes of the three receivers affecting the Nusselt number and consequently the forced convection heat loss to the environment (Table 5.3).

Comparing the effects of the insulation, it was most pronounced for the circular receiver tube because the insulated layer in the circular case covered half of the circumference of the receiver glass envelope and is the thickest. The extreme thickness of the circular receiver tube's insulated layer is produced due to the adjustment of the insulation to match the circular shape of its glass envelope (the inner surface of the insulation layer for all designs is parabolic to match the SPM shape). There is a noticeable, but smaller, effect of the insulation on the parabolic receiver tube, because the insulation covers half the perimeter of the glass envelope, but the insulation layer is thinner. The effect of the insulation on the hybrid receiver tube is negligible because the insulation layer only covers the upper portion of the glass envelope (the parabolic part), that is only 22% of the glass envelope's inner surface area.

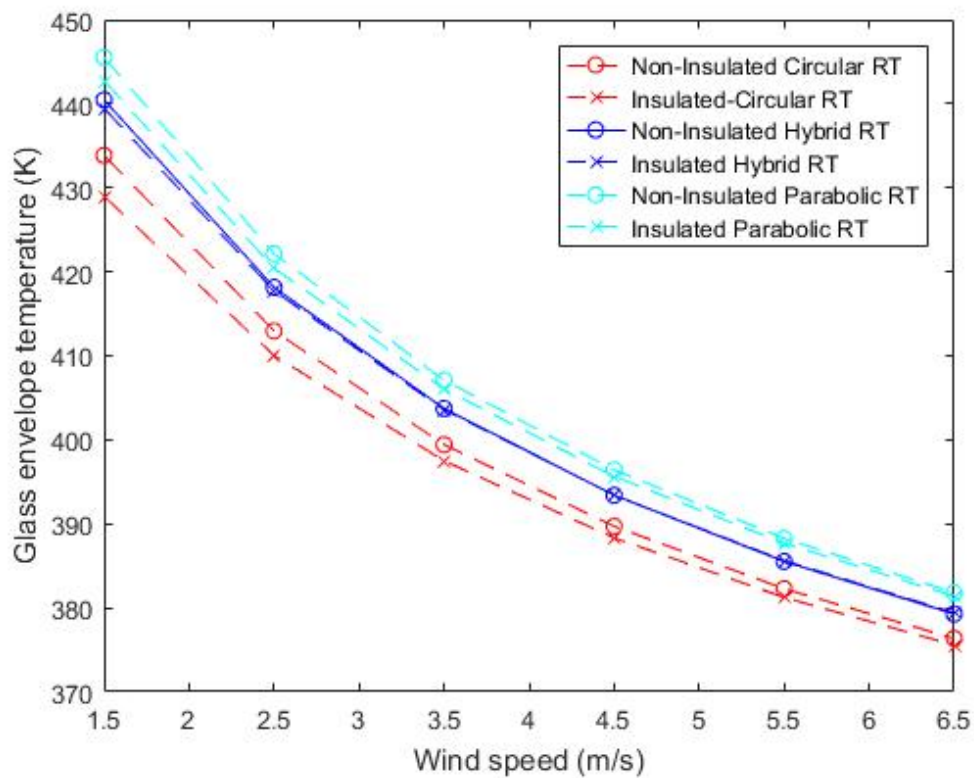


Figure 6.11: Glass envelope temperature of the insulated and non-insulated circular (red), hybrid (blue) and parabolic (green) receiver tubes under effect of wind speed variation, constant solar heat flux ( $1000 \text{ W.m}^{-2}$ ), water volume flow rate ( $0.06 \text{ L.s}^{-1}$ ) and ambient temperature ( $300 \text{ K}$ ).

### 6.4.2 System heat transfer

Figure 6.12 shows that the heat loss of all receiver tube designs is not affected by the wind speed variation (Daniel et al. 2011; PatilKale, et al. 2014).

Because the upper portion of the hybrid glass envelope is closer to the absorber tube than the circular glass envelope, there is a shorter thermal pathway from the absorber tube, reducing the thermal resistance. Therefore, without insulation, the top of the hybrid receiver is colder due to the wind influence (forced convection) and, therefore, the hybrid design has the highest heat loss. Consequently, insulating the upper portion of the hybrid glass envelope produced the highest thermal improvement. In addition, it can be seen that the heat loss of the hybrid receiver is also higher compared to the parabolic receiver tube. This is due to the air annular space of the hybrid receiver being higher, and therefore the larger volume allows hot air to circulate further around the absorber tube and, therefore, it lost more heat energy.

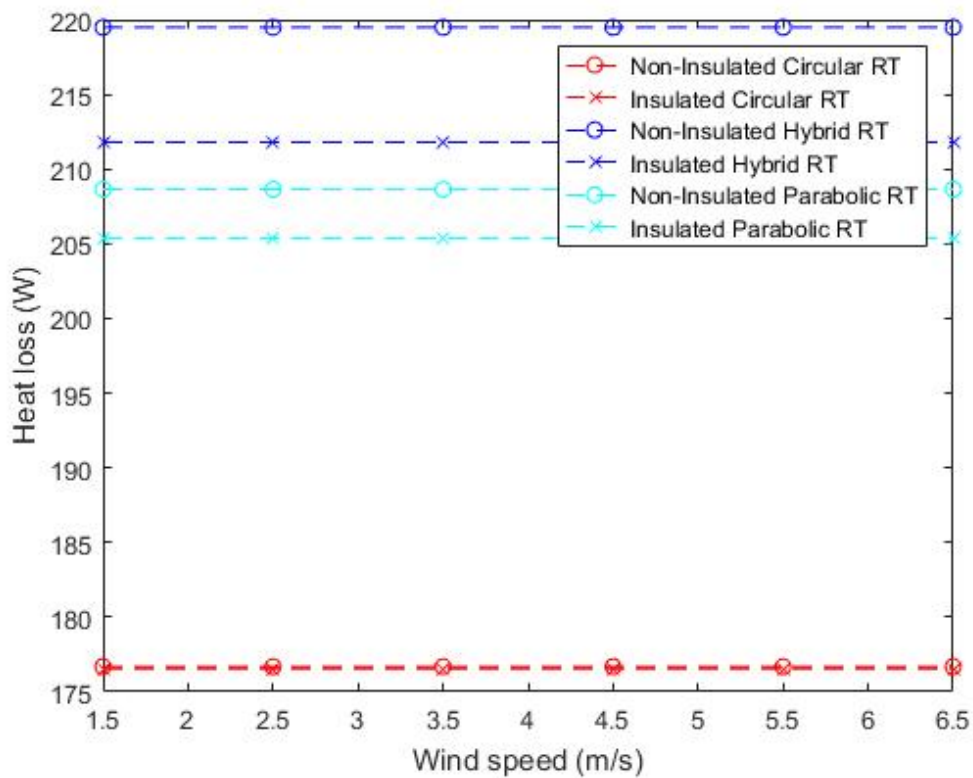


Figure 6.12: Heat loss of the insulated and non-insulated circular (red), hybrid (blue) and parabolic (green) receiver tubes under effect of wind speed variation, constant solar heat flux ( $1000 \text{ W.m}^{-2}$ ), water volume flow rate ( $0.06 \text{ L.s}^{-1}$ ) and ambient temperature ( $300 \text{ K}$ ).

As expected from the heat loss of the receivers, the efficiency of the circular receiver tube is the highest, while the hybrid receiver efficiency is the lowest (Figure 6.13). It can also be seen that the thermal improvement produced due to utilising the glass wool thermal insulation is highest for the hybrid receiver.

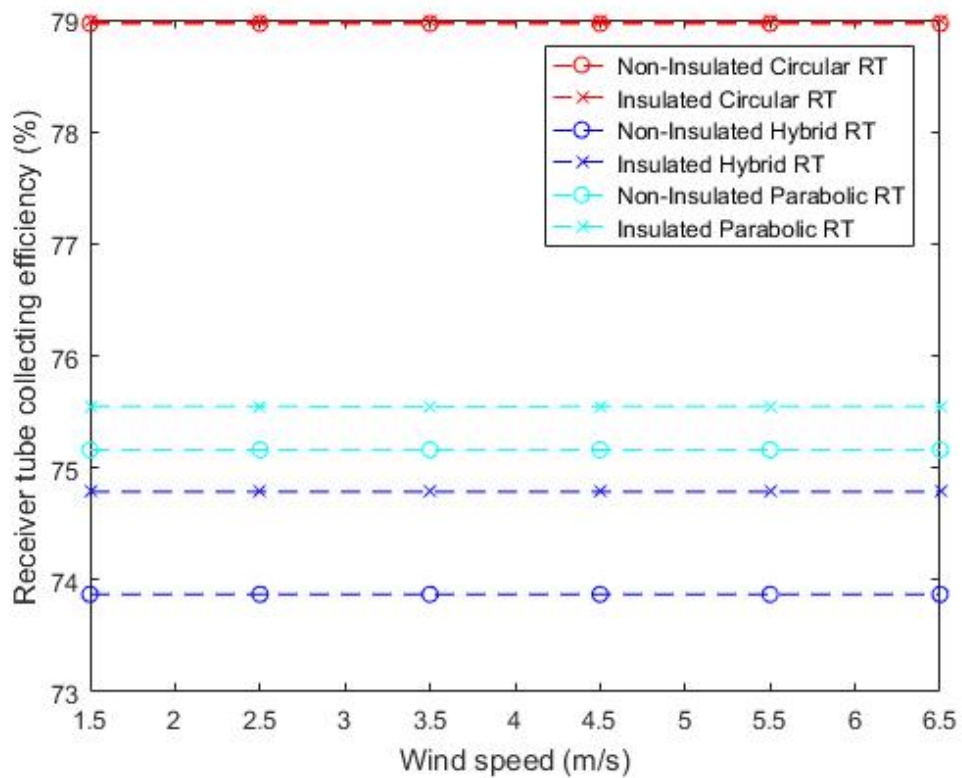


Figure 6.13: Receiver tube collecting efficiency of the insulated and non-insulated circular (red), hybrid (blue) and parabolic (green) receiver tubes under the effect of wind speed variation, constant solar heat flux ( $1000 \text{ W.m}^{-2}$ ), water volume flow rate ( $0.06 \text{ L.s}^{-1}$ ) and ambient temperature ( $300 \text{ K}$ ).

## 6.5 Summary

### 6.5.1 Outcomes of the thermal enhancement numerical investigations.

In this chapter the insulated and non-insulated circular, hybrid and parabolic receiver tubes were investigated for variations of wind speed. The main findings are as follows. Firstly, the distribution of solar heat flux on the absorber tube directly influenced the temperature distributions throughout the receiver tube. Secondly, it was found that the thermal performance of the insulated receiver tube is better than the performance of the non-insulated receiver tube for the range of wind speeds tested. This is due to the thermal insulation layer on the inner surface of the upper portion of the glass cover that reduced conduction loss across the glass envelope. This results in improving the performance of the insulated receiver tube. Finally, it was found that the thermal enhancement offered by the insulation of the receivers is generally minor, which is due to the small size of the PTSC, which is influenced by two factors. Firstly, the receiver

tube length is very short (1.2 m), and also its outer glass envelope diameter is small (0.06 m), which creates a small outer surface area that is exposed to the effect of convective cooling by the wind. In contrast, the length of the commercial receiver tube is approximately 4 m, while the total length of receiver tubes in a single row of a parabolic trough solar collector in a solar field is between 100 m and 150 m (Fernández-García et al. 2010) and its glass envelope diameter equals 0.125 m (more surface area means more heat loss). Secondly, the collector concentrating ratio was only 11.7, which resulted in producing low receiver tube domain temperatures. Therefore, the temperature difference between the receiver glass envelope and the environment was minor. In contrast, the CR in commercial applications is around 30 (Fernández-García et al. 2010), which produces a high temperature difference between the receiver tube temperature and the ambient temperature, which means more heat loss could occur. Therefore, this narrow thermal enhancement of utilising thermal insulation in the current receivers would be very worthwhile if utilised for commercial PTSC receivers that are used in different heating applications.

### **6.5.2 Thermal enhancement evaluation**

For the efficiency aspects, it found that the presented thermal solution assisted in reducing not only the receiver tube heat loss (either convection, conduction or radiation heat losses) but it also reduced the receiver tube thermal strain by creating a hot air domain on the upper part of the absorber tube surface. In contrast, previous thermal enhancement studies generally focused on reducing convection heat loss but they created other problems such as conductive heat loss (Kajavali et al. 2015), increased the absorber tube thermal strain (Ghadirijafarbeigloo et al. 2014; Jafar & Sivaraman 2017).

For the economic aspect, the presented thermal solution is simple and only requires only attaching the insulation on the inner surface of the upper part of the receiver glass envelope without any modifications in the main structure of the receiver tube components (absorber tube and glass envelope). On the other hand, most of the presented thermal enhancement studies (section 2.3.2) are complicated, costly and required major modification in the standard receiver tube design (Daniel et al. 2011; Kumar & Reddy 2012; Wang et al. 2013; Chen et al. 2015; Kajavali et al. 2015;

Fuqiang et al. 2016; Gong et al. 2017; Jafar & Sivaraman 2017; Fan et al. 2018) which could reduce their commercial opportunities

# Chapter 7 Conclusions

## 7.1 Parabolic trough solar collector heating system challenges

Through analysing the literature review, it is noticed that the major losses in the parabolic trough solar collector (PTSC) technology are the reflector optical losses and the receiver tube thermal heat losses. The PTSC optical losses occur due to reflector or receiver tube misalignments, auto-tracking errors and wind changes. All the above factors deviate the reflected sunlight from striking the collector receiver tube, and therefore it reduced the PTSC optical efficiency which consequently reduced the PTSC performance.

For the PTSC receiver tube heat losses, it is observed that these receiver tube losses (forced convective and radiative heat losses) occur due to the temperature difference between the receiver glass envelope outer surface (due to hot fluid flows inside it which reaches up to 400 °C) and the outdoor temperature. These heat losses increased as the receiver tube temperature increased or the outdoor temperature decreased.

Moreover, throughout the presented literature review, it was also observed that the receiver absorber tube surface is subjected to highly asymmetric concentrating solar radiation: the lower part of the absorber tube is subjected to the concentrating reflected solar radiation, while the upper part of the absorber is subjected only to normal solar radiation. This creates a high temperature difference on the absorber surface that could result in absorber tube thermal strain, which can cause: failed absorber tube; broken receiver tube glass envelope; reduced receiver tube operation life; and financial losses due to replacement costs and shutdowns of the solar power plant.

## 7.2 Optical solution and limitations

This section discusses the secondary reflector that was proposed to reduce the PTSC optical loss (optical gap) and the absorber tube thermal strain. The experimental design, results and limitations are also discussed.

The secondary reflector was created by sticking a mirror sheet on the inner surface of a small parabolic shape (section 3.4.1). Therefore it reflects the deviated solar radiation—irrespective of the source of the solar rays' deviation (either due to

structural misalignment or due to wind changes)—towards the upper part of the absorber tube, and also it reflects some of the absorber tube radiative heat loss onto the upper part of the absorber tube.

The solar heating system, consisting of two identical collectors (sections 3.2, 3.3 and 3.4) was designed and manufactured to investigate and evaluate the effect of the secondary reflector on solar collector performance. One collector (the standard PTSC configuration was called Cp) was used as a control during each experimental test. The other identical collector was modified by attaching the secondary reflector on the opposite side of the absorber tube to the primary collector. Therefore, the primary collector and the secondary reflector shared the same focal line; this configuration was called Cs.

The performance of the secondary reflector was experimentally investigated and evaluated under different cases. During the experimental tracking tests, when the collectors tracked the sun throughout the day from sunrise until sunset (section 3.5), the comparison of the Cs and Cp configurations (Case 1; 4.5.1) revealed that the secondary reflector slightly enhanced the optical performance of the PTSC heating system. It was found that the experimental overall average efficiency of Cp equals 99% of the Cs efficiency during case 1. This means that the experimental solution (secondary reflector) significantly improved the optical efficiency of the Cs collector, because approximately 8.5% of the collector aperture area (Cs) was blocked by the secondary reflector aperture area. On a commercial PTSC system, with a concentrating ratio 2–3 times larger, the fraction of the aperture area blocked would be much lower (it does not exceed 1%).

In order to present the effect of the secondary reflector very clearly on the PTSC performance (in case 1, the secondary reflector blocks some of the solar radiation from reaching the absorber tube or the primary mirror), another secondary parabolic was painted black (SPB). The SPB was installed, in the same manner as the secondary reflector, instead of Cp; this configuration was called Cb. Therefore, the effect of the lost direct radiation was isolated by comparing Cs and Cb directly. The experimental results of the Cs and Cb configurations in case 2 (section 4.5.2) revealed that the mirror did significantly improve the efficiency of the system. It was found that the experimental overall average efficiency of Cb equals 89% of the Cs efficiency.

Based on the tracking experimental tests, it was observed that wind variations are a major cause of PTSC optical losses, the wind vibrations cause collector vibration, and therefore reorients the primary collector away from the sun. Another major cause of optical losses are collector tracking errors caused by cloud cover, which also reorient the primary collector away from the sun. To address this problem, it was proposed to utilise the PTSC technology, incorporating the secondary reflector, as a fixed collector (i.e. the collector is always oriented in the same direction, as is frequently done for PV solar panels, section 4.6). This setup can be achieved by configuring the PTSC axis to be parallel with the East-West orientation and angling the collector aperture area based on the latitude of a site. The effect of the secondary reflector on the PTSC was investigated during the fixed stage by orienting the PTSC axis in the North-South direction and aiming the PTSC at the noon sun position throughout the day—which simulates the sun noon position throughout the year. Therefore, this novel test regime experimentally simulates the effect of the secondary reflector on the PTSC performance at midday for the entire year, only requiring a single day's test. The experimental results found that the overall annual noontime average efficiency of  $C_p$  equals 86% of the  $C_s$  (Case 3: section 4.6.1), while  $C_s$  was more efficient than  $C_b$  ( $C_b$  efficiency equals 75% of the  $C_s$  efficiency for case 4: section 4.6.2).

Moreover, the effect of adding the secondary reflector was investigated, during tracking tests, under different outdoor temperature conditions (at different times of the year), but under almost the same solar radiation and wind speed to directly observe the performance of the PTSC for different seasons (section 4.7). It was found that the secondary reflector effect was more pronounced during cold weather by reflecting additional radiative losses that occurred during the cold weather. This means that employing this element provided extra heating energy for the PTSC system during the cold weather, when any additional heating is desirable because the environment, supplied HTF and target application (e.g. fresh supply to a hot water system) are coldest.

As a result, the secondary reflector reduced not only the collector optical loss but it also decreased the absorber tube radiative heat loss, which potentially reduced the absorber tube thermal strain. Thus, this could enhance the PTSC performance and also improve the operational life of the receiver tube, which leads to the economic viability

of the modification by producing more energy and reducing the receiver tubes' replacement costs.

The major limitation of the results for the optical enhancement is the small size of the solar collector. This resulted in the secondary reflector blocking around 8.5% of the primary solar collector aperture area (this value of the blocking ratio is due to the width of the secondary reflector in the current design equals 0.06 m, and the collector aperture equals 0.7 m). Whereas, for commercial PTSC system, the secondary reflector's blocking area could be neglected. This is because of the large collector width (6.5 m) in comparison to its small receiver inner diameter (0.119 m), which serves as a base for placing the secondary mirror.

### **7.3 Thermal solution and limitations**

This section presents the thermal solution (annular thermal insulation) for the PTSC receiver tube thermal losses. The thermal enhancement was presented to reduce not only receiver tube thermal loss (thermal gap) but also to decrease the absorber tube thermal strain as well. The numerical design, results, and limitations are also discussed.

The proposed solution is summarised by adding an annular thermal insulation on the inner surface of the upper part of the receiver tube's glass envelope (section 5.3); the insulation has the same inner shape and the area as the secondary reflector. Because of the low thermal conductivity of the insulation layer, conduction heat transfer across the receiver glass envelope is shown to be reduced, and therefore the glass envelope outer surface temperature was reduced (section 6.2.3).

Insulated and non-insulated circular, hybrid and parabolic cross-sections were designed and tested numerically using computational fluid dynamics software as receiver tubes for various wind speeds. The efficiency of the circular receiver tube was the highest (section 6.4). There was little effect of the insulation on the circular receiver tube performance due to both the low collector concentrating ratio and also the short receiver length. However, there was a significant improvement by adding insulation to the other shapes because they have greater heat loss compared to the circular receiver (section 6.4.2).

The significant improvement for the insulated receivers is due to the annular thermal insulation which reduced the heat transfer loss between the glass outer surface and the atmosphere. The insulation layer was also increased the temperature of the air between the absorber tube and the glass envelope for a non-evacuated receiver tube, especially in the upper portion of this region (sections 6.2.1, 6.3.1). This produced a better temperature distribution on the absorber tube outer surface, which would reduce its propensity for thermal deformation that would be created by highly non-uniform concentrated solar flux on the absorber tube

The major limitation of the thermal solution (0.2% W) is the small size of the primary collector of the study. The small size of the collector produced two challenges.

The first one is the minor temperature difference between the receiver tube surface and its surrounding environment. This occurred due to receiver tube surface moderate temperature which was produced due to the low concentration of the incident sunlight on the absorber tube surface—which resulted from the small concentration ratio of the collector which equals 11.7. Thus, the non-insulated receiver tube heat loss been minor, and therefore the reduction of receiver tube heat loss due to the insulation was very small. The second one is the receiver surface area was small, due to its short length (1.2 m) and small diameter (0.06 m). And as result, the exposed receiver surface area to the convective cooling by the wind was small and therefore receiver heat loss was minor. And thus, the heat loss reduction due to utilizing the annular insulation layer was very limited.

However, the proposed thermal enhancement could become significant if it is employed for commercial PTSC applications. This is due to its high concentration ratio that could reach up to 30 (2.5 higher than CR of the current collector), and also due to the large surface area of its receiver tube row—the combined length of collectors in a row typically reach up to 150 m and the outer diameter of its receiver tube equals approximately 0.125 m (producing a total surface area 260 times higher than the studied receiver tube).

Furthermore, another limitation for the simulations is that only the experimental configuration from Chapter 4 could be used for validation: a prototype of the novel proposed receiver tube (insulated receiver tube) was not able to be manufactured and

there is no similar work done by others. This limits the simulations to the experimental dimensions: a receiver tube with 0.019 m diameter and 1.2 m length. Such receiver tube dimensions (an absorber tube covered by glass envelope) is not available commercially, therefore, a copper tube (without glass envelope) of those dimensions has been used as an absorber tube for this experimental work.

#### **7.4 Commercial opportunity**

Both the optical and thermal receiver tube enhancements contribute to significant potential commercial benefits for PTSC technology, especially using non-evacuated receiver tubes instead of evacuated receiver tubes (which are so expensive that they cost approximately 30% of the total solar field's components). Both enhancements will produce more heat energy, and therefore more income. For example, the modified receiver tube has the potential to earn an additional \$3 million per annum for a 100 MW parabolic trough solar thermal electric power plant, providing a payback period of less than three years (Appendix D shows the details of these financial calculations). This receiver tube can also be used effectively for PTSC solar thermal plants in addition to other PTSC heating applications.

#### **7.5 Recommendations and future work**

The experimental and numerical studies in this thesis combine to result in a proposed design for an alternative receiver tube (this is future work) by coupling the studied optical and thermal enhancements through usage of a reflecting sheet with a thermal insulation backing layer to produce a secondary reflector. This layer can be glued onto the inner surface of the upper part of the glass envelope to function as the secondary reflector and insulator at the same time. This receiver can reduce the optical and heat transfer losses in addition to improving the solar heat flux distribution and temperature distribution on the absorber tube. In addition, the reflecting sheet would successfully protect the insulation layer from excessive heat both from the absorber tube and reflected solar flux if there is enough geometric misalignment. This could successfully result in improved receiver performance and reduce its thermal deformation, which would result in improving the operation age of the receiver tube. By achieving this aim, there is an economic benefit because of improving PTSC performance (producing more heat) and reducing the maintenance and replacement costs.

In addition, based on the findings and the limitations of the presented study, it is also recommended to investigate the performance of the system operating in the fixed configuration during an entire year. This is required in order to compare between the presented results for the experimental fixed stage (experimental simulation of the seasonal behaviour at noontime) and the results of the proposed investigation. Also, it is recommended that the secondary mirror be investigated experimentally with a commercial parabolic trough collector with a high concentrating ratio at a windy site.

It is also suggested to simulate the effect of the wind fluctuation of the experimental apparatus by programming the tracking motor to produce specified vibrations in the solar collector to establish the influence of the wind on the results reported in this thesis.

It is also recommended that the annular thermal insulation be investigated numerically and experimentally in a commercial receiver tube, which should be done using a commercial receiver tube with a collector that has a high concentrating ratio. The high CR is required to produce a high difference between the receiver tube temperature and ambient temperature in order to observe clearly the effect of the insulation.

# References

- Al-Ansary, H & Zeitoun, O 2011, 'Numerical study of conduction and convection heat losses from a half-insulated air-filled annulus of the receiver of a parabolic trough collector', *Solar Energy*, vol. 85, no. 11, pp. 3036-45.
- Amina, B, Miloud, A, Samir, L, Abdelylah, B & Solano, J 2016, 'Heat transfer enhancement in a parabolic trough solar receiver using longitudinal fins and nanofluids', *Journal of Thermal Science*, vol. 25, no. 5, pp. 410-7.
- Australian electricity prices 2018, *Australian electricity prices; the cost of electricity in Australia per kWh*, BulkEnergy, viewed 1 January 2019, <<https://gobulk.com.au/australian-electricity-prices/>>.
- Bellos, E, Tzivanidis, C & Tsimpoukis, D 2017, 'Thermal enhancement of parabolic trough collector with internally finned absorbers', *Solar Energy*, vol. 157, pp. 514-31.
- Benabderrahmane, A & Benazza, A 'Numerical investigation of heat transfer enhancement inside a parabolic trough solar collector using dimpled absorber'.
- Benabderrahmane, A, Benazza, A, Aminallah, M & Laouedj, S 2016, 'Heat transfer behaviors in parabolic trough solar collector tube with compound technique', *International Journal of Scientific Research Engineering & Technology (IJSRET)*, vol. 5, no. 11.
- Bhuiya, MMK, Chowdhury, M, Ahamed, J & Azad, AK 2016, 'Heat transfer performance evaluation and prediction of correlation for turbulent flow through a tube with helical tape inserts at higher Reynolds number', *Heat and Mass Transfer*, vol. 52, no. 6, pp. 1219-30.
- Cabrera, F, Fernández-García, A, Silva, R & Pérez-García, M 2013, 'Use of parabolic trough solar collectors for solar refrigeration and air-conditioning applications', *Renewable and Sustainable Energy Reviews*, vol. 20, pp. 103-18.
- Cengel, YA 2010, *Fluid mechanics*, Tata McGraw-Hill Education.
- Chaabane, M, Mhiri, H & Bournot, P 2015, 'Effect of the water storage tank coverage with an outer glass tube on the thermal performance of an integrated collector storage solar water heater', *Journal of Solar Energy Engineering*, vol. 137, no. 1, p. 011009.
- Chafie, M, Aissa, MFB, Bouadila, S, Balghouthi, M, Farhat, A & Guizani, A 2016, 'Experimental investigation of parabolic trough collector system under Tunisian climate: design, manufacturing and performance assessment', *Applied Thermal Engineering*, vol. 101, pp. 273-83.
- Chandra, YP, Singh, A, Mohapatra, SK, Kesari, J & Rana, L 2017, 'Numerical optimization and convective thermal loss analysis of improved solar parabolic trough collector receiver system with one sided thermal insulation', *Solar Energy*, vol. 148, pp. 36-48.
- Chang, C, Xu, C, Wu, Z, Li, X, Zhang, Q & Wang, Z 2015, 'Heat transfer enhancement and performance of solar thermal absorber tubes with circumferentially non-uniform heat flux', *Energy Procedia*, vol. 69, pp. 320-7.

- Chang, C, Peng, X, Nie, B, Leng, G, Li, C, Hao, Y & She, X 2017, 'Heat transfer enhancement of a molten salt parabolic trough solar receiver with concentric and eccentric pipe inserts', *Energy Procedia*, vol. 142, pp. 624-9.
- Chen, F, Li, M, Zhang, P & Luo, X 2015, 'Thermal performance of a novel linear cavity absorber for parabolic trough solar concentrator', *Energy conversion and management*, vol. 90, pp. 292-9.
- Cheng, Z, He, Y & Cui, F 2012, 'Numerical study of heat transfer enhancement by unilateral longitudinal vortex generators inside parabolic trough solar receivers', *International Journal of Heat and Mass Transfer*, vol. 55, no. 21-22, pp. 5631-41.
- Christian, JM & Ho, CK 2010, 'Finite element modeling of concentrating solar collectors for evaluation of gravity loads, bending, and optical characterization', *ASME, Paper No. ES2010-90050*.
- Daniel, P, Joshi, Y & Das, AK 2011, 'Numerical investigation of parabolic trough receiver performance with outer vacuum shell', *Solar Energy*, vol. 85, no. 9, pp. 1910-4.
- DEWA CSP Trough Project 2019, *Concentrating Solar Power Projects*, National Renewable Energy Laboratory, viewed 1 January 2019, <<https://solarpaces.nrel.gov/dewa-csp-trough-project>>.
- Diwan, K & Soni, M 2015, 'Heat Transfer Enhancement in Absorber Tube of Parabolic Trough Concentrators Using Wire-Coils Inserts'.
- Duffie, JA & Beckman, WA 2013, *Solar engineering of thermal processes*, John Wiley & Sons.
- Dunlap, M 1994, 'Solar radiation data manual for flat-plate and concentrating collectors', *NASA STI/Recon Technical Report N*, vol. 95.
- Fan, M, Liang, H, You, S, Zhang, H, Zheng, W & Xia, J 2018, 'Heat transfer analysis of a new volumetric based receiver for parabolic trough solar collector', *Energy*, vol. 142, pp. 920-31.
- Fernández-García, A, Zarza, E, Valenzuela, L & Pérez, M 2010, 'Parabolic-trough solar collectors and their applications', *Renewable and Sustainable Energy Reviews*, vol. 14, no. 7, pp. 1695-721.
- Forman, P, Müller, S, Ahrens, M, Schnell, J, Mark, P, Höffer, R, Hennecke, K & Krüger, J 2015, 'Light concrete shells for parabolic trough collectors—conceptual design, prototype and proof of accuracy', *Solar Energy*, vol. 111, pp. 364-77.
- Fraidenraich, N, de OP Filho, MH & de castro Vilela, O 2017, 'A new approach for obtaining angular acceptance function of non-perfect parabolic concentrating collectors', *Solar Energy*, vol. 147, pp. 455-62.
- Fuqiang, W, Qingzhi, L, Huaizhi, H & Jianyu, T 2016, 'Parabolic trough receiver with corrugated tube for improving heat transfer and thermal deformation characteristics', *Applied Energy*, vol. 164, pp. 411-24.
- García-Valladares, O & Velázquez, N 2009, 'Numerical simulation of parabolic trough solar collector: Improvement using counter flow concentric circular heat exchangers', *International Journal of Heat and Mass Transfer*, vol. 52, no. 3-4, pp. 597-609.

- Ghadirijafarbeigloo, S, Zamzamian, A & Yaghoubi, M 2014, '3-D numerical simulation of heat transfer and turbulent flow in a receiver tube of solar parabolic trough concentrator with louvered twisted-tape inserts', *Energy Procedia*, vol. 49, pp. 373-80.
- Ghasemi, SE, Ranjbar, AA & Ramiar, A 2013, 'Three-dimensional numerical analysis of heat transfer characteristics of solar parabolic collector with two segmental rings', *J Math Comput Sci*, vol. 7, pp. 89-100.
- Gil, A, Medrano, M, Martorell, I, Lázaro, A, Dolado, P, Zalba, B & Cabeza, LF 2010, 'State of the art on high temperature thermal energy storage for power generation. Part 1—Concepts, materials and modellization', *Renewable and Sustainable Energy Reviews*, vol. 14, no. 1, pp. 31-55.
- Gnielinski, V 1976, 'New equations for heat and mass transfer in turbulent pipe and channel flow', *Int. Chem. Eng.*, vol. 16, no. 2, pp. 359-68.
- Gong, X, Wang, F, Wang, H, Tan, J, Lai, Q & Han, H 2017, 'Heat transfer enhancement analysis of tube receiver for parabolic trough solar collector with pin fin arrays inserting', *Solar Energy*, vol. 144, pp. 185-202.
- Grena, R 2010, 'Optical simulation of a parabolic solar trough collector', *International Journal of Sustainable Energy*, vol. 29, no. 1, pp. 19-36.
- Günther, M, Joemann, M & Csambor, S 2011, 'Parabolic trough technology', *Advanced CSP Teaching Materials*.
- Hachicha, A, Rodríguez, I & Oliva, A 2014, 'Wind speed effect on the flow field and heat transfer around a parabolic trough solar collector', *Applied Energy*, vol. 130, pp. 200-11.
- Hachicha, A, Rodríguez, I, Capdevila, R & Oliva, A 2013, 'Heat transfer analysis and numerical simulation of a parabolic trough solar collector', *Applied Energy*, vol. 111, pp. 581-92.
- Hale, M 2000, 'Survey of thermal storage for parabolic trough power plants', *NREL Report, No. NREL/SR-550-27925*, pp. 1-28.
- He, Y-L, Xiao, J, Cheng, Z-D & Tao, Y-B 2011, 'A MCRT and FVM coupled simulation method for energy conversion process in parabolic trough solar collector', *Renewable Energy*, vol. 36, no. 3, pp. 976-85.
- Heidemann, W, Spindler, K & Hahne, E 1992, 'Steady-state and transient temperature field in the absorber tube of a direct steam generating solar collector', *International Journal of Heat and Mass Transfer*, vol. 35, no. 3, pp. 649-57.
- Herrmann, U, Kelly, B & Price, H 2004, 'Two-tank molten salt storage for parabolic trough solar power plants', *Energy*, vol. 29, no. 5-6, pp. 883-93.
- Huang, W & Han, Z 2012, 'Theoretical analysis of error transfer from the surface slope to the reflected ray and their application in the solar concentrated collector', *Solar Energy*, vol. 86, no. 9, pp. 2592-9.
- Huang, W, Hu, P & Chen, Z 2012, 'Performance simulation of a parabolic trough solar collector', *Solar Energy*, vol. 86, no. 2, pp. 746-55.
- International Energy Agency 2018, *World Energy Outlook*, <https://www.iea.org/weo/>.

- Islam, M, Miller, S, Yarlagadda, P & Karim, A 2017, 'Investigation of the Effect of Physical and Optical Factors on the Optical Performance of a Parabolic Trough Collector', *Energies*, vol. 10, no. 11, p. 1907.
- Jafar, KS & Sivaraman, B 2017, 'PERFORMANCE CHARACTERISTICS OF PARABOLIC SOLAR COLLECTOR WATER HEATER SYSTEM FITTED WITH NAIL TWISTED TAPES ABSORBER', *Journal of Engineering Science and Technology*, vol. 12, no. 3, pp. 608-21.
- Jamal-Abad, MT, Saedodin, S & Aminy, M 2017, 'Experimental investigation on a solar parabolic trough collector for absorber tube filled with porous media', *Renewable Energy*, vol. 107, pp. 156-63.
- Jaramillo, O, Borunda, M, Velazquez-Lucho, K & Robles, M 2016, 'Parabolic trough solar collector for low enthalpy processes: an analysis of the efficiency enhancement by using twisted tape inserts', *Renewable Energy*, vol. 93, pp. 125-41.
- Kajavali, A, Sivaraman, B & Kulasekharan, N 2015, 'Investigation of heat transfer enhancement in a parabolic trough collector with a modified absorber', *International Energy Journal*, vol. 14, no. 4.
- Kalogirou, SA 2012, 'A detailed thermal model of a parabolic trough collector receiver', *Energy*, vol. 48, no. 1, pp. 298-306.
- Kalogirou, SA 2013, *Solar energy engineering: processes and systems*, Academic Press.
- Kaloudis, E, Papanicolaou, E & Belessiotis, V 2016, 'Numerical simulations of a parabolic trough solar collector with nanofluid using a two-phase model', *Renewable Energy*, vol. 97, pp. 218-29.
- Kearney, DW 2007, 'Parabolic trough collector overview', in *Parabolic trough workshop*.
- Krüger, D, Pandian, Y, Hennecke, K & Schmitz, M 2008, 'Parabolic trough collector testing in the frame of the REACt project', *Desalination*, vol. 220, no. 1-3, pp. 612-8.
- Kumar, KR & Reddy, K 2009, 'Thermal analysis of solar parabolic trough with porous disc receiver', *Applied Energy*, vol. 86, no. 9, pp. 1804-12.
- Kumar, KR & Reddy, K 2012, 'Effect of porous disc receiver configurations on performance of solar parabolic trough concentrator', *Heat and Mass Transfer*, vol. 48, no. 3, pp. 555-71.
- Lei, D, Li, Q, Wang, Z, Li, J & Li, J 2013, 'An experimental study of thermal characterization of parabolic trough receivers', *Energy conversion and management*, vol. 69, pp. 107-15.
- Lüpfert, E & Ulmer, S 2009, 'Solar trough mirror shape specifications'.
- Meiser, S, Schneider, S, Lüpfert, E, Schiricke, B & Pitz-Paal, R 2015, 'Evaluation and assessment of gravity load on mirror shape of parabolic trough solar collectors', *Energy Procedia*, vol. 75, pp. 485-94.
- Meiser, S, Schneider, S, Lüpfert, E, Schiricke, B & Pitz-Paal, R 2017, 'Evaluation and assessment of gravity load on mirror shape and focusing quality of parabolic trough solar mirrors using finite-element analysis', *Applied Energy*, vol. 185, pp. 1210-6.

Mier-Torrecilla, M, Herrera, E & Doblaré, M 2014, 'Numerical calculation of wind loads over solar collectors', *Energy Procedia*, vol. 49, pp. 163-73.

Mwesigye, A & Meyer, JP 2017, 'Optimal thermal and thermodynamic performance of a solar parabolic trough receiver with different nanofluids and at different concentration ratios', *Applied Energy*, vol. 193, pp. 393-413.

Mwesigye, A, Bello-Ochende, T & Meyer, JP 2013, 'Heat transfer enhancement in a parabolic trough receiver using wall detached twisted tape inserts', in *ASME 2013 International Mechanical Engineering Congress and Exposition*, American Society of Mechanical Engineers, pp. V06BT7A031-V06BT07A.

Mwesigye, A, Bello-Ochende, T & Meyer, JP 2014a, 'Minimum entropy generation due to heat transfer and fluid friction in a parabolic trough receiver with non-uniform heat flux at different rim angles and concentration ratios', *Energy*, vol. 73, pp. 606-17.

Mwesigye, A, Bello-Ochende, T & Meyer, JP 2014b, 'Heat transfer and thermodynamic performance of a parabolic trough receiver with centrally placed perforated plate inserts', *Applied Energy*, vol. 136, pp. 989-1003.

Mwesigye, A, Huan, Z, Bello-Ochende, T & Meyer, JP 2016, 'Influence of optical errors on the thermal and thermodynamic performance of a solar parabolic trough receiver', *Solar Energy*, vol. 135, pp. 703-18.

Naeeni, N & Yaghoubi, M 2007a, 'Analysis of wind flow around a parabolic collector (2) heat transfer from receiver tube', *Renewable Energy*, vol. 32, no. 8, pp. 1259-72.

Naeeni, N & Yaghoubi, M 2007b, 'Analysis of wind flow around a parabolic collector (1) fluid flow', *Renewable Energy*, vol. 32, no. 11, pp. 1898-916.

National Aeronautics and Space Administration 2019, June 1, *Global Temperatures*, <https://earthobservatory.nasa.gov/world-of-change/DecadalTemp>.

Navarro-Hermoso, J, Espinosa-Rueda, G, Heras, C, Salinas, I, Martinez, N & Gallas, M 2016, 'Parabolic trough solar receivers characterization using specific test bench for transmittance, absorptance and heat loss simultaneous measurement', *Solar Energy*, vol. 136, pp. 268-77.

Ouagued, M, Khellaf, A & Loukarfi, L 2013, 'Estimation of the temperature, heat gain and heat loss by solar parabolic trough collector under Algerian climate using different thermal oils', *Energy conversion and management*, vol. 75, pp. 191-201.

Padilla, RV, Demirkaya, G, Goswami, DY, Stefanakos, E & Rahman, MM 2011, 'Heat transfer analysis of parabolic trough solar receiver', *Applied Energy*, vol. 88, no. 12, pp. 5097-110.

Paetzold, J, Cochard, S, Vassallo, A & Fletcher, D 2014, 'Wind engineering analysis of parabolic trough solar collectors: the effects of varying the trough depth', *Journal of Wind Engineering and Industrial Aerodynamics*, vol. 135, pp. 118-28.

Paetzold, J, Cochard, S, Fletcher, D & Vassallo, A 2015, 'Wind engineering analysis of parabolic trough collectors to optimise wind loads and heat loss', *Energy Procedia*, vol. 69, pp. 168-77.

Paetzold, J, Cochard, S, Fletcher, DF & Vassallo, A 2016, 'Wind effects in solar fields with various collector designs', in *AIP Conference Proceedings*, AIP Publishing, p. 020018.

Patankar, SV & Spalding, DB 1983, 'A calculation procedure for heat, mass and momentum transfer in three-dimensional parabolic flows', in *Numerical Prediction of Flow, Heat Transfer, Turbulence and Combustion*, Elsevier, pp. 54-73.

Patil, RG, Panse, SV & Joshi, JB 2014, 'Optimization of non-evacuated receiver of solar collector having non-uniform temperature distribution for minimum heat loss', *Energy conversion and management*, vol. 85, pp. 70-84.

Patil, RG, Kale, DM, Panse, SV & Joshi, JB 2014, 'Numerical study of heat loss from a non-evacuated receiver of a solar collector', *Energy conversion and management*, vol. 78, pp. 617-26.

Patnode, AM 2006, 'Simulation and performance evaluation of parabolic trough solar power plants', M.Sc thesis, University of Wisconsin-Madison.

Pelay, U, Luo, L, Fan, Y, Stitou, D & Rood, M 2017, 'Thermal energy storage systems for concentrated solar power plants', *Renewable and Sustainable Energy Reviews*, vol. 79, pp. 82-100.

Petukhov, B 1970, 'Heat transfer and friction in turbulent pipe flow with variable physical properties', in *Advances in heat transfer*, Elsevier, vol. 6, pp. 503-64.

Pitz-Paal, R, Dersch, J, Milow, B, TÁŠllez, F, Ferriere, A, Langnickel, U, Steinfeld, A, Karni, J, Zarza, E & Popel, O 2007, 'Development steps for parabolic trough solar power technologies with maximum impact on cost reduction', *Journal of Solar Energy Engineering*, vol. 129, no. 4, pp. 371-7.

Pottler, K, Ulmer, S, Lüpfer, E, Landmann, M, Röger, M & Prah, C 2014, 'Ensuring performance by geometric quality control and specifications for parabolic trough solar fields', *Energy Procedia*, vol. 49, pp. 2170-9.

Powell, KM & Edgar, TF 2012, 'Modeling and control of a solar thermal power plant with thermal energy storage', *Chemical Engineering Science*, vol. 71, pp. 138-45.

Prah, C, Schapitz, T & Uhlig, R 2011, 'Structural Optimization of a Line-Focussing Solar Collector With Stationary Absorber Tube'.

Prah, C, Röger, M, Stanicki, B & Hilgert, C 2017, 'Absorber tube displacement in parabolic trough collectors—A review and presentation of an airborne measurement approach', *Solar Energy*, vol. 157, pp. 692-706.

Price, H, Lüpfer, E, Kearney, D, Zarza, E, Cohen, G, Gee, R & Mahoney, R 2002, 'Advances in parabolic trough solar power technology', *Journal of Solar Energy Engineering*, vol. 124, no. 2, pp. 109-25.

Quaschnig, V & Muriel, MB 2002, 'Solar power-photovoltaics or solar thermal power plants?', *VGB POWERTECH-INTERNATIONAL EDITION*-, vol. 82, pp. 48-52.

Reddy, K & Satyanarayana, G 2008, 'Numerical study of porous finned receiver for solar parabolic trough concentrator', *Engineering applications of computational fluid mechanics*, vol. 2, no. 2, pp. 172-84.

Rimex Metals Australia 2018, *SUPER MIRROR STAINLESS STEEL*, <http://rimexmetals.com.au/StainlessSteelFinishes/SuperMirrorStainlessSteel.html>>.

- Salamanca, S, Merchán, P, Pérez, E, Adán, A & Quintana, B 2015, 'A framework for the analysis of parabolic trough collectors using 3D data from laser scanners', in *Compatibility and Power Electronics (CPE), 2015 9th International Conference on*, IEEE, pp. 548-53.
- Sandeep, H & Arunachala, U 2017, 'Solar parabolic trough collectors: a review on heat transfer augmentation techniques', *Renewable and Sustainable Energy Reviews*, vol. 69, pp. 1218-31.
- SCHOTT 2019, *The receiver benchmark in CSP industry, SCHOTT PTR®70, 4th Generation*, SCHOTT North America, viewed 1 January 2019, <<https://www.us.schott.com/csp/english/schott-solar-ptr-70-receivers.html>>.
- Shams 1 2019, *Concentrating Solar Power Projects*, National Renewable Energy Laboratory, viewed 1 January 2019, <<https://solarpaces.nrel.gov/shams-1>>.
- Simonović, T, Stamenić, M, Tanasić, N & Trninić, M 2016, 'Effect of small deviation of incident angle on thermal performance of parabolic-trough solar collector', in *Environment Friendly Energies and Applications (EFEA), 2016 4th International Symposium on*, IEEE, pp. 1-4.
- Singh, PL, Sarviya, R & Bhagoria, J 2010, 'Heat loss study of trapezoidal cavity absorbers for linear solar concentrating collector', *Energy conversion and management*, vol. 51, no. 2, pp. 329-37.
- Sokhansefat, T, Kasaeian, A & Kowsary, F 2014, 'Heat transfer enhancement in parabolic trough collector tube using Al<sub>2</sub>O<sub>3</sub>/synthetic oil nanofluid', *Renewable and Sustainable Energy Reviews*, vol. 33, pp. 636-44.
- Song, X, Dong, G, Gao, F, Diao, X, Zheng, L & Zhou, F 2014, 'A numerical study of parabolic trough receiver with nonuniform heat flux and helical screw-tape inserts', *Energy*, vol. 77, pp. 771-82.
- Stynes, JK & Ihas, B 2012, *Slope Error Measurement Tool for Solar Parabolic Trough Collectors: Preprint*, National Renewable Energy Laboratory (NREL), Golden, CO.
- Swinbank, WC 1963, 'Long-wave radiation from clear skies', *Quarterly Journal of the Royal Meteorological Society*, vol. 89, no. 381, pp. 339-48.
- Trieb, F, Schillings, C, O'sullivan, M, Pregar, T & Hoyer-Klick, C 2009, 'Global potential of concentrating solar power', in *SolarPACES Conference*, pp. 15-8.
- U.S. Energy Information Administration 2018, *International Energy Outlook 2017*, <https://www.eia.gov/todayinenergy/detail.php?id=32912>>.
- Wang, P, Liu, D & Xu, C 2013, 'Numerical study of heat transfer enhancement in the receiver tube of direct steam generation with parabolic trough by inserting metal foams', *Applied Energy*, vol. 102, pp. 449-60.
- Wendelin, T, Dobos, A & Lewandowski, A 2013, 'SolTrace: a ray-tracing code for complex solar optical systems', *Contract*, vol. 303, pp. 275-3000.
- Wu, Y-T, Liu, S-W, Xiong, Y-X, Ma, C-F & Ding, Y-L 2015, 'Experimental study on the heat transfer characteristics of a low melting point salt in a parabolic trough solar collector system', *Applied Thermal Engineering*, vol. 89, pp. 748-54.

- Wu, Z, Li, S, Yuan, G, Lei, D & Wang, Z 2014, 'Three-dimensional numerical study of heat transfer characteristics of parabolic trough receiver', *Applied Energy*, vol. 113, pp. 902-11.
- Xiao, X, Zhang, P, Shao, D & Li, M 2014, 'Experimental and numerical heat transfer analysis of a V-cavity absorber for linear parabolic trough solar collector', *Energy conversion and management*, vol. 86, pp. 49-59.
- Xu, Li, L, Li, H, Huang, W & Li, Y 2014, 'Performance comparison of solar parabolic trough system with glass and film reflector', *Energy conversion and management*, vol. 85, pp. 581-90.
- Xu, L, Wang, Z, Li, X, Yuan, G, Sun, F, Lei, D & Li, S 2014, 'A comparison of three test methods for determining the thermal performance of parabolic trough solar collectors', *Solar Energy*, vol. 99, pp. 11-27.
- Yang, B, Zhao, J, Xu, T & Zhu, Q 2010, 'Calculation of the concentrated flux density distribution in parabolic trough solar concentrators by Monte Carlo ray-trace method', in *Photonics and Optoelectronic (SOPO), 2010 Symposium on*, IEEE, pp. 1-4.
- Yang, H, Wang, Q, Huang, X, Li, J & Pei, G 2018, 'Performance study and comparative analysis of traditional and double-selective-coated parabolic trough receivers', *Energy*, vol. 145, pp. 206-16.
- Zhao, C, Zhou, D & Wu, Z 2010, 'Heat transfer enhancement of phase change materials (PCMs) in low and high temperature thermal storage by using porous materials', in *2010 14th International Heat Transfer Conference*, American Society of Mechanical Engineers, pp. 435-41.
- Zhao, D, Xu, E, Wang, Z, Yu, Q, Xu, L & Zhu, L 2016, 'Influences of installation and tracking errors on the optical performance of a solar parabolic trough collector', *Renewable Energy*, vol. 94, pp. 197-212.
- Zhu, G & Lewandowski, A 2012, 'A new optical evaluation approach for parabolic trough collectors: first-principle optical intercept calculation', *Journal of Solar Energy Engineering*, vol. 134, no. 4, p. 041005.

# Appendix A Circular receiver tube

This appendix presents the glass envelope, insulation and air temperature distribution of the circular receiver tube under variation of wind speed from 1.5 m/s to 6.5 m/s.

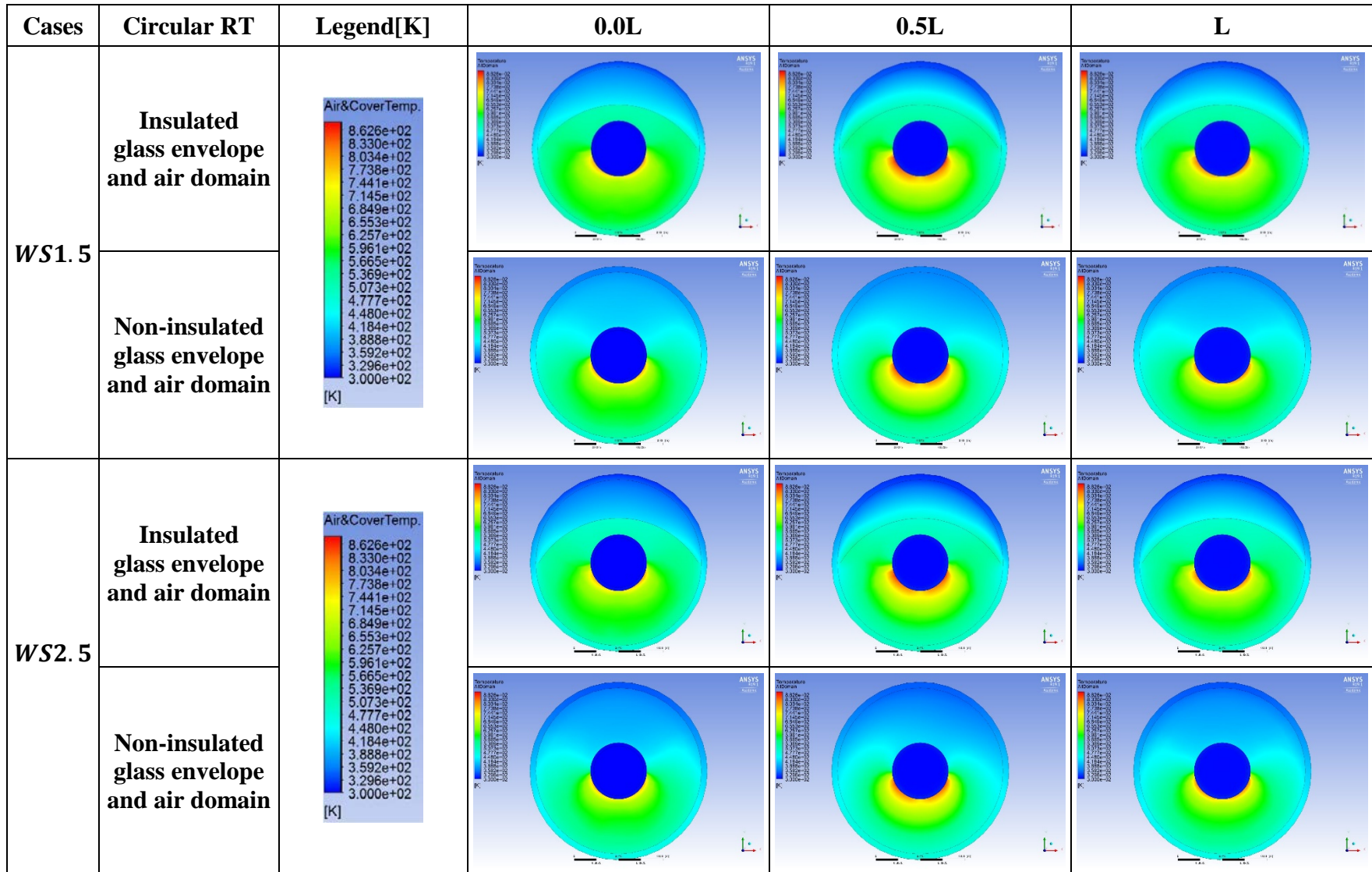


Figure A.1: Temperature distribution of annular air and glass cover domain of insulated and non-insulated circular receiver tube for smallest and largest variation wind speed (WS): 1.5 m/s and 2.5 m/s. Results are shown for different stations along the tube (0.0L, 0.5L and L).

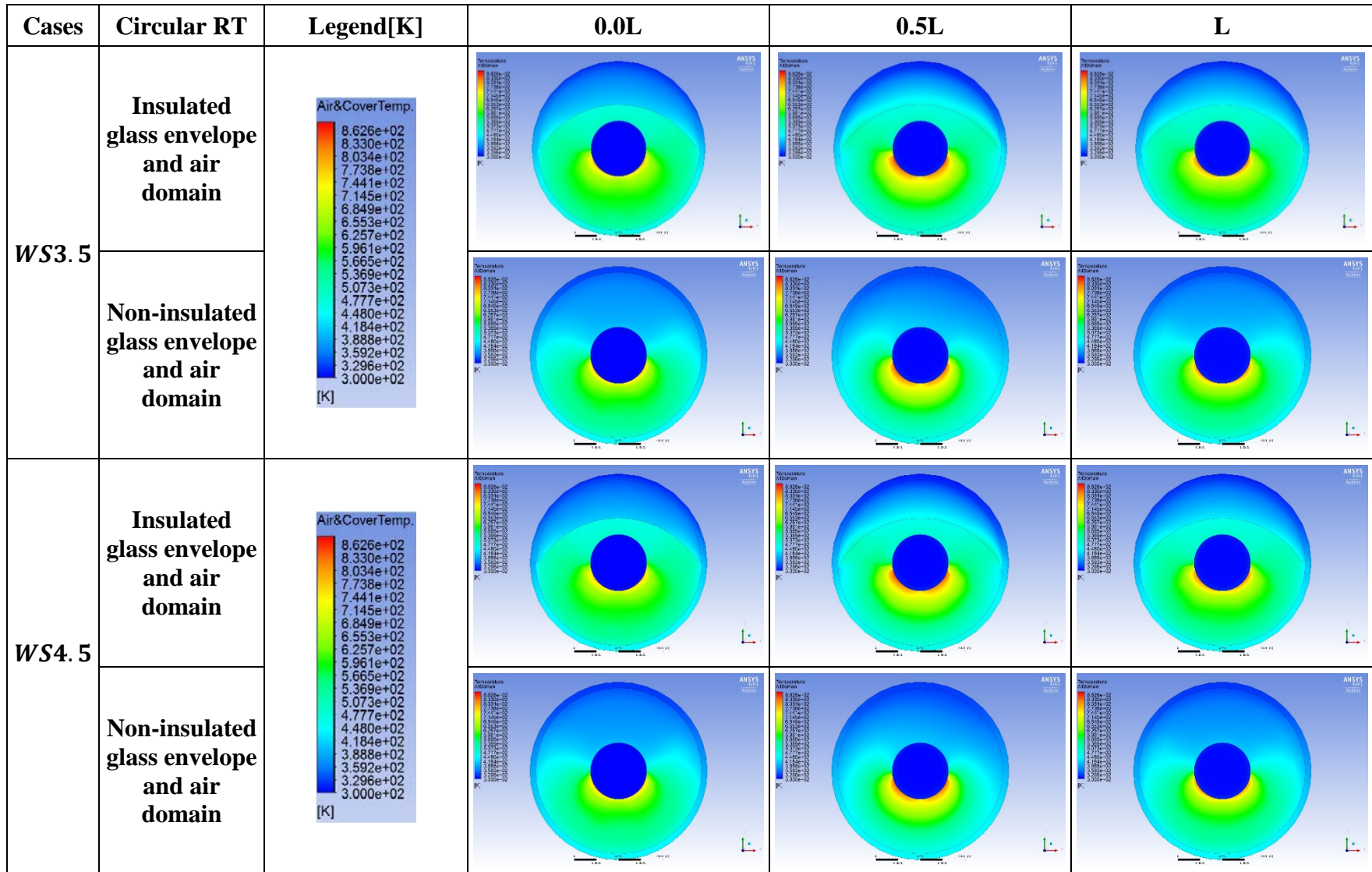


Figure A.2: Temperature distribution of annular air and glass cover domain of insulated and non-insulated circular receiver tube for smallest and largest variation wind speed (WS): 3.5 m/s and 4.5 m/s. Results are shown for different stations along the tube (0.0L, 0.5L and L).

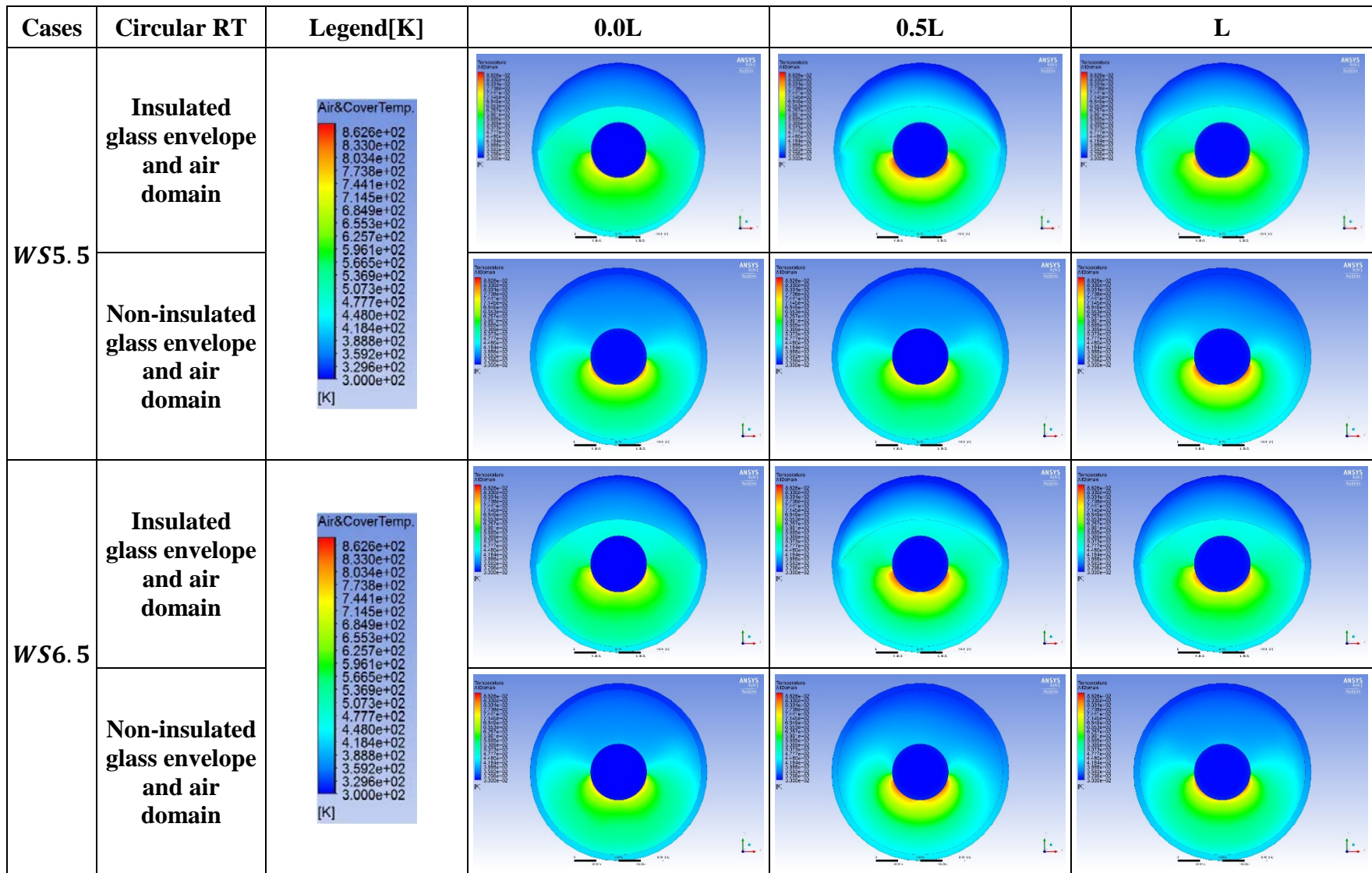


Figure A.3: Temperature distribution of annular air and glass cover domain of insulated and non-insulated circular receiver tube for smallest and largest variation wind speed (WS): 5.5 m/s and 6.5 m/s. Results are shown for different stations along the tube (0.0L, 0.5L and L).

# Appendix B Hybrid receiver tube

This appendix presents the glass envelope, insulation and air temperature distribution of the hybrid receiver tube under variation of wind speed from 1.5 m/s to 6.5 m/s.

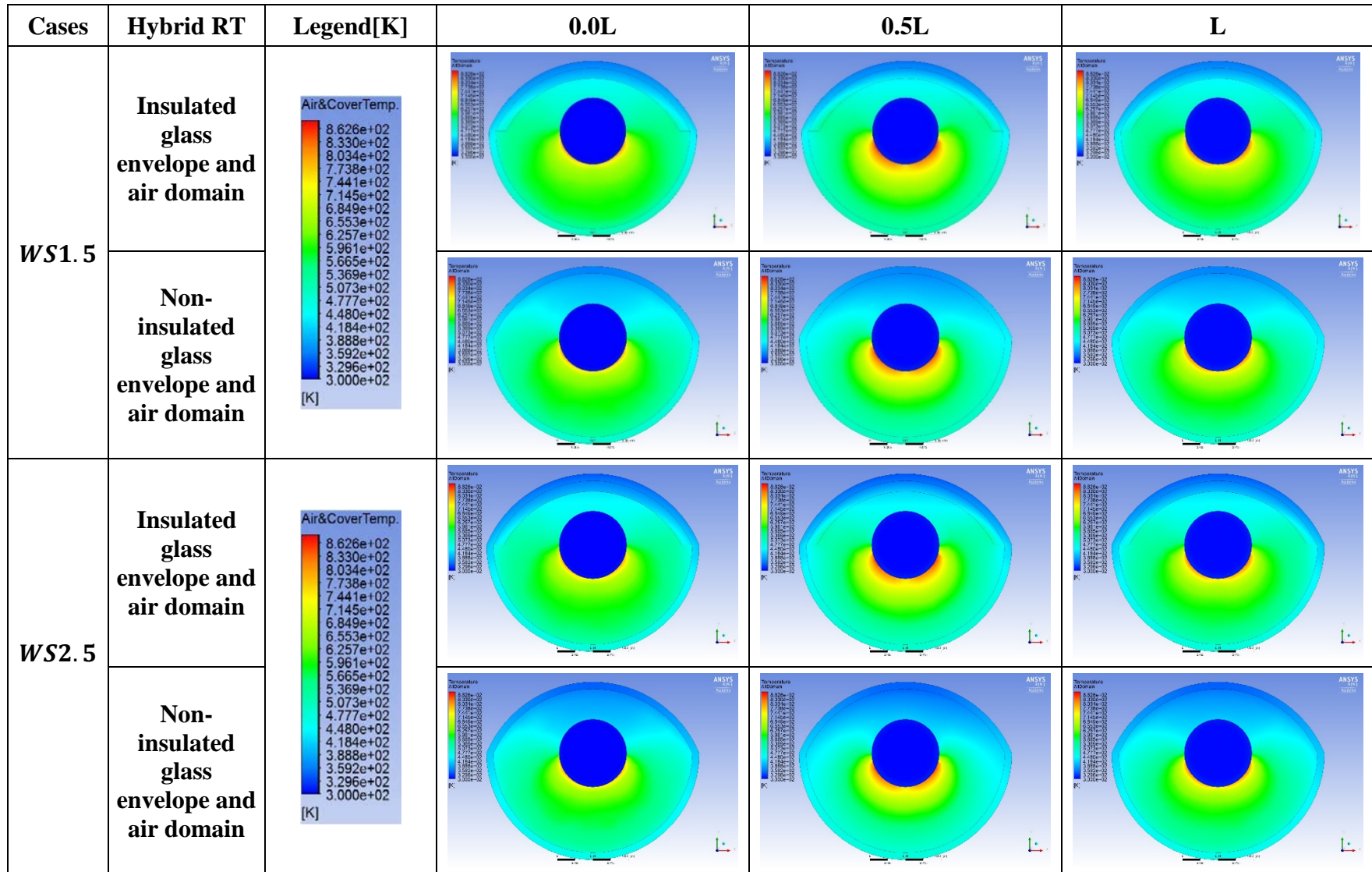


Figure B.1: Temperature distribution of annular air and glass cover domains of insulated and non-insulated hybrid receiver tube for smallest and largest variation wind speed (WS): 1.5 m/s and 2.5 m/s. Results are shown for different stations along the tube (0.0L, 0.5L and L).

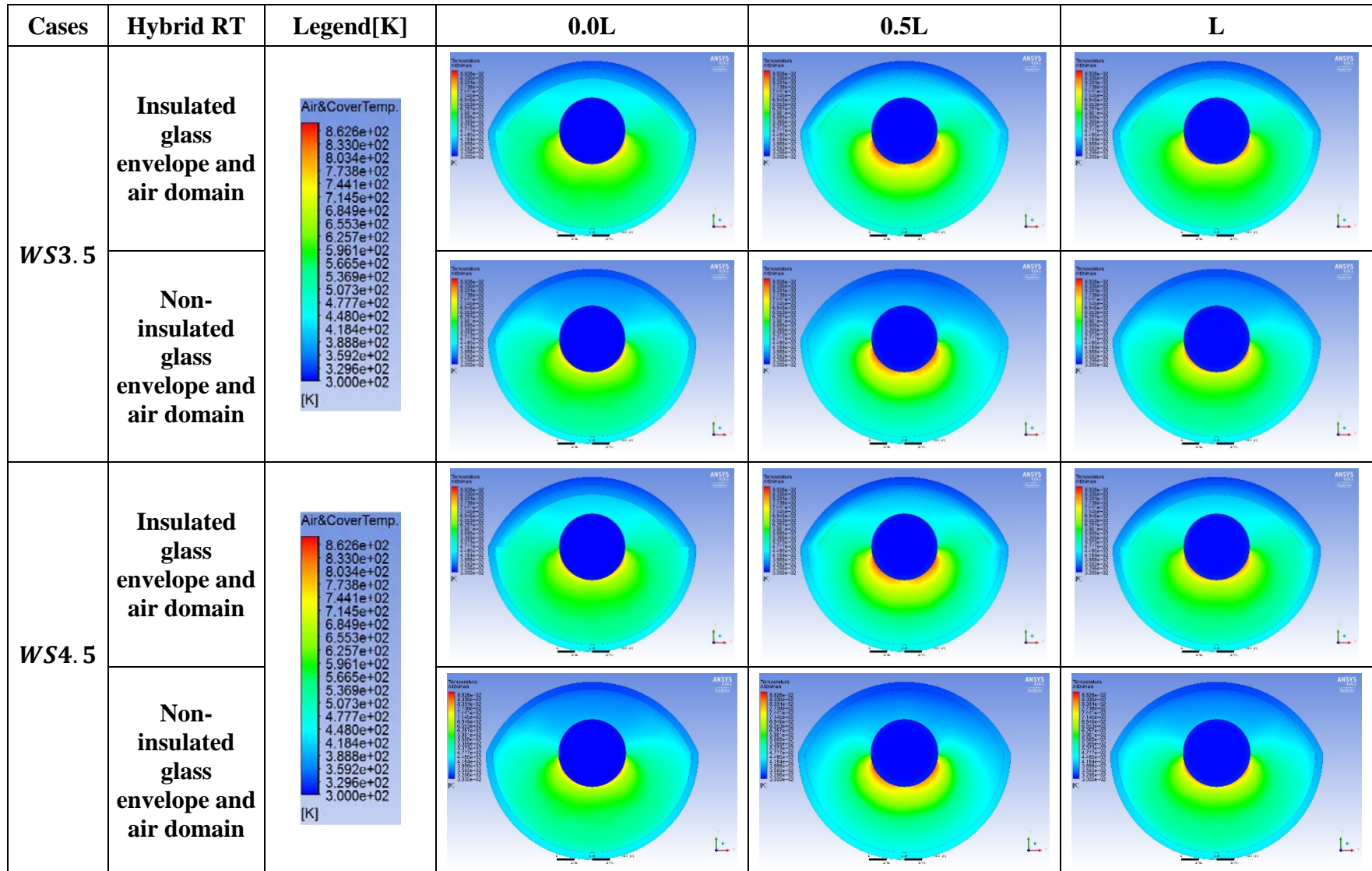


Figure B.2: Temperature distribution of annular air and glass cover domains of insulated and non-insulated hybrid receiver tube for smallest and largest variation wind speed (WS): 3.5 m/s and 4.5 m/s. Results are shown for different stations along the tube (0.0L, 0.5L and L).

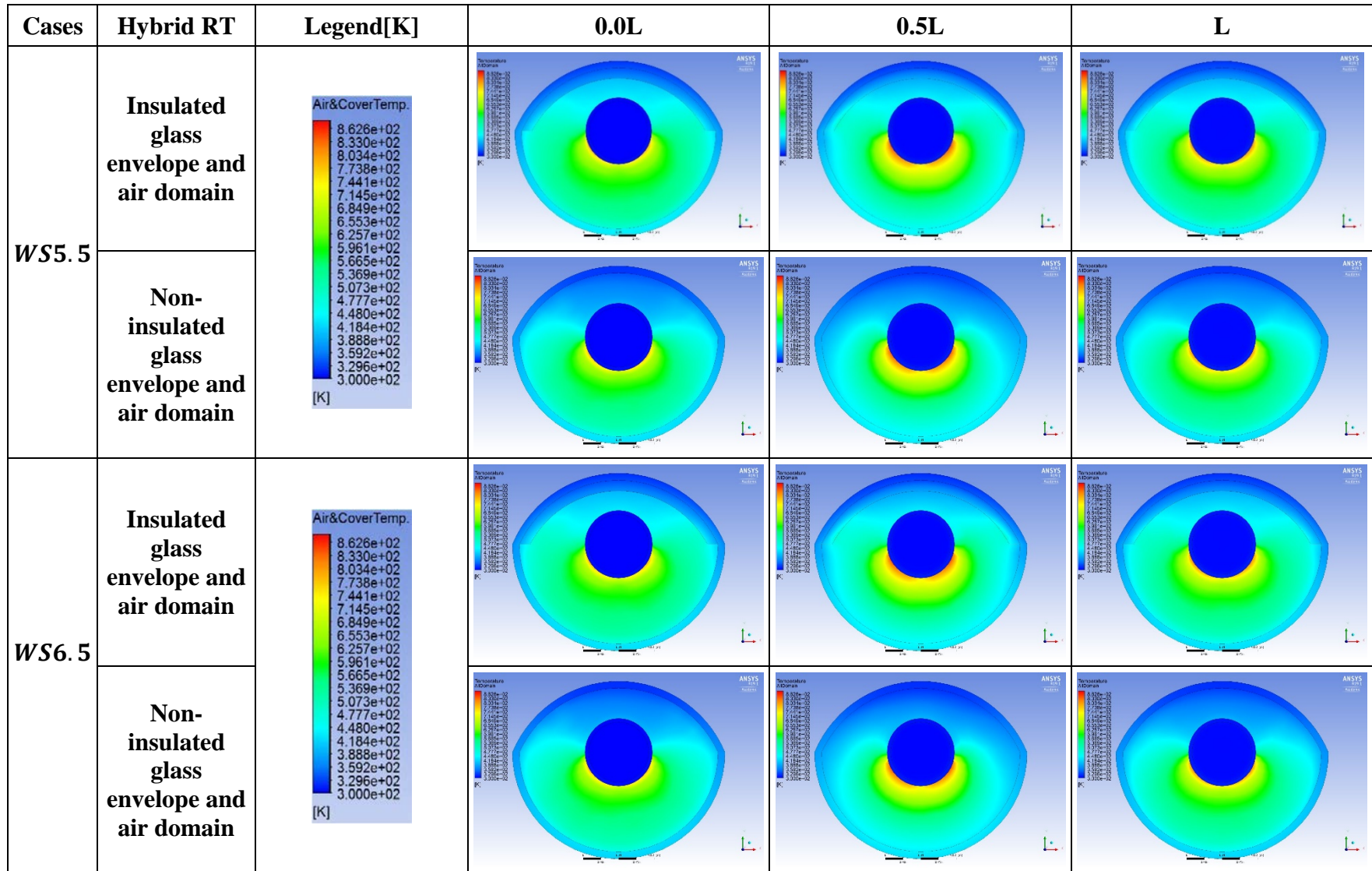


Figure B.3: Temperature distribution of annular air and glass cover domains of insulated and non-insulated hybrid receiver tube for smallest and largest variation wind speed (WS): 5.5 m/s and 6.5 m/s. Results are shown for different stations along the tube (0.0L, 0.5L and L).

# Appendix C Parabolic receiver tube

This appendix presents the glass envelope, insulation and air temperature distribution of the parabolic receiver tube under variation of wind speed from 1.5 m/s to 6.5 m/s. tests.

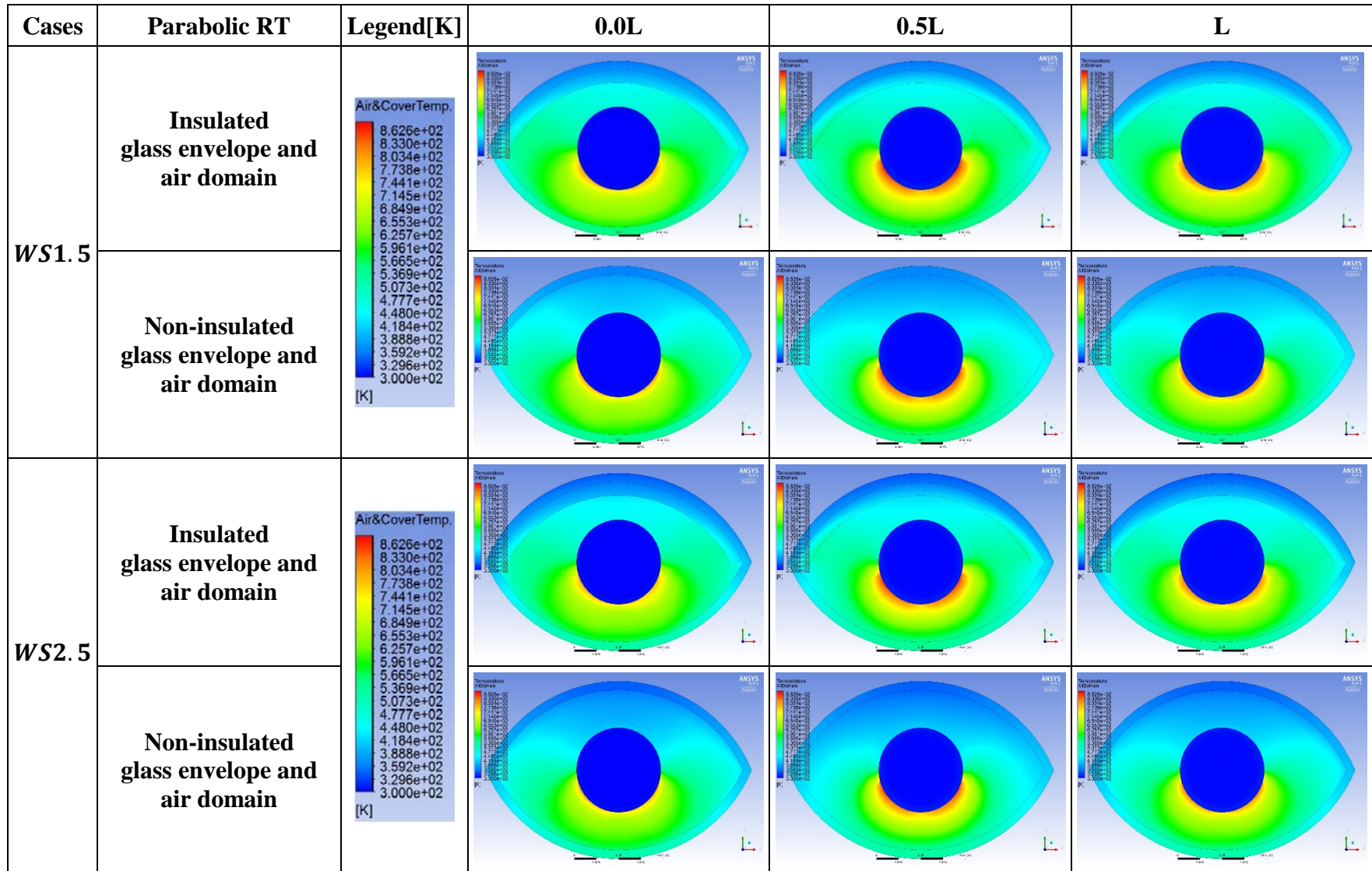


Figure C.1: Temperature distribution of annular air and glass cover domains of insulated and non-insulated parabolic receiver tube for smallest and largest variation wind speed (WS): 1.5 m/s and 2.5 m/s. Results are shown for different stations along the tube (0.0L, 0.5L and L).

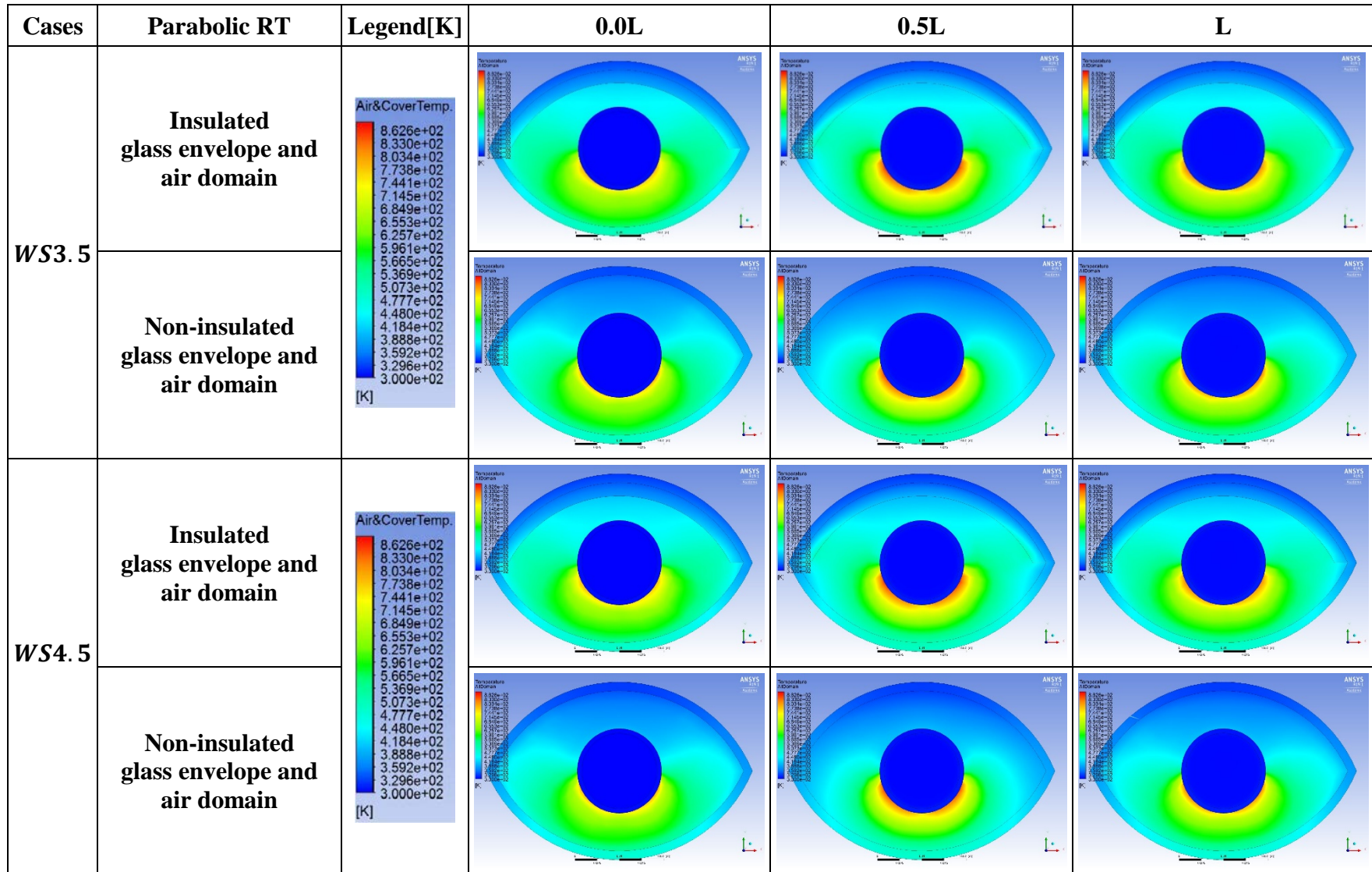


Figure C.2: Temperature distribution of annular air and glass cover domains of insulated and non-insulated parabolic receiver tube for smallest and largest variation wind speed (WS): 3.5 m/s and 4.5 m/s. Results are shown for different stations along the tube (0.0L, 0.5L and L).

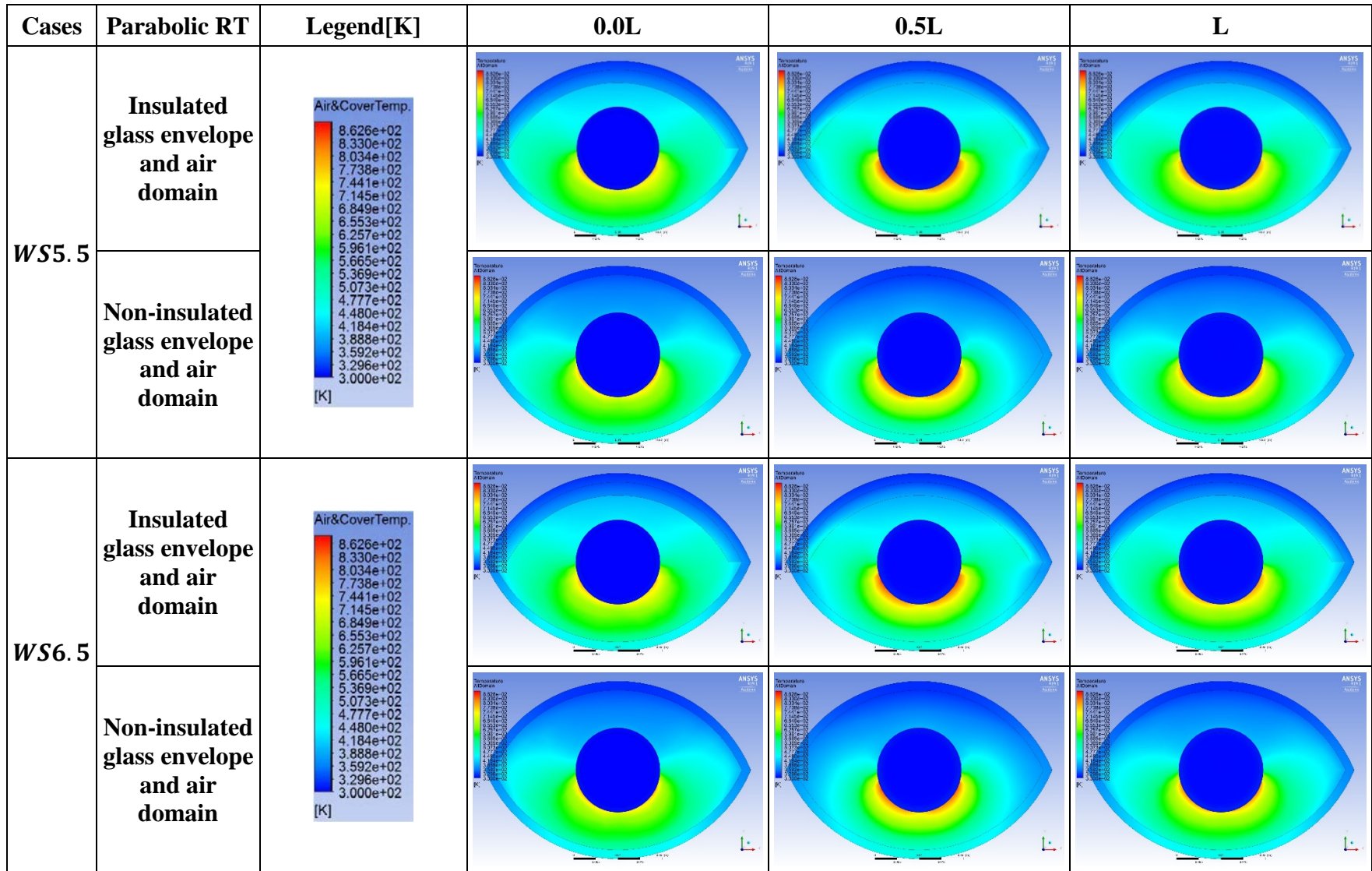


Figure C.3: Temperature distribution of annular air and glass cover domains of insulated and non-insulated parabolic receiver tube for smallest and largest variation wind speed (WS): 5.5 m/s and 6.5 m/s. Results are shown for different stations along the tube (0.0L, 0.5L and L).

# Appendix D Economic calculations for the modified receiver tubes

Appendix D Economic calculations for the modified receiver tubes.

This appendix contains the economic calculations showing the financial viability of the modified receiver tubes.

The average value of 1 MWh is approximately \$95 (Australian electricity prices 2018) and the cost of producing 1 MWh by solar plant is \$50; the Shams 1 power plant 100 MW PTSC electricity thermal plant (Shams 1 2019) is used in the below calculations as an example.

The yearly expected income of the 100MW PTSC electricity plant (using the modified receiver) is:

$$\$95/\text{MWh} * 100 \text{ MW} * 18 \text{ hrs/day} * 365 \text{ days} = \$62.4 \text{ million.}$$

The annual generation cost of the PTSC electricity plant is:

$$\$50/\text{MWh} * 100 \text{ MW} * 18 \text{ hrs/day} * 365 \text{ days} = \$32.8 \text{ Million.}$$

Therefore, the solar plant's yearly net financial income equals \$29.6 million. Therefore the additional financial income for the solar plant due to utilizing the modified receiver tube (that enhanced the power plant electricity generation by around 10%) equals approximately \$2.96 million.

The cost of the PTSC commercial evacuated receiver tube is approximately \$1000.

The total number of the receiver tubes for 100 MW PTSC plant is 27 684.

The expected cost for manufacturing the modified receiver tube is around 130% of the initial receiver tube cost (\$1000), thus the modified receiver tubes each cost approximately \$1300.

The total additional capital cost for installing the modified receiver tubes of the 100MW PTSC plant = \$8.3 million,

The payback period for the modified receiver tubes is the additional capital cost (\$8.3 million) versus the additional income (\$2.96 million per year), which is approximately equal to 2.8 years.